



HAL
open science

High-repetition-rate relativistic electron acceleration in plasma wakefields driven by few-cycle laser pulses

Dominykas Gustas

► **To cite this version:**

Dominykas Gustas. High-repetition-rate relativistic electron acceleration in plasma wakefields driven by few-cycle laser pulses. Accelerator Physics [physics.acc-ph]. Université Paris Saclay (COMUE), 2018. English. NNT: 2018SACLX118 . tel-02091135v2

HAL Id: tel-02091135

<https://pastel.hal.science/tel-02091135v2>

Submitted on 5 Apr 2019

HAL is a multi-disciplinary open access archive for the deposit and dissemination of scientific research documents, whether they are published or not. The documents may come from teaching and research institutions in France or abroad, or from public or private research centers.

L'archive ouverte pluridisciplinaire **HAL**, est destinée au dépôt et à la diffusion de documents scientifiques de niveau recherche, publiés ou non, émanant des établissements d'enseignement et de recherche français ou étrangers, des laboratoires publics ou privés.

High-repetition-rate relativistic electron acceleration in plasma wakefields driven by few-cycle laser pulses

Thèse de doctorat de l'Université Paris-Saclay
préparée à l'École Polytechnique

École doctorale n°572 ondes et matières (EDOM)
Spécialité de doctorat: Physique des plasmas

Thèse présentée et soutenue à Palaiseau, le 14 décembre 2018, par

Dominykas Gustas

Composition du Jury :

Patrick Audebert Directeur de recherche, École Polytechnique, LULI	Président
Philippe Balcou Directeur de recherche, Université de Bordeaux, CELIA	Rapporteur
Alexander Thomas Associate professor, University of Michigan, NERS	Rapporteur
Guy Bonnaud Professeur, INSTN, CEA	Examineur
Marie-Emmanuelle Couprie Directrice de recherche, SOLEIL synchrotron	Examinatrice
Jérôme Faure Directeur de recherche, École Polytechnique, LOA	Directeur de thèse

Contents

1	Introduction	5
1.1	Context	5
1.2	Objectives	7
1.3	Outline	8
2	Physics of laser wakefield accelerators	9
2.1	Ponderomotive force	10
2.2	Qualitative description	12
2.3	Laser-driven wakefield generation formalism	13
2.4	Accelerator injection schemes	23
2.5	LWFA limiting factors	27
2.6	Plasma effects on laser pulse propagation	30
2.7	Electron bunch propagation	35
2.8	Physics of gas jets	38
3	Experimental tools	43
3.1	Overview of the project	44
3.2	Laser system	46
3.3	Electron beam diagnostics	52
3.4	Target characterisation	57
3.5	Numerical modelling	62
4	Acceleration experiments	65
4.1	MeV electrons at kHz repetition rate	66
4.2	Shocked nozzle experiments	77
4.3	Stable MeV electrons due to tight focusing	83
4.4	Laser pulse duration influence study	91
4.5	CEP effect measurements	98
5	Discussion, future perspectives and conclusions	103
A	Additional results	107
A.1	Plasma lensing	107
A.2	Observation of electron rings	108
	Bibliography	111
	Publications	119

Acknowledgements

The results presented in this thesis is the outcome of collective work of many team members. Most of the credits definitely go to Jérôme Faure, whose expertise and diligence led to a very well designed project with clear path and objectives to work on. His high quality standards permitted having an output of several international level publications that may be found at the back of this book, and patience discussing various physical aspects left the author of this manuscript as well as the other group members with few knowledge loopholes on how to aim for this quality. Secondly, nothing would have been possible without a long-term dedication and leadership by Rodrigo Lopez-Martens, whose team has for many years been devotedly developing the state-of-the-art laser system used in all the described experiments, introducing numerous highly innovative solutions on the way. Of greatest importance has been Aline Vernier, the main person behind putting the ideas of the two group leaders work in practice, always in the most clean and elegant way. Her efforts have made the setup as convenient to operate as possible, and her multi-skillfulness helped to overcome many unexpected obstacles of various sorts during the project. Diego Guénot has been the main driver of experimental execution during the first half of this thesis, when the most important breakthroughs were achieved. However, among the intense moments of fixing the never-ending final bugs he has always found time to teach the newly-arrived author the very basics of optics laboratory skills, which eventually permitted successful continuation with less human resources after his departure. Benoit Beaurepaire, the first PhD student of the project, delivered a lot of first hardware design and preliminary plasma acceleration studies, without which the later push to a higher maturity output could not have happened. Crucial has also been the major laser system upgrade by Frederik Böhle, whose hands were later just as well replaced by Marie Ouillé. The implementation of the CEP control tool by her together with Stefan Hässler allowed obtaining one of the most interesting sets of experimental data presented in this manuscript. A lot of troubles have been avoided by using microstructured plasma targets suggested and provided by François Sylla from SourceLab. Finally, it was a great pleasure to receive a lot of attention and input from Agustin Lifschitz, one of the best experts of numerical studies in the field, bringing a significantly clearer perspective into interpreting our results.

For other contributions through practical help or motivating scientific discussions the author would also like to thank lab colleagues Isabel, Geoffrey, Maxence, Mariusz, Neil, Sadman, Shankar, Jean-Baptiste, Melek, Magali, Maimouna, Natalia, Zhao, Dan, Domenico, Florian, Francesco, Bernard and Jean-Lou. The efficient administrative support from Carole, Catherine, Sandrine and Patricia as well as quick solutions to IT problems by Maxence have made it much easier to focus on the experimental work. The PhD adventure would not have been as exciting without Parisian friends Behrang, Michell, Silvia, Thomas, Aude, Carla, Ceren, Elena, Francesco, Hana, Marco, Aldo, Anaëlle, Barbara, Francesca, Gabriele, Giorgio, Oussama, Otávio, Zineb, Johanna, Nicolas, Ricardo, Abhishek, Matthias, Liburn, Clarisse, Ludovica, Beatrice, Gabrielè, Lipsa, Anna, Olga, Kotryna, Lukas, Julija, Ieva, Laura, Marija and whoever could have been briefly forgotten at this moment of writing the Acknowledgements' section shortly before the fast approaching submission deadline. Special thanks from the author goes to his family, always supportive of his endeavours.

Résumé en français

Le progrès continu de la technologie laser a récemment permis l'avancement spectaculaire d'accélérateurs de particules par onde de sillage. Cette technique permet la génération de champs électriques très forts, pouvant dépasser de trois ordres de grandeur ceux présents dans les accélérateurs conventionnels. L'accélération résultante a lieu sur une distance très courte, par conséquent les effets de la charge d'espace et de la dispersion de vitesse sont considérablement réduits. Les paquets de particules ainsi générés peuvent alors atteindre des durées de l'ordre de la femtoseconde, qui en fait un outil prometteur pour la réalisation d'expériences de diffraction ultra-rapide avec une résolution inégalée de l'ordre de quelques femtosecondes. La génération de tels paquets d'électrons avec des lasers de 1 J et d'une durée de 30 fs est à présent bien établie. Ces paramètres permettent de produire des faisceaux d'électrons de quelques centaines de MeV, et sont donc inadaptés aux expériences de diffraction. De plus, le taux de répétition de ces lasers de haute puissance est limité à quelques Hz, ce qui est insuffisant pour des expériences exigeant une bonne statistique de mesure. Les travaux présentés dans ce manuscrit utilisent un laser de pointe développé au laboratoire par le groupe PCO du Laboratoire d'Optique Appliquée générant des impulsions de quelques millijoules, d'une durée de 3.4 fs - à peine 1.3 cycle optique - à une cadence de 1 kHz, pour accélérer des électrons par onde de sillage. L'obtention de cette durée était possible grâce à un système d'élargissement spectral de post-compression, et cela a permis l'éclairement sur cible de l'ordre de $2 - 3.5 \times 10^{18} \text{ W/cm}^2$, donc au début du régime relativiste.

Le chapitre 1 introduit le sujet et donne une histoire brève des accélérateurs de particules et leur évolution conceptuelle. Le chapitre 2 rappelle des concepts de physique d'interaction laser-plasma requis pour la compréhension de la suite de l'exposé. Le chapitre 3 présente des lois d'échelle pour l'accélération par sillage et le système utilisé pour les expériences. Le laser, le détecteur et le spectromètre d'électrons, et aussi les différentes cibles de gaz sont caractérisés. Le chapitre 4 expose les résultats expérimentaux accumulés pendant le projet. Les premiers faisceaux de particules relativistes (4 – 7 MeV) sont obtenus, mais la stabilité n'est pas satisfaisante et les paramètres dépendent fortement de la dérive de fréquence imposée sur le laser. Le mécanisme d'injection par un choc hydrodynamique est ensuite étudié, produisant des électrons de 0.5 – 1 MeV. Avec une focalisation plus forte, $f/2$ au lieu de $f/3$, et une buse supersonique de l'échelle micrométrique un faisceau relativiste est récupéré, cette fois considérablement plus stable et contenant plus de charge, mais aussi plus sensible aux propriétés de la cible. Les observations sont expliquées à l'aide de simulations numériques. Les dernières campagnes expérimentales étudient les dépendances de la largeur spectrale des impulsions ultra-courtes et leur phase de porteuse (CEP). Les annexes présentent quelques résultats supplémentaires curieux.

Ce manuscrit de thèse présente d'une part la première démonstration d'un accélérateur des particules relativistes opéré dans le régime de la bulle à haute cadence. De plus, cette thèse vise à l'élargissement de notre compréhension des lois d'échelle d'accélération laser-plasma. Nous espérons que notre travail visant à la fiabilisation et l'optimisation de cette source permettra à terme de proposer un instrument accessible et fiable à la communauté scientifique, que ce soit pour la diffraction d'électrons, l'irradiation ultra-brève d'échantillons ou la génération d'impulsions de rayons X femtosecondes.

1

Introduction

Contents

1.1	Context	5
1.2	Objectives	7
1.3	Outline	8

1.1 Context

Over the last 150 years particle accelerators have become very important both for fundamental scientific research and, what is perhaps somewhat less brought to public awareness, various applications in our daily life. First accelerators were assembled unknowingly in mid-to-late XIX century and were based on electrostatic fields created between two electrodes with an applied DC voltage. Placed in an evacuated glass tube, the electrodes would create glowing structures that adjusted their behaviour depending on the voltage, vacuum level, and also responded to external magnetic fields (Goldstein, 1876), (Crookes, 1879), implying some charged matter was responsible for the phenomenon. Experimenting with and trying to explain these so-called cathode rays led J. J. Thomson to the discovery of the electron, the earliest determined subatomic particle (Thomson, 1901), and permitted W. Röntgen to generate and give a first solid description of X-rays (Röntgen, 1896), that have henceforth been extensively utilized in material science (Bragg, 1913) and medicine (Figure 1.1). By the end of 1950s cathode ray tubes had not only aided reseachers for numerous purposes, such as revealing the structure of the DNA molecule (Watson & Crick, 1953) via X-ray diffraction, but were already present in millions of households that owned a television device, inside which the phosphorescence triggered on the screen by a stream of accelerated electrons would be used to create images. Higher energy beams could be obtained by Cockcroft-Walton and Van de Graaff generators, permitting the



Figure 1.1 – First X-ray photograph of a human hand (Röntgen, 1896).

split of an atom and further major breakthroughs in nuclear science (Cockcroft & Walton, 1932) (Van de Graaff, Compton, & Van Atta, 1933).

In the meantime, a more complex class of accelerators has been developed in laboratories, in which electrodynamic radio-frequency (RF) fields instead of static ones would be used to speed particles up. Due to the oscillations in field strength and polarity synchronized with the particle propagation, gradients higher by more than an order of magnitude (> 100 MV/m in modern systems) could be supported before an electrical breakdown between the electrodes would occur. Two most popular designs of this kind are linear accelerators (Widerøe, 1928) and synchrotrons (McMillan, 1945), the former having a comparative size and cost disadvantage, the latter suffering from energy losses via synchrotron radiation owing to the circular beam trajectory. A well-known combination of both, the Large Hadron Collider at CERN, is 27 kilometers in circumference and is currently able to yield 7 TeV proton bunches. Head-to-head collisions of such ultraenergetic nucleons resulted in detection of a long-anticipated new particle, the Higgs boson (ATLAS Collaboration, 2012), the last remaining piece of the Standard Model puzzle. Modern basic research on matter is also greatly supported by active developments of fourth-generation light sources, known as free electron lasers, which use the output of kilometer-long linear accelerators to generate brilliant flashes of coherent X-rays (Emma et al., 2010).

Evidently scaling up particle energies even further would require enormous resources, as the only way to do so with the given methodology is to proceed building larger facilities. This has motivated continued research in alternative accelerator techniques. A very promising direction was theoretically proposed by T. Tajima and J. M. Dawson (Tajima & Dawson, 1979), who showed that relativistic electron bunches could be obtained over very short distances from waves created behind an intense laser pulse ($> 10^{18}$ W/cm²) propagating in a tenuous plasma due to the nonlinear ponderomotive force (Figure 1.2).

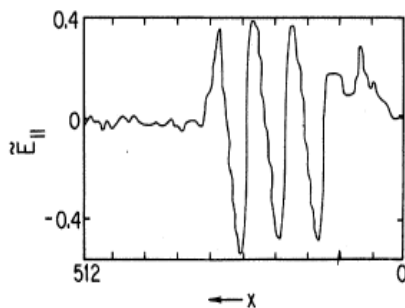


Figure 1.2 – Simulated longitudinal electric field profile in a plasma perturbed by an intense laser pulse (Tajima & Dawson, 1979).

They predicted electric fields of 100 GV/m, or larger by three orders of magnitude than typical RF systems. A 1 GeV electron beam would thus require acceleration length of 1 cm only, as opposed to 10 meters with the traditional method, to which an even larger additional distance of beam transport in-between different stages needs to be added. Using the analogy to a trail of disturbed water left on the sea surface by the passage of a ship (the *wake*), the process has been named laser wake-field acceleration (LWFA). The first demonstrations and subsequent improvements of LWFA were largely parallel to advancements in laser technology, powered by the chirped-pulse amplification (CPA) concept (Strickland & Mourou, 1985), which allowed entering the necessary high-intensity regime. MeV-scale electrons were demonstrated with ≈ 1 ps multi-terawatt pulses (Nakajima et al., 1995) (Modena et al., 1995), and the beam quality would later get dramatically enhanced with joule-class titanium-sapphire ultrashort (≈ 30 fs) laser systems developed in several laboratories (Malka et al., 2002) (Leemans et al., 2002) (Mangles et al., 2004) (Geddes et al., 2004) (Faure et al., 2004). This brought improved understanding of underlying physics, and emphasized the significance of good target parameter control. Using light guiding in a preformed plasma channel, first GeV-scale particle bunches were obtained soon thereafter (Leemans et al., 2006). Ever since these important demonstrations, the number

of scientists working in the field has surged, and a lot of studies pushing the boundaries further, optimizing different beam properties or validating proof-of-concept schemes for various applications have been done. Nevertheless, the technology has not yet managed to cross the border between its testing phase and providing a reliable facility or a commercial product. The presence of many competing nonlinear laser-plasma interaction processes still results in high shot-to-shot fluctuations, overly wide energy spread, lack of confident tunability and unsatisfying beam divergence, making such sources improper for practical use at this moment.

1.2 Objectives

In addition to strong gradients (or, as to be seen later, to a large extent *because of* them), relativistic electron bunches obtained by LWFA have also been observed to feature extremely short durations, all the way down to sub-5 fs level (Lundh et al., 2011). This triggers immediate interest for applications in ultrafast material science, i. e. the study of dynamic evolution of excited states of matter. It has already become an established research domain through the use of modified DC and RF accelerators, where only the initial injection of particles is aided by an ultrashort laser pulse (Sciaini & Miller, 2011). This short particle bunch then propagates within the cavity, until it reaches the required energy through interaction with the electric fields. It is then made to hit a thin crystal sample, getting the particles diffracted in several directions defined by the inner sample geometry, which is the subject of the study. Moreover, one may deliberately induce a short-lived structural change in the material, e. g. by another femtosecond laser pulse, in such circumstances also called the *pump*. By varying the delay between the pump and the electron bunch (or the *probe*) one can make movies of ultrafast geometry variations within the sample. Now, due to several intrinsic limitations of collective particle propagation, pump-probe experiments with better than 100 fs temporal resolution have so far not been produced, and thus LWFA appears plausible for an improvement by one or even two orders of magnitude. In order to achieve this goal, the mentioned stability problems have to be resolved, which can be done in two ways – reducing shot-to-shot uncertainties through better control of the process or increasing the repetition rate to wash out these fluctuations by averaging. Our group is tackling both by employing a diode-pump-based kilohertz laser system *Salle Noire* developed by the group *Physique du Cycle Optique* (PCO) at Laboratoire d’Optique Appliquée (LOA) (Böhle et al., 2014) to drive particle acceleration in continuous-flow gas jets. Limited by crystal thermal effects, operation at such high repetition rate is currently accessible at $\lesssim 10$ mJ energies only. Hence in order to achieve the necessary relativistic intensities, the standard ≈ 30 fs pulse defined by the titanium-sapphire emission spectrum bandwidth has to be further temporally post-compressed to nearly a single optical cycle, or < 4 fs. This has been done by spectral broadening in a helium-filled hollow-core fiber and compensating the chromatic dispersion with a set of broadband multilayered chirped mirrors.

The primary aim of the work presented in this thesis is to prove experimentally that such laser pulses are capable of driving an MeV-scale electron accelerator. Once established, further goal is to understand the physics particular to this rather exotic regime, explore which laser-plasma interaction phenomena come into play, and to what extent. Differences with the preceding LWFA experiments may be expected. Single-cycle optical pulses challenge the concept of averaged ponderomotive force, responsible for driving the wakefield. They have an octave-spanning spectral bandwidth, which may lead to significant plasma dispersion effects. This is even more likely to be emphasized at high density plasmas, which as we shall see later are required here for matching wakefield resonance conditions. To exactly

reproduce the acceleration process with each shot, carrier-envelope phase might turn out to be important. Knowledge on all these influences is necessary in order to optimize the particle beam for highest charge and stability, appropriate energy, lowest divergence and possibly even the shortest duration. This thesis presents several experiments aimed at understanding some of the different phenomena and attempting to maximize control on the electron source output parameters. Analysis of real data has been aided by numerical simulation tools. The work serves as a preparatory stage for an expected future upgrade to an ultrafast electron diffraction facility.

1.3 Outline

The manuscript is organized as follows. Chapter 2 overviews the general theory of LWFA and introduces the necessary concepts required for later discussion of the experiments. Chapter 3 explores the particular features of this project and describes the accelerator equipment. Measurements characterizing the laser system, electron beam diagnostics and various plasma targets are presented, the numerical code used to model our experiments is briefly reviewed. Chapter 4 reports on the different campaigns, displays and analyses the important accumulated data and discusses the performance of our accelerator as well as the possible reasons for various observations, either qualitatively or through supporting numerical studies. Finally, Chapter 5 gives a brief summary of the thesis and suggests guidelines for possible future developments. Several additional peculiar results are presented in the appendix.

2

Physics of laser wakefield accelerators

Contents

2.1	Ponderomotive force	10
2.2	Qualitative description	12
2.3	Laser-driven wakefield generation formalism	13
2.3.1	1D plasma wave model	13
2.3.2	Wakefields driven by weak Gaussian pulses	15
2.3.3	Strongly driven wakefields and the blowout regime	21
2.4	Accelerator injection schemes	23
2.4.1	External injection	23
2.4.2	Self-injection by wave breaking	23
2.4.3	Colliding-pulse injection	24
2.4.4	Ionization-induced injection	24
2.4.5	Density-downramp injection	25
2.4.6	Other injection types due to wakefield slow-down	26
2.4.7	Combined injection methods	27
2.5	LWFA limiting factors	27
2.5.1	Diffraction	27
2.5.2	Laser depletion	28
2.5.3	Dephasing	28
2.5.4	Beam loading	29
2.6	Plasma effects on laser pulse propagation	30
2.6.1	Relativistic self-focusing	30
2.6.2	Dispersion	32
2.6.3	Ionization-induced defocusing	34
2.6.4	Ionization-induced compression	34

2.7	Electron bunch propagation	35
2.7.1	Velocity dispersion	35
2.7.2	Space-charge	36
2.8	Physics of gas jets	38
2.8.1	Subsonic gas jets	38
2.8.2	Supersonic gas jets	38
2.8.3	Supersonic gas jets with a shock	40

Chapter overview

In this chapter the principal components of a laser wakefield accelerator are discussed and the underlying physical processes described. Main advantages and limitations of the technique are presented. Few target design concepts are introduced to counter these limitations.

2.1 Ponderomotive force

When a charged particle oscillates in a spatially or/and temporally inhomogeneous electromagnetic field, the total experienced force over a positive half-cycle is not exactly compensated after the sign reversal. Consequently, the particle may gain or lose net energy during the process (Boot & Harvie, 1957) (Meyerhofer, Knauer, McNaught, & Moore, 1996). This can be attributed to a term called the *ponderomotive force*. It is easily demonstrated in the non-relativistic case (Rax, 2005). Suppose a particle of mass m and charge q is located at position $\mathbf{r} = (x, y, z)$ in a transversely polarized electromagnetic field propagating in the z -direction and therefore described by

$$\mathbf{E}(\mathbf{r}, t) = \mathbf{E}(\mathbf{r}) \cos(kz - \omega t),$$

$$\mathbf{B}(\mathbf{r}, t) = \mathbf{B}(\mathbf{r}) \cos(kz - \omega t),$$

where k is the absolute value of the wave vector, ω is the angular frequency, and t is time. Here we assume the variation scale for respective electric and magnetic field amplitudes $\mathbf{E}(\mathbf{r})$ and $\mathbf{B}(\mathbf{r})$ to be much larger than the wavelength $\lambda = 2\pi/k$. The equation of motion for the test particle is thus

$$\frac{d^2\mathbf{r}}{dt^2} = \frac{q}{m}\mathbf{E}(\mathbf{r}) \cos \phi(t) + \frac{q}{m} \frac{d\mathbf{r}}{dt} \times \mathbf{B}(\mathbf{r}) \cos \phi(t), \quad (2.1)$$

where $\phi(t) = kz - \omega t$. In the non-relativistic regime, to a first approximation, the magnetic term can be ignored. One may therefore write

$$\mathbf{r}(t) = \mathbf{r}_0 + \mathbf{r}_l(t) + \mathbf{r}_{nl}(t),$$

where \mathbf{r}_0 is the initial position of the test particle, $\mathbf{r}_l(t)$ is the first-order perturbation which solves

$$\frac{d^2\mathbf{r}_l}{dt^2} = \frac{q}{m}\mathbf{E}(\mathbf{r}) \cos \phi(t),$$

and $\mathbf{r}_{nl}(t)$ is a higher-order correction term. The above equation can be easily integrated:

$$\mathbf{r}_l(t) = -\frac{q}{m\omega^2}\mathbf{E}(\mathbf{r}) \cos \phi(t).$$

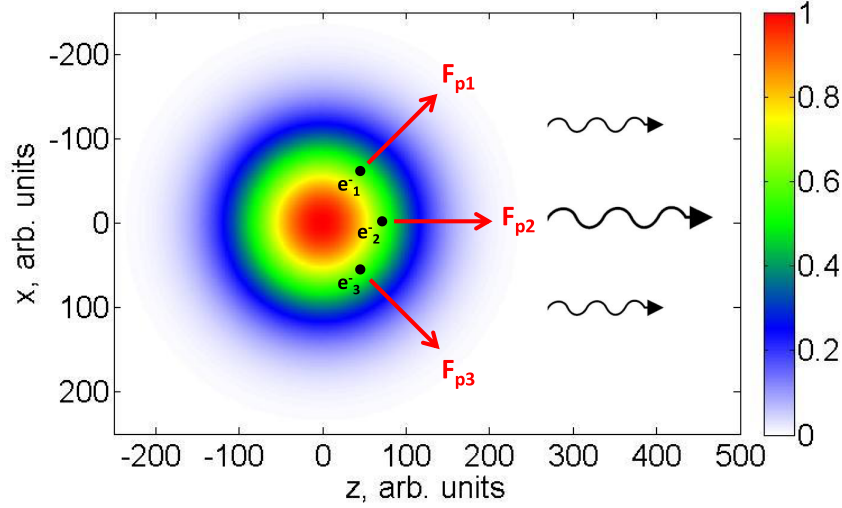


Figure 2.1 – Schematic overview of the ponderomotive force. A laser pulse with spherically symmetric Gaussian intensity distribution (normalized color scale) is propagating towards the right (black arrows). Three test electrons are encountered on the way, at some instant positioned at equal radial distances from the pulse center. They experience respective forces F_{p1} , F_{p2} and F_{p3} , that are equal in magnitude, but pointing in different directions radially outwards (red arrows), pushing electrons 1 and 3 away from the optical axis.

The factor $1/\omega^2$ appears due to the integral of $\phi(t)$. We now go back to the full equation 2.1 and expand the E-field term around \mathbf{r} as a Taylor series:

$$\frac{m}{q} \frac{d^2 \mathbf{r}}{dt^2} = (\mathbf{E}(\mathbf{r}) + \mathbf{r}_l \nabla \mathbf{E}(\mathbf{r})) \cos \phi(t) + \frac{d\mathbf{r}}{dt} \times \mathbf{B}(\mathbf{r}) \cos \phi(t).$$

Using the expression for \mathbf{r}_l and considering again the fact that the terms with \mathbf{r}_{nl} are relatively small yields

$$\begin{aligned} \frac{m}{q} \frac{d^2 \mathbf{r}_{nl}}{dt^2} &= \mathbf{r}_l \nabla \mathbf{E}(\mathbf{r}) \cos \phi(t) + \frac{d\mathbf{r}_l}{dt} \times \mathbf{B}(\mathbf{r}) \cos \phi(t) \\ &= -\frac{q}{m\omega^2} \mathbf{E}(\mathbf{r}) \nabla \mathbf{E}(\mathbf{r}) \cos^2 \phi(t) - \frac{q}{m\omega} \mathbf{E}(\mathbf{r}) \times \mathbf{B}(\mathbf{r}) \cos^2 \phi(t). \end{aligned}$$

Finally, we average the cosine function over a full rapid cycle, and use the vector identity $(\mathbf{E} \cdot \nabla) \mathbf{E} = \frac{1}{2} \nabla E^2 - \mathbf{E} \times (\nabla \times \mathbf{E})$, combined with Faraday's law, to obtain

$$\left\langle \frac{d^2 \mathbf{r}_{nl}}{dt^2} \right\rangle = -\frac{q^2}{4m^2 \omega^2} \nabla E^2.$$

Hence we conclude the "slow" force is proportional to the gradient of the electric field intensity, and the minus sign implies the particle is being pushed away from the strong-field zones towards the areas where the field is weak (Figure 2.1). A further interesting point is that such behavior is independent of the wave polarization. This effect is defined as the *ponderomotive force*. When particle interaction with intense laser fields is considered ($I > 10^{18} \text{ W/cm}^2$), the assumption that $\mathbf{r}_l(t)$ and $\mathbf{r}_{nl}(t)$ are small compared to \mathbf{r}_0 is no longer valid, making the Taylor expansion inappropriate and the general relativistic treatment more complex (Quesnel & Mora, 1998). However, the final result is qualitatively the same – the force being proportional to the intensity gradient and pointing to its opposite direction.

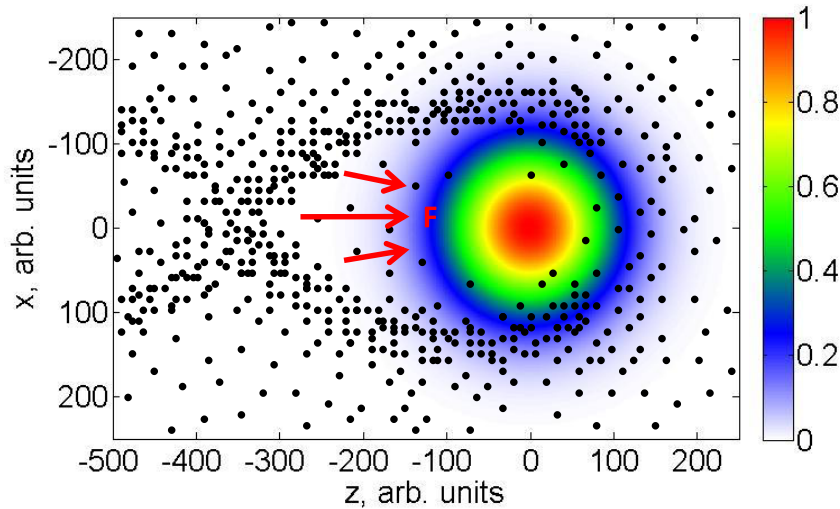


Figure 2.2 – Schematic view of a wakefield structure. A laser pulse with spherically symmetric Gaussian intensity distribution (normalized color scale) is propagating towards the right, pushing the encountered electrons, here depicted as a collection of particles (black dots). This push causes density perturbations and excites plasma waves. Areas of strong Coulomb fields (red arrows) are thus created, that may accelerate appropriately placed test electrons to relativistic velocities. Note that off-axis these fields also have a radial component that can focus the beam. A more common way is to consider the electrons as a charged fluid, and this approach will be preferred later.

2.2 Qualitative description

The principle of laser wakefield acceleration usually relies on sending a single intense and ultrashort laser pulse into a gas target (Mangles et al., 2004) (Geddes et al., 2004) (Faure et al., 2004). The intensity achieved around the focal plane is orders of magnitude larger than the one required to ionize the gas, thus a volume of plasma is created in the proximity of the optical axis already before the main part of the pulse arrives. Hence it can often be assumed the laser is interacting directly with ionized matter. Since a light pulse has finitely extended spatio-temporal profile, plasma electrons are indeed exposed to an inhomogeneous electromagnetic field, and all the previous considerations regarding the ponderomotive force apply. While heavy ions effectively remain at their initial positions, the electrons get pushed away from the optical axis, leaving a net positive charge in this area. After the laser pulse passes by, this positive charge attracts the displaced electrons back, and a Langmuir oscillation is initiated (Tonks & Langmuir, 1929). A periodic structure of electronic density modulations then forms along the optical axis, and consequently it contains areas of Coulomb fields that may reach enormous amplitudes if driven by strong ponderomotive gradients (Figure 2.2). This waveform follows the light pulse with a phase velocity v_p equal to the laser group velocity v_g^{las} , which depends on the plasma density and is close to c . Such structure has also been observed directly in an experiment (Matlis et al., 2006) (Buck et al., 2011). If a co-propagating relativistic electron could be placed at an appropriate phase of this wave, it may "surf" the inner Coulomb field and gain additional energy. The "placement" of the electron can be external or occur automatically due to various reasons during the interaction between the plasma and the wakefield driver. Several known injection schemes with their advantages and disadvantages will be presented in section 2.4. In addition to high accelerating gradients, the wake structure possesses strong focusing forces, permitting improved output beam quality

in comparison to other laser-plasma interaction regimes. Even more, these focusing fields may cause accelerated particles to oscillate transversely to the direction of motion, creating a betatron X-ray source (Corde, Ta Phuoc, et al., 2013) that may turn out to be applicable in high-resolution imaging in medicine or industry. In the following the main concepts will be explored in greater detail.

2.3 Laser-driven wakefield generation formalism

2.3.1 1D plasma wave model

Good intuition about the behaviour of plasma waves and the transition between linear and nonlinear regimes can be obtained from a relatively simple one-dimensional model, as developed in (Dawson, 1959). Suppose a finite homogeneous collection of electrons gets perturbed in one dimension only. Let $X(x_0)$ be the displacement of an electron with equilibrium position x_0 , the motion being identical for all the particles in the given yz -plane. We assume the ordering of electrons is preserved, which is true if the change in X for a change Δx_0 of the equilibrium position is larger than $-\Delta x_0$. This condition can be formulated as

$$\frac{\partial X}{\partial x_0} > -1. \quad (2.2)$$

The total electron coordinate is given by $x = x_0 + X(x_0)$. While moving a distance $X(x_0)$ the electrons from the equilibrium plane x_0 pass by an amount of positive charge equal to en_0X per unit area, where e is the elementary charge, and n_0 is the unperturbed plasma density. Hence, if X is taken positive for the sake of the argument, we now have an excess positive charge en_0X per unit area on the negative side of the electron sheath, and an excess negative charge $-en_0X$ per unit area on the positive side. From Gauss' theorem one can write the E-field at the electron to be

$$E = \frac{1}{\epsilon_0} en_0X,$$

yielding an equation of motion for the particle:

$$m_e \frac{d^2 X}{dt^2} = -eE = -\frac{1}{\epsilon_0} e^2 n_0 X,$$

or

$$\frac{d^2 X}{dt^2} = -\omega_p^2 X,$$

where ϵ_0 is the vacuum permittivity, m_e is the electron mass, and $\omega_p = \sqrt{\frac{e^2 n_0}{m_e \epsilon_0}}$ is defined as the plasma frequency. This is a usual equation of motion for a harmonic oscillator with the well-known general solution given by

$$X(x_0) = X_1(x_0) \sin \omega_p t + X_2(x_0) \cos \omega_p t.$$

Therefore, each electron undergoes harmonic oscillations about its equilibrium position independently of other particles. Let us consider now a particular solution of this equation described by

$$X_1(x_0) \equiv 0, \quad X_2(x_0) = A \sin kx_0,$$

so that at $t = 0$ we have:

$$\begin{aligned} X &= A \sin kx_0, \\ E &= \frac{1}{\epsilon_0} en_0 A \sin kx_0, \\ x &= x_0 + X = x_0 + A \sin kx_0. \end{aligned}$$

This is of special interest considering the previously discussed concept of ponderomotive force, which has zero transverse component right on the optical axis (we could assign $x_0 = 0$ there, so that also the initial displacement $X_{t=0}$ is zero), and grows larger further away from it, until one starts exiting the laser field. Let us plot now E/E_{max} as a function of x , the curve being described by the parametrisation:

$$\begin{cases} x = x_0 + A \sin kx_0, \\ \frac{E}{E_{max}} = \sin kx_0, \end{cases}$$

where $E_{max} = \frac{1}{\epsilon_0} en_0 A$ and x_0 is the parameter. We can immediately find that E/E_{max} will be zero for

$$x = \frac{\pi l}{k}, \quad l \in \mathbb{Z}.$$

If we limit ourselves to one full sinusoidal cycle we find three zeros at $x = -\pi/k$, $x = 0$ and π/k . To further determine the shape of the curve we estimate the first derivatives with respect to x_0 :

$$\begin{cases} \frac{d}{dx_0} x = 1 + Ak \cos kx_0, \\ \frac{d}{dx_0} \frac{E}{E_{max}} = k \cos kx_0. \end{cases}$$

We see that in case $A < 1/k$ the function x is strictly increasing, but it ceases to be so for $A \geq 1/k$. One may also deduce that E/E_{max} has a maximum at

$$x = \frac{\pi}{2k} + A,$$

and a minimum at

$$x = -\frac{\pi}{2k} - A.$$

For $A \ll 1/k$ the additive amplitude term is negligible, and thus $E/E_{max}(x)$ has a sinusoidal profile. As A grows, however, this shape is deformed with the extrema starting to move away from $x = 0$. When $A = 1/k$, the curve has vertical tangents at $x = \pm\pi/k$, and for $A > 1/k$ the function $E/E_{max}(x)$ turns multivalued (Figure 2.3). Clearly this is physically unfeasible, and in practice it means our condition 2.2 is no longer satisfied. This is considered as the point of *wave breaking*, where the electron trajectories necessarily begin to cross, damping the plasma wave. Assuming the particles oscillate with the wave number $k = \omega_p/c$, one may write at $A = 1/k$:

$$E_0 = E_{max}|_{A=1/k} = \frac{1}{\epsilon_0} en_0 \frac{c}{\omega_p} = \frac{cm_e \omega_p}{e}. \quad (2.3)$$

This is defined as the cold nonrelativistic wave breaking field, limiting the amplitude of plasma wave that can be supported. Note that this edge is reached once the oscillation amplitude becomes comparable to the plasma wavelength.

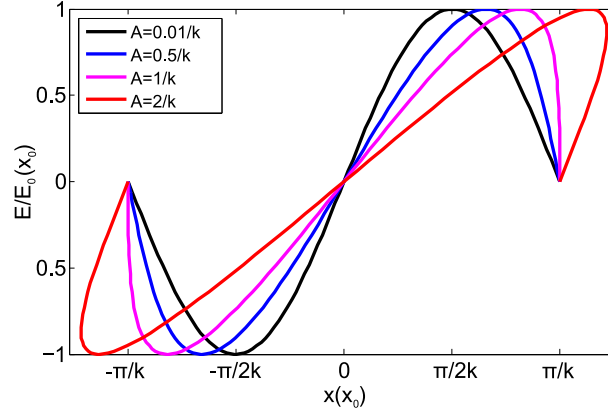


Figure 2.3 – Parametric curves for $E/E_0(x_0)$ against $x(x_0)$ for different values of the oscillation amplitude A .

2.3.2 Wakefields driven by weak Gaussian pulses

With the intuition gained in the previous section, one may now proceed to the 3D description of the laser wakefield generation process. In the case of weakly driven underdense plasmas, it is possible to find analytic expressions to relate the main parameters. We start with the Maxwell's equations:

$$\nabla \cdot \mathbf{E} = \frac{\rho}{\epsilon_0}, \quad (\text{Gauss's law}) \quad (2.4)$$

$$\nabla \cdot \mathbf{B} = 0, \quad (\text{Gauss's law for magnetism}) \quad (2.5)$$

$$\nabla \times \mathbf{E} = -\frac{\partial \mathbf{B}}{\partial t}, \quad (\text{Faraday's law}) \quad (2.6)$$

$$\nabla \times \mathbf{B} = \frac{1}{c^2} \frac{\partial \mathbf{E}}{\partial t} + \mu_0 \mathbf{J}. \quad (\text{Ampère's law revised by Maxwell}) \quad (2.7)$$

Here ρ is the charge density, μ_0 is the vacuum permeability, and \mathbf{J} is the current density. To reduce the number of variables in the system we use the standard potential formulation (Griffiths, 2008):

$$\mathbf{B} = \nabla \times \mathbf{A}, \quad (2.8)$$

$$\mathbf{E} = -\nabla\Phi - \frac{\partial \mathbf{A}}{\partial t}. \quad (2.9)$$

\mathbf{A} and Φ are known as electrodynamic vector and scalar potentials, respectively. In addition, we will need two fluid equations, namely the one for continuity:

$$\frac{\partial n}{\partial t} + \nabla \cdot (n\mathbf{v}) = 0, \quad (2.10)$$

and the equation of motion in electromagnetic fields:

$$\left(\frac{\partial}{\partial t} + \mathbf{v} \cdot \nabla \right) \mathbf{p} = -e(\mathbf{E} + \mathbf{v} \times \mathbf{B}). \quad (2.11)$$

In the above, $n(\mathbf{r}, t)$ is the plasma density, $\mathbf{v}(\mathbf{r}, t)$ is its velocity, and $\mathbf{p} = \gamma(\mathbf{v})m_e\mathbf{v}$ is the relativistic momentum. Evidently we are assuming the plasma to be a cold fluid. As a next step, we make a choice to work in Coulomb gauge, which implies $\nabla \cdot \mathbf{A} = 0$ (Griffiths, 2008). Combining this condition with equations 2.4 and 2.9 leads to the Poisson equation:

$$\nabla^2 \Phi = \frac{e}{\epsilon_0} (n - n_0) = \frac{e}{\epsilon_0} \delta n, \quad (2.12)$$

where $n_0(\mathbf{r})$ is the equilibrium plasma density, and $\delta n = n - n_0$ is the plasma density perturbation. We observe that the scalar Φ is dependent only on the plasma parameters, therefore all the information on the high-frequency laser field must be encoded in the vector potential \mathbf{A} . This separability is a great advantage of using the Coulomb gauge in our description.

We may now plug the potential expressions 2.8 and 2.9 into Ampère's law (eq. 2.7). After applying the vector identity $\nabla \times (\nabla \times \mathbf{A}) = \nabla(\nabla \cdot \mathbf{A}) - \nabla^2 \mathbf{A}$ and the gauge condition $\nabla \cdot \mathbf{A} = 0$ one gets the wave equation for \mathbf{A} :

$$\left(\nabla^2 - \frac{1}{c^2} \frac{\partial^2}{\partial t^2} \right) \mathbf{A} = \mu_0 e n \mathbf{v} + \frac{1}{c^2} \frac{\partial}{\partial t} \nabla \Phi. \quad (2.13)$$

The same can be done for the equation of motion:

$$\left(\frac{\partial}{\partial t} + \mathbf{v} \cdot \nabla \right) \mathbf{p} = e \left(\nabla \Phi + \frac{\partial \mathbf{A}}{\partial t} - \mathbf{v} \times \nabla \times \mathbf{A} \right). \quad (2.14)$$

To simplify the above, we need to demonstrate one mathematical property for the term $(\mathbf{v} \cdot \nabla) \mathbf{p}$. The following standard vector identity will be used again:

$$\nabla \frac{p^2}{2} = (\mathbf{p} \cdot \nabla) \mathbf{p} + \mathbf{p} \times (\nabla \times \mathbf{p}) = m_e \gamma ((\mathbf{v} \cdot \nabla) \mathbf{p} + \mathbf{v} \times (\nabla \times \mathbf{p})).$$

As a second step, from the definition

$$\gamma = \left(1 + \frac{p^2}{m_e^2 c^2} \right)^{\frac{1}{2}}$$

one can derive:

$$\nabla \gamma = \frac{1}{m_e^2 c^2 \gamma} \nabla \frac{p^2}{2}.$$

Combining these expressions yields the necessary property:

$$(\mathbf{v} \cdot \nabla) \mathbf{p} = m_e c^2 \nabla \gamma - \mathbf{v} \times (\nabla \times \mathbf{p}). \quad (2.15)$$

Plugging it in the equation 2.14 gives:

$$\frac{\partial}{\partial t} (\mathbf{p} - e \mathbf{A}) = \nabla (e \Phi - m_e c^2 \gamma) + \mathbf{v} \times (\nabla \times (\mathbf{p} - e \mathbf{A})).$$

Knowing that the curl of a gradient is always zero, the last trick is to take the curl of the above expression to obtain:

$$\frac{\partial}{\partial t} (\nabla \times (\mathbf{p} - e \mathbf{A})) = \nabla \times \mathbf{v} \times (\nabla \times (\mathbf{p} - e \mathbf{A})).$$

The key observation now is that at time $t = 0$ the right hand side of the equation is zero, as before any perturbation occurs we have both $\mathbf{p} = \mathbf{0}$ and $\mathbf{A} = \mathbf{0}$, and thus $\nabla \times (\mathbf{p} - e \mathbf{A}) = \mathbf{0}$. This implies that $\nabla \times (\mathbf{p} - e \mathbf{A}) = \mathbf{0}$ at all times, and hence a reduced equation of motion can be concluded:

$$\frac{\partial \mathbf{p}}{\partial t} = e \nabla \Phi + e \frac{\partial \mathbf{A}}{\partial t} - m_e c^2 \nabla \gamma. \quad (2.16)$$

To tidy up the expressions, we introduce a set of normalized quantities: $\phi = e \Phi / m_e c^2$, $\mathbf{a} = e \mathbf{A} / m_e c$ and $\mathbf{u} = \mathbf{p} / m_e c$, so that $\gamma = (1 + u^2)^{1/2}$. This allows us to write a fully general relativistic set of equations for our cold plasma:

$$\left(\nabla^2 - \frac{1}{c^2} \frac{\partial^2}{\partial t^2}\right) \mathbf{a} = k_p^2 \frac{1}{\gamma} \frac{n}{n_0} \mathbf{u} + \frac{1}{c} \frac{\partial}{\partial t} \nabla \phi, \quad (\text{Wave equation}) \quad (2.17)$$

$$\frac{\partial n}{\partial t} + c \nabla \cdot (n \mathbf{u} / \gamma) = 0, \quad (\text{Continuity equation}) \quad (2.18)$$

$$\nabla^2 \phi = k_p^2 \frac{\delta n}{n_0}, \quad (\text{Poisson's equation}) \quad (2.19)$$

$$\frac{\partial \mathbf{u}}{\partial t} = c \nabla (\phi - \gamma) + \frac{\partial \mathbf{a}}{\partial t}. \quad (\text{Fluid equation of motion}) \quad (2.20)$$

In the above $k_p = \sqrt{n_0 e^2 / m_e c^2 \epsilon_0}$ is the plasma wave number. In order to continue developing the 3D model, certain assumptions must now be made. To begin with, we require that the plasma be tenuous, so that $\omega_p \ll \omega_0$, where ω_0 is the frequency of the driving field. This allows separating the fluid motion into two parts – a fast-varying one due to the high-frequency field, and the slow motion due to the evolving plasma perturbations, i. e. $\mathbf{u} = \mathbf{u}_{\text{fast}} + \mathbf{u}_{\text{slow}}$ (Mora & Antonsen, 1997). This permits separating the fluid equation of motion (2.20) into fast and slow parts:

$$\mathbf{u}_{\text{fast}} = \mathbf{a}, \quad (2.21)$$

and

$$\frac{\partial \mathbf{u}_{\text{slow}}}{\partial t} = c \nabla (\phi - \langle \gamma \rangle), \quad (2.22)$$

where $\langle \dots \rangle$ indicates averaging over a full period of high-frequency oscillations. We further assume a weakly relativistic case, which yields $a \ll 1$, $\delta n \ll n_0$, $u \ll 1$ and $\gamma \approx 1$. The continuity equation taken to first order becomes

$$\frac{\partial}{\partial t} \delta n + c n_0 \nabla \cdot \mathbf{u}_{\text{slow}} = 0.$$

Taking the temporal derivative and combining it with equations 2.19 and 2.22 yields:

$$\begin{aligned} 0 &= \frac{\partial^2}{\partial t^2} \frac{\delta n}{n_0} + c \nabla \cdot \frac{\partial \mathbf{u}_{\text{slow}}}{\partial t} \\ &= \frac{\partial^2}{\partial t^2} \frac{\delta n}{n_0} + c^2 \nabla^2 (\phi - \langle \gamma \rangle) \\ &= \left(\frac{\partial^2}{\partial t^2} + \omega_p^2 \right) \frac{\delta n}{n_0} - c^2 \nabla^2 \langle \gamma \rangle \\ &= \left(\frac{\partial^2}{\partial t^2} + \omega_p^2 \right) \frac{\delta n}{n_0} - c^2 \nabla^2 \langle (1 + u^2)^{\frac{1}{2}} \rangle. \end{aligned}$$

One may now apply the binomial expansion:

$$(1 + u^2)^{\frac{1}{2}} \approx 1 + \frac{1}{2} u^2 = 1 + \frac{u_{\text{fast}}^2}{2} + \frac{u_{\text{slow}}^2}{2} + \mathbf{u}_{\text{fast}} \cdot \mathbf{u}_{\text{slow}}.$$

We have seen that $u_{\text{fast}} = a$, hence the first term scales as a^2 . On the other hand, u_{slow} term originates due to the driver's ponderomotive force, which has been shown to be proportional to the intensity, and $I \propto a^2$. Therefore, u_{slow}^2 scales as a^4 , and $\mathbf{u}_{\text{fast}} \cdot \mathbf{u}_{\text{slow}}$ scales as a^3 , meaning

the last two expansion terms can be neglected in the weakly relativistic case. We conclude that

$$\left(\frac{\partial^2}{\partial t^2} + \omega_p^2\right) \frac{\delta n}{n_0} = c^2 \nabla^2 \frac{\langle a^2 \rangle}{2}, \quad (2.23)$$

and similarly:

$$\left(\frac{\partial^2}{\partial t^2} + \omega_p^2\right) \phi = \omega_p^2 \frac{\langle a^2 \rangle}{2}. \quad (2.24)$$

A second important assumption is known as the *quasistatic* approximation. We first impose a coordinate system that is following the laser pulse, and thus the wake structure: $t' = t$, $\zeta = z - ct$. Since a tenuous plasma is considered, the group velocity of the laser pulse is indeed close to c . Then the derivatives are given by:

$$\begin{aligned} \frac{\partial}{\partial t} &= \frac{\partial}{\partial t'} - c \frac{\partial}{\partial \zeta}, \\ \frac{\partial^2}{\partial t^2} &= \frac{\partial^2}{\partial t'^2} - 2c \frac{\partial^2}{\partial \zeta \partial t'} + c^2 \frac{\partial^2}{\partial \zeta^2}, \\ \frac{\partial}{\partial z} &= \frac{\partial}{\partial \zeta}, \end{aligned}$$

and the equation 2.24 can be expressed as:

$$\left(\frac{\partial^2}{\partial t'^2} - 2c \frac{\partial^2}{\partial \zeta \partial t'} + c^2 \frac{\partial^2}{\partial \zeta^2} + \omega_p^2\right) \phi = \omega_p^2 \frac{\langle a^2 \rangle}{2}.$$

The quasistatic approximation supposes that in this new reference frame both the laser pulse and the plasma wave evolve slowly with time. This allows cancelling out all the terms that involve $\partial/\partial t'$ in the above to obtain:

$$\left(\frac{\partial^2}{\partial \zeta^2} + k_p^2\right) \phi = k_p^2 \frac{\langle a^2 \rangle}{2}. \quad (2.25)$$

One can now solve this equation for a linearly polarized Gaussian driver pulse (Gorbunov & Kirsanov, 1987). It may be described by the normalized vector potential:

$$\mathbf{a} = \hat{a}(r, \zeta) \cos(k_0 \zeta) \mathbf{e}_x,$$

where the Gaussian envelope is given by

$$\hat{a}^2(r, \zeta) = a_0^2 \exp(-\zeta^2/L_0^2) \exp(-r^2/\sigma^2).$$

Here $k_0 = 2\pi/\lambda_0$ is the laser wave number, with λ_0 being the light wavelength, $L_0 = c\tau_{\text{FWHM}}/(2\sqrt{\ln 2})$ is the driver pulse length with τ_{FWHM} the full width at half maximum (FWHM) pulse duration, r is the perpendicular distance from the optical axis, and σ determines the transverse beam size. The equation 2.25 takes the variable a^2 averaged over the high-frequency optical cycles, hence one gets an additional factor of 1/2 before deducing a similar expression with respect to the envelope \hat{a} :

$$\left(\frac{\partial^2}{\partial \zeta^2} + k_p^2\right) \phi = k_p^2 \frac{\hat{a}^2}{4}. \quad (2.26)$$

This can be solved by finding an appropriate Green's function that satisfies

$$\left(\frac{\partial^2}{\partial \zeta^2} + k_p^2 \right) G(\zeta, \zeta') = \delta(\zeta - \zeta').$$

Here $\delta(\zeta - \zeta')$ is the Dirac delta function. It can be shown that the general Green's function for the above equation is given by

$$G(\zeta, \zeta') = C_1 \exp(ik_p \zeta) + C_2 \exp(-ik_p \zeta) + \begin{cases} 0, & \text{if } \zeta < \zeta', \\ \frac{1}{k_p} \sin k_p(\zeta - \zeta'), & \text{if } \zeta \geq \zeta', \end{cases}$$

where C_1 and C_2 are arbitrary constants. We require a solution that drops to zero as $\zeta \rightarrow +\infty$ (no plasma waves excited before the laser pulse arrives). This is then provided by

$$G(\zeta, \zeta') = (\Theta(\zeta - \zeta') - 1) \frac{\sin k_p(\zeta - \zeta')}{k_p}.$$

In the above $\Theta(\zeta - \zeta')$ is the Heaviside step function, which is equal to 1 for a positive argument, and 0 for a negative one. Finally, one may write down the solution to the equation 2.26:

$$\phi(\zeta) = \int_{-\infty}^{+\infty} G(\zeta, \zeta') k_p^2 \frac{\hat{a}(\zeta')}{4} d\zeta' = -\frac{k_p}{4} \int_{\zeta}^{+\infty} \hat{a}^2(\zeta') \sin k_p(\zeta - \zeta') d\zeta'.$$

For potential far behind the laser pulse, or $\zeta < -L_0$, we may still integrate between $-\infty$ and $+\infty$:

$$\phi(\zeta) = -\frac{k_p}{4} \left(\sin k_p \zeta \int_{-\infty}^{+\infty} \hat{a}^2(\zeta') \cos k_p \zeta' d\zeta' + \cos k_p \zeta \int_{-\infty}^{+\infty} \hat{a}^2(\zeta') \sin k_p \zeta' d\zeta' \right).$$

Note that $\hat{a}^2(\zeta')$ is an even function, thus its product with $\sin k_p \zeta'$ is odd, and the second integral vanishes. What remains is then

$$\phi(\zeta) = -\frac{k_p}{4} a_0^2 e^{-r^2/\sigma^2} \sin k_p \zeta \int_{-\infty}^{+\infty} e^{-\zeta'^2/L_0^2} \cos k_p \zeta' d\zeta'.$$

The last integral is in fact equivalent to a Fourier transform of a Gaussian function, and it may be looked up in many sources:

$$\int_{-\infty}^{+\infty} e^{-\zeta'^2/L_0^2} \cos k_p \zeta' d\zeta' = \sqrt{\pi} L_0 e^{-k_p^2 L_0^2/4}.$$

This determines the final expression for the normalized scalar potential:

$$\phi(\zeta) = -\sqrt{\pi} a_0^2 \frac{k_p L_0}{4} e^{-k_p^2 L_0^2/4} e^{-r^2/\sigma^2} \sin k_p \zeta. \quad (2.27)$$

The slow-varying electric field may then be determined in cylindrical coordinates from

$$\mathbf{E} = -\nabla \Phi = -\frac{m_e c^2}{e} \nabla \phi = -\frac{m_e c^2}{e} \left(\mathbf{e}_r \frac{\delta}{\delta r} + \mathbf{e}_z \frac{\delta}{\delta z} \right) \phi.$$

We conclude that for $\zeta < -L_0$ the longitudinal and transverse electric fields can be respectively expressed by

$$\frac{E_z}{E_0} = \sqrt{\pi} a_0^2 \frac{k_p L_0}{4} e^{-k_p^2 L_0^2 / 4} e^{-r^2 / \sigma^2} \cos k_p \zeta, \quad (2.28)$$

$$\frac{E_r}{E_0} = -\sqrt{\pi} \frac{a_0^2}{2} e^{-k_p^2 L_0^2 / 4} \frac{L_0 r}{\sigma^2} e^{-r^2 / \sigma^2} \sin k_p \zeta, \quad (2.29)$$

where $E_0 = \frac{cm_e \omega_p}{e}$ is the already encountered nonrelativistic wave breaking field for cold plasmas. Few things can be deduced from here. Firstly, we see that both fields vary sinusoidally in ζ with the same period. However, they are offset by a phase of $\pi/2$. This means that only for one quarter of the period the wakefield will be both accelerating and focusing. In addition, the laser spot size plays an important role through dependence of the focusing field amplitude on $\propto e^{-r^2/\sigma^2}/\sigma^2$. Finally, one can show that the maximum amplitude of the longitudinal field will be achieved when the parameters of plasma and laser pulse duration are set so that

$$k_p L_0 = \sqrt{2}.$$

In practical units, this resonance condition yields the following expression for choosing the plasma density:

$$n_{res}(\text{cm}^{-3}) = \frac{1.7 \times 10^{21}}{\tau_{\text{FWHM}}^2(\text{fs})}, \quad (2.30)$$

where τ_{FWHM} is the FWHM duration of the driver pulse, expressed in femtoseconds. In addition, from Poisson's equation (2.19) one may calculate the density perturbation:

$$\frac{\delta n}{n_0} = \frac{1}{k_p^2} \nabla^2 \phi = -\frac{1}{k_p E_0} \nabla \cdot \mathbf{E} = -\frac{1}{k_p E_0} \left(\frac{1}{r} \frac{\partial(rE_r)}{\partial r} + \frac{\partial E_z}{\partial \zeta} \right).$$

Separating the two corresponding contributions into $\delta n = \delta n_r + \delta n_z$, we obtain the longitudinal density perturbation:

$$\frac{\delta n_z}{n_0} = \sqrt{\pi} a_0^2 \frac{k_p L_0}{4} e^{-k_p^2 L_0^2 / 4} e^{-r^2 / \sigma^2} \sin k_p \zeta, \quad (2.31)$$

and the radial term:

$$\frac{\delta n_r}{n_0} = \frac{\delta n_z}{n_0} \frac{4}{\sigma^2 k_p^2} \left(1 - \frac{r^2}{\sigma^2} \right). \quad (2.32)$$

We conclude that, as expected, the axial electric fields reach maximum values on optical axis ($r = 0$). Moreover, as the phase for $\delta n_z/n_0$ as compared to E_z/E_0 , is also offset by $\pi/2$, the peak accelerating gradients in the direction of laser propagation ($E_z < 0$) are reached halfway between maxima and minima of the longitudinal density perturbation (Figure 2.4).

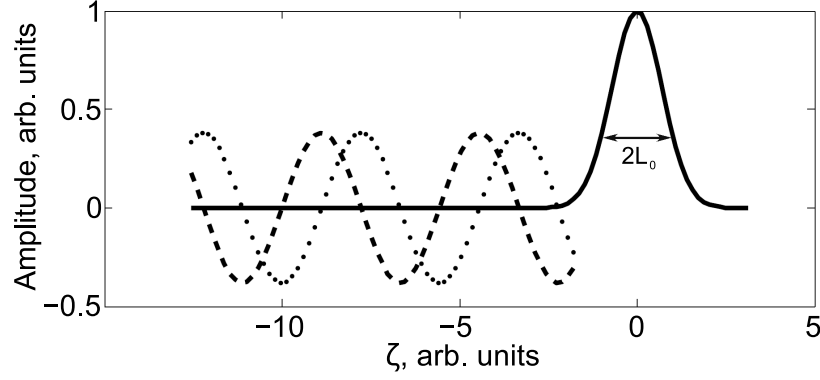


Figure 2.4 – Curves depicting the on-axis solutions of normalized equations 2.28 (longitudinal electric field E_z/E_0 , dashed line) and 2.31 (longitudinal density perturbation $\delta n_z/n_0$, dotted line) behind a Gaussian laser pulse (solid line) travelling to the right with the resonance condition 2.30 satisfied. The regions with negative E_z/E_0 would accelerate a test electron in the direction of light propagation.

2.3.3 Strongly driven wakefields and the blowout regime

When the plasma is driven by a strong, relativistic laser pulse ($a_0 > 1$), the previous model is no longer valid, and in fact analytic solutions for a 3D case have not been demonstrated. To study this interaction regime, numerical particle-in-cell (PIC) simulations are normally used (Dawson, 1983). The observed behavior, however, is highly reminiscent of the 1D plasma wave model described in section 2.3.1. Figure 2.5 shows an example of electron density maps and on-axis longitudinal electric field profiles obtained in weak and mildly relativistic driver cases using the PIC code CALDER-CIRC (Lifschitz et al., 2009). Here a resonant density plasma is driven by a 5 fs laser pulse with a normalized amplitude $a_0 = 0.5$ (plots a) and b)), and $a_0 = 1.2$ (plots c) and d)). In the first case one may confirm that both

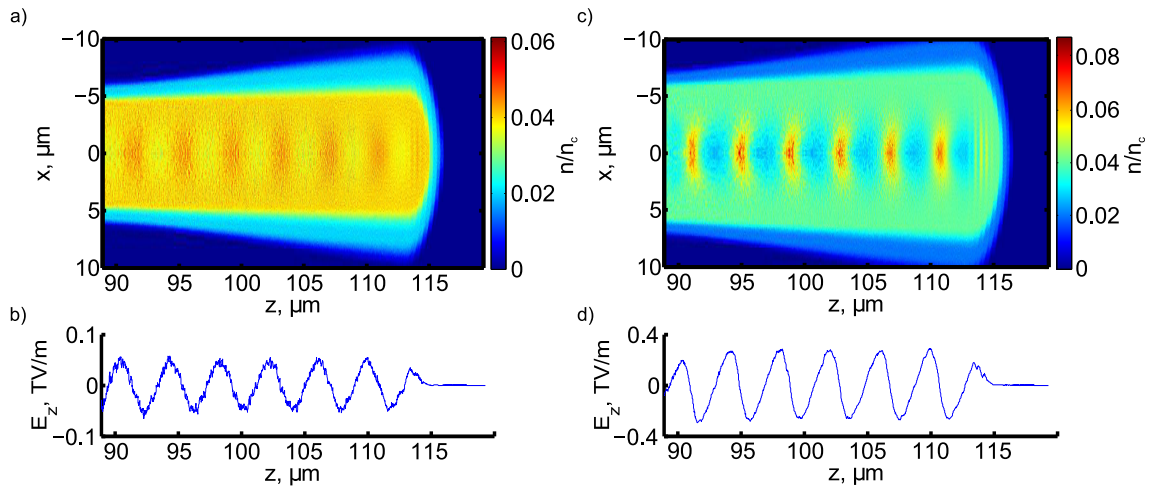


Figure 2.5 – PIC simulation results of a 5 fs laser pulse propagating in a resonant density plasma. a) Electron density map with a driver of sub-relativistic peak normalized amplitude ($a_0 = 0.5$). b) On-axis longitudinal electric field (E_z) profile for the same case, showing a sinusoidal profile. c) Density map in the case of a mildly relativistic driver ($a_0 = 1.2$). d) The corresponding on-axis longitudinal electric field, clearly following a deformed sinusoidal pattern and reaching much higher amplitudes. The outer regions coloured in blue correspond to non-ionized gas.

the density perturbation and the electric field profiles match the linear model predictions very well, as compared with Figure 2.4. However, the results obtained for $a_0 = 1.2$ are quite different. The respective z -positions for maxima and minima of E_z are shifted, exactly as before in the 1D model (Figure 2.3), and the peak field values are significantly higher.

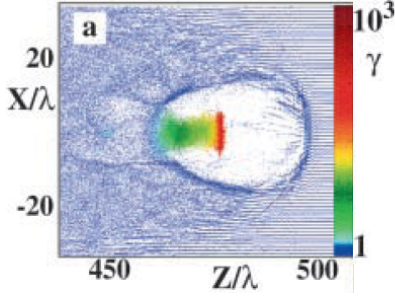


Figure 2.6 – Energetic electrons accelerated in a bubble-like structure created by a strong laser pulse (Pukhov & Meyer-ter-Vehn, 2002).

Continuing the increase of driver amplitude a_0 towards strongly relativistic values would lead to further shifts of the extrema, to the point where the function $E_z(z)$ becomes multi-valued, implying particle trajectory crossing and wave breaking. As will be discussed in section 2.4.2, this breaking can be used for injecting electrons in the wakefield. One may additionally notice in Figure 2.5c) that the plasma perturbations have become really large, with certain areas close to the optical axis coming near zero density levels, i. e. $\delta n \approx n_0$. This implies approaching a regime first described in (Pukhov & Meyer-ter-Vehn, 2002), where the space behind the laser pulse becomes essentially void of electrons (Figure 2.6). It is now commonly known as the bubble, or blowout regime, and is often preferred during experiments both due to its high accelerating gradients and extended regions having focusing properties (i. e. the wakefield is *both* accelerating and focusing for $> 1/4$ of the plasma wave period). In addition, it is possible to obtain beams with narrow energy spreads (Mangles et al., 2004) (Geddes et al., 2004) (Faure et al., 2004) (Tsung et al., 2006), which is often a desired property. In order to access the bubble regime, several conditions should be matched (Lu et al., 2007). Firstly, the pulse needs to be intense enough to expel all electrons away from the optical axis. Simulations indicate that normalized laser amplitudes $a_0 \gtrsim 2$ are necessary, equivalent to peak intensities $I \gtrsim 10^{19}$ W/cm². Additionally, the driving pulse should fulfil the bubble resonance condition:

$$c\tau_{\text{FWHM}} \approx \sigma \approx \lambda_p/2, \quad (2.33)$$

where the plasma wavelength λ_p is obtained accounting for a relativistic correction factor:

$$\lambda_p = \sqrt{a_0} \frac{2\pi}{k_p}, \quad (2.34)$$

and all the other terms are as defined before. With these requirements satisfied, it is possible to determine the total expected energy gain in this regime, limited by dephasing (see later section 2.5.3):

$$\Delta E[\text{GeV}] \approx 1.7 \left(\frac{P[\text{TW}]}{100} \right)^{1/3} \left(\frac{10^{18}}{n[\text{cm}^{-3}]} \right)^{2/3} \left(\frac{0.8}{\lambda_0[\mu\text{m}]} \right)^{4/3}. \quad (2.35)$$

We conclude that for an appropriate titanium-sapphire 100 TW laser system one should be able to obtain GeV-scale electrons. This has also been proved experimentally (Leemans et al., 2006).

2.4 Accelerator injection schemes

After describing the formation of plasma waves, it is necessary to discuss the second crucial component of a wakefield accelerator – the particle injection mechanism. In order to experience net energy gain, a test electron has to get *trapped*, which requires satisfying certain initial conditions that concern its velocity and position within the plasma wave (i. e. the wave phase). As the wakefield is propagating nearly at the speed of light, the particle also needs to reach relativistic velocity within a single accelerating half-period of the plasma wave – otherwise the wave would outrun the particle, placing it in the decelerating region and ultimately leading to approximately zero total energy gain. An initially stationary electron could also be injected, provided the wakefield is sufficiently strong, and the particle is placed at an optimal phase. Multiple wakefield injection schemes have been described in literature by now.

2.4.1 External injection

The conceptually simplest technique is using an external particle injector. However, this idea runs into many difficulties. To begin with, we note that typical plasma wavelengths in LWFA are on the order of few tens of, or even few microns only. Hence the witness electron bunch duration should be significantly below 100 fs in order for all of its slices to experience a similar net effect. This is a big challenge even today, and was unachievable back in the period when such injection method was first attempted. Secondly, the particle beam needs to be focused to a spot size significantly smaller than the laser spot size, or otherwise again the fields experienced by different parts of the bunch would not be the same. Finally, for reproducibility of results the wakefield driver and the particle bunch need to be synchronized at the femtosecond level, which, depending on the exact method to pre-accelerate particles, might be another great challenge due to electronic jitter issues. All points considered, it is not surprising that this concept, although successfully verified (Everett et al., 1994) (Amiranoff et al., 1998), hardly produced beams of satisfactory quality and has not been overly popular. Notable exceptions are the more exotic cases of ultrahigh-energy particle-driven accelerators, where the used plasma wavelengths are larger by orders of magnitude (Litos et al., 2014) (Gschwendtner et al., 2016) (Adli et al., 2018) (Doche et al., 2017).

2.4.2 Self-injection by wave breaking

It has been discussed in the section 2.3 how strong driving of plasma waves mathematically leads to the longitudinal electric field function $E_z(z)$ turning multi-valued for the considered model. Physically such a situation is clearly unfeasible and in practice it implies a violation of the assumption that there are no plasma electron trajectory crossings (equation 2.2). This is known as the wave breaking, which limits the wake amplitude and may sometimes lead the surplus electrons (i. e. the ones that are no longer part of the wake structure) to occur in regions where the conditions are favorable for trapping in the plasma wave (Katsouleas & Mori, 1988), (Bulanov, Pegoraro, Pukhov, & Sakharov, 1997), (Bulanov, Naumova, Pegoraro, & Sakai, 1998), (Kostyukov, Nerush, Pukhov, & Seredov, 2009). As predicted by theory, self-injection has been demonstrated to be a threshold effect (Mangles et al., 2012), and higher plasma densities are required for running with lower power lasers, increasing the influence of various nonlinear light-matter interaction phenomena and leading to below-average source stability. In addition, multiple self-injection regimes have been shown to exist, having slightly different properties (Corde, Thauray, et al., 2013). Finally, since both the wakefield generation and particle injection are due to a single driver pulse, this method does not provide many

tuning knobs to control the electron beam parameters. Despite these drawbacks, self-injection has been frequently preferred in experiments, mainly because of its simplicity.

2.4.3 Colliding-pulse injection

To counter the drawbacks mentioned in the previous section and at least partially decouple the wakefield generation and injection mechanisms, using an additional laser pulse has been proposed. The initial idea was to give an additional kick to a collection of electrons in a confined area by the ponderomotive force of a perpendicular propagating injector pulse (Umstadter, Kim, & Dodd, 1996). Later it has been suggested that a beat wave generated by the interference between two counterpropagating laser beams could do this job even better due to sharper ponderomotive gradients as well as symmetry reasons (Esarey, Hubbard, Leemans, Ting, & Sprangle, 1997) (Fubiani, Esarey, Schroeder, & Leemans, 2004) (Figure 2.7). This technique has been experimentally confirmed to not only produce electrons with a narrow energy spread thanks to well-defined position of injection, but also allow energy tunability by adjusting the collision point within the plasma channel through an optical delay line (Faure et al., 2006). On the other hand, the need to overlap two laser beams both spatially and temporally implies such a system is significantly more difficult to align.

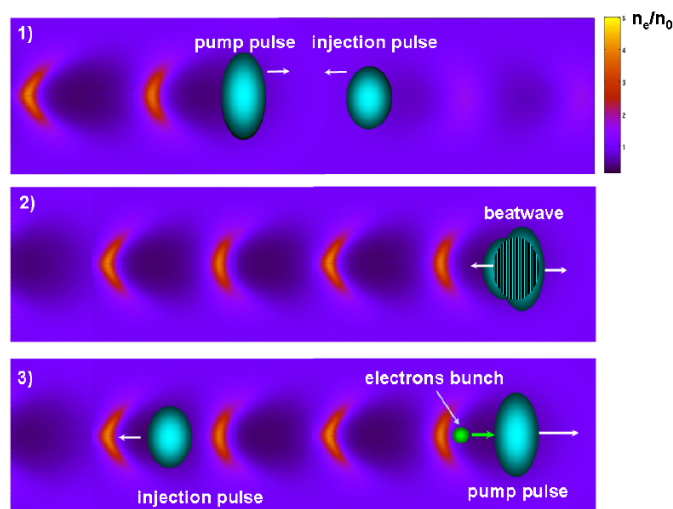


Figure 2.7 – Illustration of the colliding-pulse injection technique. An intense pump pulse drives a plasma wakefield. At some point it encounters a counter-propagating injection pulse, and a beat wave is created in the overlap region. This beat wave may trigger an injection of an electron bunch in the plasma wave. Taken from (Faure, 2014).

2.4.4 Ionization-induced injection

One of the two well-known controlled injection schemes that require only one laser pulse relies on the fact that gases with higher atomic numbers have electrons with several very different ionization potential levels. For example, the first five outer-shell (L-shell) electrons of nitrogen require below 100 eV of energy to dissociate from the parent molecule. Using the barrier-suppression ionization model (Delone & Krainov, 1998), the required light intensity may be calculated via

$$I [\text{W}/\text{cm}^2] = 4 \times 10^9 \frac{E_i^4 [\text{eV}]}{Z^2} \quad (2.36)$$

to be below $1.5 \times 10^{16} \text{ W/cm}^2$. Here E_i is the corresponding ionization potential level and Z is the resultant charge of the ion after the ionization event given in atomic units. This value is orders of magnitude below the peak intensities at which LWFA is normally operated, and hence the leading edge of the laser pulse is sufficient to completely strip away the considered particles from the nitrogen parent molecules. However, the ionization of the first K-shell electron that is close to the nucleus requires an energy of 552 eV to dissociate, corresponding to $I \approx 1 \times 10^{19} \text{ W/cm}^2$. Such intensities are usually reached only at the center of the laser pulse, hence the $\text{N}^{5+} \rightarrow \text{N}^{6+}$ electrons are born already inside the first wakefield period (Figure 2.8). If the plasma wave is strong enough, these particles may then be captured and accelerated to relativistic velocities. This technique is experimentally fairly simple, and has been widely used since its first demonstrations (Pak et al., 2010) (McGuffey et al., 2010). However, by default it does not offer many beam control tools, and in order to avoid broad electron energy distributions more advanced target design is required (Pollock et al., 2011) (Vargas et al., 2014).

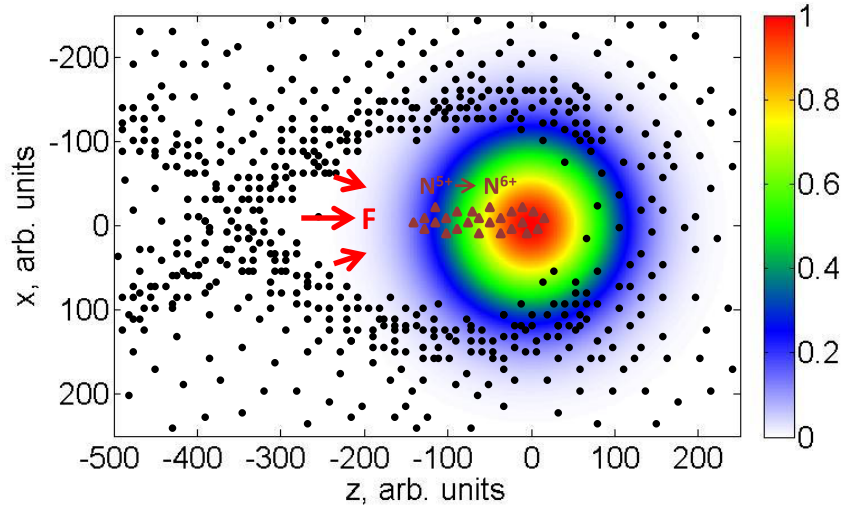


Figure 2.8 – Illustration of the ionization injection principle. The front of a wakefield-driving intense laser pulse completely ionizes the L-shell of nitrogen gas (black dots). At the center of the pulse, where the light field is the strongest, some K-shell electrons may also be ionized (brown triangles). However, they do not experience the same ponderomotive force and thus do not follow the same trajectories as the particles born at the front. They remain close to the optical axis, and, if the wakefield is strong enough, may be trapped. N_2 is most commonly used for the technique, but other gases are possible, as well.

2.4.5 Density-downramp injection

Another well-known injection mechanism is based on deliberate variations of the plasma density profile encountered by the driver pulse. As discussed before, electrons may be trapped by the wakefield as long as the latter does not outrun them, placing the particles in its decelerating phase, where no energy gain could be reached. Two parameters are of importance here – the amplitude of the wakefield, affecting how quickly the particles may get accelerated to the wake phase velocity $v_p \lesssim c$, and the phase velocity itself. If it could be lowered, then initially slower electrons would also be able to catch up with the wave. For a varying density profile the plasma equation under quasistatic approximation (2.25) reads:

$$\left(\frac{\partial^2}{\partial \zeta^2} + k_p^2(z) \right) \phi = k_p^2(z) \frac{\langle a^2 \rangle}{2}. \quad (2.37)$$

Following the same procedure as before, one may show that the solution behind the laser pulse has the form:

$$\phi(\zeta, z) = \phi_0(z) \sin k_p(z)\zeta, \quad (2.38)$$

where $\phi_0(z) = -\sqrt{\pi}a_0^2 k_p(z) L_0 \exp(-k_p(z)^2 L_0^2/4) \exp(-r^2/\sigma^2)/4$ is the wakefield amplitude (compare eq. 2.27), and $\psi = k_p(z)\zeta = k_p(z)(z - ct)$ is its phase. Bear in mind we are still assuming tenuous plasmas, so that one may continue to claim that the group velocity $v_g(z, t) \approx c$ (otherwise one would need to use $\zeta = z - v_g(z)t$, making the change of variables $(z, t) \rightarrow (\zeta, t)$ more complicated). It is then straightforward to obtain the local wave frequency and wave number:

$$\begin{aligned} \omega(\zeta, z) &= -\partial\psi/\partial t = k_p(z)c = \omega_p(z), \\ k(\zeta, z) &= \partial\psi/\partial z = k_p(z) + \zeta \partial k_p/\partial z. \end{aligned}$$

This may be used to obtain the local phase velocity:

$$v_p(\zeta, z) = \frac{\omega(\zeta, z)}{k(\zeta, z)} = \frac{c}{1 + \frac{1}{k_p} \zeta \frac{\partial k_p}{\partial z}}. \quad (2.39)$$

For a downward density gradient one has $\partial k_p/\partial z < 0$. Behind the laser pulse we also have $\zeta < 0$. Hence, for a decreased wave number k_p one also obtains a decrease in the phase velocity, which eases the electron trapping. First suggested and demonstrated for mild transitions (Bulanov et al., 1998) (Geddes et al., 2008), the method applied to sharp density drops created by obstacles placed in supersonic gas flow or by hydrodynamic expansion of pre-ionized gas allowed obtaining beams with a few-percent energy spread, some tunability and good reproducibility (Suk, Barov, Rosenzweig, & Esarey, 2001) (Faure, Rechatin, Lundh, Ammoura, & Malka, 2010) (Gonsalves et al., 2011) (Buck et al., 2013).

2.4.6 Other injection types due to wakefield slow-down

In the previous section we have discussed how the back of the wakefield could be deliberately slowed down by plasma density tailoring. This, however, is not the only reason the wake phase velocity v_p could face a reduction, aiding particle injection. The evolution of the driving laser pulse while it propagates in the plasma may also produce similar effects. Experimentally such processes are difficult to distinguish from simple self-injection due to wave breaking, but numerical studies have provided a lot of interesting evidence for their occurrence possibilities. One such case has been discussed in (Beaurepaire, Lifschitz, & Faure, 2014) for ultrashort broad-bandwidth drivers, which experience rapid self-phase modulation in high-density plasma, symmetrically redshifting the front and blueshifting the back of the Gaussian light packet (Watts et al., 2002). This occurs simultaneously with strong dispersion effects that lead to the red wavelengths slipping behind the blue ones (i. e. building up a negative chirp), the final result being an overall redshift of the entire spectrum. Such modification significantly reduces the laser group velocity v_g , which in turn results in the wakefield slow-down, relaxing the requirements for electron trapping. It has been also suggested that the first wake period

may undergo an expansion due to laser diffraction (Kalmykov, Yi, Khudik, & Shvets, 2009) or the expansion may be forced by the ponderomotive force of a counter-propagating injection pulse (Lehe, Lifschitz, Davoine, Thaury, & Malka, 2013). In both cases the wake phase velocity is reduced, enhancing the particle trapping.

2.4.7 Combined injection methods

The schemes that have been discussed above essentially form a complete set of currently known LWFA injection methods. Several original approaches, however, that combine more than one described technique in an experiment, have also been suggested. A fusion of ionization-induced and density transition injection schemes has been demonstrated to yield a reliable source with tunable energy (Thaury et al., 2015). Potentially even higher quality beams could be obtained by colliding two laser pulses to cause K-shell ionization only in the region of their overlap (Wan et al., 2016), however in practice this approach might be hard to set up. An even more ambitious scheme utilizes two transverse laser beams that collide exactly on the optical axis at a carefully defined distance behind the driver pulse to give an initial kick to nearby electrons via induced ponderomotive force (Chen et al., 2014) or once again to ionize the K-shell of high-Z gas in a tightly localized region (Li et al., 2013). So far these methods remain theoretical, but it would be very interesting to see what technical solutions may later be used to implement this practically and what would be the parameters of such electron source.

2.5 LWFA limiting factors

Naturally the acceleration process will stop at a certain point. In this section we discuss what are the main limiting factors of LWFA.

2.5.1 Diffraction

It is well known that a light beam may not stay focused for an arbitrarily long distance due to diffraction effects. A typical Gaussian laser beam intensity evolution is defined by the focusing geometry. If we focus the beam at an angle $\theta \approx \tan \theta = w(z)/z$ with respect to the optical axis, the achievable spot size (i. e. beam waist) in vacuum is given by:

$$w_0 \approx \frac{\lambda_0}{\pi\theta}, \quad (2.40)$$

where λ_0 is the laser wavelength. It is common to define the *Rayleigh length* as the distance from the focal plane where the beam intensity drops by a factor of two (Figure 2.9). It is related to the spot size via

$$z_R = \frac{\pi w_0^2}{\lambda_0}. \quad (2.41)$$

The beam radius at a distance z from the focal plane is given by

$$w(z) = w_0 \sqrt{1 + \left(\frac{z}{z_R}\right)^2}. \quad (2.42)$$

Evidently in the absence of guiding the laser pulse will not be able to maintain the high relativistic intensities required for wakefield generation over a distance significantly longer

than z_R . On the other hand, as seen from equation 2.41, increasing z_R means also increasing the focal spot size, leading to lower peak intensity. Therefore the focusing geometry needs to be chosen carefully for an experiment. On the other hand, in case of a very strong driver, diffraction may to a great extent be outcompeted by relativistic self-focusing, which will be discussed in a later section.

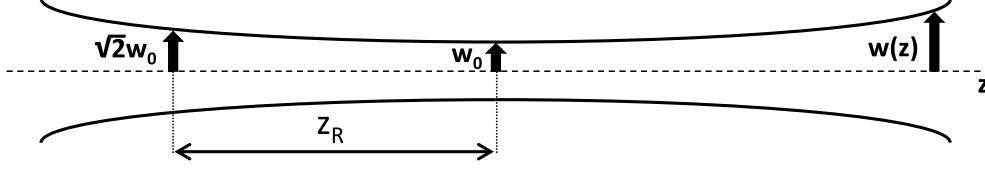


Figure 2.9 – Gaussian beam waist $w(z)$ as a function of the on-axis distance from the focal plane z ($w(z = 0) = w_0$) for a given Rayleigh length z_R .

2.5.2 Laser depletion

As the laser pulse continuously excites the wakefield, naturally it is losing its own energy. After some distance of propagation inside the plasma it will no longer be intense enough to generate waves. This distance is known as the pulse *depletion length* L_{pd} , and may be estimated using energy conservation. For tenuous plasmas in the weakly driven case, one may write $E_L^2 L_0 = E_z^2 L_{pd}$, where E_L and E_z are the laser and the longitudinal plasma wave field amplitudes, respectively, and L_0 is the driver pulse length (Esarey, Sprangle, Krall, & Ting, 1996). Since $E_L = mc\omega_0 a_0/e$, assuming the resonance condition $k_p L_0 = \sqrt{2}$ is satisfied and using equation 2.28, one gets

$$L_{pd} = \frac{E_L^2}{E_z^2} L_0 = \frac{\omega_0^2}{\omega_p^2} \frac{8}{\pi a_0^2} e L_0 \approx \frac{\omega_0^2}{\omega_p^2} \frac{c \tau_{\text{FWHM}}}{a_0^2}. \quad (2.43)$$

In the nonlinear regime ($a_0 \gg 1$), it is given by (Bulanov, Inovenkov, Kirsanov, Naumova, & Sakharov, 1992) (Lu et al., 2007)

$$L_{pd} = \frac{\omega_0^2}{\omega_p^2} c \tau_{\text{FWHM}}. \quad (2.44)$$

2.5.3 Dephasing

Once electrons are injected into the wakefield, their velocities very rapidly approach the speed of light c . At some point the bunch may become faster than the plasma wave itself, propagating at $v_p = v_g^{\text{las}}$, where $v_g^{\text{las}} \lesssim c$ is the laser pulse group velocity. This way it enters the decelerating wakefield region and the energy gain stops. This is characterised by the *dephasing length* L_{deph} , which may be estimated from the phase relation $k_p \zeta = k_p (L_{deph} - v_p t_{deph}) = \pi$, where t_{deph} is the dephasing time. Assuming the electrons are moving at a constant speed of light, one gets $L_{deph} = ct_{deph}$, and consequently $k_p (ct_{deph} - v_p t_{deph}) = \pi$. Hence follows that $L_{deph} = \lambda_p / (2(1 - \beta_p))$, where $\beta_p = v_p/c$. In the case $\gamma_p \gg 1$, this simplifies to

$$L_{deph} \approx \gamma_p^2 \lambda_p. \quad (2.45)$$

This equation can be further rearranged using the electromagnetic wave dispersion relation in a plasma:

$$\omega_0^2 = \omega_p^2 + c^2 k^2. \quad (2.46)$$

One may obtain the driver pulse group velocity:

$$v_g = \frac{\partial \omega_0}{\partial k} = \frac{1}{2} \frac{2c^2 k}{(\omega_p^2 + c^2 k^2)^{1/2}} = c \left(1 - \frac{\omega_p^2}{\omega_0^2} \right)^{1/2}$$

For a strongly underdense plasma we have $\omega_p \ll \omega_0$, so that it follows:

$$v_g \approx c \left(1 - \frac{1}{2} \frac{\omega_p^2}{\omega_0^2} \right),$$

which implies

$$\gamma_p^2 = \gamma_g^2 = 1 - \frac{v_g^2}{c^2} \approx \frac{1}{2} \frac{\omega_0^2}{\omega_p^2}.$$

Assuming additionally that the resonance condition $k_p L_0 = \sqrt{2}$ is satisfied, one gets

$$L_{deph} \approx \frac{1}{2} \frac{\omega_0^2}{\omega_p^2} \frac{2\pi}{\sqrt{2}} c \tau_{FWHM} \approx \frac{\omega_0^2}{\omega_p^2} c \tau_{FWHM} \quad (2.47)$$

in the weakly driven case, and

$$L_{deph} \approx \frac{\omega_0^2}{\omega_p^2} \sqrt{a_0} c \tau_{FWHM} \quad (2.48)$$

in the strongly nonlinear case ($a_0 \gtrsim 2$, equation 2.34). We conclude that for sub-relativistic driver intensities LWFA is predominantly limited by dephasing ($L_{pd} > L_{deph}$), however for high intensities the two characteristic lengths become comparable. In addition, both of these distances significantly reduce for short laser pulses (small τ_{FWHM}) operated in resonant regime (high ω_p). Rephasing limitation can be tackled by target profile tailoring, leading to a decrease in plasma wavelength (Guillaume, Döpp, Thaury, Ta Phuoc, et al., 2015).

2.5.4 Beam loading

It is known that particle beams can also be efficiently used to drive wakefields (Litos et al., 2014) (Adli et al., 2018). In fact, if the electron bunch injected in a laser-driven scheme contains enough charge, it may generate its own plasma wave that would interfere with the original one. This limits the total injected charge and the achievable particle energy (Rechatin et al., 2009) (Guillaume, Döpp, Thaury, Lifschitz, et al., 2015). Maximum number of accelerated electrons in the bubble regime can be estimated to be (Lu et al., 2007)

$$N \approx 3.1 \times 10^8 \lambda_0 [\mu\text{m}] \sqrt{P[\text{TW}]} \quad (2.49)$$

If the bunch profile is carefully shaped, the beam loading could in theory help reduce the electron energy spread by reshaping the longitudinal wakefield component in a way that all the bunch slices felt the same force. However, this is experimentally difficult to control, and in practice the effect often leads to further spectral broadening. Another potential benefit of beam loading is avoiding particle injection in multiple wake periods (Lundh, Rechatin, Lim, Malka, & Faure, 2013), which increases the final bunch duration. The electrons injected in the first wake period may load the plasma wave, and destroy any trailing plasma oscillations (Pukhov & Meyer-ter-Vehn, 2002). To ensure that the particles are first trapped in the cavity right behind the laser pulse and at a fast rate, sharp density transition injection method could be used (Massimo, Lifschitz, Thaury, & Malka, 2017).

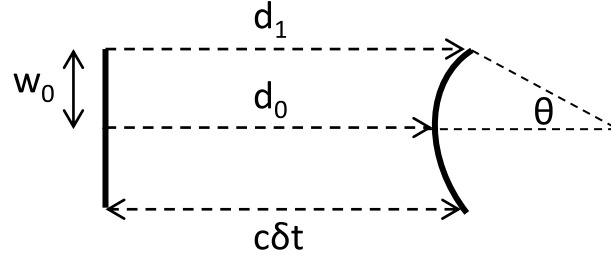


Figure 2.10 – Optical beam wave front curving due to relativistic self-focusing.

2.6 Plasma effects on laser pulse propagation

In this section several important laser-plasma interaction effects that tend to reshape a light pulse driving LWFA are going to be discussed. Some of them will turn out to be beneficial, others detrimental, frequently it depends on the other circumstances and experimental goals. Ways to mitigate the harmful effects will be mentioned.

2.6.1 Relativistic self-focusing

The refractive index of a tenuous plasma with frequency ω_p for an electromagnetic wave at frequency ω_0 is commonly known to be given by

$$\eta = \sqrt{1 - \frac{\omega_p^2}{\omega_0^2}} \approx 1 - \frac{1}{2} \frac{\omega_p^2}{\omega_0^2}. \quad (2.50)$$

However, when plasma electron motion approaches relativistic velocities, Lorentz correction factor needs to be included:

$$\eta = 1 - \frac{1}{2\gamma(r)} \frac{\omega_p^2}{\omega_0^2}. \quad (2.51)$$

In the above we assume γ to be dependent on the distance from optical axis r only, which is appropriate for a symmetric Gaussian laser driver causing the motion. This implies that such a light pulse will experience higher refractive index for the intense central part ($r \approx 0$) than on the sides, leading to a possibility of self-focusing and optical guiding. For an approximate derivation, suppose now an optical pulse with a minimum Gaussian waist w_0 propagates in a constant density plasma through its focus, therefore with a flat wave front. After a small time δt the central part will shift by a distance

$$d_0 = \frac{c}{\eta} \delta t = c \delta t \left(1 + \frac{1}{2\gamma(0)} \frac{\omega_p^2}{\omega_0^2} \right) = c \delta t \left(1 + \frac{1}{2} \frac{\omega_p^2}{\omega_0^2} \left(1 - \frac{a_0^2}{2} \right) \right),$$

where $\gamma(0)$ was developed assuming weakly relativistic optical on-axis field ($a_0 \ll 1$), and a Taylor approximation $1/(1-x) \approx 1+x$ is permitted by the tenuous plasma condition ($\omega_p \ll \omega_0$). The side part of the beam is less intense ($\gamma(w_0) \approx 0$), therefore it will cover a distance

$$d_1 = c \delta t \left(1 + \frac{1}{2} \frac{\omega_p^2}{\omega_0^2} \right).$$

The light beam then gets focused and starts to converge at a small angle (Figure 2.10)

$$\theta \approx \frac{d_1 - d_0}{w_0} = \frac{\delta t}{w_0} \frac{\omega_p^2}{\omega_0^2} \frac{a_0^2}{4}.$$

In the neighbourhood of this region the beam diameter varies as $dw(z)/cdt = -\theta$, hence

$$\left. \frac{d^2w}{c^2 dt^2} \right|_{self-foc} = -\frac{\omega_p^2}{\omega_0^2} \frac{a_0^2}{4w_0} = -\frac{k_p^2 w_0^3 a_0^2}{16z_R^2}.$$

This effect is opposed by diffraction, governed by (compare eq. 2.42)

$$w = w_0 \sqrt{1 + \left(\frac{ct}{z_R}\right)^2}.$$

One may then also calculate:

$$\frac{d^2w}{c^2 dt^2} = \frac{2w_0}{z_R^2} \left(1 + \left(\frac{ct}{z_R}\right)^2\right)^{-1/2} - \frac{4w_0 c^2 t^2}{z_R^4} \left(1 + \left(\frac{ct}{z_R}\right)^2\right)^{-3/2}.$$

Considering being close to the focus, i. e. where $ct/z_R \ll 1$, this reduces simply to

$$\left. \frac{d^2w}{c^2 dt^2} \right|_{diff} \approx \frac{2w_0}{z_R^2}.$$

Adding the two terms yields an equation governing the spot size:

$$\frac{d^2w/w_0}{c^2 dt^2} = \frac{2}{z_R^2} \left(1 - \frac{k_p^2 w_0^2 a_0^2}{32}\right). \quad (2.52)$$

Again, as we are close to the focus, the first derivative dw/dt is zero, and the behaviour of the spot size is determined by the second derivative. For low a_0 , the right hand side of the above will be dominated by the diffraction term, and the spot will grow. At a certain threshold value of a_0 , the self-focusing term will become comparable, thus optical guiding may be achieved. A more exact and common way to quote this result is through the critical power for relativistic self-focusing

$$P_{cr}[\text{GW}] = 17.4 \frac{\omega_0^2}{\omega_p^2} = 17.4 \frac{n_{cr}}{n}, \quad (2.53)$$

where n_{cr} is the plasma critical density, and n , as before, is the plasma density (Sprangle, Tang, & Esarey, 1987). If the laser pulse reaches power higher than P_{cr} , it will be self-guided (Monot et al., 1995). A more subtle phenomenological treatment of the bubble regime case specifically (Lu et al., 2007) gives another conveniently applied condition for the self-guiding to occur:

$$a_0 > (n_{cr}/n)^{1/5}. \quad (2.54)$$

This equation assumes implicitly all the necessary blowout resonance requirements.

2.6.2 Dispersion

As seen from equation 2.50, the plasma refractive index is dependent not only on the plasma properties through ω_p , but also on the laser frequency ω_0 . Since femtosecond light pulses by their nature have a broad bandwidth, dispersion effects may not be negligible and could lead to pulse lengthening, reducing the driver intensity. A fairly standard demonstration of this problem considers a transform-limited Gaussian laser pulse described by the envelope approximation:

$$E(t) = A \exp(-t^2/4\tau^2) \exp(-i\omega_0 t),$$

or in the frequency domain:

$$\tilde{E}(\omega) = \tilde{A} \exp(-(\omega - \omega_0)^2 \tau^2).$$

where A and \tilde{A} are normalization constants and τ is the standard deviation pulse duration. Passing through a dispersive medium of thickness d yields a frequency-dependent phase gain $\Delta\phi(\omega) = k(\omega)d$, so that the pulse may then be described by

$$\tilde{E}(\omega) = \tilde{A} \exp(-(\omega - \omega_0)^2 \tau^2) \exp(ik(\omega)d).$$

We may develop the wave number $k(\omega)$ as a truncated Taylor series:

$$k(\omega) = k(\omega_0) + k'(\omega_0)(\omega - \omega_0) + \frac{1}{2}k''(\omega_0)(\omega - \omega_0)^2.$$

With this expression it is possible to inverse-transform $\tilde{E}(\omega)$ to obtain a time-domain expression of the pulse after the medium:

$$E_d(t) = A_d \exp\left(-\frac{(t - k'(\omega_0)d)^2}{4(\tau^2 - ik''(\omega_0)d/2)}\right) \exp i(k(\omega_0)d - \omega_0 t)$$

Taking the square magnitude of this yields the intensity:

$$I_d(t) \propto \exp\left(-\frac{(t - k'(\omega_0)d)^2}{2\left(\tau^2 + \left(\frac{k''(\omega_0)d}{2\tau}\right)^2\right)}\right).$$

We conclude that the output pulse duration is modified only by the second derivative term $k''(\omega_0)$. It is commonly known as the group velocity dispersion (GVD). The final pulse duration is given by:

$$\tau_d = \sqrt{\tau^2 + \left(\frac{k''(\omega_0)d}{2\tau}\right)^2}. \quad (2.55)$$

For obtaining FWHM values, the equality $\tau_{\text{FWHM}} = 2\sqrt{2 \ln 2} \tau$ should be used. Now, in a plasma with frequency ω_p the wave vector for a light wave with frequency ω is given by (eq. 2.50)

$$k(\omega) = \frac{\omega}{c} \sqrt{1 - \frac{\omega_p^2}{\omega^2}}.$$

The group velocity dispersion may then be expressed as

$$\frac{d^2k}{d\omega^2} = -\frac{1}{c} \frac{1}{\left(1 - \frac{\omega_p^2}{\omega^2}\right)^{3/2}} \frac{\omega_p^2}{\omega^3}. \quad (2.56)$$

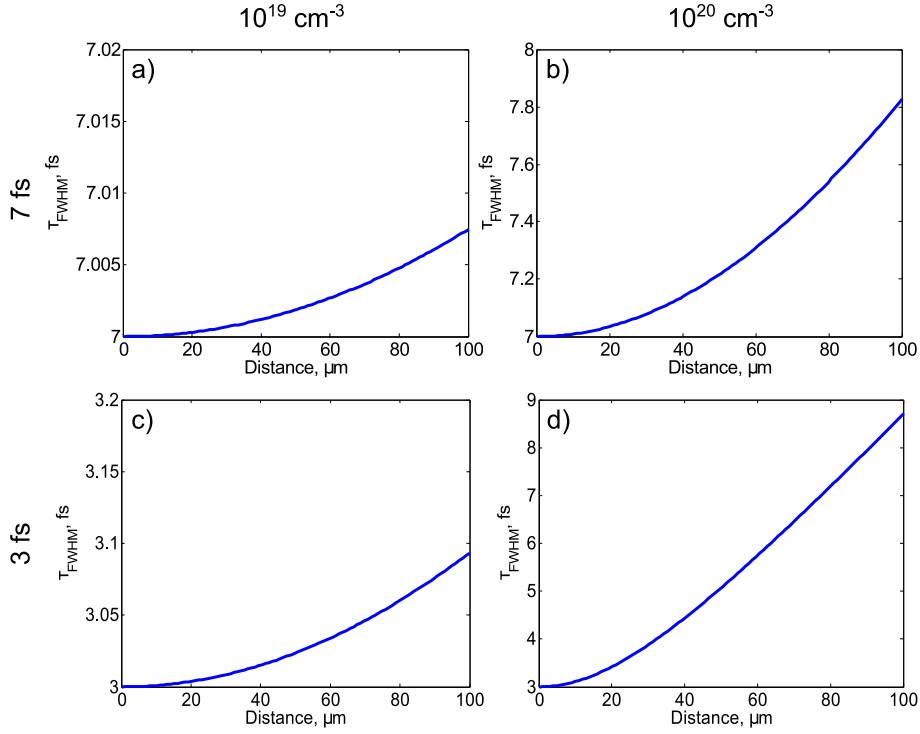


Figure 2.11 – Pulse lengthening due to dispersion for 7 fs (a) and b)) and 3 fs (c) and d)) pulses centered at $\lambda_0 = 800$ nm for homogeneous plasma densities of 10^{19} cm^{-3} and 10^{20} cm^{-3} .

One can use equations 2.55 and 2.56 to calculate the effect on laser pulse lengthening by a given density plasma. Figure 2.11 shows how initially transform-limited pulses of $\tau_{\text{FWHM}} = 7$ fs (top) and 3 fs (bottom), both centered at $\lambda_0 = 800$ nm, evolve when they propagate in a homogeneous plasma with density $n = 10^{19}$ cm^{-3} (left) or 10^{20} cm^{-3} (right). We see that the 7 fs pulse lengthens only by around 0.1% after a 100 μm of propagation in the lower-density target, hence the intensity loss is negligible. However, in a density higher by an order of magnitude, the pulse lengthening exceeds 10% over the same distance, which could already be of significant importance. For the 3 fs pulse the effect is even more pronounced – pulse gets longer by 0.3% after 100 μm of lower-density gas, and almost triples in duration for $n = 10^{20}$ cm^{-3} , implying a reduction in peak intensity also by a factor of 3.

Another way to look at this is via defining a characteristic dispersion length L_{disp} as the distance after which a transform-limited light pulse lengthens by a factor $\sqrt{2}$. From equation 2.55,

$$L_{\text{disp}} = \frac{2\tau^2}{k''(\omega_0)}.$$

Assuming a tenuous plasma and using equation 2.56 one may write:

$$L_{\text{disp}} = 2c\tau^2 \frac{\omega_0^3}{\omega_p^2} = 4\pi c^2 \tau^2 \frac{\lambda_p^2}{\lambda_0^3}. \quad (2.57)$$

Including the bubble regime resonance condition (eq. 2.33) yields

$$L_{\text{disp}} = \frac{2}{\ln 2} \pi \frac{c^4 \tau_{\text{FWHM}}^4}{\lambda_0^3}. \quad (2.58)$$

Plugging numbers for $\lambda_0 = 800$ nm gives characteristic lengths of 12 μm , 340 μm and 12 cm for pulses of 3 fs, 7 fs and 30 fs duration, respectively. As common LWFA experiments are

done with 30 fs titanium-sapphire laser pulses, for which the resonant densities lie between $10^{18} - 10^{19} \text{ cm}^{-3}$, it is natural to neglect the dispersion phenomenon. However, when few-cycle driver pulses are considered, they may need to be accounted for.

2.6.3 Ionization-induced defocusing

As discussed in section 2.4.4, there exist certain threshold optical intensities that are required to ionize electrons from different orbitals in specific materials. For a typical Gaussian laser pulse it might occur that this threshold gets exceeded around the optical axis, however is not achieved on its weaker sides. In such case the plasma density would be higher close to the optical axis than further away from it. The refractive index can also be written as (compare eq. 2.50)

$$\eta(r) \approx 1 - \frac{1}{2} \frac{n(r)}{n_{cr}},$$

meaning that the central part of the beam will experience a lower index as compared to the edges. This is essentially an effect of a divergent lens, defocusing the pulse and preventing it from achieving its diffraction-limited intensity (Rae, 1993) (Chessa et al., 1999). It may thus obviously hinder the formation of strongly nonlinear wakefields. In order to avoid this issue one would want to arrive at the gas target already with an intensity much higher than needed to ionize the matter, so that the leading pulse edge would create a homogeneous plasma that would then be experienced by the main part of the pulse. Possible strategies are using low- Z gases (e. g. Helium is completely ionized for $I \approx 10^{16} \text{ W/cm}^2$) and targets with lengths scales significantly smaller than the driver beam Rayleigh length z_R (Figure 2.12).

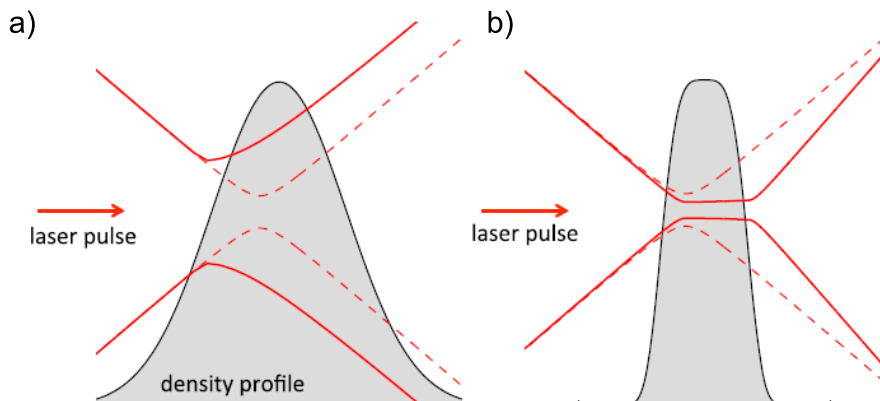


Figure 2.12 – Schematic of laser beam propagation in high- Z gas jets with various width. The dashed lines represent the shape of the laser beam in vacuum, whereas the solid lines account for plasma effects. a) density up-ramp is longer than z_R , so that the pulse starts interacting with the gas before reaching high intensity. Ionization-induced defocusing thus shifts the focal plane and increases the minimum spot size. b) laser pulse reaches the gas up-ramp already at high intensity, therefore coupling into the jet is optimized. Relativistic self-focusing may also be triggered in an easier manner.

2.6.4 Ionization-induced compression

It is also worth to examine what could happen to a Gaussian pulse around some ionization threshold intensity in the temporal domain. We may consider the plasma refractive index as a

function of the synchronized coordinate system variable $\zeta = z - ct$:

$$\eta(\zeta) \approx 1 - \frac{1}{2} \frac{n(\zeta)}{n_{cr}}.$$

At the front of the pulse, before it reaches the ionization threshold, the plasma density will be lower, therefore the refractive index higher. When the more intense part of the pulse arrives, the index starts dropping until a new constant value is reached before/at the intensity peak (Figure 2.13). After propagating a distance δz the pulse will accumulate a phase shift of $\phi(t) = -\eta(\zeta) \frac{\omega_0}{c} \delta z$. The instantaneous frequency variation will then be given by

$$\delta\omega(t) = \frac{d}{dt} \phi(t) = -\frac{d\eta}{d\zeta} \frac{d\zeta}{dt} \frac{\omega_0}{c} \delta z = \frac{d\eta}{d\zeta} \omega_0 \delta z.$$

Since $d\eta/d\zeta \geq 0$, all but the leading below-threshold part of the pulse will experience a blueshift (Yablonovitch, 1974). Due to negative plasma dispersion, the pulse may then get compressed to even shorter durations than originally (Fourcade Dutin et al., 2010) (He, Nees, Hou, Krushelnick, & Thomas, 2014). Nevertheless, although this would be a positive consequence, it comes simultaneously with the above-discussed defocusing, so great care should be taken if intending to make use of the considered effect to gain light intensity. Similar compression may also occur owing to density modulations due to the ponderomotive plasma wave creation itself (Faure et al., 2005).

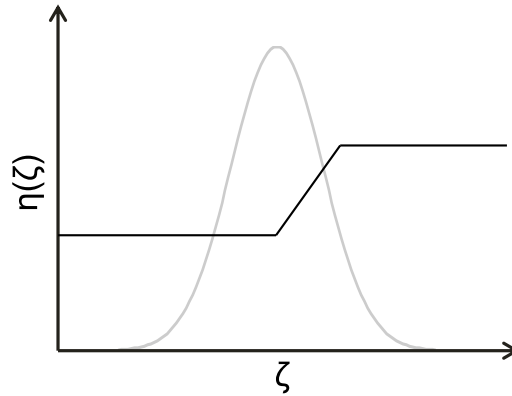


Figure 2.13 – Refractive index $\eta(\zeta)$ (black line) experienced by different parts of a Gaussian optical pulse (grey line, pulse front on the right).

2.7 Electron bunch propagation

As the electron bunch propagates, even in the absence of external fields it undergoes deformations that may change its shape dramatically before reaching the point of detection. This is important for any application that requires ultrashort electron bunches for time-resolved pump-probe experiments. In this section we will discuss the two main effects – velocity dispersion and space-charge.

2.7.1 Velocity dispersion

Accelerated electron bunches are never perfectly monoenergetic, and thus they tend to lengthen while propagating in free space simply because the slower particles lag behind. Assuming a

linear bunch chirp (i. e. any more energetic particle propagating ahead of any less energetic particle) to begin with and high enough energies ($\gamma \gg 1$), it is easy to give an estimate of this effect. Suppose the electrons at the back have energy corresponding to a gamma factor γ (we denote their velocity v_γ), while the fastest electrons propagate at $\gamma + \delta\gamma$ (velocity $v_{\gamma+\delta\gamma}$), where $\delta\gamma$ yields the energy spread. The time in the laboratory frame that will take for the back of the bunch to advance a distance L_d is expressed by:

$$t_\gamma = \frac{L_d}{v_\gamma} = \frac{L_d}{c} \frac{1}{\sqrt{1 - \frac{1}{\gamma^2}}} \approx \frac{L_d}{c} \left(1 + \frac{1}{2} \frac{1}{\gamma^2} \right).$$

The front of the bunch will, however, cover the same distance slightly faster:

$$t_{\gamma+\delta\gamma} = \frac{L_d}{v_{\gamma+\delta\gamma}} = \frac{L_d}{c} \frac{1}{\sqrt{1 - \frac{1}{(\gamma+\delta\gamma)^2}}} \approx \frac{L_d}{c} \left(1 + \frac{1}{2} \frac{1}{(\gamma+\delta\gamma)^2} \right) \approx \frac{L_d}{c} \left(1 + \frac{1}{2} \frac{1}{\gamma^2} \left(1 - 2 \frac{\delta\gamma}{\gamma} \right) \right).$$

Hence the bunch will temporally stretch by

$$dt = t_\gamma - t_{\gamma+\delta\gamma} = \frac{L_d}{c} \frac{\delta\gamma}{\gamma^3}. \quad (2.59)$$

For example, after only 10 cm of free propagation, a 2 MeV electron bunch with an energy spread of 1% will lengthen by 210 fs. A 5 MeV bunch, however, would disperse just by 30 fs. Due to a combination of this reason and consequential instrument limitations, pump-probe diffraction experiments with a 100 keV electron beam from a wakefield driven by a kilohertz sub-relativistic intensity laser could not achieve better than a picosecond level temporal resolution (He et al., 2016).

2.7.2 Space-charge

When a collection of electrons is propagating in free space, they repel each other due to the Coulomb force. This effect may be very significant for high-charge dense electron bunches, which not only expand spatially, but also get their energy distribution altered. Electrons at the front of the bunch will feel a net force pointing forward, the particles at the rear will experience a force backwards. In addition, the bunch will also be stretched transversely, increasing its divergence. To estimate the relativistic scalings, consider the set of electrons as an infinitely long cylinder with charge density $en(r)$ moving at velocity $\mathbf{v} = v_z \mathbf{e}_z$ (Wangler, 1998). With the usual cylindrical coordinates, the net electric field at a radius r from the axis will be directed radially outward and may be obtained from Gauss's law:

$$E_r(r) = \frac{e}{\epsilon_0 r} \int_0^r n(r) r dr.$$

Similarly, the total magnetic field may be estimated from Ampère's circuital law and it will be azimuthal:

$$B_\theta(r) = \frac{ev\mu_0}{r} \int_0^r n(r) r dr = \frac{v}{c^2} E_r.$$

The total radial Lorentz force is then

$$F_r = q(E_r - vB_\theta) = qE_r(1 - \beta^2) = qE_r/\gamma^2.$$

This shows that for high velocities the focusing magnetic term will nearly completely compensate the electric repulsion. The transverse equation of motion can be written as

$$F_r = m_e c \frac{d(\gamma\beta_r)}{dt} = m_e c (\dot{\gamma}\beta_r + \gamma\dot{\beta}_r) \approx \gamma m_e \dot{v}_r,$$

since the first term in the brackets is small ($\beta_r \ll \beta_z$, $\gamma = 1/\sqrt{1 - \beta_z^2 - 2\beta_r^2}$ varies slowly for any change in β_r). Therefore,

$$\dot{v}_r = qE_r/m_e\gamma^3, \quad (2.60)$$

and the defocusing effect for the spatial terms scales as $1/\gamma^3$. For the longitudinal deformation, consider the electron bunch now as a sphere with charge density a distance s away from the sphere center $en(s)$ and velocity $\mathbf{v} = v_z\mathbf{e}_z$. By Gauss's law applied in the reference frame of the bunch, the longitudinal electric field for an on-axis electron is equivalent to the expression before (except the integration now being over a spherical, not cylindrical coordinate):

$$E_z(s) = \frac{e}{\epsilon_0 s} \int_0^s n(s) s ds.$$

The key difference is that now there is no magnetic term to compensate for this force term. One may write the equation of motion:

$$F_z = m_e c \frac{d(\gamma\beta_z)}{dt} = m_e c (\dot{\gamma}\beta_z + \gamma\dot{\beta}_z) = m_e c (\dot{\beta}\gamma^3\beta\beta_z + \gamma\dot{\beta}_z) \approx m_e c (\dot{\beta}_z\gamma^3\beta_z^2 + \gamma\dot{\beta}_z)$$

where the replacement of β by β_z is due to $\beta_r \ll \beta_z$. This can be further simplified to:

$$\dot{v}_z = F_z/m_e\gamma^3, \quad (2.61)$$

so that once again the effect scales as $1/\gamma^3$. Hence the strongly-driven wakefield technique, for which the gradients are very high and electron bunches reach large values of γ extremely quickly, does not suffer from space-charge forces as significantly as more traditional constant field or RF acceleration methods. This permits obtaining electron pulses with few-fs duration only (Lundh et al., 2011). On the contrary, pump-probe diffraction experiments with an RF accelerator yielding relativistic 3.5 MeV particles, but obtained over a longer length due to a weaker gradient, have so far managed to reach a temporal resolution of 100 fs (Musumeci, Moody, Scoby, Gutierrez, & Westfall, 2010). Methods used with traditional acceleration techniques to mitigate the undesired space-charge effect include minimizing the number of bunch electrons, which brings down the value of the integral $\int n(r)rdr$ (Kealhofer et al., 2016), or applying precisely tuned electric fields to pre-compensate the resultant positive position-velocity correlation (Maxson, Cesar, Calmasini, Ody, & Musumeci, 2017).

2.8 Physics of gas jets

Target design plays a very important role in laser-plasma interaction. In LWFA, typically gas nozzles or gas cells provide the medium in an otherwise vacuum environment, where the laser beam shapes the accelerating structure. The plasma profile experienced by the driver pulse can influence the particle injection, dephasing, laser depletion or dispersion, and many other processes contributing to the final particle beam properties. It is worth noting that such an intense laser may not be focused to a point that is too close to any solid surface of the nozzle or the cell, as damage would immediately occur. Hence it is unavoidable to have some degree of free gas expansion into a vacuum, and the fluid dynamics of this process needs to be considered. This section will discuss a couple of important gas nozzle examples.

2.8.1 Subsonic gas jets

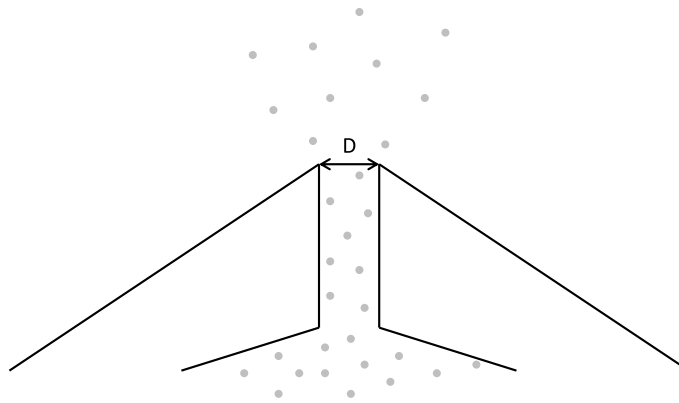


Figure 2.14 – Diagram of a subsonic gas nozzle.

A simplest way to create an underdense plasma target is a simple gas nozzle with a hole, connected to a variable pressure backing reservoir (Figure 2.14). An economical alternative could be thin glass capillaries, often used for chromatography applications and thus widely accessible. The total gas throughput will obviously depend on the hole diameter D , to some extent the hole aspect ratio, and the reservoir backing pressure P_{back} . When the gas exits the nozzle, it encounters vacuum, and therefore rapidly expands due to inner pressure forces, approaching free molecular flow regime. As mentioned, in a LWFA experiment laser may not be shot very close to the nozzle tip without damaging it, hence the gas profile encountered by the laser pulse will be significantly wider and with up-/downramp characteristic lengths larger than D . This may sometimes turn important, as it influences the driver evolution before it reaches an optimum density point (e. g. resonance condition 2.30). In addition, this rapid expansion may create vertical density gradients, causing asymmetries in the accelerating channel.

2.8.2 Supersonic gas jets

In order to reduce the discussed jet widening effects, one may want to increase the vertical (as in Figure 2.14) velocity of the gas at the point it leaves the nozzle. Then at a height where it is already "safe" to position the laser beam, the gas stream will not have spread as much as in the previous case, leading to plasma profiles on the optical axis of thickness similar to D and with much sharper gradients. This may be achieved using a converging-diverging geometry, also known as the de Laval nozzle (Figure 2.15). The way it works is widely understood by now,

mostly due to developments in aerospace engineering (Zucker & Biblarz, 2002). For a simple model, several assumptions about the gas should be made first:

- The flow of the gas is time-independent, i. e. a *steady state* is reached.
- The flow inside the nozzle is 1-dimensional, so that the fluid velocity component along the jet symmetry axis is much larger than the transverse components; all the molecules in a plane perpendicular to the direction of motion move alike.
- The fluid is *compressible*, which means that its density may vary.
- The fluid is an *ideal gas*.
- There is no energy dissipation due to friction or any other heat exchange with the surroundings.

In the analysis we are going to use the conservation laws of mass, energy and momentum, as well as the equation of state for an ideal gas. To begin with, the specific energy must be conserved at any point:

$$c_p T + \frac{v^2}{2} = \text{const} \quad (2.62)$$

where c_p is the specific heat capacity at constant pressure for the considered gas, T and v are the temperature and velocity of the fluid, respectively. It follows that:

$$\frac{dT}{dv} = -\frac{v}{c_p},$$

and therefore:

$$\frac{dT}{T} = -\frac{v^2}{c_p T} \frac{dv}{v} = -\frac{v^2}{c_p a^2} k R \frac{dv}{v},$$

where $a = \sqrt{kRT}$ is the speed of sound for an ideal gas with a specific constant $R = c_p - c_v$, $k = c_p/c_v$ is the ratio of specific heats, and c_v in the two previous expressions is the specific heat capacity at constant volume. It is trivial to show that

$$\frac{1}{c_p} k R = k - 1.$$

In addition, we define the *Mach number* $M = v/a$, the ratio of the fluid velocity to its local speed of sound. We may now conclude:

$$\frac{dT}{T} = -(k - 1) M^2 \frac{dv}{v}. \quad (2.63)$$

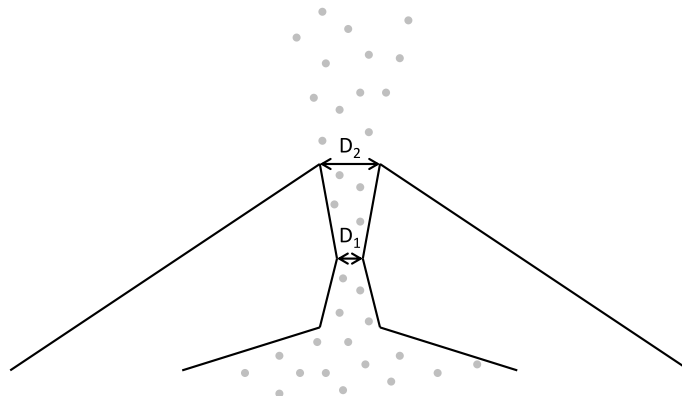


Figure 2.15 – Diagram of a supersonic gas nozzle.

Moreover, it is known that for an isentropic ideal gas flow the following relation holds:

$$\frac{P}{\rho^k} = \text{const.}$$

Here ρ is the fluid density. Consequently,

$$\frac{dP}{d\rho} = \frac{P}{\rho^k} k \rho^{k-1} = k \frac{P}{\rho} = kRT = a^2,$$

and hence

$$a^2 d\rho = dP = -\rho v dv,$$

where the last equality is due to momentum conservation. We finally obtain that

$$\frac{d\rho}{\rho} = -M^2 \frac{dv}{v}. \quad (2.64)$$

Now, from the conservation of mass we have

$$d(\rho v A) = 0,$$

or equivalently:

$$\frac{d\rho}{\rho} + \frac{dv}{v} + \frac{dA}{A} = 0, \quad (2.65)$$

where A is the nozzle area. It follows from equation 2.64 that

$$\frac{dA}{A} = -\frac{dv}{v} - \frac{d\rho}{\rho} = (M^2 - 1) \frac{dv}{v}. \quad (2.66)$$

The conclusion is that for subsonic fluid velocities ($M < 1$) decreasing the channel area A is accompanied by an increase in fluid velocity, and the other way round. This behaviour seems fairly intuitive. However, if our considered de Laval nozzle is able to speed up the fluid up to $M = 1$ at its narrowest point, then in the divergent part the velocity may become supersonic (depending on the pressure differential between the gas reservoir and the outlet). Looking at the equation above, one may now see that the fluid will continue to accelerate, thus reaching much higher speeds before exiting the nozzle. This will let the molecules propagate further into the vacuum before the jet expands transversely due to inner pressure forces, yielding plasma targets with narrower profiles and steeper ramps (Schmid & Veisz, 2012), as well as reduced vertical gradients.

2.8.3 Supersonic gas jets with a shock

Most readers are probably aware of the effect when, observing an object moving with a supersonic speed, e. g. a fighter jet plane during a military parade, no sound caused by its engines could be heard until a moment split-second after it would pass straight above one's head. Then the volume would grow high and very suddenly. The encountered phenomenon is called a "shock wave", and it marks the fundamental difference between subsonic and supersonic fluid flow. As the "information" about any object on the way spreads within the gas at the speed of sound, a supersonic fluid cannot "sense" its presence and smoothly adjust the flow. This creates surfaces with sharp fluid property changes accross them. Quantitatively these changes may similarly be estimated through mass, energy and momentum conservation laws (Zucker & Biblarz, 2002). An oblique shock, i. e. a shock front that is not perpendicular

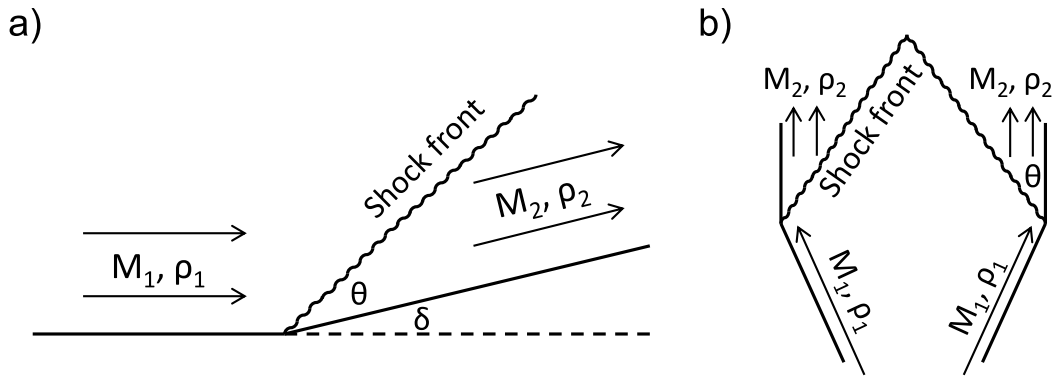


Figure 2.16 – a) Diagram of an oblique shock front formation due to a flow turn. b) Conical shock front due to a forced flow turn at the exit of a de Laval nozzle.

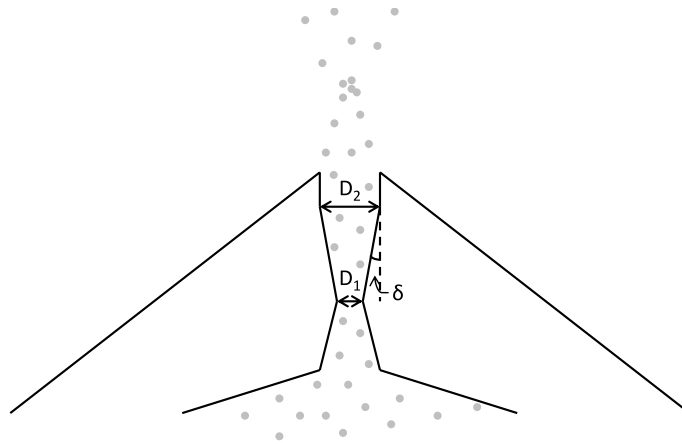


Figure 2.17 – Diagram of a supersonic shocked gas nozzle.

to the flow direction, is depicted in Figure 2.16a. Here a supersonic fluid with Mach number M_1 and density ρ_1 encounters a slight turn by an angle δ imposed by the nozzle walls. As discussed, the part of the flow which is not immediately in touch with the wall, will take some time to "find out" it needs to make a turn, and this way a shock front forms at an angle θ to the new flow direction. After the shock, the fluid will have a new Mach number M_2 and a density ρ_2 . The angle of the shock front is given by an implicit equation:

$$\tan \delta = 2(\cot \Theta) \frac{M_1^2 \sin^2 \Theta - 1}{M_1^2(k + \cos 2\Theta) + 2}, \quad (2.67)$$

where $\Theta = \theta + \delta$, with θ and δ as shown in the figure. Now, if one takes a typical cylindrically symmetric de Laval nozzle and adds a slight wall-turn at the end of the diverging section, a conical shock front may be created in 3D (Figure 2.16b). If the angles are well chosen for corresponding spatial dimensions and gas type (defining the value of k), the region with sharp density transitions may even extend into the space out of the nozzle channel, possibly as far as the "safe" height, i. e. where the laser optical axis could be placed without damage risk. Due to these sharp density changes and the ability to efficiently collect gas particles to a confined area (Figure 2.17), such nozzle may be of high interest in the context of density transition injection in LWFA, and also for proton/ion acceleration (Mollica, 2016).

3

Experimental tools

Contents

3.1 Overview of the project	44
3.1.1 Particle source for UED experiments	44
3.1.2 Benefits of high repetition rate	45
3.1.3 Scaling the bubble regime	45
3.2 Laser system	46
3.2.1 Hollow-core fiber compression	46
3.2.2 Pulse duration measurement	47
3.2.3 Peak intensity estimation	50
3.2.4 CEP stabilization	51
3.3 Electron beam diagnostics	52
3.3.1 Beam detection and charge estimation	52
3.3.2 Electron spectrometer	55
3.4 Target characterisation	57
3.4.1 Method	57
3.4.2 Subsonic jet	58
3.4.3 Supersonic gas nozzle	59
3.4.4 Supersonic gas nozzle with a shock	60
3.5 Numerical modelling	62

Chapter overview

In this chapter the general project motivation and the main experimental tools are reviewed. We describe the laser system used to drive the accelerator and show its temporal characterisation data. Later the setup for electron diagnostics is summarized and its calibration procedure

presented. The method for gas target characterisation is discussed together with collected data. Finally we introduce a numerical tool used to aid the understanding of underlying physical processes in our experiment.

3.1 Overview of the project

3.1.1 Particle source for UED experiments

As briefly mentioned in Chapter 1, an important particular feature of LWFA technique is its ability to generate extremely short electron bunches, down to sub-5 fs level (Lundh et al., 2011). This triggers an interest in utilising such a source for ultrafast science, e. g. material dynamics studies through ultrafast electron diffraction (UED) (Sciaini & Miller, 2011). What makes LWFA different from other acceleration methods that have already been established in UED? Table 3.1 makes a comparison between two main traditional techniques – direct field (DC) electron guns and radio-frequency (RF) cavities – and LWFA. One can see that modern DC accelerators can sustain up to 10 MV/m constant electric field without experiencing a breakdown even in ultrahigh vacuum conditions. As there is an additional trade-off between the value of the field and the distance over which it may be applied, the achievable kinetic particle energies are at most 100 keV, which is still sub-relativistic ($\gamma = 1.2$). Due to this

	UED state of the art		LWFAs
	DC electron guns	RF photoinjectors	
Accelerating gradient	≤ 10 MV/m	100 MV/m	100 GV/m
Achievable e^- energies	10-100s of keV	Few MeVs	< few GeVs
Record bunch durations	< 30 fs	< 25 fs	< 5 fs
Bunch charges for the above	1.6×10^{-4} fC	10 fC	15 pC
Jitter-free?	✓	✗	✓

Table 3.1 – Comparison of output parameters for different electron acceleration techniques. Note that the available bunch charges may differ for various parameters. E. g., a 30 fs DC electron gun has only been demonstrated for single-particle packets.

reason the space-charge forces lead to significant bunch expansion during propagation, limiting the achievable duration and thus the temporal resolution in ultrafast experiments. Best sources have been measured to produce bunches of ≈ 30 fs (Gliserin, Walbran, Krausz, & Baum, 2015) (Kealhofer et al., 2016). This has been achieved using single-electron packets, where the internal Coulomb repulsion is completely suppressed, and the duration is limited by quantum uncertainties in the process of particle emission from the photocathode (Baum, 2013). However, the issue remains that with such low charge particle pulses it would be required to make long pump-probe scans in order to accumulate a set of meaningful diffraction patterns, causing not only operational inconvenience, but also possible difficulties while maintaining the studied system under constant conditions. Running at much higher repetition rates (such sources could operate at $\gg 1$ MHz) is also excluded, since the laser flux required to pump the studied sample would lead to its thermal destruction. For this reason standard UED experiments with DC guns are now commonly operated only at ≈ 300 fs temporal resolution.

RF photoinjectors can sustain much higher, up to 100 MV/m accelerating gradients, which may be kept for long distances, so that relativistic particle energies could easily be achieved, mitigating space-charge expansion even for bunches with large electron numbers. With a compensation of the residual Coulomb effect by oscillating longitudinal electric fields that

invert the resultant velocity chirp, sub-10 fs electron bunches have been measured (Maxson et al., 2017). However, another important consideration for a time resolved experiment is the synchronization between the pump and the probe pulses, which for RF cavities suffers from an electronic jitter problem. Therefore, with these traditional acceleration methods that use RF fields the best temporal resolution achieved in UED has so far been around 100 fs (Musumeci et al., 2010) (van Oudheusden et al., 2010), suggesting LWFA may again provide an improvement by 1-2 orders of magnitude. This is because the accelerating gradient in plasma wakefields can reach 100 GV/m, or a factor of 1000 more than for RF cavities, meaning the particles reach relativistic velocities *much faster*, so that there is very little space-charge expansion even in the initial acceleration stages, before it gets drastically suppressed due to the $1/\gamma^3$ scaling (section 2.7.2). LWFA would also allow perfect optical synchronization, so that the temporal resolution in a pump-probe experiment would in principle only be limited by the bunch duration. The remaining issues, however, are the typical instability of the method, broad resultant particle spectrum, and generally too high final energies that would diffract by very low angles and be difficult to resolve. A stable, monoenergetic source of 1 – 10 MeV electrons is thus something we are in the search for.

3.1.2 Benefits of high repetition rate

Typical LWFA experiments have to this day been done with titanium-sapphire laser systems delivering 30 fs pulses that contain > 1 Joule of energy. Current laser technology limits such systems to a repetition rate of 1 – 10 Hz at best. Increasing this repetition rate is important for a wide variety of reasons. Firstly, kilohertz-class laser systems exhibit better shot-to-shot stability, which could naturally be expected to translate into the stability of an electron source. Secondly, it may allow the possibility to optimize the electron beam through active feedback control with a deformable mirror or otherwise (He et al., 2015). Moreover, it boosts the average current of the source, which would be important for any dose-related applications, such as medical treatment (Malka et al., 2008) and electronics hardness studies (Hidding et al., 2017). Finally, industrial (Ben-Ismaïl et al., 2011) or medical (Döpp et al., 2018) radiography as well as any pump-probe experiment would greatly benefit from high repetition rate due to faster data collection and better statistics improving the signal-to-noise ratio. Hence the development of such accelerators could be impactful for many fields of science and applications.

3.1.3 Scaling the bubble regime

From the laser technology perspective, the most straightforward condition that would allow increasing the repetition rate is running at lower pulse energy. To evaluate whether or not weaker laser pulses could be capable of driving a high-quality wakefield accelerator, we look back at the bubble regime and determine the scaling laws. We have seen before that being close to the bubble resonance condition is desired (equation 2.33):

$$c\tau_{\text{FWHM}} \approx \sigma \approx \lambda_p/2.$$

Furthermore, in order to obtain a strong wakefield, keeping the high laser intensity around focus ($\sigma = w_0$) is necessary. The intensity is defined as the power per unit area:

$$I \propto \frac{E_{\text{pulse}}}{\tau_{\text{FWHM}} w_0^2},$$

where E_{pulse} is the laser pulse energy. From the resonance condition we know that $w_0 \propto \tau_{FWHM}$, and therefore:

$$I \propto \frac{E_{pulse}}{\tau_{FWHM}^3}. \quad (3.1)$$

We conclude that the bubble regime may be efficiently obtained with 1000 times less pulse energy than some already established case, provided we also use laser pulses with 10 times shorter duration. That would allow increasing the repetition rate of the system by a factor of 1000. In addition, it can be shown that for a constant peak intensity the maximum electron energy scales as (Lu et al., 2007):

$$E \propto \lambda_p^2 \propto \tau_{FWHM}^2. \quad (3.2)$$

Hence the same 10-fold reduction in driver duration should yield electrons of 100 times lower energy. Now, a typical 1 J, 30 fs system used for LWFA is known to deliver electrons in the 100 MeV-GeV range. Therefore, a scaled-down version of 1 mJ, 3 fs pulses enables to expect an electron output with 1 – 10 MeV energies. As already discussed, this would be the desired range for UED applications.

3.2 Laser system

3.2.1 Hollow-core fiber compression

A standard titanium-sapphire crystal has an emission spectrum that may support Fourier-limited output pulses down to ≈ 20 fs in duration. To go beyond this, additional techniques are required. The most robust known way is compression in hollow-core fused silica waveguides filled with noble gas. In such a setup, the pulse is focused into the entrance of a fiber, with a spot size carefully tailored to the core diameter. While propagating along via grazing reflections off the inner glass surface, it experiences self-phase modulation (SPM), which generates new wavelengths, so that much shorter broad bandwidth pulses may be produced at the end. This technique has permitted the first multi-GW sub-5 fs laser sources (Nisoli et al., 1997), and has been advancing ever since.

The system *Salle Noire* developed in Laboratoire d'Optique Appliquée follows the same principle (Böhle et al., 2014) (Figure 3.1). A 23 fs, 10 mJ double-CPA laser beam is converted to circular polarization by a quarter-wave plate, and focused into a fiber that has a 536 μm diameter hollow core filled with high-purity helium. The waveguide inlet is connected to a pumped vacuum chamber whereas the outlet is joined to a chamber kept at a desired helium pressure, letting the gas steadily flow through the core and establishing a pressure gradient along the fiber, so that the pulse would accumulate nonlinear effects gradually. The light transmission can be adjusted by tailoring the temporal pulse profile by a programmable acousto-optic modulator (Dazzler by Fastlite) upstream in the chain, and has been observed to reach around 50%. Figure 3.2 compares the laser spectra after the fiber in the case when the post-chamber is evacuated (a), or kept at a constant pressure of 1200 mbar (b). In the first case we observe a typical titanium-sapphire emission spectrum, whereas with the gas we obtain a much broader pattern, covering nearly the entire 400 – 1000 nm range that could support even sub-3 fs Fourier-limited pulses. The polarization is then converted back to linear by another quarter-wave plate, and the beam is sent via a glass window to a vacuum environment again. Since the passage through the gas-filled waveguide and the window introduces residual chromatic pulse dispersion, another post-compression stage is required. This is done with a set of broadband chirped mirrors, which unfortunately cut most of the light below 450 nm. To

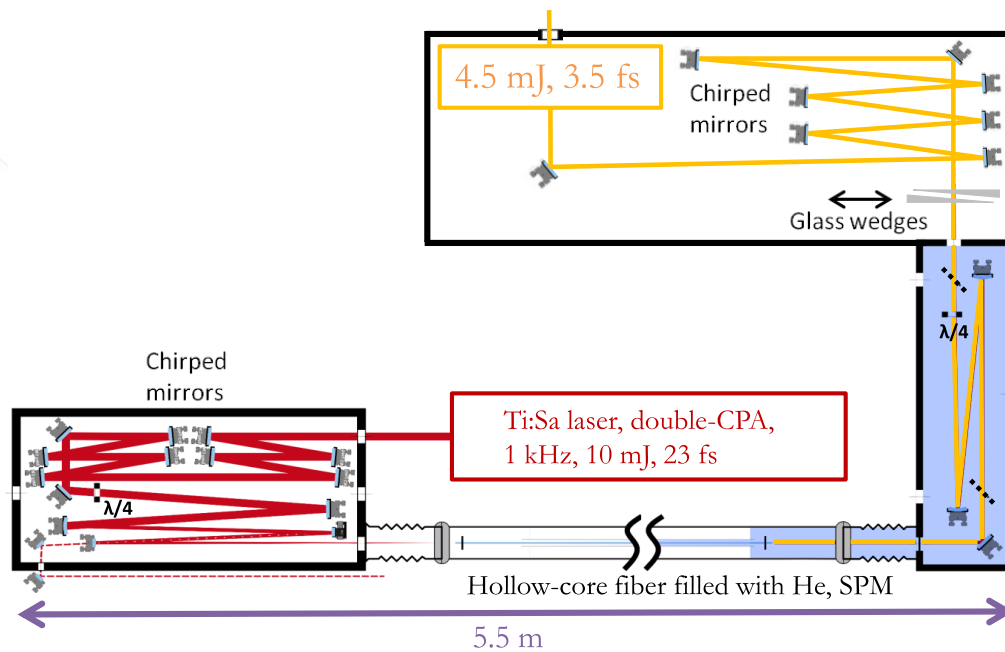


Figure 3.1 – Schematic view of the laser pulse compression system.

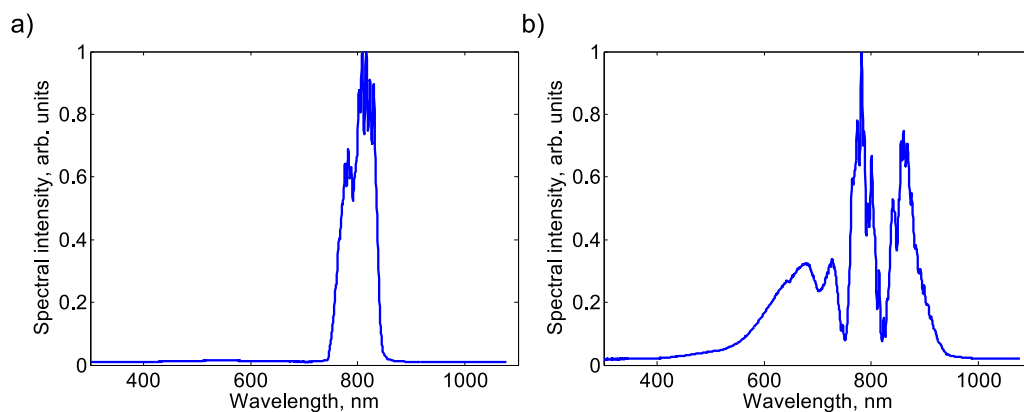


Figure 3.2 – Laser spectra after the hollow-core fiber with: a) post-chamber kept in vacuum, so that the core is evacuated, and b) post-chamber kept at constant 1200 mbar helium pressure.

fine-tune the point of best compression, a pair of motorized fused silica wedges are used. They also allow the possibility to deliberately chirp the laser pulses before sending them towards the experiment. Naturally, only reflective optics with special ultralow-dispersion coatings are utilised from this point. A final important note about the discussed technique is that the degree of compression may also be varied simply by the choice of helium pressure. This way laser pulses with any intermediate Fourier-limited duration may be produced. After the losses in the chirped mirrors and all the remaining beam transport, 2.5 – 3 mJ light packets could be delivered to the experiment.

3.2.2 Pulse duration measurement

To characterise the laser pulses temporally and determine the required wedge insertion for optimum compression, an innovative "d-scan" setup was installed under vacuum (Sphere Ultrafast Photonics) (Miranda et al., 2012) (Figure 3.3). This technique is capable of measuring few-fs pulses in a significantly more user-friendly manner than the commonly encountered FROG or SPIDER methods. After passing the pair of motorized wedges and the set of chirped

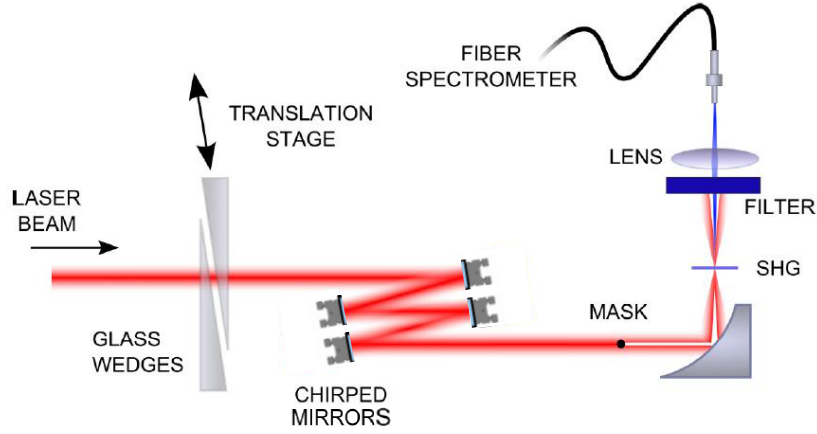


Figure 3.3 – Schematic view of the d-scan pulse characterisation setup. Adapted from (Miranda et al., 2012).

mirrors, the laser is focused into a second harmonic generation (SHG) crystal by an off-axis parabola. The generated broad frequency-doubled spectrum is then filtered and delivered to a fiber spectrometer. This is performed for a range of wedge positions, which can make the pulse negatively or positively chirped with respect to the yet unknown best compression condition. The width of the SHG spectrum depends on the incident laser pulse electric field profile, and the wedge insertion where the bandwidth turns out to be the broadest will define the optimum point. To recover the full temporal profile of the pulse, an iterative algorithm is used. It makes an initial guess of the spectral phases describing the pulse to combine them with knowledge of the fundamental laser spectrum and thus obtain the complex spectral amplitude:

$$\tilde{E}(\omega) = |\tilde{E}(\omega)| \exp[i\phi(\omega)].$$

Then the algorithm adds a calculated phase accumulated due to a corresponding additional amount of wedge glass d . Note that d may be negative as the amount of glass is measured against the thickness corresponding to the best compression position. Given the glass dispersion curve $k(\Omega)$, we may then perform an inverse Fourier transform to obtain the pulse profile in the temporal domain:

$$E(t) \propto \int_{-\infty}^{+\infty} \tilde{E}(\Omega) \exp[idk(\Omega)] \exp(i\Omega t) d\Omega.$$

The SHG process depends on the square of the electric field. Using this, we may obtain the resultant temporal profile of the frequency-doubled pulse, Fourier-transform it again, and calculate the SHG spectrum given by the initially assumed pulse:

$$S(\omega, d) \propto \left| \int_{-\infty}^{+\infty} \left(\int_{-\infty}^{+\infty} \tilde{E}(\Omega) \exp[idk(\Omega)] \exp(i\Omega t) d\Omega \right)^2 \exp(-i\omega t) dt \right|^2.$$

Such spectra are obtained for each value of d , and a comparison can then be made with the spectrometer measurements. The algorithm evaluates the discrepancies, improves on the guess, and continues this iteration until the modelled 2D map $S(\omega, d)$ converges to the data. The temporal pulse profile is then obtained by an inverse Fourier transform of this final best-guess expression.

Figure 3.4 shows a comparison between a typical measured $S(\omega, d)$ map (left), and one retrieved from the best assumption of the pulse profile (right). Here the y-scale corresponds to

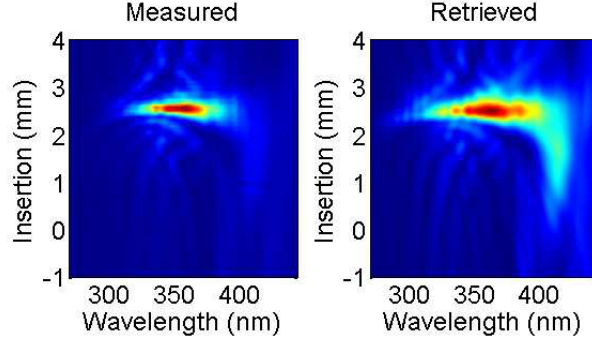


Figure 3.4 – Typical d-scan trace for a few-fs laser pulse. Measured (left) and numerically produced (right) 2D maps of SHG spectra for different glass wedge insertion thicknesses are shown.

a nominal value of the motorized insertion stage. We clearly see that the best compression occurs for an insertion of around 2.5 mm, and the set of d values consistent with the formulas above is then obtained with respect to this reference. Figure 3.5a shows the measured laser spectrum (note the cut below 450 nm as compared to Figure 3.2b due to the limited chirped mirror bandwidth!) together with the reconstructed spectral phase ϕ in the wavelength domain. Using this data, the temporal pulse electric field profile could be reconstructed (Figure 3.5b), as well as its intensity profile (Figure 3.5c). The FWHM value of the latter curve is estimated to be $\tau_{\text{FWHM}} = 3.5$ fs, corresponding to ≈ 1.3 optical cycles at $\lambda_0 = 800$ nm. Plugging this into the bubble resonance condition (eq. 2.33) yields a required plasma wavelength $\lambda_p \approx 2 \mu\text{m}$. For mildly relativistic pulses ($a_0 \approx 1$) this translates to an electron density of $2.8 \times 10^{20} \text{ cm}^{-3}$, higher by two orders of magnitude than in typical LWFA experiments.

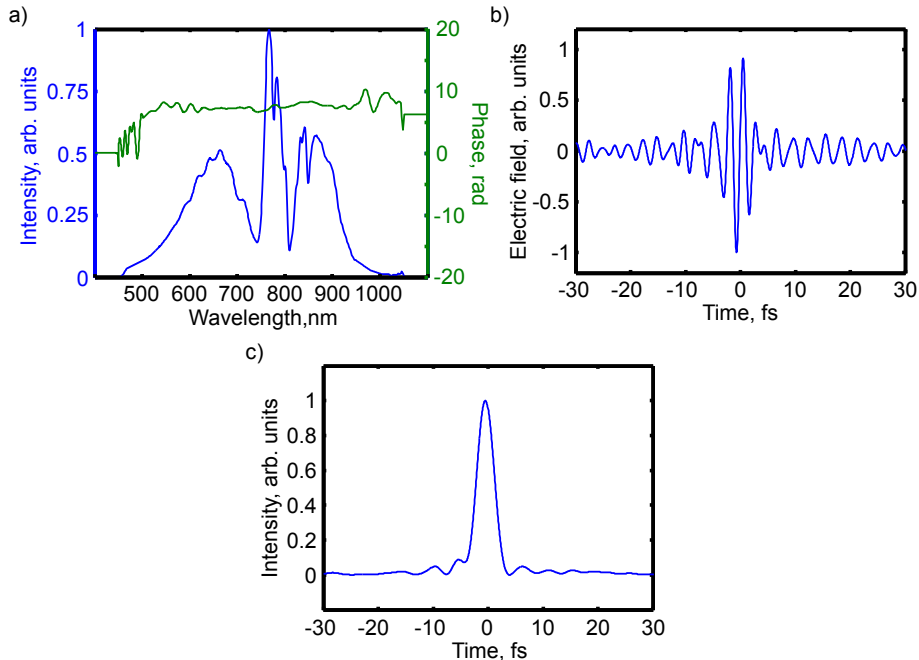


Figure 3.5 – Results of a pulse measurement with the d-scan technique. a) the spectrum measured by the spectrometer for the fundamental light (blue) together with the determined spectral phase (green). b) The reconstructed electric field profile. c) The reconstructed intensity profile. The estimated FWHM duration of the pulse is $\tau_{\text{FWHM}} = 3.5$ fs.

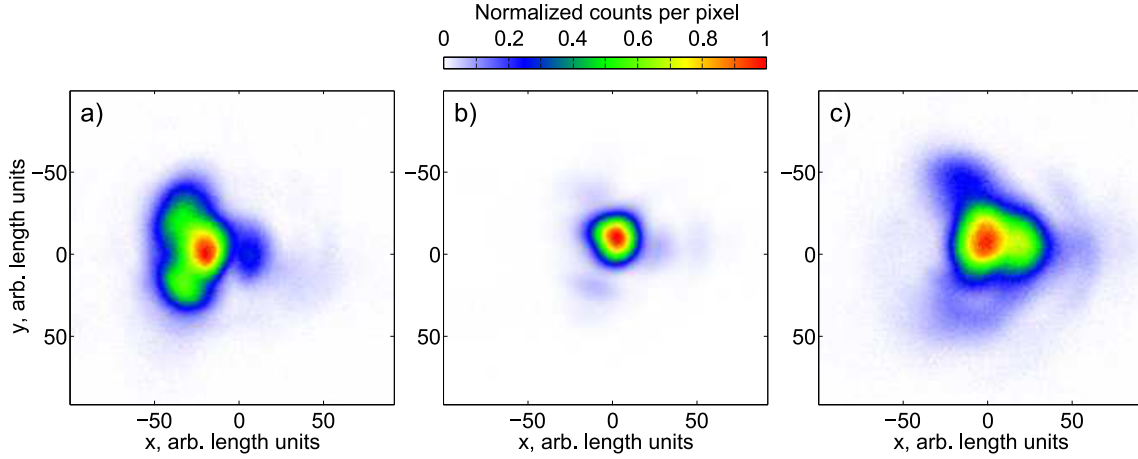


Figure 3.6 – Images of the laser beam 50 μm before the focus (a), at focus (b), and 50 μm after the focus (c).

3.2.3 Peak intensity estimation

Another benefit of using the hollow-core fiber technique is that it delivers an excellent spatial mode yielding good beam refocusability. We look at the focal spot of our laser at the experimental point of interaction, where we could insert a microscope objective to image the focal plane or any other selected nearby plane onto a CCD camera. As obviously the full-energy beam may not be sent onto the objective, a reflective attenuator and a thin pellicle are inserted into the path while doing the measurement, so that the wavefront is not distorted. The combined attenuation factor is of the order of 10^5 . Figure 3.6 shows images of the laser 50 μm before the focus of a parabola in $f/3$ configuration (a), at its focus (b), and 50 μm afterwards (c). We see that the resultant spot is only slightly elliptical near-perfect Gaussian ($3.5 \times 3.7 \mu\text{m}$ FWHM), which is important for generating symmetric wakefields. Slightly out of focus the symmetry degrades, indicating mild beam misalignment, however most of the intensity is still contained around the center. This allows to expect creation of a high quality accelerating channel over distances extending to the Rayleigh length.

The peak intensity I_0 may then be estimated as follows. Assuming a perfect Gaussian distribution $I(r, t) = I_0 \exp\left(-4 \ln 2 \frac{t^2}{\tau_{\text{FWHM}}^2}\right) \exp\left(-2 \frac{r^2}{w_0^2}\right)$, one may write the total energy contained within the laser pulse as:

$$\begin{aligned}
 E_{\text{laser}} &= \int_{-\infty}^{+\infty} \int_0^{+\infty} \int_0^{2\pi} I(r, t) d\theta r dr dt \\
 &= 2\pi I_0 \int_{-\infty}^{+\infty} \exp\left(-4 \ln 2 \frac{t^2}{\tau_{\text{FWHM}}^2}\right) dt \int_0^{+\infty} r \exp\left(-2 \frac{r^2}{w_0^2}\right) dr \\
 &= \frac{\pi I_0 w_0^2}{2} \frac{\sqrt{\pi} \tau_{\text{FWHM}}}{\sqrt{4 \ln 2}} \\
 &\approx \frac{\pi I_0 w_0^2}{2} \tau_{\text{FWHM}}.
 \end{aligned}$$

Therefore, the peak intensity is equal to:

$$I_0 \approx \frac{2E_{\text{laser}}}{\tau_{\text{FWHM}} \pi w_0^2}. \quad (3.3)$$

For a real beam with some deviations from a true Gaussian profile, this should then be scaled by two factors. The first one is the ratio of the value of the normalized temporal integral for a perfect Gaussian over the numerical integral of the normalized temporal intensity profile measured by the d-scan technique:

$$C_{temporal} = \frac{\sqrt{\pi}\tau_{FWHM}}{2\sqrt{\ln 2}} \frac{1}{\int_{-\infty}^{+\infty} I_{norm}(t)dt}.$$

The second one is the corresponding factor for the spatial profile deviation from a perfect Gaussian:

$$C_{spatial} = \frac{w_0^2}{4} \frac{1}{\int_0^{+\infty} r I_{norm}(r)dr},$$

where $I_{norm}(r)$ is the normalized intensity profile measured by the CCD camera, and r is taken with respect to the maximum point. This becomes ill-defined for badly shaped beams. The real peak intensity is then

$$I_{real} = C_{temporal}C_{spatial}I_0. \quad (3.4)$$

Typical value for $C_{temporal}$ in our experiment lies at around 0.7, whereas $C_{spatial}$ is very sensitive to the beam transport and parabola alignment, and would vary between 0.5 and 0.7. For the focal spot depicted in Figure 3.6 and its corresponding temporal profile measurement the estimated real peak intensity is $I_{real} \approx 2.0 \times 10^{18}$ W/cm², equivalent to $a_0 \approx 0.9$.

3.2.4 CEP stabilization

For few-cycle laser pulses the carrier-envelope phase (CEP) becomes an important parameter and may need to be controlled (Jones et al., 2000). Our laser is equipped with a home-built standard f -to- $2f$ interferometry setup that monitors the beam at the end of the chain, and sends the measured signal to a phase stabilization system (Menlo Systems APS800), which in turn modulates the power of the oscillator pump diode laser. This way the strength of Kerr lensing for the short pulses is adjusted, and their effective optical cavity length is stabilized (Holzwarth et al., 2000). Figure 3.7 shows a measurement of relative CEP values for a 7.5-minute run with a locked laser. The estimated standard deviation is 152 mrad, where each data point corresponds to 30 integrated laser shots. The system also allows manually setting different relative CEP values, which has later been used for studying relevant effects for LWFA.

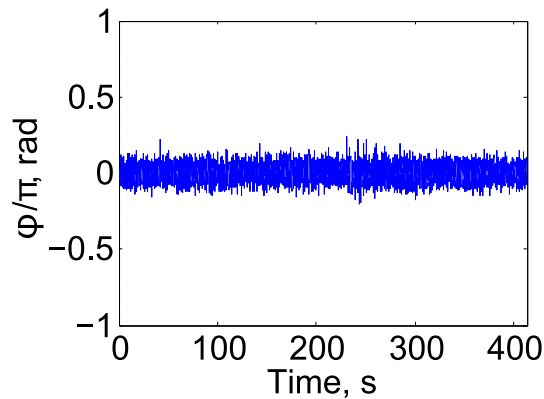


Figure 3.7 – Measurement of relative carrier-envelope phase stability.

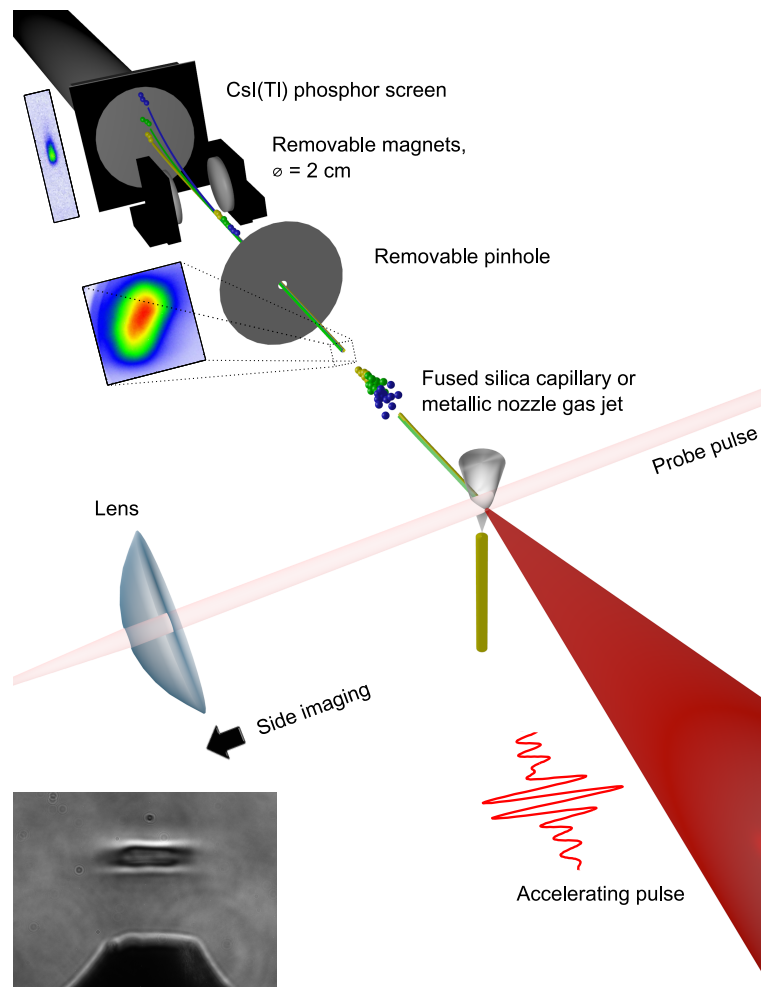


Figure 3.8 – Scheme of the experimental setup

3.3 Electron beam diagnostics

3.3.1 Beam detection and charge estimation

We now review how the electron beam is detected and characterized. Figure 3.8 shows the setup used for the wakefield acceleration experiments in this project. The ultrashort laser pulse is focused into a gas target created by either a subsonic flow glass capillary, or a special microstructured gas jet (section 2.8). The very leading edge of the pulse creates the plasma, more intense parts then excite a highly nonlinear wave, where some plasma electrons can be trapped and accelerated. If the magnetic spectrometer is removed from the way, the particles arrive directly onto a CsI(Tl) fiber optic scintillator (FOS), which converts them into photons. The screen is covered by a thin layer of aluminium foil to block the laser light, which also stops electrons with energies lower than approximately 100 keV. The scintillator plane is then imaged by a system of two lenses onto a 14-bit CCD camera (QImaging EXi Blue) to observe the electron beam profile.

The accelerated beam charge may then be estimated in the following manner. When a particle hits the screen, it deposits energy into the matter through multiple collisions. The amount of deposited energy is dependent on the incident particle energy, and may be obtained via computer modelling. Figure 3.9 shows a result of GEANT4 simulation based on Monte Carlo methods which estimates the relative energy deposited by different energy electrons in a FOS

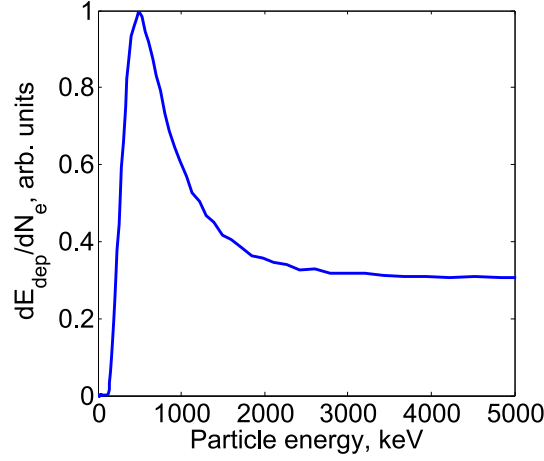


Figure 3.9 – GEANT4 simulation results showing the dependence of deposited energy on the incident particle energy.

plate, covered by a $60 \mu\text{m}$ layer of aluminium foil, equivalent to experimental conditions. We see that 500-keV particles deposit nearly three times more energy than the ones at 2 MeV. On the other hand, the response above 2 MeV turns fairly flat. Also note that the curve drops to zero below 120 keV, which is due to the inclusion of aluminium foil that blocks these low-energy electrons. We then assume that the amount of radiated light is proportional to the deposited energy, i. e.

$$\frac{dE_{rad}}{dN_e} = \epsilon \frac{dE_{dep}}{dN_e},$$

which is valid when the scintillator is not saturated. Finding the proportionality coefficient ϵ has to be done experimentally.

Then one has to consider the emission spectrum $f(\lambda)$ of the FOS plate. We normalize this quantity so that

$$\int_0^{+\infty} f(\lambda) d\lambda = 1,$$

therefore $f(\lambda)d\lambda$ is the probability that a photon with a wavelength λ is emitted. The number of emitted photons at λ per $d\lambda$ by one electron is then

$$\frac{d^2 N_{ph}^{(em)}}{dN_e d\lambda} = \frac{dE_{rad}}{dN_e} f(\lambda) \frac{\lambda}{hc},$$

where hc/λ gives the energy of one photon. We furthermore need to know the transmission of the optical system $T(\lambda)$, its solid angle of collection $\delta\Omega$, as well as the emission distribution of the screen $g(\theta)$. For the FOS we can use an isotropic distribution law, $g(\theta) = 1/(2\pi)$. The number of collected photons at λ per $d\lambda$ per electron is then

$$\frac{d^2 N_{ph}^{(coll)}}{dN_e d\lambda} = \frac{dE_{rad}}{dN_e} f(\lambda) \frac{\lambda}{hc} T(\lambda) \delta\Omega g(\theta).$$

Assuming no losses in the imaging system, these photons will be converted to camera counts. To get the correct count number, two intrinsic camera parameters are required, the quantum efficiency $Q_e(\lambda)$, and the coefficient that tells how many photoelectrons generated in the CCD chip are required to produce one count, we shall denote it r . r is dependent on the reading

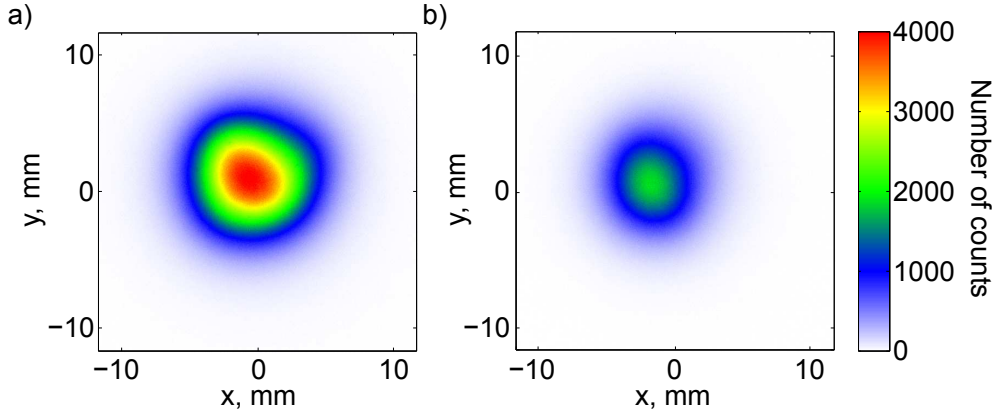


Figure 3.10 – Electron beam profiles obtained at the linear accelerator. a) typical profile of a 64.4 pC/shot beam. b) typical profile of a weaker beam with 35.5 pC/shot.

parameters of the camera, such as the reading rate or the applied gain. The number of counts due to photons emitted at λ per $d\lambda$ is thus

$$\frac{d^2 N_{cam}}{dN_e d\lambda} = \frac{dE_{rad}}{dN_e} f(\lambda) \frac{\lambda}{hc} T(\lambda) \delta\Omega g(\theta) \frac{Q_e(\lambda)}{r}.$$

By integrating over all wavelengths we obtain the total number of camera counts per electron:

$$\frac{dN_{cam}}{dN_e} = \frac{dE_{rad}}{dN_e} \frac{\delta\Omega g(\theta)}{hcr} \int_0^{+\infty} T(\lambda) Q_e(\lambda) f(\lambda) \lambda d\lambda.$$

For brevity, we denote $\Lambda = \int_0^{+\infty} T(\lambda) Q_e(\lambda) f(\lambda) \lambda d\lambda$. The number of electrons at energy E per dE is then given by

$$\frac{dN_e}{dE} = \frac{dN_{cam}}{dE} \frac{1}{\frac{dE_{rad}}{dN_e}} \frac{1}{\Lambda} \frac{hcr}{\delta\Omega g(\theta)}.$$

Finally, we integrate this expression over all the energies to obtain the total number of electrons:

$$N_e = \frac{1}{\Lambda} \frac{hcr}{\delta\Omega g(\theta)} \int_0^{+\infty} \frac{dN_{cam}}{dE} \frac{1}{\frac{dE_{rad}}{dN_e}} dE. \quad (3.5)$$

If all the electrons are accelerated to high enough energies ($\gtrsim 2$ MeV), $\frac{dE_{rad}}{dN_e}$ becomes constant, so that the expression simplifies to

$$N_e = \frac{1}{\Lambda} \frac{hcr}{\delta\Omega g(\theta)} \frac{1}{\frac{dE_{rad}}{dN_e}} N_{cam}.$$

Otherwise the particle spectrum $\frac{dN_{cam}}{dE}$ also needs to be fully measured for a correct estimation of charge. Using the simplified expression and a coefficient only applicable to high energy electrons would overestimate the total number by a factor of 3 at worst.

The remaining part of the puzzle is determination of the constant ϵ that yields the curve dE_{rad}/dN_e from the numerical simulation. To establish this, we went to a linear accelerator facility (Laboratoire de l'Accélérateur Linéaire in Orsay, France), where a monoenergetic electron beam at 3.8 MeV delivering bunches with a charge of 30 – 70 pC was available (Figure 3.10). The charge could be measured with a locally installed integrating current transformer (ICT). In order to reduce any additional uncertainties of our detection system, we brought the

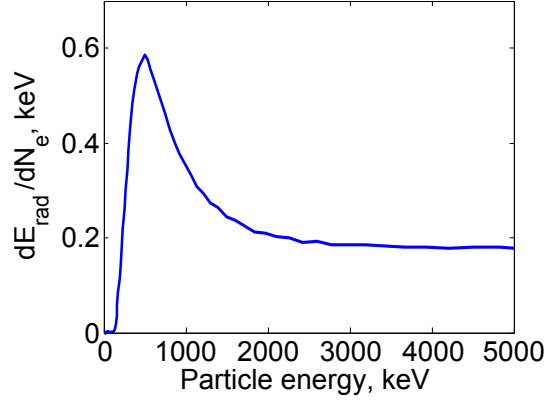


Figure 3.11 – Calibrated GEANT4 simulation curve showing the dependence of radiated energy on the incident particle energy.

whole setup to the accelerator facility and set it up preserving the original geometry. This way rather than determining the coefficient dE_{rad}/dN_e for a monoenergetic 3.8 MeV beam, we could obtain the entire constant

$$\frac{1}{\Lambda} \frac{hcr}{\delta\Omega g(\theta)} \frac{1}{\frac{dE_{rad}}{dN_e}}$$

by comparing the camera counts N_{cam} with the charge measurements on ICT. This cross-calibration allowed us to appropriately scale the curve seen in Figure 3.9 to get correct estimations of charge for beams of larger energy spreads in LWFA experiments (equation 3.5). Using the value $\delta\Omega = 0.07$ obtained from the geometry of our detection system, isotropic emission law $g(\theta) = 1/(2\pi)$, camera parameter $r = 1.4$ verified during previously done comparisons with a different known CCD instrument, and the value for the integral Λ estimated from curves $T(\lambda)$, $Q_e(\lambda)$ and $f(\lambda)$ as described in the equipment data sheets, we calculated an average $dE_{rad}/dN_e = 0.23$ for the image sequence of the 64.4 pC beam, and $dE_{rad}/dN_e = 0.15$ for the lower charge data. Unable to give priority to any of the two data series due to any obvious technical reason, we took the average value $dE_{rad}/dN_e = 0.19$ to accordingly scale the GEANT4 curve for all the future estimations of charge (Figure 3.11).

3.3.2 Electron spectrometer

It is well known that a charged particle moving in a constant magnetic field \mathbf{B} will start changing its direction due to the Lorentz force:

$$\mathbf{F}_{\text{Lorentz}} = -e\mathbf{v} \times \mathbf{B}.$$

This force always acts perpendicular to the direction of motion, thus providing the centripetal force:

$$\mathbf{F}_{\text{centripetal}} = \frac{\gamma m_e v^2}{r_g},$$

where r_g is known as the radius of gyration. It can be obtained by equating the two expressions:

$$r_g = \frac{\gamma m_e v}{eB},$$

or in an alternative way for electrons of energy E given in MeV:

$$r_g = \frac{\sqrt{E(E+1)}}{0.3B}, \quad (3.6)$$

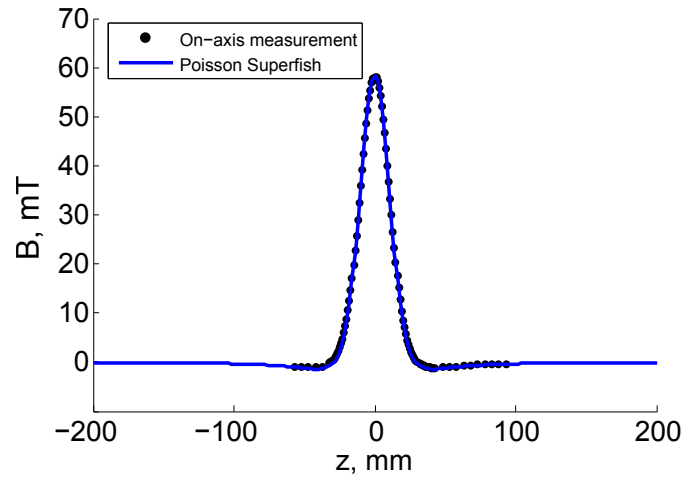


Figure 3.12 – On-axis magnetic field for a magnetic spectrometer. Black dots – experimental measurement with a magnetometer. Blue line – modelling with the code Poisson Superfish.

where B is in Tesla. If we place magnets with dimensions smaller than r_g , the particles leave the magnetic field and continue travelling in a straight line, but with a modified direction. This deviation can then be detected as a position displacement on the same scintillator screen as used for charge estimation. Knowing the complete geometry of the system allows extracting the particle energy. This is the principle of our electron spectrometer. Two motorized stages could insert a 1 cm-thick lead plate with a 500 μm -diameter pinhole (leading to a spectrometer acceptance angle of ≈ 4 mrad) and a stage with two holders for 2 cm-diameter circular magnets into the beam path (Figure 3.8). The size of the pinhole limits the spectrometer resolution (particles with an according energy difference passing through the top and through the bottom of the hole respectively could end up at the same point on the screen), and it was the smallest possible to machine with the tools available in our laboratory's workshop. Magnets of different thicknesses could be placed into the holders, yielding different peak magnetic field values. The thickness would be chosen in line with the expected electron energies for a given experiment. Naturally, the magnet surface planes are parallel, the line connecting their centers is perpendicular to these surfaces, and the point of maximum B -field as well as the center of the pinhole are carefully aligned to be on the optical axis.

Now, for the magnet size that we are using we could not simply apply equation 3.6 and draw conclusions from it, since the magnitude of the magnetic field B varies sharply with the particle position. To deal with this, we use the freely available Poisson Superfish code to model the exact field profiles. The blue curve in Figure 3.12 shows the numerically obtained on-axis magnetic field for 5-mm thickness magnets whose surfaces are separated by 34 mm. To confirm the obtained profile, we did an on-axis measurement with a magnetometer. The obtained data points (black dots in Figure 3.12) show an extremely good fit. Therefore, for magnets of different strength we would not repeat the measurement and completely rely on the Poisson Superfish simulations.

Due to symmetry of the configuration, the on-axis magnetic field profile is sufficient to obtain a map in the whole plane equidistant to the two magnet surfaces. As the electrons move in this plane only (as imposed by the pinhole), it remains to solve the equations of motion numerically to obtain their trajectories between the magnets and the displacement from the optical axis in the scintillator plane. Doing this for test particles with a range of different energies, we may pair up these displacements and energies, generating a datafile that is later used to deconvolve the measured electron spectra. Figure 3.13 shows how much electrons

of various velocities are dispersed, and what is the spectrometer resolution at corresponding energy ranges for 5-mm magnets and the 500 μm pinhole with the geometry as explained in the caption. We see that the particles below 2 MeV are well-resolved, however in the 6 – 8 MeV range the uncertainties become high due to the finite pinhole size. It may be improved by using stronger magnets for example, but this could lead to the weak electrons being directed beyond the edge of the detector. Last thing to be taken account for correct spectral calibration is the response curve (Figure 3.9) scaled using the linear accelerator data. If this was not considered, the low-energy part of the spectrum (corresponding to the peak of the response curve) would appear stronger than it should be.

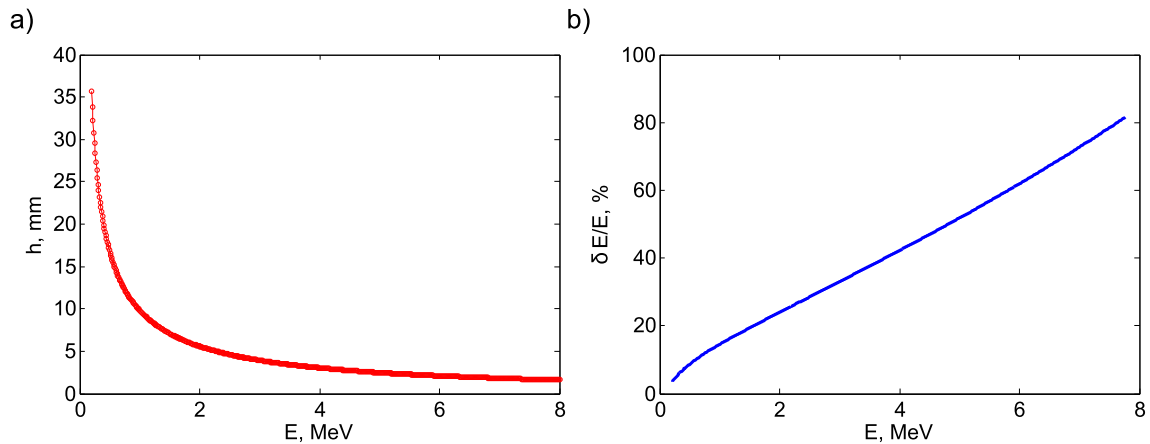


Figure 3.13 – Output of an electron trajectory simulation for 5-mm-thick magnets separated by 34 mm. a) Vertical displacement of electrons at various energies on a screen 33 mm away from the line connecting the magnet centers. b) Spectrometer resolution at different energies for the described configuration and with a 500 μm pinhole 92 mm away from the magnet center line and 128 mm from the electron source.

3.4 Target characterisation

3.4.1 Method

To be able to draw conclusions and make reliable predictions for laser-plasma experiments one wants to know the target properties as well as possible. Typical ways to characterise gas jets involve an interferometric measurement of a phase change for a collimated light beam passing through the gas (Semushin & Malka, 2001). As the refractive index depends on the density, this phase change is also scaled accordingly, and the density profile can be extracted using the Abel inversion. One important condition for the method to work is that the target needs to be cylindrically symmetric. Otherwise tomographic scans are required, complicating the setup and the algorithm (Landgraf, Schnell, Sävert, Kaluza, & Spielmann, 2011). Measurements may also be done with plasma directly, taking the optical axis as the axis of symmetry (and using the "probe pulse" in Figure 3.8). This way, gas targets with no cylindrical symmetry may also be characterised (Thaury et al., 2015). Working directly with plasmas might even be preferred in case of low-density experiments ($n < 10^{19} \text{ cm}^{-3}$ for target thickness of order $\approx 100 \mu\text{m}$), since the phase shift can be too weak to be detected with a good signal-to-noise ratio. However, at high densities ($n > 10^{20} \text{ cm}^{-3}$ for laser beam size $\lesssim 10 \mu\text{m}$) the phase shift due to a plasma might become more than 2π , so that the reconstruction becomes ambiguous and measuring the phase shift in a non-ionized gas becomes the only option.

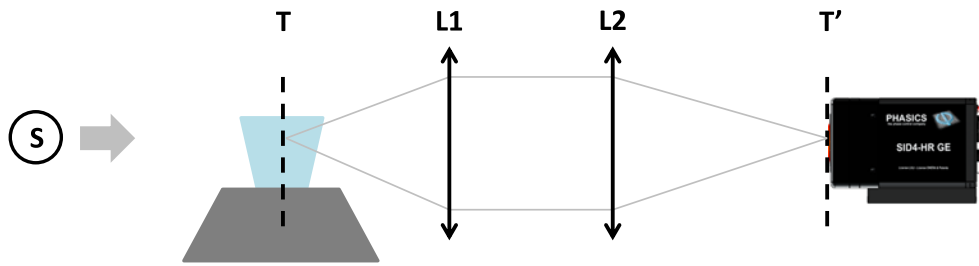


Figure 3.14 – Gas jet characterisation setup. S – a collimated light source. T – the target plane, imaged by two lenses $L1$ and $L2$ onto the detection plane T' . The signal is detected by a wavefront sensor based on quadriwave lateral shearing interferometry (SID4-HR by Phasics).

We have characterised all our targets with a light-emitting diode producing sufficiently collimated white light, and a quadriwave lateral shearing interferometry-based (Chanteloup, 2005) wavefront sensor (SID4-HR by Phasics) that directly measures the phase of an arriving beam (Figure 3.14). By comparing the detected phase when the gas source is switched off and when the flow is released, we obtain a map of phase shifts induced by the cylindrically symmetric target. The camera software has a built-in feature to do the Abel inversion and output the molecular density profile of the gas nearly live. The experimental plasma density shape may then be deduced via multiplying this curve by the expected amount of electrons contributed by one molecule. The latter can be obtained from knowing the achievable laser intensity and the intensities required to ionize electrons from different energy levels. For example, as we have already discussed, nitrogen requires only $\approx 10^{16}$ W/cm² to release the entire L-shell, however the first K-shell particles are obtained only at $\approx 10^{19}$ W/cm². Therefore, with our laser reaching $\approx 3 - 5 \times 10^{18}$ W/cm², for N₂ gas we may assume a multiplication factor of 10 (5 L-shell electrons from each of the two atoms in the molecule). Slight discrepancies in reality may however exist if the laser self-focuses and starts ionizing higher levels. However, as this should happen only close to the optical axis as well as at a different longitudinal position within the laser pulse, and thus is not expected to contribute to the wakefield formation, we will be ignoring these corrections.

Further important remark is that all the LWFA experiments would be run at continuous flow, since valves that could be opening at a kilohertz repetition rate for such high backing pressures (P_{back}) and with good synchronization are difficult to obtain and might nevertheless cause instabilities due to mechanical vibration. Continuous operation and high required densities due to bubble regime scaling yield a big load on the vacuum pumping system and immediately call for very narrow gas supply channels to be used in the setup. As we could experimentally determine the backing pressure at which our turbomolecular pumps break down for a particular gas type, and since the achievable peak densities scale linearly with P_{back} (Zucker & Biblarz, 2002), the interferometric measurements tell us the maximum obtainable peak densities for each gas nozzle.

3.4.2 Subsonic jet

The simplest way to produce a gas target for laser-matter interaction is a straight narrow channel connected via special mounts and wide pipes to a high-pressure supply. We have used both a metallic nozzle where the gas would travel a 350 μm long, 100 μm diameter hole before exiting into the vacuum chamber, or a fused silica capillary, where a 2-cm segment of same inner diameter would be cut off with a diamond blade from a commercially available roll and used for providing the gas. The first method permits more mechanical stability (the capillary

is fairly flexible), the second one allows easier replacement in case of laser damage. Despite the differences in the channel length, both geometries would yield similar density profiles for same backing pressures. Figure 3.15a shows a 2D density map measured for a metallic nozzle at $P_{back} = 22$ bar. The map features a quick drop as we move away from the exit. Figure 3.15b shows a cut of this map (black dots) perpendicularly to the target channel axis and $100 \mu\text{m}$ away from the exit, the closest "safe" distance observed with our laser system, when the high-intensity beam would still not damage the mechanical structures. This profile could be well-approximated by a Gaussian curve (blue line) with $1.6 \times 10^{20} \text{ cm}^{-3}$ peak plasma density and $\approx 85 \mu\text{m}$ $1/e$ waist. Figure 3.15c pictures how the density drops with the distance from the nozzle exit. The black dots represent the amplitudes of Gaussian fits for cuts at different heights (e. g. the point at $100 \mu\text{m}$ height corresponds to the peak value of the blue curve in Figure 3.15b). The blue curve here is a decreasing exponential function fit, estimating that the maximum density falls to $1/e$ of its value at the nozzle exit after shifting only 40 microns away. A backing pressure of 22 bar for this nozzle also represents the limit of what our vacuum system could cope with in continuous flow.

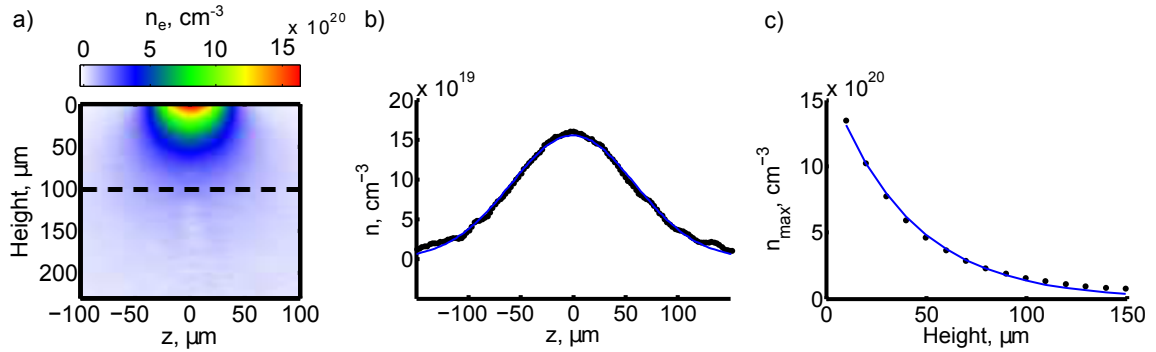


Figure 3.15 – Wavefront sensor-based density measurements of a $100 \mu\text{m}$ diameter subsonic nozzle at $P_{back} = 22$ bar. a) 2D density map obtained after applying the Abel inversion to the measured phase. A laser pulse propagating along the black dashed line would experience a plasma density profile showed in b) (black dots), approximated by a Gaussian curve (blue line) with $1.6 \times 10^{20} \text{ cm}^{-3}$ peak plasma density and $\approx 85 \mu\text{m}$ waist. c) Black dots – maximum density values at different heights above the nozzle. Blue curve – exponential fit with $40 \mu\text{m}$ distance of $1/e$ decrease.

3.4.3 Supersonic gas nozzle

As discussed in section 2.8, one way to prevent rapid widening of a gas jet while it expands into vacuum is to utilise converging-diverging nozzles, inside which the molecules are accelerated to supersonic velocities before they reach the exit. Such nozzles were designed for our experiments and manufactured by micro-spark erosion. Figure 3.16 shows the characterisation data for a de Laval nozzle with a circular throat of diameter $D_1 = 40 \mu\text{m}$ and exit diameter $D_2 = 120 \mu\text{m}$ (denoted as in Figure 2.15) for $P_{back} = 21$ bar. The throat and exit planes are separated by $350 \mu\text{m}$. We see in Figure 3.16a that the jet penetrates much further into vacuum compared to the subsonic case before it self-expands significantly. The cut along the dashed line at $100 \mu\text{m}$ height is depicted in Figure 3.16b (black dots). Even though it has a noisy pattern close to its peak that is attributable to numerical errors of the Abel inversion algorithm (as the radial distance approaches zero), the remaining points are enough to find a good Gaussian approximation giving $1.6 \times 10^{20} \text{ cm}^{-3}$ peak plasma density and $\approx 50 \mu\text{m}$ $1/e$ waist (blue line). Note that the peak density is the same as for the subsonic jet case before,

but the target width is ≈ 1.7 times thinner. Figure 3.16c shows the drop of the peak density with height above the nozzle exit. This time the exponential fit (blue line) gives a slightly worse approximation for the data (black dots), which comes together with the fact that the profile shape at different heights evolves from a top-hat function very close to the exit to a Gaussian at around $50 \mu\text{m}$ and above. The $1/e$ distance of the blue curve is nevertheless much longer than for the subsonic case and is equal to $105 \mu\text{m}$. Since this nozzle has a throat of $40 \mu\text{m}$ only, running it at 21 bar would still not exhaust all our vacuum pumping power. The limit would rather be reached for $P_{back} = 55 - 60$ bar, implying that significantly higher peak densities (by a factor of ≈ 3) could be obtained in continuous flow mode.

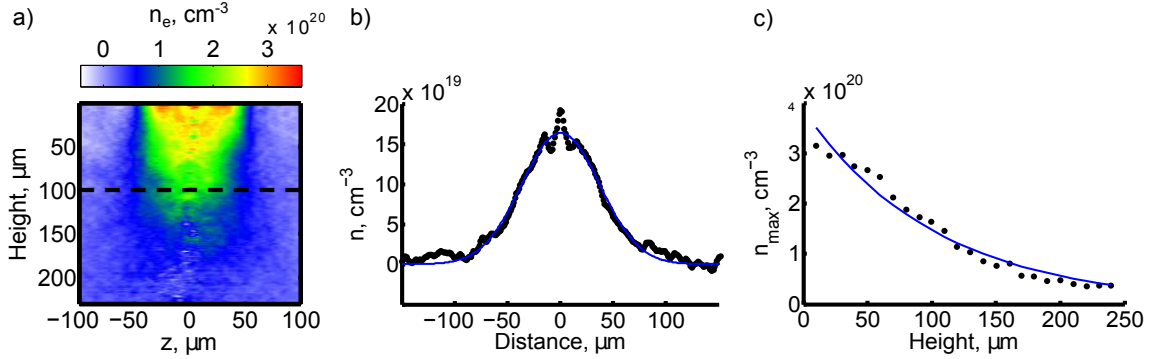


Figure 3.16 – Wavefront sensor-based density measurements of a supersonic nozzle with a $40 \mu\text{m}$ throat at $P_{back} = 21$ bar. As in Figure 3.15, part a) shows a 2D density map. Black dots in b) correspond to a transverse cut $100 \mu\text{m}$ away from the nozzle exit (dashed line in a), approximated by a Gaussian curve (blue line) with $1.6 \times 10^{20} \text{ cm}^{-3}$ peak plasma density and $\approx 50 \mu\text{m}$ waist. c) Black dots – maximum density values at different heights above the nozzle. Blue curve – exponential fit with $105 \mu\text{m}$ distance of $1/e$ decrease.

3.4.4 Supersonic gas nozzle with a shock

In both of the previously discussed cases the maximum densities and narrowest gas profiles exist right at the exit of the nozzle, where they cannot be utilised due to laser damage. In section 2.8.3 we introduced a concept of a supersonic nozzle with an additional structure to create shock fronts. We discussed that they may create very sudden density variations, and a cylindrically symmetric shock front could be produced, resulting in a small region containing high plasma density, potentially located far away from the nozzle exit. Figure 3.17 gives a technical drawing of a shocked nozzle we designed for use in electron acceleration. It starts with a de Laval configuration of $50 \mu\text{m}$ throat, $180 \mu\text{m}$ exit and $400 \mu\text{m}$ separation between the two end planes, but then it is extended by an extra $100 \mu\text{m}$ distance of vertically straight walls. To estimate where the tip of the conical shock front is expected to be located, we would want to use equation 2.67 (for angle definitions refer to section 2.8.3):

$$\tan \delta = 2(\cot \Theta) \frac{M_1^2 \sin^2 \Theta - 1}{M_1^2(k + \cos 2\Theta) + 2}. \quad (2.67)$$

From the nozzle geometry it is easy to obtain that $\delta = 9.4^\circ$, and one may find that for nitrogen at room temperature the heat capacity ratio is $k = 1.4$. However, we are still missing information on the value of Mach number that should be achieved right before the walls turn vertical. This may be obtained from the following formula from (Zucker & Biblarz, 2002),

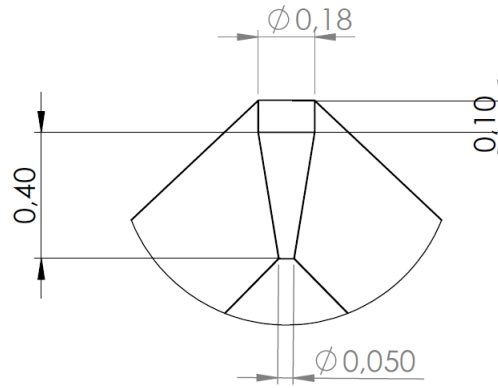


Figure 3.17 – Technical drawing of a shocked nozzle design.

which can be derived in a similar way as equation 2.66:

$$\frac{A}{A^*} = \frac{1}{M} \left(\frac{1 + \frac{k-1}{2} M^2}{1 + \frac{k-1}{2}} \right)^{\frac{k+1}{2(k-1)}},$$

where M is the Mach number at a plane where the channel area is equal to A , and A^* is the area of the nozzle throat. At the turning point it becomes

$$12.96 = \frac{1}{M} \left(\frac{1 + 0.2M^2}{1.2} \right)^3.$$

This may be solved numerically to give $M \approx 4.2$. Now the equation for the shock angle (2.67) turns into

$$\tan 9.4^\circ = 2 \cot(\theta + 9.4^\circ) \frac{4.2^2 \sin^2(\theta + 9.4^\circ) - 1}{4.2^2(1.4 + \cos 2(\theta + 9.4^\circ)) + 2}.$$

One may again numerically find a solution in the physically plausible range to be $\theta = 11.5^\circ$. This would yield a shock at $180 \mu\text{m}/2 \tan 11.5^\circ - 100 \mu\text{m} \approx 340 \mu\text{m}$ away from the nozzle tip, safely far to shoot the laser. However, this is a very approximate estimation, which assumes a conical shock front with perfectly straight surfaces. In reality, as one exits into the vacuum, the post-shock gas starts self-expanding, modifying its Mach number, and thus the shock front may start to bend and lose its sharpness. Numerical fluid simulations are required to justify the design, they were performed, and are to be presented with the experimental measurement.

Manufacturing such a carefully shaped nozzle turned out to be a big challenge. Out of 8 samples only 2 exhibited expected features, and shape imperfections could be spotted by examination with a simple optical microscope. More advanced methods than micro-spark erosion should probably be sought for fabrication. Figure 3.18 gives data of interferometric measurements with the most successful sample for $P_{back} = 53.5$ bar, and compares it with numerical simulations for $P_{back} = 50$ bar using commercial ANSYS Fluent software. Figure 3.18a gives the 2D density map obtained from the Abel inversion, showing that the maximum density is reached in a very narrow area at a height of $160 \mu\text{m}$ (corresponding to the dashed black line). Note the asymmetries close to the exit which are produced by the structure imperfections. Figure 3.18b shows the plasma density profile along the $160 \mu\text{m}$ cut. It is characterised by a very tall spike of 10^{21} cm^{-3} peak density and $27 \mu\text{m}$ FWHM. Lineout 3.18c gives the plasma density along the nozzle's vertical axis. Figures 3.18d, e and f show the corresponding profiles obtained from numerical simulations. We see that the cut at the shock

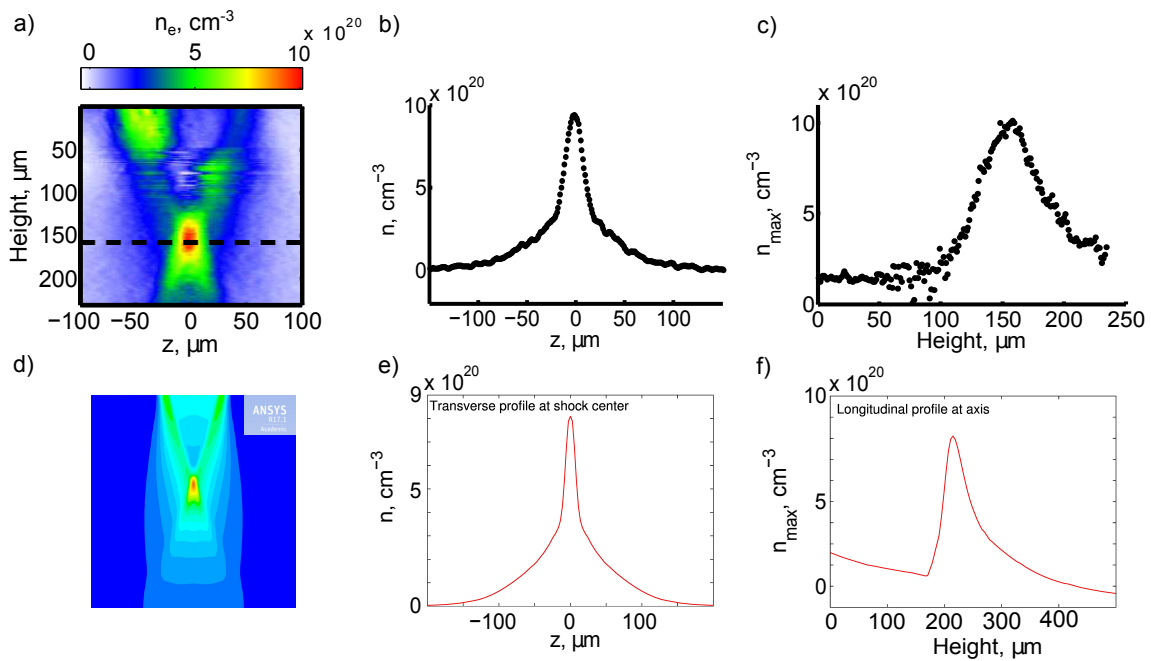


Figure 3.18 – Wavefront sensor-based density measurements of the specially designed shocked nozzle at $P_{back} = 53.5$ bar. As in Figure 3.15, part a) shows a 2D density map. Black dots in b) correspond to a transverse cut $160 \mu\text{m}$ away from the nozzle exit (dashed line in a), giving a spiked profile with 10^{21} cm^{-3} peak plasma density and a FWHM width of $27 \mu\text{m}$. c) Density values at different heights above the nozzle along the axis of cylindrical target symmetry. The maximum is reached at a height of $160 \mu\text{m}$. d), e) and f) – same as a), b) and c), except all data is from simulations with ANSYS Fluent software for $P_{back} = 50$ bar, and the cut for e) is taken at the height of maximum point in f), or around $220 \mu\text{m}$.

height is described by a very similar spike of $8 \times 10^{20} \text{ cm}^{-3}$ peak density and a FWHM of $30 \mu\text{m}$. The height of the shock, however, is $220 \mu\text{m}$, which is in between the naive theoretical prediction and the experimental measurement. The height of the shock was also observed in practice to vary slightly with the backing pressure (Figure 3.19). The best position is still not difficult to find in an acceleration experiment by observing the plasma length on the side-imaging camera and minimizing it. Running this target at $P_{back} = 50$ bar would bring our vacuum pumping system to its limit, however usually much less would be required due to really high peak density present at this pressure. We tried this gas jet both as a stand-alone target and as an injector for density-downramp injection (section 2.4) in a two-nozzle configuration.

3.5 Numerical modelling

To better understand laser-plasma experiments it is always helpful to perform numerical particle-in-cell (PIC) simulations (Dawson, 1983). PIC methods typically assign a discrete mesh to the continuous space, and calculate relevant macro-quantities, i. e. the electric and magnetic fields, as well as plasma and current densities, only on this defined grid. The particles themselves can meanwhile be situated anywhere on the continuous domain. Such a code consists of two main parts – the *field solver*, performing necessary interpolations and obtaining the macro-quantity values by solving Vlasov-Maxwell partial differential equations, and the *particle pusher*, which determines particle position changes from the Lorentz force equation. The two procedures are alternated for advancing in time at pre-defined discrete steps. If applied straightforwardly in 3-dimensional situation, however, this method still remains

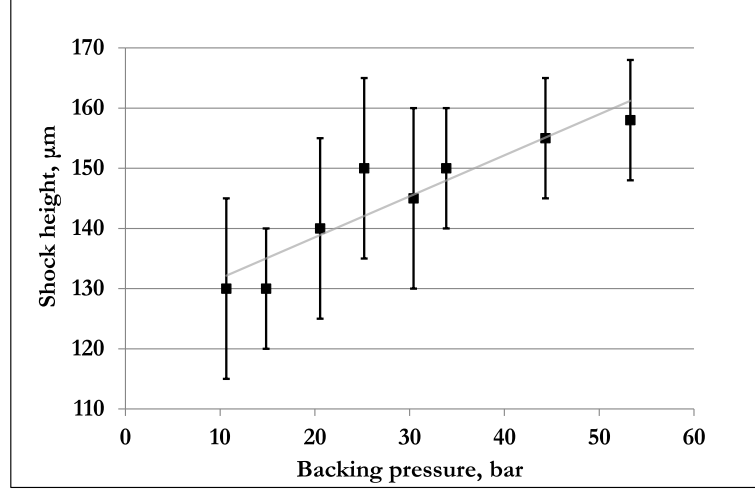


Figure 3.19 – Dependence on the backing pressure P_{back} of the height above the shocked nozzle exit of the spiked profile with the highest peak density.

very computationally expensive, as the space coordinates normally need to be resolved at sub-laser-wavelength level, and the number of particles to be traced, even if they are grouped, is large for realistic plasma experiments.

In our project we use the code CALDER-CIRC (Lifschitz et al., 2009). This code utilizes the fact that the wakefield accelerator geometry is cylindrically symmetric to perform 3-dimensional modelling at a quasi-2-dimensional computational cost. It is achieved by decomposing the total electric and magnetic fields as a Fourier series with respect to the azimuthal angle θ in cylindrical coordinate system where the z -axis coincides with the optical axis:

$$F(r, z, \theta) = \Re \left(\sum_{m=0}^{\infty} \tilde{\mathbf{F}}^m(r, z) \exp(-im\theta) \right) \quad (3.7)$$

$$= \mathbf{F}_{real}^0(r, z) + \mathbf{F}_{real}^1(r, z) \cos \theta + \mathbf{F}_{im}^1(r, z) \sin \theta \quad (3.8)$$

$$+ \mathbf{F}_{real}^2(r, z) \cos 2\theta + \mathbf{F}_{im}^2(r, z) \sin 2\theta + \dots$$

For a linear polarization of light, it is straightforward to see that the laser pulse is described by the two $m = 1$ terms, while the first term ($m = 0$) corresponds to the wakefield contribution. The remaining terms are required for an accurate description of arising coupling between the two strongest modes, and the physical parameters used in the simulation determine how many higher-order modes might need to be included. Simulations would be run with a mesh $\Delta z = 0.1k_0^{-1}$ and $\Delta r = 0.5k_0^{-1}$, where $k_0 = 2\pi\lambda_0^{-1}$, so that the high-frequency laser field is well-resolved. Ionization effects are also taken into account by implementing the ADK field ionization model (Nuter et al., 2011). There is a further option to input the exact laser field profile as measured with the d-scan technique rather than its approximation with a perfectly Gaussian spectrum, and this has been observed as an important feature to bring the computational results close to the experiment.

4

Acceleration experiments

Contents

4.1 MeV electrons at kHz repetition rate	66
4.1.1 Beam properties	66
4.1.2 Dispersion effects	69
4.1.3 PIC simulations	71
4.1.4 Experiments with argon	73
4.1.5 Sub-MeV beams due to down-ramp injection	75
4.2 Shocked nozzle experiments	77
4.2.1 Acceleration in the shocked nozzle	77
4.2.2 Acceleration with two-nozzle configuration	79
4.3 Stable MeV electrons due to tight focusing	83
4.3.1 Stable beams with high charge	83
4.3.2 Statistical reduction of fluctuations due to high repetition rate	85
4.3.3 Influence of the plasma density profile	86
4.3.4 PIC simulation and multiple injection regimes	87
4.3.5 Experiments with supersonic jets of argon	89
4.4 Laser pulse duration influence study	91
4.4.1 Relativistic particles from a high-density target driven by several-cycle pulses	91
4.4.2 Dispersion effects for the different regimes	94
4.4.3 Strongly focused relativistic electron beam	95
4.5 CEP effect measurements	98

Chapter overview

This chapter presents the main experimental results achieved during the thesis project. The beginning campaign demonstrates the proof-of-principle and studies the first MeV-scale beam as well as its sensitivity to the driver pulse chirp. Acceleration with the shocked nozzle is explored later, however, mostly yielding lower-energy particles. A more stable operation is achieved with the supersonic gas jet and tighter laser focusing. Effects of slight plasma profile variations on the output beam have been investigated in this campaign, showing striking sensitivity. Moreover, we make use of the fact that our laser system allows fairly easy tuning of the laser spectral width, and study the possibility to accelerate with longer than single-cycle transform-limited pulses (4 – 10 fs). Finally we explore what influence the carrier-envelope phase might have on LWFA with sub-4 fs laser driver.

4.1 MeV electrons at kHz repetition rate

4.1.1 Beam properties

The measurements presented in this thesis correspond to a continuation of the previous work on the project after a significant upgrade of the *Salle Noire* kilohertz laser system. Earlier experiments had been performed without the hollow-core fiber-based compressor, using 22 fs duration light pulses of similar energy to demonstrate electron acceleration to $\gtrsim 100$ keV only, with very irregular spatial distributions (Beaurepaire et al., 2015). After building the compressor, the laser could be routinely prepared for sub-4 fs pulses with > 2 mJ on-target energy. The shortest reliably measured pulses had $\tau_{\text{FWHM}} = 3.4$ fs, corresponding to < 1.3 optical cycles at $\lambda_0 = 800$ nm. The light beam was focused by an $f/3$ parabola into a subsonic continuous-flow gas jet produced by a fused silica capillary with $100 \mu\text{m}$ inner diameter. Depending on the measured focal spot profile, the vacuum peak intensities would be estimated to reach $2 - 3 \times 10^{18}$ W/cm². Relativistic MeV-scale beams were for the first time obtained when running the gas supply at the limit of our vacuum system capabilities and after bringing the capillary to $< 100 \mu\text{m}$ separation from the optical axis, or at the very edge of the damage zone. At $P_{\text{back}} = 22$ bar, this corresponds to a Gaussian plasma density profile with 1.8×10^{20} cm⁻³ peak and $100 \mu\text{m}$ waist, similar to the measurement illustrated in Figure 3.15. Judging from the sideview images of the laser-created plasma shape, in order to obtain relativistic electrons the target had to be placed in a way that the peak density plane would be located $20 - 60 \mu\text{m}$ after the focal plane of the focusing parabola, i. e. the laser beam would be focused into the *up-ramp* of the plasma target.

Figure 4.1 shows a profile of a typical obtained electron beam in the few-MeV range. Its rather small divergence of ≈ 45 mrad FWHM indicates the presence of strong focusing forces within the accelerating channel, suggesting we were operating not very far from the bubble regime conditions. The given image was integrated over 500 ms, equivalent to 500 shots, and the total estimated charge is 147 fC/shot. At this exposure time the beam shows good pointing stability, with fluctuations amounting to few mrad only, or a small fraction of the divergence. Figure 4.2 depicts the measured spectrum of the same electron beam. We observe a fairly flat energy distribution in the 4.5 – 6.5 MeV interval, with some particles reaching up to 8 MeV. As seen from the shaded grey area in Figure 4.2b, the curve remains quite remarkably stable over 1 s exposure time intervals chosen for recording data with a good signal-to-noise ratio.

Another interesting feature is seen in Figure 4.3, where main electron parameters were measured for different longitudinal positions of the target with respect to the laser focal point.

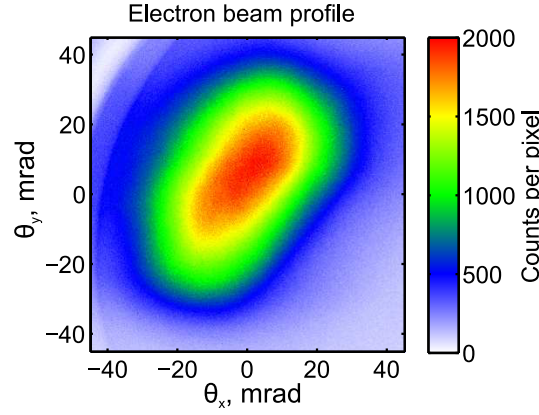


Figure 4.1 – Profile of an MeV-scale electron beam obtained using a Gaussian plasma target with $1.8 \times 10^{20} \text{ cm}^{-3}$ peak density and $100 \mu\text{m}$ waist. The image integrates over 500 shots and the estimated charge is 147 fC/shot.

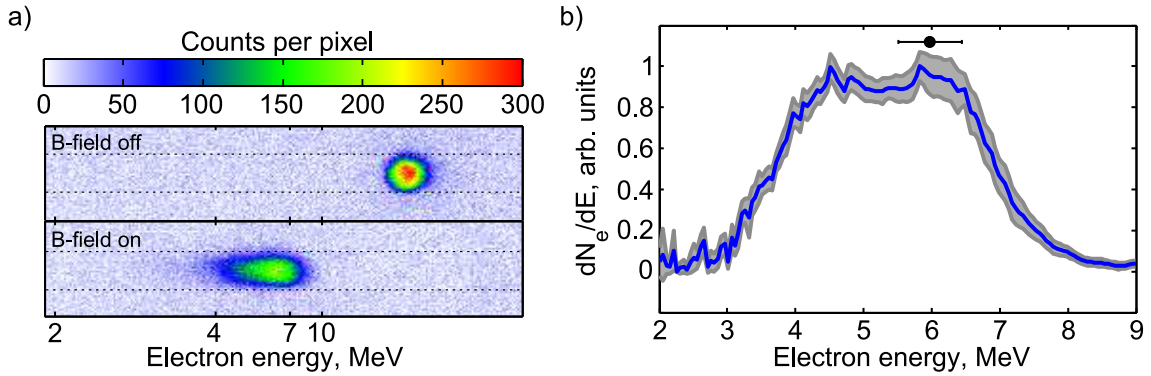


Figure 4.2 – Average electron spectrum for the beam depicted in Figure 4.1. a) raw data for only the pinhole inserted (top) and with a pair of magnets added after the pinhole (bottom). b) deconvolved spectrum. One measurement accumulated 1000 laser shots, and the blue curve gives an average of 20 such measurements. The shaded area corresponds to the standard deviation of one measurement from the average. The black dot with uncertainty bars yields the spectrometer resolution for 6 MeV particles.

We see that for mild displacements from the optimum the particle energy distribution remains very stable, even though the accelerated charge may vary by more than an order of magnitude. It suggests that the wakefield formation in this arrangement is a relatively stable process (perhaps unsurprisingly for displacements of order $10 \mu\text{m}$, when the estimated Rayleigh length $z_R \approx 50 \mu\text{m}$), but the injection mechanism is much more sensitive to minor changes.

The situation becomes a little different when we look into the effect of peak plasma density. Figure 4.4 visualises main output beam parameters as we adjust the peak particle density by moving the capillary exit closer to or further from the optical axis. In this case some variation in spectral distribution is observed, which can be attributed to the fact that the wakefield structure transforms due to changes in plasma wavelength λ_p , leading to different laser depletion and dephasing distances. There is also a significant increase in total accelerated charge at higher peak densities, which could be explained by stronger relativistic self-focusing, leading to heavier injection by self-wave breaking or ionization of the N^{5+} ion. At the maximum peak density that could be reached without damaging the gas capillary or overloading the vacuum pumps, the electron bunches contain $\approx 0.5 \text{ pC}$ per shot with 30 – 40% standard deviation for measurements at 500 ms exposure time. Occasional images containing 1 pC per shot have

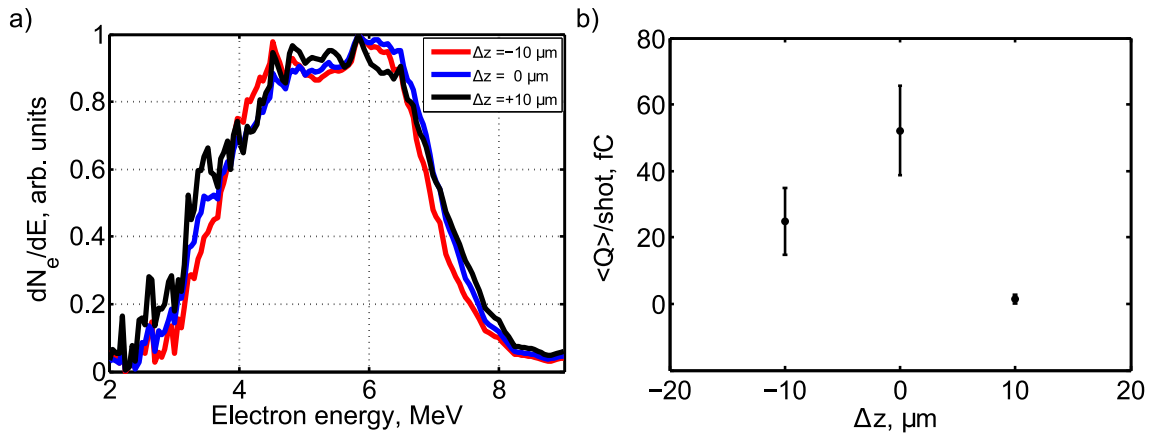


Figure 4.3 – Main beam parameter dependencies on the relative longitudinal position of the target with respect to the laser focus. a) average spectra for three different longitudinal positions. b) average charge (black dots) and its standard deviation (black error bars) for the same longitudinal positions. $\Delta z = 0$ corresponds to laser focal plane located $\approx 30 - 50 \mu\text{m}$ before the target density peak.

also been recorded.

It is necessary to point out that this is not a very "clean" scan in density, since varying the separation between the target tip and the laser axis changes not only the peak density, but also the width of the Gaussian plasma profile. As we shall see later, it might also have large effects on the beam, especially at relatively short Rayleigh lengths. A generally better way to do such measurement is to keep the geometry constant, while adjusting the backing pressure P_{back} . However, the former method had been chosen due to the fact that varying P_{back} would also mechanically move the capillary, changing the geometry in a less predictable way. This has been considered the main disadvantage of this target type against metallic nozzles that would be used later.

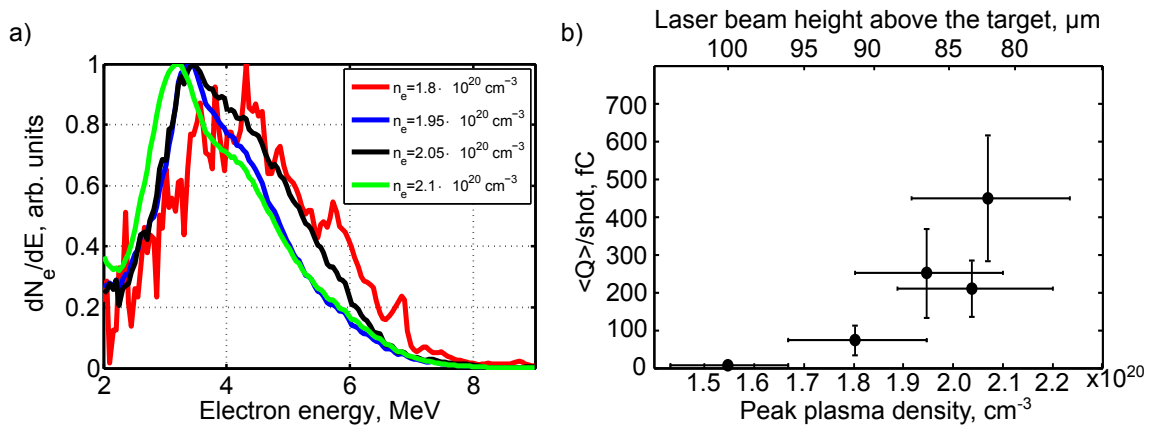


Figure 4.4 – Main beam parameter dependencies on the peak plasma density. a) average spectra for different peak plasma densities. b) average charge (black dots) for various plasma densities with estimated uncertainties (black error bars). Note that the peak plasma density here was varied by moving the target away or towards the optical axis, which neglects the variation of the Gaussian profile width.

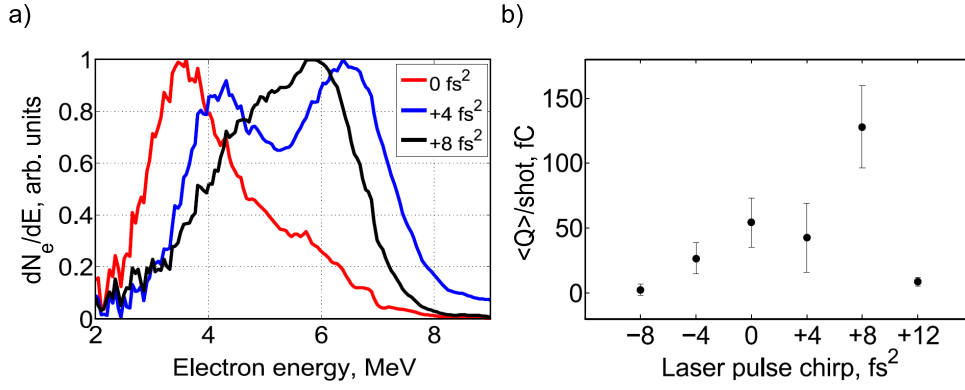


Figure 4.5 – Main beam parameter dependencies on the driver pulse chirp. a) average electron spectra for optimally compressed and slightly positively chirped laser pulses. b) average accelerated charge (black dots) with standard deviation (black error bars) for differently chirped drivers.

4.1.2 Dispersion effects

As described in section 2.6.2, broad bandwidth laser pulses such as used for this experiment may experience significant dispersion effects (Figure 2.11d). Tens of microns of propagation in densities of the order 10^{20} cm^{-3} may quickly lengthen a near-single-cycle pulse by a factor of two and more, rapidly dropping the peak intensity. Such magnitudes are very close to our actual target parameters in the discussed campaign. For this reason in order to optimize the particle beam we would extensively use the pair of motorized fused silica wedges, shown in Figure 3.1, to slightly detune our system from the maximum pulse compression, and send chirped pulses into the experiment. Using material data for this type of glass, it is easy to estimate that adding (subtracting) $100 \mu\text{m}$ of wedge thickness introduces approximately $+4$ (-4) fs^2 of group delay dispersion (GDD), defined as the product of GVD (recall section 2.6.2) and the distance of propagation. This creates a positive (negative) chirp, meaning that red (blue) wavelengths shift to the front of the light pulse. In this discussion, we will be ignoring higher-order dispersion terms.

Figure 4.5 compares main electron beam parameters for an optimally compressed (0 fs^2), and chirped laser drivers. One can see much more significant changes in the energy distribution than in any of the previous cases. In fact, the highest average energy particle source is achieved with a $+8 \text{ fs}^2$ pulse, which also gives the largest amount of charge per shot. Both peak energy and the total charge per bunch is higher by a rough factor of two in this chirped case than for the best-compressed laser pulse. On different running days, depending on the exact plasma conditions, the best acceleration conditions have been observed to vary between a chirp of $+4 \text{ fs}^2$ and $+8 \text{ fs}^2$, however it would not be optimal for a 0 fs^2 driver. As seen in Figure 4.5b, introducing a negative chirp also creates unfavorable conditions to trap many electrons. We explain this in a straightforward way – since plasma introduces negative dispersion, extra amount of glass compensates for the accumulated dispersion in the Gaussian up-ramp, and allows achieving best compression as well as the highest intensities deeper inside the target, where the plasma densities reach close-to-resonant magnitudes. To justify this argument, we make the following simplified calculation. Recalling equation 2.56, the GDD for a constant density plasma of thickness d may be expressed as:

$$GDD = \frac{d^2k}{d\omega^2}d = -\frac{1}{c} \frac{1}{\left(1 - \frac{\omega_p^2}{\omega^2}\right)^{3/2}} \frac{\omega_p^2}{\omega^3} d. \quad (4.1)$$

In our case, however, we have a varying density profile, thus $\omega_p = \omega_p(z)$, and to estimate the dispersion accumulated between two points with z -coordinates a and b we need to integrate:

$$GDD = \int_a^b \frac{d^2 k(z)}{d\omega^2} dz = -\frac{1}{c} \int_a^b \frac{1}{\left(1 - \frac{\omega_p^2(z)}{\omega^2}\right)^{3/2}} \frac{\omega_p^2(z)}{\omega^3} dz. \quad (4.2)$$

This integral can be easily obtained numerically. The center of the gas jet is imposed as $z = 0$. We want to explore the evolution of acquired GDD by the laser pulse arriving from far away ($a = -\infty$) to a certain point within the plasma target, neglecting any other effects. We limit ourselves to the first half of the target profile ($b \leq 0$), since experimentally the relativistic beam would only be observed when the driver is focused inside this up-ramp, thus the particle injection and strongest wakefield formation is expected to happen here. The function $\omega_p^2(z)$ is directly obtained from the density profile, and ω is evaluated for $\lambda_0 = 800$ nm. Numerically we take a to be a finite number with an absolute value enough larger than the target Gaussian waist; $a = -250 \mu\text{m}$ was chosen for the particular calculation. Figure 4.6 shows the results of such numerical integration for a target with $1.8 \times 10^{20} \text{ cm}^{-3}$ peak density and $100 \mu\text{m}$ waist (blue curve). The accumulation of GDD (green curve) speeds up as the pulse approaches higher-density regions, and reaches a value of -8 fs^2 around $40 \mu\text{m}$ before the jet center. This agrees really well with the approximate position of the experimental focal plane inside the target and the fact the particle beam parameters would in practice get optimized for a driver chirped by $+8 \text{ fs}^2$. By the time it arrives at the gas jet center, the pulse acquires a GDD of -14 fs^2 . These numbers may shift slightly if we take into account the real estimated central wavelength λ_0 after broadening in the hollow core fiber, which is varying day-to-day in the 750-800 nm range, and of course there is an adjustment for different density profiles. However, this calculation yields a very good agreement with observations of optimal acceleration conditions for a driver chirped by $+4$ - 8 fs^2 .

Interestingly, similar dispersion effect has also been observed for wakefield acceleration with 28 fs petawatt laser pulses in highly tenuous, but much longer, several-centimeter-scale plasma channel (Kim et al., 2017). In this experiment using chirped driver has allowed tuning a GeV-scale accelerator and shifting the energy peak to a value higher by $> 50\%$ compared to the optimally compressed case.

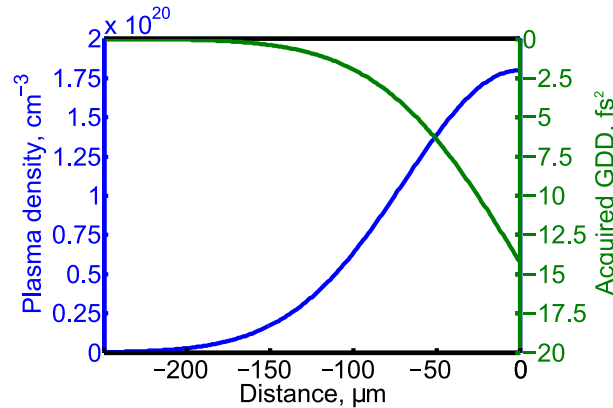


Figure 4.6 – Accumulation of negative group delay dispersion (green curve) by a laser pulse with $\lambda_0 = 800$ nm traversing half of a Gaussian plasma profile with $1.8 \times 10^{20} \text{ cm}^{-3}$ peak density and $100 \mu\text{m}$ waist (blue curve). Approaching from the left with 0 fs^2 initial GDD, the pulse experiences increasing negative dispersion and accumulates a chirp of -14 fs^2 at the middle of the jet.

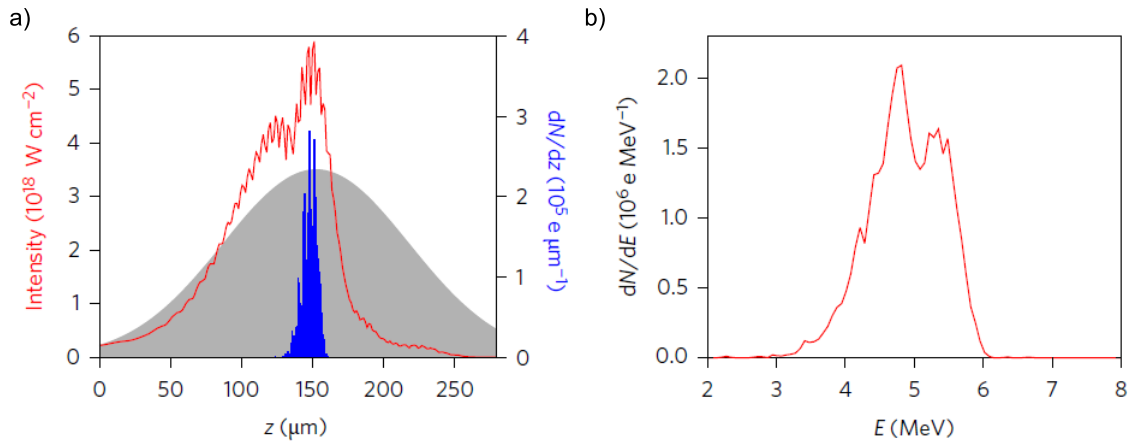


Figure 4.7 – Laser-plasma interaction dynamics and final electron properties given by PIC simulations. a) peak laser pulse intensity evolution (red curve) as it propagates through a Gaussian plasma profile with $1.6 \times 10^{20} \text{ cm}^{-3}$ peak density and $100 \mu\text{m}$ waist (grey area). Blue histogram represents the amount of electrons injected at particular positions within the plasma profile. b) electron energy distribution at the plasma exit.

4.1.3 PIC simulations

To gain a more sophisticated insight into the processes occurring within our experiment, we ran numerical PIC simulations with the code CALDER-CIRC. Simulations were performed using a mesh with $\Delta z = 0.1 k_0^{-1}$ and $\Delta r = 0.5 k_0^{-1}$, and the first two modes of the Fourier decomposition (see section 3.5). A neutral nitrogen gas Gaussian profile with $100 \mu\text{m}$ waist and a peak density $n_N = 3.2 \times 10^{19} \text{ cm}^{-3}$, yielding a peak electron density $n = 1.6 \times 10^{20} \text{ cm}^{-3}$, is initiated and gets ionized by the light pulse via tunnel ionization. There are 500 macroparticles of N per cell, corresponding to $500 \times 5 = 2500$ macro-electrons per cell after full L-shell ionization. The experimentally determined laser field, and its chirped modifications using numerically estimated spectral phases for a corresponding insertion thickness of wedge glass, were used as an input. To reduce the amount of free parameters, the focal plane of the laser beam was permanently set at $25 \mu\text{m}$ before the target center. Figure 4.7 presents the data for a driver chirped by $+4 \text{ fs}^2$, which turned out to be the optimum regime in the simulations. The red curve in Figure 4.7a represents the evolution of the peak laser intensity within the plasma. We see that close to the density peak (grey shaded area, centered at $z = 150 \mu\text{m}$ here) there is a large amount of self-focusing that increases the intensity almost to $6 \times 10^{18} \text{ W/cm}^2$, or double the peak value in vacuum. This is enough to obtain sufficient probability for ionizing a substantial amount of $N^{5+} \rightarrow N^{6+}$ electrons and inject them into the created wakefield. The blue histogram in the graph represents original positions of electrons that eventually get accelerated to relativistic velocities and reach the end of the plasma. All of them turn out to emerge from the K-shell of nitrogen atoms, hence we deduce that ionization injection mechanism is fully responsible for the obtained particle beam. Moreover, due to rapid dispersion and depletion close to the density peak, as well as strong diffraction due to tight focusing geometry, the driver intensity starts dropping very sharply, switching off the injection process. This leads to a beam of relatively narrow energy spread (Figure 4.7b). Note that this simulated final spectrum is fairly close to the ones measured in experiments.

Another consequence of such localized injection can be seen in Figure 4.8. Here the red-orange colour scale represents the laser pulse intensity right after it passes the target center. Clearly the pulse is already strongly modulated due to multiple light-matter interaction effects. The blue-white colour scale illustrates the plasma density, and a highly nonlinear wakefield is

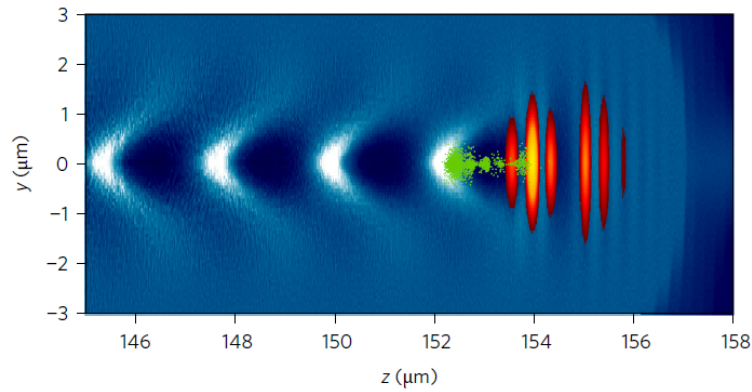


Figure 4.8 – Simulated wakefield structure (blue-white colour scale) and the injected electron bunch (green dots) right after the middle of the gas jet. Note the spatial extent of the bunch is less than $2 \mu\text{m}$, implying sub-fs duration at this point. The red-orange colour scale represents the cycle-resolved laser intensity.

visible. The green dots are the injected K-shell electrons. We see that all of them are contained within a $2 \mu\text{m}$ -long distance interval. At the plasma exit this electron bunch reaches 1 fs duration only, making it a great candidate for ultrafast probe in material science, provided it is appropriately transported. The bunch contains 400 fC of charge and has a divergence of $\approx 20 \text{ mrad}$, both parameters reproducing the experiment fairly well.

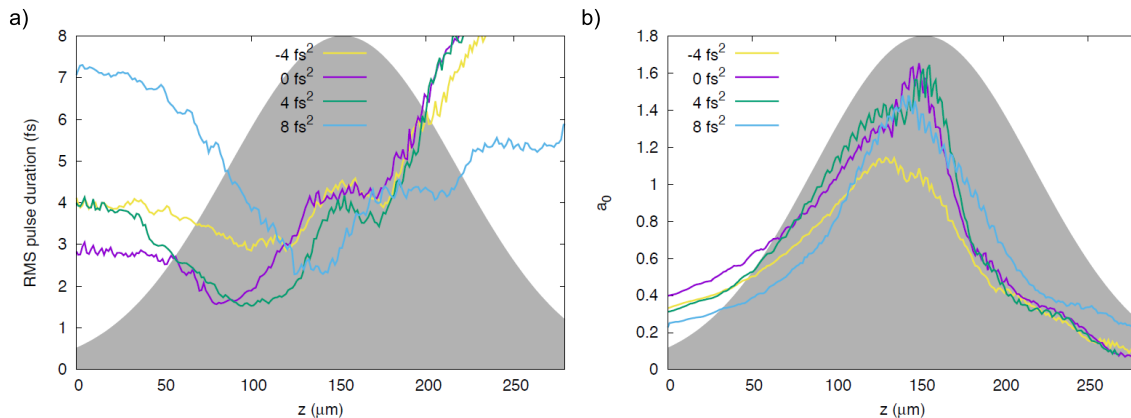


Figure 4.9 – Laser-plasma interaction dynamics obtained in PIC simulations. a) pulse duration evolution for differently chirped driver pulses as they propagate within the plasma. b) evolution of peak normalised vector potential for differently chirped pulses as they propagate within the plasma.

The subtleties of dealing with differently chirped pulses are partially summarized in Figure 4.9. Figure 4.9a gives the evolution of RMS pulse duration and Figure 4.9b – the peak normalized light field potential for pulses chirped by -4 , 0 , $+4$ and $+8 \text{ fs}^2$, as they propagate within the plasma (grey shaded area again). The negatively chirped pulse is initially slightly compressed, most likely via ionization-compression (section 2.6.4), however at higher densities it is only elongating and barely reaches $a_0 = 1$. No relativistic electrons are observed in this case. For the other pulses we can see in Figure 4.9a that the position of maximum temporal compression can be efficiently adjusted by varying chirp. The goal is to be both compressed and focused at the same time, thus, ignoring other effects such as ionization-induced shifting of the focal plane, one wants to have the minimum of the curve to be as close as possible to $z = 125 \mu\text{m}$.

We see that the +4 fs² pulse (green curve) satisfies this condition the best. This allows driving a strong wakefield and reaching the self-focusing threshold efficiently. It also gives the highest charge and highest energy electron bunches. The +8 fs² pulse in this case becomes the shortest already too deep into the target, after the focal plane. It therefore arrives at the density peak with lower power, and thus self-focusing is not as effective (Figure 4.9b, blue curve). These numerically observed trends further confirm our hypotheses about optimizing the particle beam using chirped laser pulses.

4.1.4 Experiments with argon

Relativistic electrons have been also successfully obtained using an argon jet instead of nitrogen. Let us first discuss the difference between these two gases, which also clarifies why nitrogen has initially been our preferred choice. We don't consider low-molecular weight gases, such as hydrogen or helium, as they are much more difficult to pump with turbomolecular pumps, and give only few plasma electrons per molecule, hence we were not able to reach densities relevant to the LWFA bubble regime scaled for our laser. Table 4.1 gives the ionization energies, expressed in eV, of multiple ion levels of nitrogen and argon. Using equation 2.36, one may estimate the corresponding light intensities needed to create a high probability of an ionization event, according to the barrier-suppression model (Delone & Krainov, 1998). The appealing thing about nitrogen is that the energies for N^{4+} and N^{5+} levels are well-separated, and require intensities of 1.5×10^{16} W/cm² and 10^{19} W/cm², respectively. This feature is unique among all the easily accessible gas types. For our laser parameters close to focus it creates two distinct populations of particles – the ones born at the leading edge of the pulse, forming the wakefield, and others born only where the intensity reaches maximum, which may get injected and accelerated. We saw this in the presented PIC simulations, where a pulse above 5×10^{18} W/cm² is already capable of ionizing substantial amounts of K-shell electrons, some of which in turn get successfully trapped. For argon (or other high-Z gases) the situation is quite different. Light intensities required to ionize Ar^{8+} and Ar^{9+} argon levels are 1.6×10^{18} and 2.1×10^{18} W/cm², which is an intermediate regime that could contribute both to the wakefield formation (since the transverse component for the ponderomotive force in the regions where these thresholds are reached may be non-negligible) as well as particle injection. In addition, these electrons could have significant impact on the driver evolution via ionization-related effects such as defocusing or compression. Despite such lack of separation of roles played by electrons originating from different orbitals, it might also turn out to be possible to obtain more particle trapping and therefore higher-charge bunches.

Figure 4.10 gives electron beam profiles obtained with a laser pulse chirped by +4 fs² using the two different gases in similar conditions. In the argon case, light was focused into a

	0	1+	2+	3+	4+	5+	6+	7+	8+	9+	10+	11+
N ₂	14.5	29.6	47.4	77.5	97.9	552	667					
Ar	15.8	27.6	40.7	59.8	75.0	91.0	124	143	422	479	539	618

Table 4.1 – Energies (in eV) required to ionize different ion levels of nitrogen and argon gases. Numbers in regular font correspond to levels that are easily ionized by the leading edge of the laser pulse using experimental parameters. Numbers in bold mark the levels that are difficult to ionize with the used light beam, and they could only be reached at the center of the driver pulse. Italic font marks the intermediate energy levels, so that a large region within the driver pulse might be able to induce ionization.

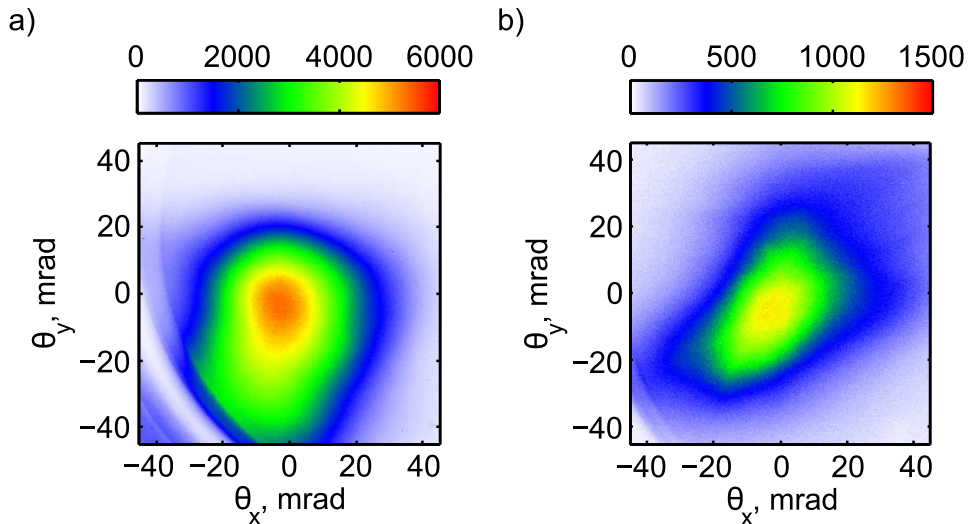


Figure 4.10 – Profile comparison for beams originating from argon and nitrogen targets with similar conditions. a) argon case. $Q = 281 \pm 130\%$ fC/shot, average divergence is 35×50 mrad (200 ms exposures). b) nitrogen case. $Q = 42.6 \pm 78\%$ fC/shot, average divergence of 35×35 mrad (500 ms exposures). Colour bars denote counts per pixel measured by the CCD camera. Beam pointing deviation is only few mrad in both of the cases.

Gaussian target profile with peak atomic density $n_{Ar} = 2.3 \times 10^{19} \text{ cm}^{-3}$ and $100 \mu\text{m}$ waist. Assuming the ionization of first 8 electron levels by the leading driver edge, this implies a peak plasma density of $1.8 \times 10^{20} \text{ cm}^{-3}$. For the N_2 target, as before, the peak plasma density is also $1.8 \times 10^{20} \text{ cm}^{-3}$ (assuming the first five levels are ionized), and the waist is again equal to $100 \mu\text{m}$. Hence, neglecting the two "intermediate" levels of argon, situations are equivalent. The beam measured with the argon target contains more charge – 281 fC/shot. However, it is also very unstable, with standard charge deviation exceeding 130% (200 ms exposures). The nitrogen electron source, fairly consistently with the previously presented data, is estimated to yield $42.6 \pm 78\%$ fC/shot (500 ms exposures). The FWHM divergence of the two cases is 35×50 mrad and 35×35 mrad, respectively.

In addition to larger instability, the particle beam from the argon target was significantly less energetic. Figure 4.11 compares spectra for the two cases. While 5 MeV is approximately the maximum energy obtained with argon, it stays below the mean when nitrogen is used instead. Few quick possible explanations for this arise. Firstly, the discussed ionization of Ar^{8+} and Ar^{9+} electrons may defocus important regions of the driver, reducing peak intensities and thus the strength of the wakefield. In addition, these intermediate electrons increase the local plasma density λ_p , and thus may shorten the dephasing length (equation 2.45). Finally, the larger injected charge could load and weaken the wakefield. However, since all the light-matter interaction processes are even more coupled here, a definitive answer would require a very extensive experimental and/or numerical study. We are only able to provide some evidence that defocusing indeed plays an important role in the process. Figure 4.12 gives sideview shadowgraphic images of the glass capillary (top) and the plasma created by a laser beam (propagating from right to left) for the two different gases, corresponding to the measurements presented above. We can notice that for the argon source the plasma shape gets transversely larger by $15 - 20 \mu\text{m}$ at the same marked longitudinal position within the jet. This allows to deduce that the light beam diverges at a larger angle, which would be a direct consequence of stronger defocusing. Similar shape differences, correlated with weaker electron spectra and present long low-energy tails, were observed in most of the later attempts to use argon targets.

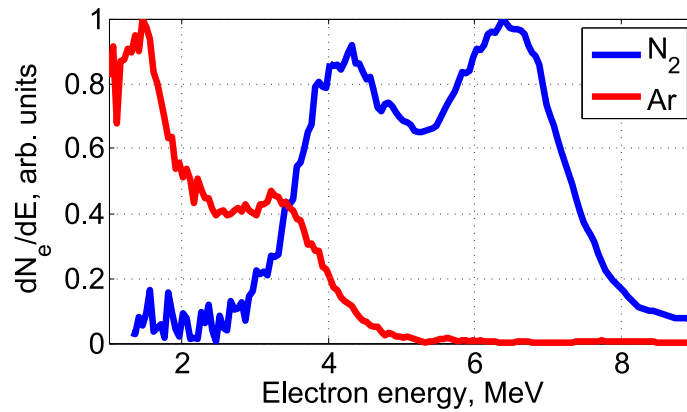


Figure 4.11 – Spectra comparison for beams originating from argon (red line) and nitrogen (blue line) targets with similar conditions.

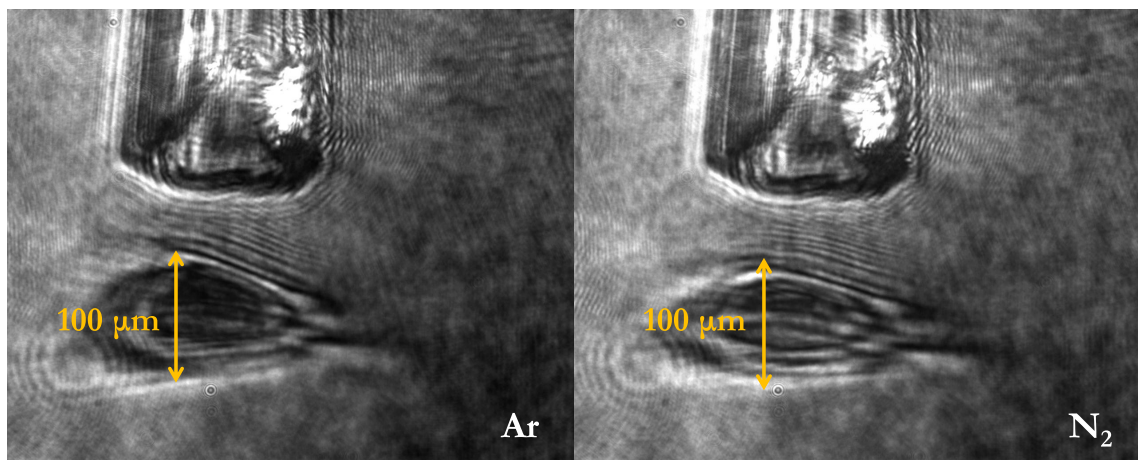


Figure 4.12 – Sideview shadowgraphic images of a glass capillary providing subsonic flow gas and resultant plasma ionized by a laser pulse propagating from right to left. The shape of the plasma allows to roughly visualize the shape of the laser beam. In the first image, the gas that flows into the experimental chamber is argon. At the marked position, the transverse size of the plasma is $100\ \mu\text{m}$. In the picture on the right, nitrogen is used. The same $100\ \mu\text{m}$ marker is placed at the same longitudinal position. However, the transverse size of the plasma appears $15 - 20\ \mu\text{m}$ smaller, suggesting the defocusing effect is stronger in argon.

4.1.5 Sub-MeV beams due to down-ramp injection

A different regime of laser-plasma acceleration was observed with much lower densities and with the target placed few tens of microns before the focal plane of the light beam, i. e. the laser focused in the *down-ramp* of the plasma profile, contrary to the previous situation. Figure 4.13a shows a profile of an electron source obtained with an argon plasma target described by a Gaussian function with peak electron density of $3.2 \times 10^{19}\ \text{cm}^{-3}$ and $120\ \mu\text{m}$ waist. The vertically elongated spot shape ($15 \times 47\ \text{mrad}$ FWHM) remained very stable and its point of maximum intensity would drift by less than $3\ \text{mrad}$. However, with the magnetic spectrometer inserted, the particles are completely deviated from the screen, meaning they are all below $1\ \text{MeV}$ (still above $100\ \text{keV}$, otherwise they would be stopped by the aluminium foil). Without knowing the energy distribution, we can not determine the exact accelerated charge value. Assuming all of them are at $495\ \text{keV}$ (peak of the curve 3.9), we may evaluate it to be $2.1 \pm 11\% \text{ fC/shot}$. This underestimates the actual value by at most a factor of 3, which still makes it orders of magnitude below the previously demonstrated cases.

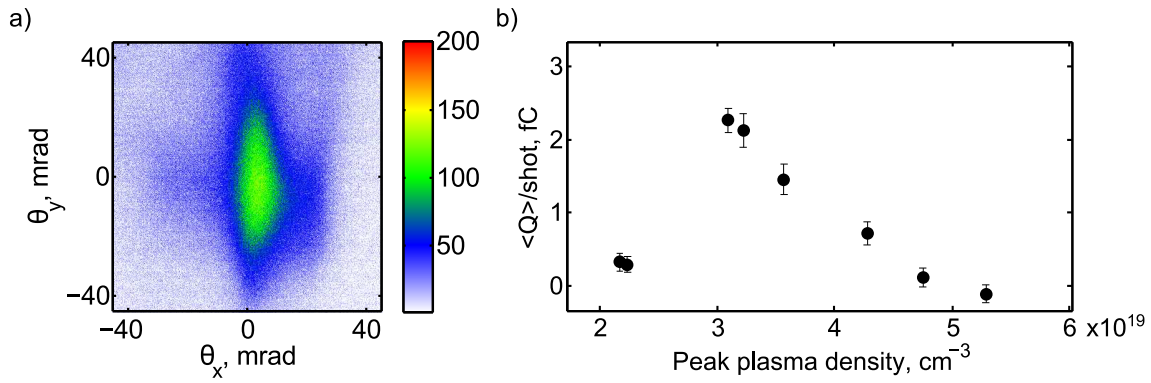


Figure 4.13 – a) a typical electron beam profile in the low-density, down-ramp focusing regime. The accelerated charge is between 2 and 6 fC/shot, with 11% standard deviation fluctuations. FWHM divergence amounts to 15×47 mrad. Integration time was 500 ms. b) accelerated charge dependence on the peak plasma density.

We also observed the beam evolution as the backing pressure is varied ($P_{back} = 3 - 7$ bar), changing the peak density and preserving the $120 \mu\text{m}$ Gaussian target waist. Since sufficiently low values of P_{back} were applied, the mechanical displacement of the glass capillary target was negligible. As seen from Figure 4.13b, the signal appears when the peak plasma density reaches $2 \times 10^{19} \text{ cm}^{-3}$, becomes the strongest at around $3 \times 10^{19} \text{ cm}^{-3}$, and disappears again when one exceeds $5.5 \times 10^{19} \text{ cm}^{-3}$. It seems the lower densities simply don't generate strong enough wakefields to trap any electrons, and at high pressures the laser pulse gets too strongly modulated and depleted as it crosses more than half of the plasma profile, so that the intensity at the focal plane is no longer sufficiently high. The particles would only be accelerated with the laser focused into the target down-ramp, thus it is reasonable to expect that density-transition injection is the responsible mechanism here. Overall this regime resembles the electron beams obtained with 22 – 30 fs driving pulses (Beaurepaire et al., 2015) (He et al., 2013), and we do not study them further.

Conclusions

In this section we have demonstrated the first MeV-scale wakefield electron accelerator operating continuously at a kilohertz repetition rate. We have shown that with the used single-cycle laser pulses dispersion effects have significant influence on the beam charge and spectral distribution. PIC simulations have fairly closely reproduced the experimental output and suggested a possible bunch duration of only 1 fs at the plasma exit. However, the beam stability so far remains very unsatisfactory and ways to deal with this issue need to be further investigated.

4.2 Shocked nozzle experiments

In the previous section the concept of relativistic electron acceleration with near-single-cycle pulses has been demonstrated. However, several important issues remain present. Firstly, the source has turned out to be very unstable regarding the injected amount of charge. Secondly, the charge seemed to be only increasing for higher peak plasma densities, but we could not push any further with the subsonic jet without damaging the target with the laser or overloading the vacuum pumps by increasing the flow. The shocked nozzle presented in section 3.4.4 appears to be an interesting candidate to tackle these problems. The stability might be addressed by accessing density-transition rather than ionization injection mode, which is a natural expectation for a target profile with such sharp density gradients. Moreover, shocked nozzle has been seen to provide the highest peak densities far away from the nozzle tip, where the laser beam could be placed without any problem. This section will explore wakefield acceleration using this rather exotic target.

4.2.1 Acceleration in the shocked nozzle

The shocked nozzle experiments have been performed on several different days, with the *Salle Noire* laser providing 2.4 – 2.5 mJ kilohertz pulses of duration measured in the 3.5 – 3.9 fs range. An $f/3$ parabola would focus them to a near-Gaussian spot with 3.3 – 4.0 μm FWHM, resulting in peak vacuum intensities of $1.8 - 2.4 \times 10^{18}$ W/cm². The continuous-flow nozzle connected to a nitrogen supply would be positioned so that the center of the high-density region (Figure 3.18) is at the laser focus. The sideview shadowgraph, and in particular minimizing the length of the plasma shadow, is used to optimize the coordinates with respect to all three axes. At $P_{back} = 15$ bar, the target would have a spike-like profile with a peak plasma density of 8×10^{19} cm⁻³ and 45 μm FWHM.

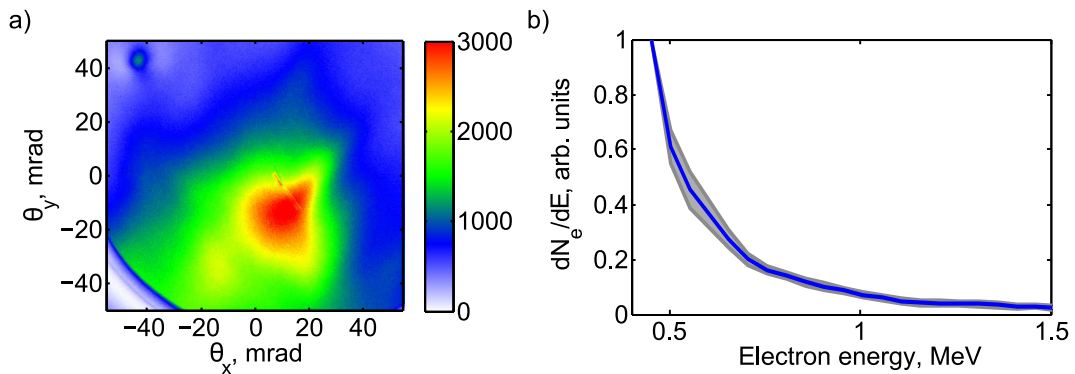


Figure 4.14 – Features of a typical electron beam accelerated in the shocked nozzle. a) profile of a beam containing between 0.5 and 1.5 pC/shot, fluctuations are only 4.6%. Average FWHM divergence is 55×60 mrad (100 ms exposures). b) average spectrum (blue line) with standard deviation (grey area). Most of the electron beams obtained in this configuration would have a long energy tail extending up to ≈ 1 MeV.

Obtaining an electron signal turned out to be much easier in this configuration, however the measured energies are significantly lower. Figure 4.14 shows the main parameters of a typical particle beam emerging from the shocked nozzle. It contains between 0.5 and 1.5 pC per shot (uncertain as the spectrum is not measured below 400 keV) and features a relatively low 4.6% standard deviation in absolute charge (integration time for one image – 100 ms). The beam divergence is a little larger than in the previous cases and averages only mildly elliptical

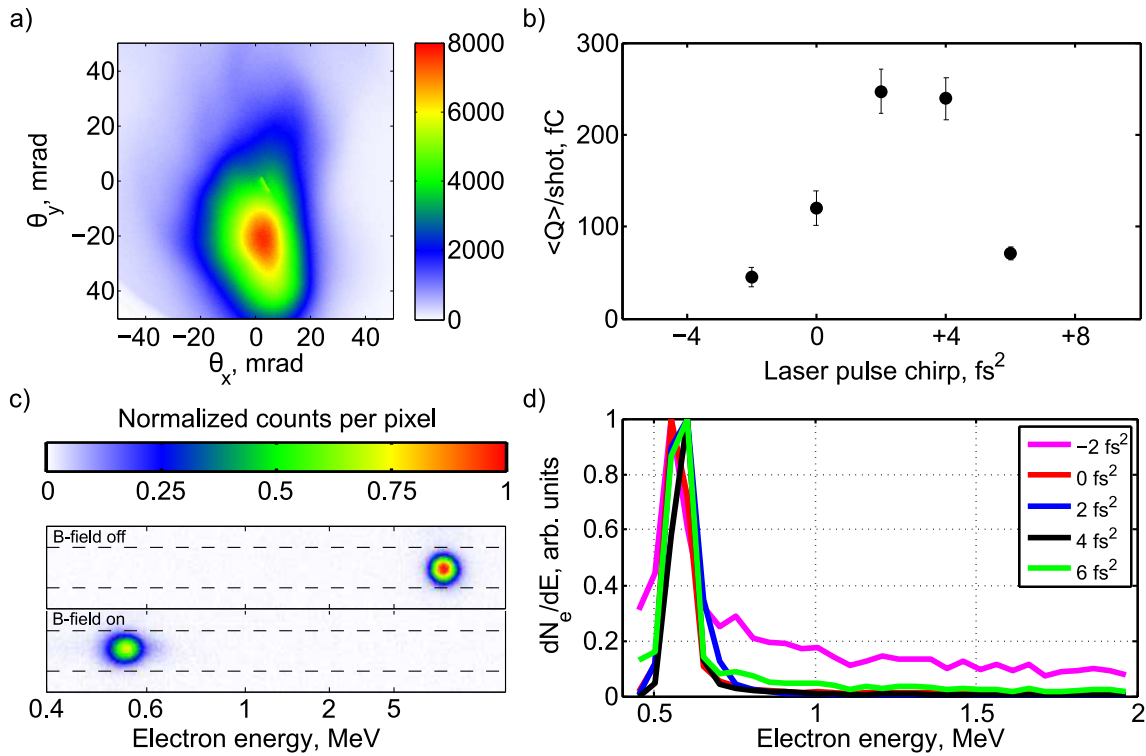


Figure 4.15 – Features of an electron beam accelerated in the shocked nozzle. a) profile of a beam containing $Q = 247 \pm 9.7\%$ fC/shot. Average FWHM divergence is 25×45 mrad (200 ms exposures). b) dependence of the total accelerated charge on the driver chirp. c) raw data from electron spectrum measurement when the laser pulse was chirped by $+4$ fs². Top line – image with the pinhole inserted only for spatial filtering. Bottom line – image when the magnets are inserted into the beam path to deviate the particles. d) reconstructed electron spectra for different driver chirps.

55×60 mrad FWHM. The profile is very stable, with pointing fluctuations not exceeding 2 mrad. The spectral distribution was measured with twice weaker magnets than before, and electrons down to 400 keV could be detected. A Boltzmann-like spread extending up to 1.2 MeV is obtained, and this would not alter dramatically neither for chirped pulses, nor for varied pressures (the interval $P_{back} = 10 - 40$ bar was explored). The maximum achievable energy is much more sensitive to the exact target positioning, especially in the horizontal direction, when centering transversely to the optical axis. This does not come as a big surprise, since the gas jet is cylindrically symmetric, therefore a sharp density drop in the mentioned direction is also present. Moving sideways by $2 - 3 \mu\text{m}$ only could often modify the beam so much that making meaningful comparisons between any two cases where there is a danger of slight jet geometry alteration while switching in between (e. g. adjusting peak density by changing the backing pressure, which also affects the tension in the elastic gas pipes connected to the target), or reproducing certain special results turns out to be hard.

One set of such "special results" is depicted in Figure 4.15. Plot a shows the spot of a beam obtained also in the above-described conditions at 200 ms integration time. This profile has a divergence of 25×45 mrad and contains $247 \pm 9.7\%$ fC/shot charge. Figure 4.15b gives the dependence of the number of accelerated electrons on the pulse chirp. It shows that, as before, mildly positively chirped pulses are favorable. Graph c demonstrates the raw energy measurement data, which shows that although the beam is sub-relativistic, it is also surprisingly monoenergetic, with the deviated spot (bottom line) similar in size to

the pinhole-filtered-only spot (top line). This means that the reconstructed energy spread $\Delta E/E_{peak} \approx 20\%$ is close to our spectrometer resolution. Finally, Figure 4.15d displays that the spectrum is insensitive to the pulse chirp in this case, supporting the fact that the injection process does not involve N^{5+} ionization. Density down-ramp injection, on the other hand, is much more dependent on the plasma profile encountered by the laser pulse, hence the final particle spectrum may also be expected to not vary with mild alterations of the driver. The reconstructed spectral curve peaks at 550 keV. Unfortunately, this kind of electron beam was recorded only once, and we were not successful at reproducing it later. This suggests precision on the micron scale, both in target engineering and its positioning, is required to have satisfying control over laser interaction with such target type.

4.2.2 Acceleration with two-nozzle configuration

There may be many reasons why the particles could not be accelerated to high energies in the shocked nozzle alone. Possibly after injection region the density drops down too rapidly so that strong wakefields are maintained only for a short distance. It is also probable that, as the bubble continues elongating, the trapped electrons reach dephasing very quickly. In order to boost the sub-relativistic electrons obtainable from the shocked nozzle, we thought of placing a second continuous-flow nozzle providing another jet of nitrogen right after the shock (Figure 4.16a). This gives an additional knob to control the sharpness of the density drop and provide high enough plasma density for a longer acceleration distance.

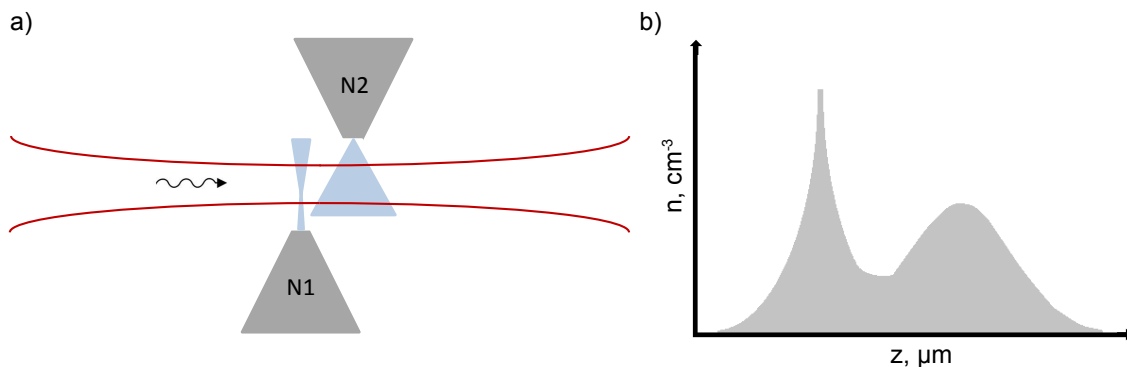


Figure 4.16 – a) scheme of acceleration using a two-nozzle combination. b) typical expected plasma profile experienced by the laser pulse in this configuration, assuming a simple addition of the two measured profiles for isolated jets. This assumption becomes less and less valid when the nozzles are brought closer to each other, so that the gas flows perturb each other.

The supersonic nozzle (Figure 3.16) was used as the electron energy booster. As before, the shocked nozzle was supplied with $P_{back,1} = 15$ bar of nitrogen, resulting in a spiked target profile with $8 \times 10^{19} \text{ cm}^{-3}$ peak density and $45 \mu\text{m}$ FWHM. Figure 4.17 shows a particle beam obtained with the supersonic nozzle placed $160 \mu\text{m}$ above the optical axis with $P_{back,2} = 10$ bar, so that the target profile provided by this nozzle alone would be a Gaussian with $4 \times 10^{19} \text{ cm}^{-3}$ peak density and $130 \mu\text{m}$ FWHM (we switch to FWHM units in this section even for the Gaussian targets in order to have a direct comparison with the dimensions of the shocked jets, for which a waist is not defined). The combined target profile when both of the flows are present has not been measured. As a rough approximation, we may take a simple addition of the two profiles, but naturally this treatment becomes less and less reliable as we bring the two jets closer together, so that the gas streams start interacting (Figure 4.16b). For the beam in Figure 4.17, the two nozzle cylindrical symmetry axes were separated

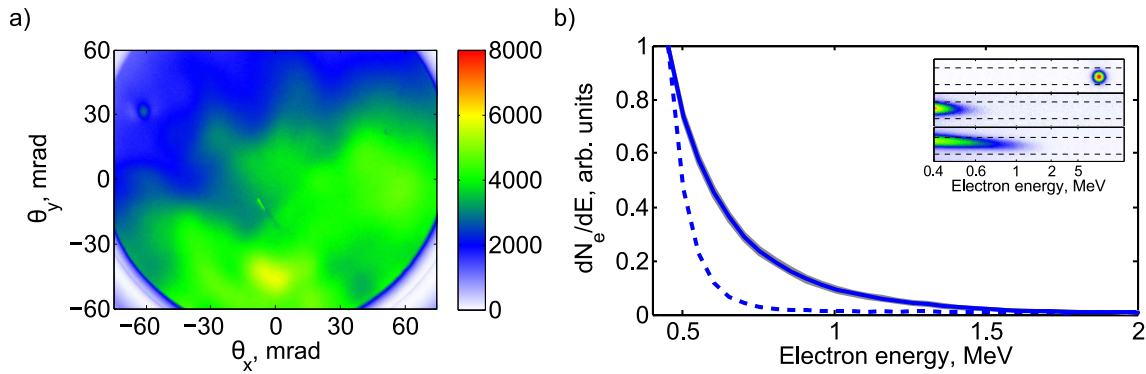


Figure 4.17 – Features of an electron beam accelerated in the two-nozzle configuration. a) profile of a beam containing between 1.8 and 5.4 pC/shot. The uncertainty in charge is 8.2% for 100 ms exposures. The divergence is not well-defined due to the irregular shape and limited size of the detector, but exceeds 100 mrad. b) solid line – electron spectrum in the two-nozzle configuration. Dashed line – particle spectrum once the post-accelerating nozzle is removed. Inset – raw spectral measurement data.

by $\approx 220 \mu\text{m}$. The spot profile seen in subplot a appears to be much more divergent than before, and contains between 1.8 and 5.4 pC/shot. Ignoring the spectral differences, that is roughly a factor of 3 more than when the second nozzle was removed far from the optical axis, which led to a beam with between 0.6 and 1.8 pC per shot (not shown). The beam stability is similar for the two cases, with standard deviations of 8.2% and 7.7%, respectively. The integration time for one image was 100 ms. The most interesting feature can be seen in Figure 4.17b, where the spectrum of this two-nozzle beam (solid line) is compared to the spectrum measured without the post-accelerator (dashed line). Even though the shape is again Boltzmann-like, a clear increase in maximum energy is observed – from roughly 800 keV to around 1.5 MeV. This demonstrates that, although the beam quality still raises concerns, using the shocked-nozzle as an electron injector together with a flatter and broader plasma profile appears to be a prospective technique.

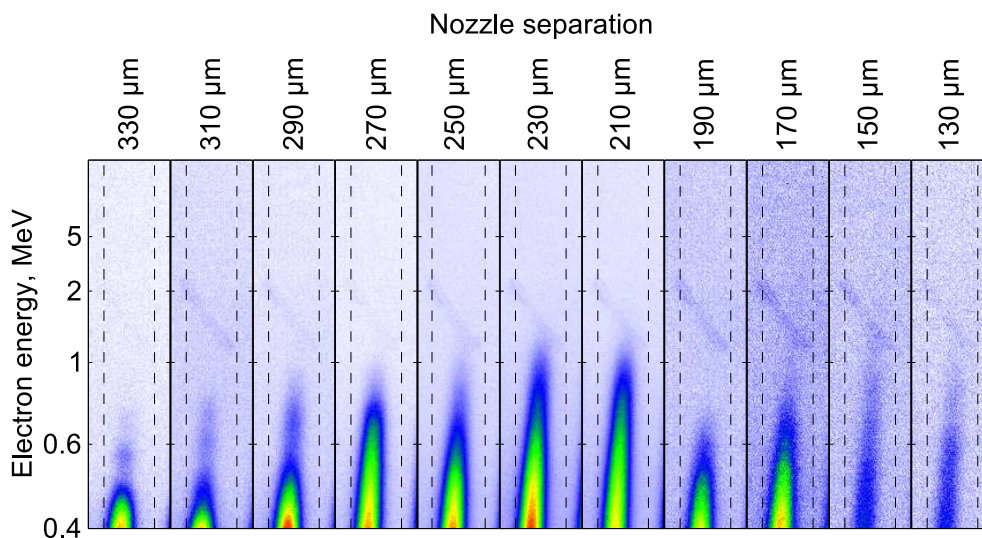


Figure 4.18 – Raw electron spectra for different distances between the nozzle symmetry axes. A continuous increase in peak energy is observed as the separation is reduced from $330 \mu\text{m}$ to $210 \mu\text{m}$, however the trend is lost when the targets are brought closer than $200 \mu\text{m}$. The visible diagonal feature corresponds to a screen damage.

To explore the potential of particle beam tunability using this method, we analyzed how the beam behaves when the longitudinal position of the second nozzle is varied. Keeping the backing pressures and the shocked target position constant, we moved the second jet along the optical axis and recorded the main beam parameters. Figure 4.18 shows the raw electron beam spectra for different separations between the nozzle symmetry axes. When the distance is kept at $330\ \mu\text{m}$, the supersonic nozzle has no influence on the electron beam, and the spectrum stays the same as from the shocked nozzle alone. As we approach closer, there is a clear increase in energy for the $300 - 200\ \mu\text{m}$ separation range, with some electrons eventually exceeding $1\ \text{MeV}$. Hence there is convincing evidence of post-acceleration and spectral tunability. However, at around $200\ \mu\text{m}$ the peak energy suddenly drops, and no trend can be seen for the further scan.

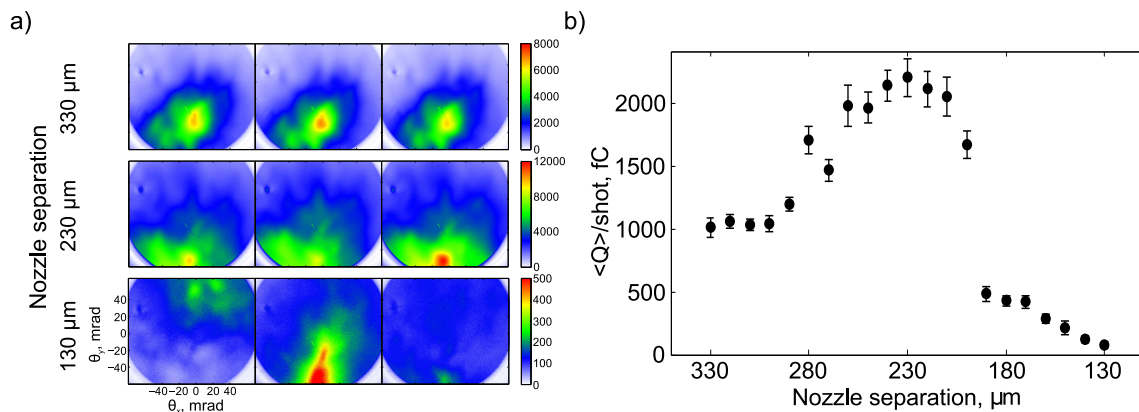


Figure 4.19 – Electron beam features for different distances between the nozzle symmetry axes. a) beam spot images for different separations. Three arbitrarily chosen images in the top line corresponding to $330\ \mu\text{m}$ distance show high reproducibility. Only slightly decreased stability is seen when comparing the three images in the middle line, associated with $230\ \mu\text{m}$ separation. At $130\ \mu\text{m}$ (bottom line), however, the particle beam becomes very unstable both in pointing and spot shape. b) accelerated charge comparison at different distances between nozzle symmetry axes. We see that the charge keeps increasing for the $330 - 230\ \mu\text{m}$ interval, briefly stabilizes, and then suddenly drops down at $200\ \mu\text{m}$. As electron spectra are not completely determined, the lower bound for estimated charge is given (higher bound $\approx \times 3$). Spectral differences are ignored in the comparison.

A similar $200\ \mu\text{m}$ -threshold has been observed while studying the total accelerated charge and beam stability dependencies. Figure 4.19a gives several 100-ms exposure images of the electron spot at three different separations. For a value of $330\ \mu\text{m}$ (top line), a very high degree of stability is observed. For a $230\ \mu\text{m}$ distance (middle line), the spot becomes larger and gets deviated slightly towards the bottom of the screen, however the pattern still remains fairly constant. However, at $130\ \mu\text{m}$ (bottom line), the beam appears of a random shape and with an unpredictable pointing direction for each 100-ms measurement. Figure 4.19b shows the measured charge values for the longitudinal distance scan. Again, the trend is familiar – starting with $1\ \text{pC}$ at large separation (lower bound for the uncertain charge measurement is used here, spectral differences ignored in the comparison), the amount of injected electrons keeps increasing until a plateau at $230\ \mu\text{m}$ is reached, and then a sudden drop follows after the $200\ \mu\text{m}$ mark. This behavior is consistent with the live sideview shadowgraphy observations of increased plasma shape fluctuations. We conclude that the main reason for such performance deterioration is the turbulent disturbances the two flows exert onto each other when brought closely, making the gas flow chaotic. We managed to slightly reduce this effect by turning

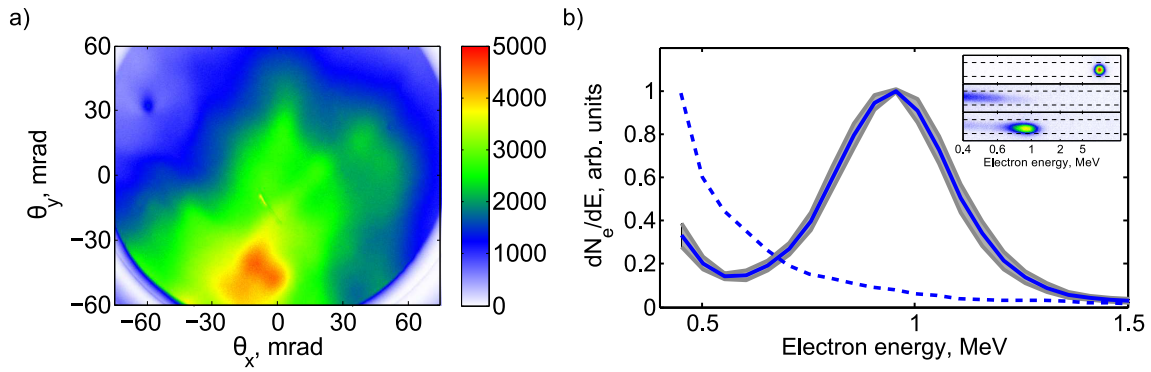


Figure 4.20 – Generation of a quasimonoenergetic particle beam in the two-nozzle configuration. a) beam profile, containing 1.7 pC/shot, with 9.7% uncertainty for 100 ms exposures. b) solid line – electron spectrum in the two-nozzle configuration. Dashed line – particle spectrum once the post-accelerating nozzle is removed. Inset – raw spectral measurement data.

the nozzles around the optical axis by 20° in the opposite directions, so that the flow axes would make a 40° angle. An ideal solution could be placing them perpendicularly to each other, as then the two jets would only interact at a point. However, that would have required more radical rearrangement of our setup and was therefore not attempted.

Just as in the previous subsection, a very interesting though not repeatable due to extreme geometric sensitivity result was obtained. Figure 4.20 gives the main features of one particular case for a post-acceleration attempt. Graph a shows an electron beam profile obtained in a two-nozzle configuration. While the shocked nozzle was kept at conditions as before, the supersonic one at $P_{back,2} = 10$ bar was placed $210 \mu\text{m}$ above the optical axis, so that its standalone plasma profile is described by a Gaussian with $2 \times 10^{19} \text{ cm}^{-3}$ peak density and $175 \mu\text{m}$ FWHM. The separation between the two jet axes was $240 \mu\text{m}$. The measured beam contains $1.7 \pm 9.7\%$ pC/shot. The solid line in plot b yields the electron spectrum, which now shows a clear quasimonoenergetic peak at around 1 MeV. This can be compared to the dashed line in the same graph, which shows the particle spectrum when the supersonic nozzle is moved far away from the optical axis. The monoenergetic electron beam remained stable up to the point one of the targets was mechanically moved, and it could never be recovered again. This data suggests again that the shocked nozzle might be suitable for monoenergetic source generation, however, finding the correct arrangement may be troublesome.

Conclusions

We have demonstrated the capabilities and limitations of shocked gas jet use in wakefield acceleration both as a stand-alone target and as a sharp density-transition injector in a two-nozzle configuration. The former method has only provided sub-MeV electron particles, while the latter has boosted the energy above 1 MeV and offered some tunability, however it appears to suffer from turbulence occurring due to the two gas flows perturbing each other. This could possibly be solved by setting up the gas jets perpendicularly with respect to each other, however it would have been hard to implement and verify in our experimental chamber. One clear benefit of this scheme is more stable beam profiles and estimated beam charge values, suggesting that utilizing this injection regime may indeed be the key to our stability problem.

4.3 Stable MeV electrons due to tight focusing

Acceleration with the shocked nozzle has been shown to yield more reproducible electron bunches. However, particle energies would mostly remain below 1 MeV, and the obtained spectra are usually very broad. Boosting the energy with a second gas jet appears to be limited by turbulence effects between the two fluid flows. In this section, we present data collected with a different approach of staying safely above the injection threshold – simply focusing the laser beam tighter to get more light intensity as compared to section 4.1. The drawback of this modification is shorter Rayleigh length, likely reducing the length of the acceleration channel and thus possibly the final particle energy.

4.3.1 Stable beams with high charge

For the series of experiments described in this section, a 12.5 cm focal length parabola was replaced by one with $f = 5$ cm. In addition, a laser beam expander that would increase the beam diameter from roughly 2.5 cm to 4 cm was removed from the path. Consequently, the focusing configuration becomes $f/2$, compared to $f/3$ previously, and some energy is gained due to reduction in the number of optics. 3.8 fs, 2.6 mJ *Salle Noire* kilohertz pulses have been focused into a $2.9 \times 2.5 \mu\text{m}$ (FWHM) focal spot to yield peak vacuum intensity $3.5 \times 10^{18} \text{ W/cm}^2$. In the first run a subsonic flow nozzle has been used to create the target. This way Gaussian profiles with minimum waist of $100 \mu\text{m}$ and a range of peak densities up to $2 \times 10^{20} \text{ cm}^{-3}$ could be explored. However, no relativistic particles have been obtained. Being confident about our measured intensity increase, this surprised us initially, since, as mentioned, shorter Rayleigh length had only led to expectations of beams with lower energy due to shorter acceleration channel, rather than an increased difficulty in obtaining any signal at all. But there is another slightly more subtle point related to ionization effects, and defocusing in particular (section 2.6.3). For a Gaussian jet with a fixed width that is comparable to or larger than the driver Rayleigh length, a more tightly focused beam may begin interacting with the gas before reaching high intensity (Figure 4.21a). This can possibly lead to significant defocusing in the plasma up-ramp not only for the very leading edge of the pulse, but also for its central part, preventing us from achieving the measured peak vacuum intensities deeper inside the target. A self-suggesting way to circumvent this problem is using thinner gas jets, where the density

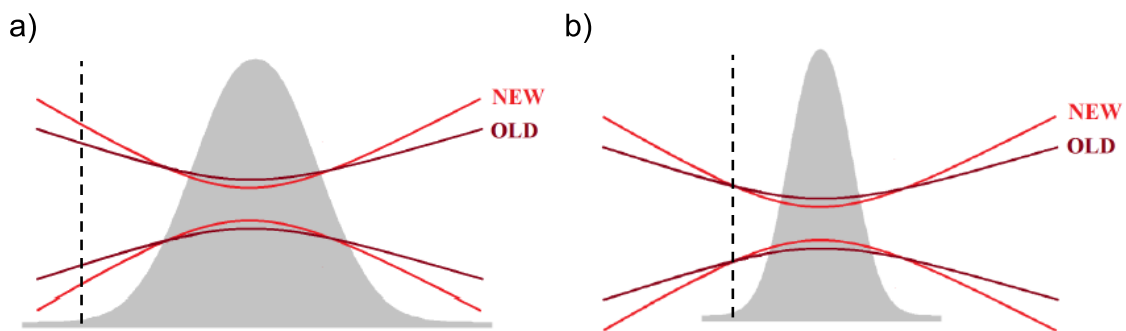


Figure 4.21 – Focusing of a laser beam into a Gaussian gas target. a) wide profile target. We see that a laser beam tightly focused into the jet center plane still has a larger diameter, and therefore lower intensity, at the plane where the gas density up-ramp begins (dashed line), as compared to a more loosely focused beam. b) narrow profile target. In this case, at the plane where the gas density starts growing (dashed line), both the loosely and the tightly focused beams have reached the same intensity.

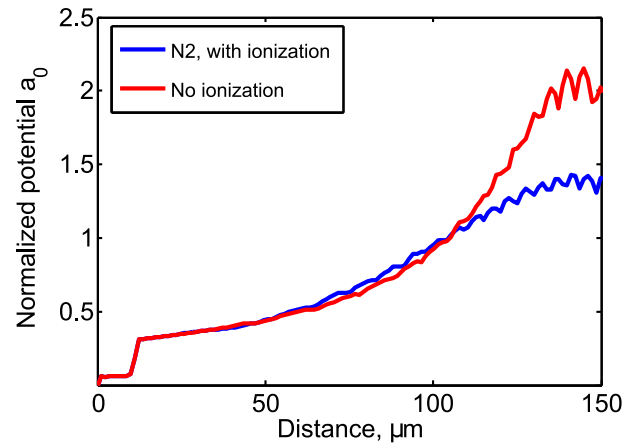


Figure 4.22 – PIC simulations of laser pulse peak normalized potential evolution in the first half of a subsonic jet. Blue curve – recalculated from the intensity curve in Figure 4.7a. Red curve – same simulation parameters, except the plasma is pre-ionized, so that any ionization-related effects on the laser pulse are excluded. We see that much higher intensities are reached at the jet center (distance $150 \mu\text{m}$) in the latter case.

up-ramp would begin where the tightly focused beam has already reached an intensity equal to or higher than a corresponding value in the looser-focusing configuration (Figure 4.21b). Then the effect of divergent plasma lens can be only as strong as in the older case, and one may expect to recover the electron beam.

The importance of ionization-induced defocusing for the relevant experimental parameters has also been confirmed by PIC simulations. Figure 4.22 compares the laser pulse evolution for the case already considered in section 4.1 with the situation when the gas target is considered to be pre-ionized. We see that the normalized vector potential reaches values higher by $> 40\%$ in the second case, implying peak intensities larger by a factor of 2 or more. This is a large difference, and thus even more significant ionization-induced defocusing effects are to be expected with the $f/2$ parabola. Hence we switched to using supersonic nitrogen nozzles, which have been seen to provide jets narrower by a factor of 2.

After replacing the target, recovering a relativistic electron beam turned out fairly straightfor-

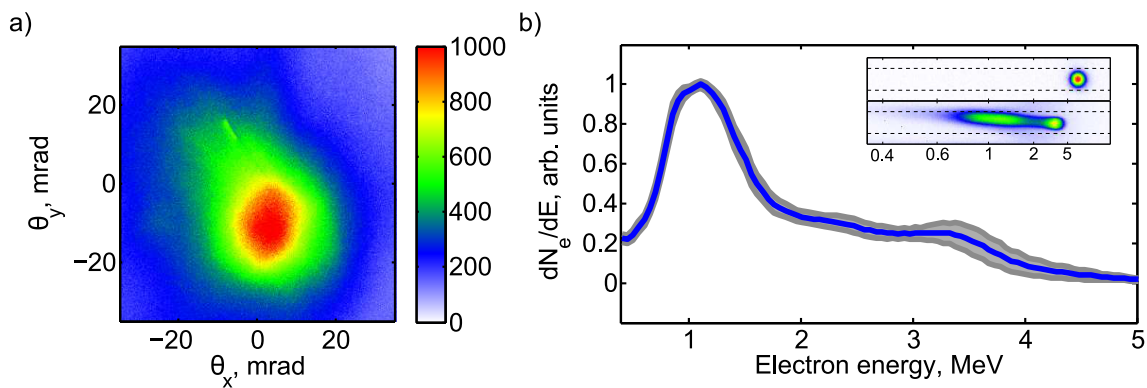


Figure 4.23 – Features of an electron beam obtained with $f/2$ focusing into supersonic microjet. a) single-shot electron spot profile. A series of 40 shots had an average charge of $23.3 \pm 15.3\%$ pC and an average divergence of 32×34 mrad with 4.5 mrad pointing deviations. b) energy spectrum (blue line) with standard deviation (grey area). Inset – raw spectral measurement data.

ward. Figure 4.23 shows typical main electron source features obtained with $1.7 \times 10^{20} \text{ cm}^{-3}$ peak plasma density and $55 \mu\text{m}$ Gaussian waist. This time the bunches contained enough charge to take single-shot exposure images with a good signal-to-noise ratio. The presented spot image belongs to a sequence of 40 recorded shots with an average charge of 23.3 pC and a standard deviation of 15.3%. In addition, the measured average FWHM divergence is $32 \times 34 \text{ mrad}$, and the pointing stability is $\approx 4.5 \text{ mrad}$. Figure 4.23b shows a corresponding electron spectrum having a peak at 1.2 MeV, a lower plateau between 2 – 3.5 MeV, and some more particles up to 5 MeV. The detected amount of relativistic charge is more than an order of magnitude higher than in any of the previous cases. However, energies in the 5 – 9 MeV range could no longer be accessed, possibly as expected due to shorter acceleration channel. In addition, we examined the behaviour of these main parameters as the driver chirp is varied. Figure 4.24a shows different spectra obtained with chirped pulses. One can see that there is fairly little effect for the 1.2 MeV peak, however, the plateau region gets modified noticeably. This brings suspicion that more than one injection regime might be present in the process. Overall the chirp effect on the spectrum is less dramatic than in the previous case of $f/3$ focusing, suggesting we have lifted off the injection threshold. Further and even more convincing evidence for this can be observed in Figure 4.24b, where total accelerated charge is given at different laser chirp values. Rather than having one optimal point as in Figure 4.5b, now there is a wide plateau extending from -6 to 16 fs^2 , where the charge variation is fairly small. Hence using tight laser focusing with narrow supersonic microjets permitted us to stay safely above the injection threshold and increasing the bunch charge by more than an order of magnitude together with significantly improved stability.

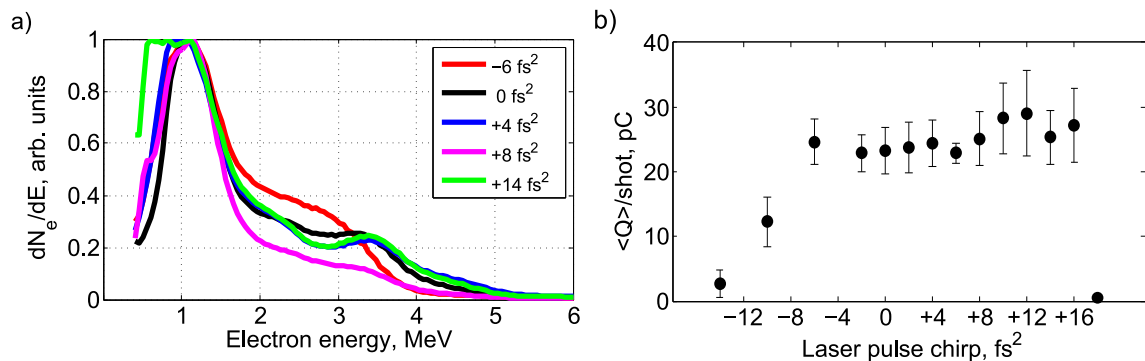


Figure 4.24 – Main beam parameter dependencies on the driver pulse chirp. a) average electron spectra for differently chirped laser pulses. b) average accelerated charge (black dots) with standard deviation (black error bars) for differently chirped drivers.

4.3.2 Statistical reduction of fluctuations due to high repetition rate

As mentioned earlier in the general overview of the project, one of the main motivations for running at high repetition rate is to be able to do statistical averaging. LWFA acceleration is a highly nonlinear process, therefore any small random variation of the interaction conditions may lead to significantly differing beam output parameters. Typical shot-to-shot charge stability in LWFA experiments exceeds 10%, and this has also been the case for the high-charge bunches presented in the previous section. On the other hand, some intended applications, such as time-resolved electron diffraction, require detection of sub-percent-level alterations in diffraction peak intensities. It is known from the central limit theorem in statistics (Rouaud, 2013) that comparing multiple images averaged over n shots could wash out these random fluctuations and, assuming there are no systematic variations, reduce the standard deviation

spread by a factor of $1/\sqrt{n}$. Here we study whether or not this type of statistical improvement actually works in our case.

The $f/2$ *Salle Noire* laser beam was focused into the up-ramp of a Gaussian target with $1.0 \times 10^{20} \text{ cm}^{-3}$ peak plasma density and $70 \mu\text{m}$ waist, provided by a supersonic nitrogen jet. This led to a fairly strong particle beam with a charge in the 12 – 35 pC range and energies up to 750 keV. We compare the statistics of a series of single-shot images to frames averaged over 100 shots. As directly exposing the CCD camera for 100 ms would lead to saturation, a hundred 10 ms files were acquired and later stacked to produce 10×100 -shot beam profiles. Figure 4.25 shows five randomly selected images from each of the two series. For the single-shot case (a, top line), charge standard deviation is 22%. For 100-shot images (b, bottom line) it was estimated to be 11%, or better by a factor of two. It is an important difference, even though the theoretical expectation is an order-of-magnitude improvement. It implies some non-random effects, as slow drifts in the system, must have been present. This is supported by a reduction in measured charge per shot, which has been lower by 14% for taking the second data series. In addition, averaging tends to improve the beam pointing stability at the expense of larger divergence. In the single-shot case the beam pointing standard deviation is estimated to be 3.5 mrad, and the average FWHM divergence is 52×39 mrad. For the 100-shot images the corresponding values are 2.1 mrad and 81×61 mrad. We conclude that running at kilohertz repetition rate yields an important improvement, however, sources of non-random slow drifts in the system are still to be sought for and hopefully removed.

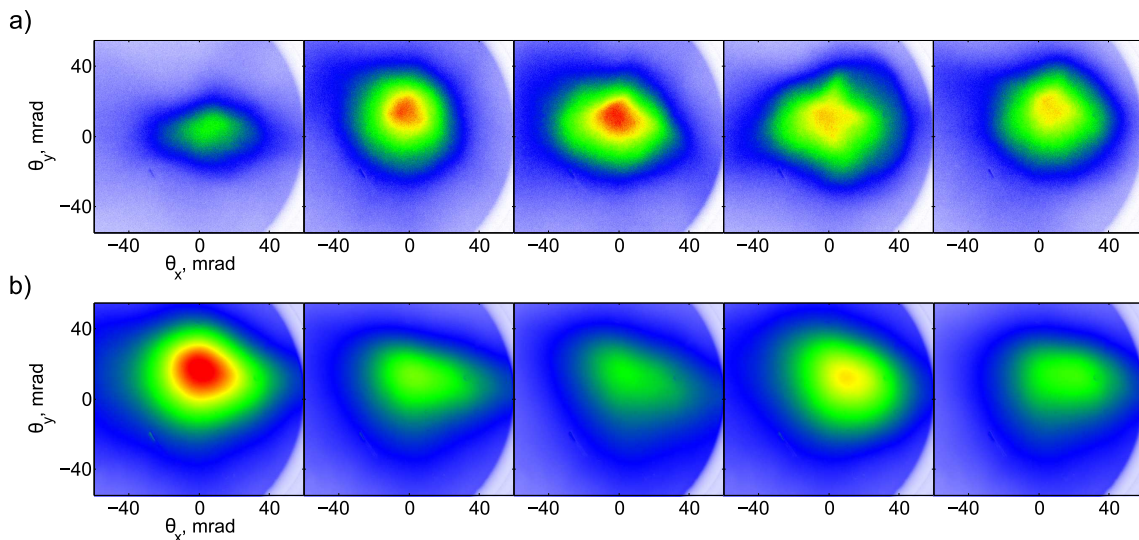


Figure 4.25 – Sequences of images of a typical electron beam for a) single-shot exposures and b) integration over a hundred shots. For the single shot case, charge standard deviation is 22%, average beam divergence is 52×39 mrad and pointing fluctuations are 3.5 mrad. When integrated over 100 ms, charge standard deviation reduces to 11%, average beam grows to 81×61 mrad and pointing fluctuations are 2.1 mrad.

4.3.3 Influence of the plasma density profile

Already in the first experiments it was observed that using such high-density targets with relatively sharp gradients makes the electron beam very sensitive to exact nozzle positioning with respect to the optical axis. After introducing the supersonic microjets this became even more pronounced. Displacing the nozzle by only $3 - 5 \mu\text{m}$ in any dimension could change the main features radically. In addition, we have struggled to recover the signal for the tight

focusing case until thinner nitrogen gas targets were placed in the setup. This motivates exploring fine detail effects of the Gaussian plasma profile, namely alterations in both the $1/e$ waist and peak density. The former can be controlled independently by changing the distance between the nozzle exit and the optical axis, whereas the second parameter may then be adapted by adjusting the gas backing pressure. An optimally compressed laser beam with specifications as described in section 4.3.1 was initially focused into a target with $1.45 \times 10^{20} \text{ cm}^{-3}$ peak plasma density and $65 \mu\text{m}$ waist, resulting in electron bunches of 2.5 pC, 14% single-shot standard deviation and most particles distributed in the 2 – 5 MeV range (Figure 4.26a, case 1 and Figure 4.26b, solid line). In this regime, the particle beam could be altered by chirping the driver pulse. For example, introducing a small negative chirp (-4 fs^2) approximately preserves the total charge, but produces a quasimonoenergetic peak, centered around 3.5 MeV (Figure 4.26b, dashed line). Then a higher peak density ($1.7 \times 10^{20} \text{ cm}^{-3}$) and thinner profile ($55 \mu\text{m}$ waist) was obtained by moving the nozzle closer to the optical axis. An order-of-magnitude increase in charge was detected (24.4 pC, 15% st. dev.), accompanied by an appearance of a very strong peak around 1 MeV, with the previous plateau-like spectral feature in the 2 – 5 MeV range preserved (Figure 4.26a, case 2 and Figure 4.26c). Small chirp variations did not produce any obvious trends, except minor alterations in the high-energy part of the spectrum, similarly as in Figure 4.24a. Finally, the nozzle was again moved further away from the laser to produce a thicker profile ($70 \mu\text{m}$ waist), but the backing pressure was raised to obtain a peak density more similar to the case 2 ($1.6 \times 10^{20} \text{ cm}^{-3}$). Twofold decrease in charge was observed (12.9 pC, 24% st. dev.), as well as disappearance of the high-energy feature and lengthening of the low-energy tail (Figure 4.26a, case 3 and Figure 4.26d). This clear behavioral distinction between the different parts of the spectrum suggests two separate electron populations likely to arise from two injection processes. This will be explored further with the aid of PIC simulations.

The presented data shows clear sensitivity not only to the peak plasma density, but also to the profile width. Hence both of the parameters should be considered as potential accelerator tuning knobs, and precise control over them is desired. Physically this helps to balance the influence between detrimental ionization-defocusing and dispersion effects and relativistic self-focusing which aids reaching higher driver intensities. All in all, introduction of supersonic microjets permitted reaching a stable operation mode with low shot-to-shot fluctuations and predictable spectra (Figure 4.26b-d, grey areas).

4.3.4 PIC simulation and multiple injection regimes

To get more insight into the physics of the considered accelerator, we performed PIC simulations with the CALDER-CIRC code. The ionization effects were included. The neutral N gas density profile was set to be a Gaussian with a peak value of $1/5 \times 1.7 \times 10^{20} \text{ cm}^{-3}$ and $55 \mu\text{m}$ waist, corresponding to the experimental case 2. The exact measured laser pulse temporal field profile was used as an input, whereas the beam focal spot was approximated by a perfectly symmetric two-dimensional Gaussian of a size $2.7 \mu\text{m}$ FWHM.

The simulations reproduced the experimental features well. The black curve in Figure 4.27a shows the simulated spectrum at the exit of the plasma that is fairly similar to the one for Case 2 in Figure 4.26, and the total accelerated charge is 10 pC. Beam divergence is around $20 \times 40 \text{ mrad}$, which is also within acceptable agreement. A more detailed analysis provides interesting insight on the injection mechanism, confirming our earlier hypothesis on the existence of multiple electron populations. Around $10 - 20 \mu\text{m}$ before the density peak, the laser self-focuses to reach $a_0 \approx 1.8$, triggering localized ionization injection of roughly 3 pC

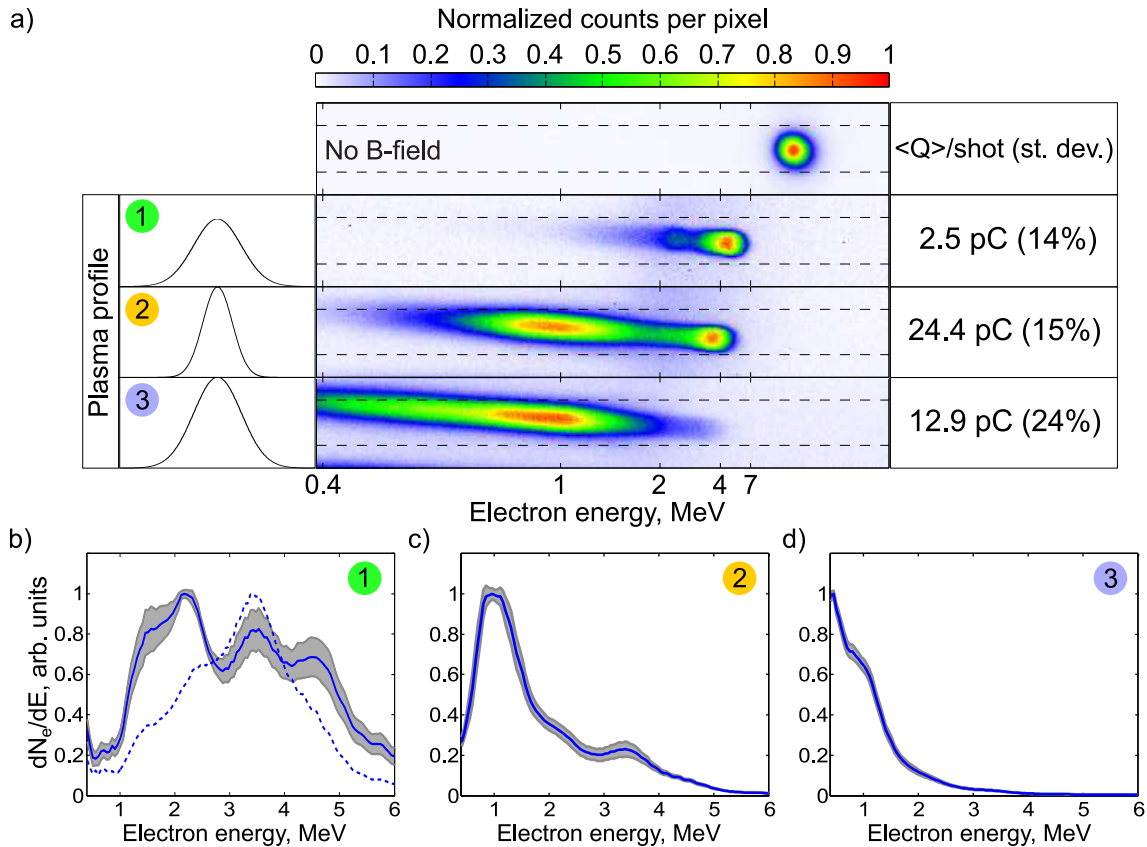


Figure 4.26 – Electron spectra and measured average charges for three different target density profiles in the $f/2$ focusing configuration. a) raw spectral data and average charge values. Top row – electron beam spatially filtered by a pinhole but not deviated by magnets. Case 1 – data for a Gaussian plasma profile with $1.45 \times 10^{20} \text{ cm}^{-3}$ peak density and $65 \mu\text{m}$ $1/e$ waist. Case 2 corresponds to $1.7 \times 10^{20} \text{ cm}^{-3}$ peak density and $55 \mu\text{m}$ waist, case 3 – $1.6 \times 10^{20} \text{ cm}^{-3}$ peak density and $70 \mu\text{m}$ waist. b) deconvolved spectrum 1 (blue solid line) with standard deviation (grey area). Dashed line – deconvolved spectrum when the driver pulse was negatively chirped by -4 fs^2 (raw data not provided). c) and d) deconvolved spectra 2 and 3 with corresponding standard deviations.

K-shell electrons. Eventually they form a peak at around 4 MeV, as seen from the blue curve in Figure 4.27a. The yellow histogram in Figure 4.27b gives injection positions of these electrons within the plasma density profile. So far everything is very similar to the previous simulation for the $f/3$ focusing in a subsonic jet. However, later on a second injection process occurs, this time entirely dominated by L-shell electrons. Surprising fact is that it is activated already when the laser intensity has dropped (orange histogram, Figure 4.27b). The phase space analysis shows that the mechanism here is similar to the one described in section 2.4.6 or (Beaurepaire et al., 2014). Figure 4.27c-d depicts how the laser pulse (red curve) slows down due to redshifting with respect to the front of the simulation window that moves to the right at the vacuum speed of light. Even though the intensity has decreased, leading also to a weaker wakefield (black curve), this reduction of wake phase velocity aids a massive particle self-injection that at the end results in a strong spectral peak at 2 MeV. We additionally note that a small population of L-shell electrons is also trapped during the first injection stage, and they are responsible for the 6 – 8 MeV plateau in the final spectrum. An important feature is that all the K-shell electrons are injected in the second plasma cavity, eventually entering the first one while maintaining a single sub-fs bunch. However, the remaining particles are trapped

further behind the laser. As seen in Figure 4.27e, these two electron groups are spatially separated at the plasma exit. This may have consequences for ultrafast science applications – to have the shortest bunch one may want to "kill" the second mechanism, especially when spectra for the two populations are partially overlapping, turning their separation with a set of permanent magnets impossible. The experimental data suggests the desired suppression might be achieved through careful target profile tailoring.

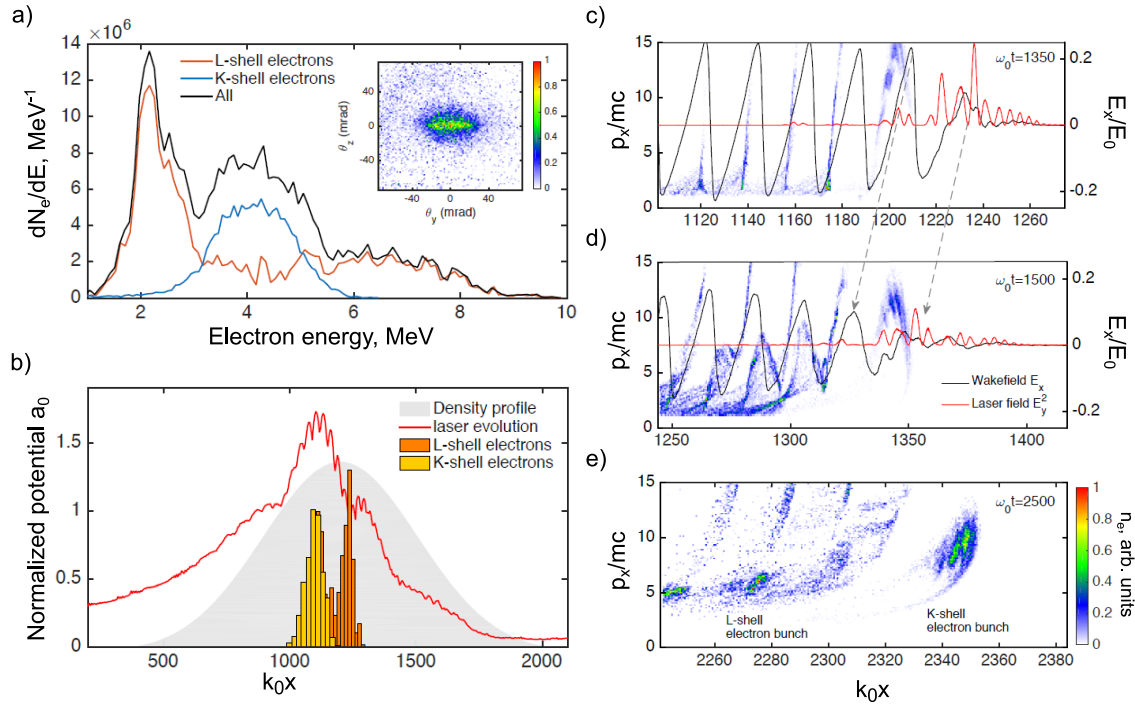


Figure 4.27 – Laser-plasma interaction dynamics and accelerated electron bunch properties given by PIC simulations for the experimental case 2 (Figure 4.26). a) energy spectrum (black curve). It may be decomposed to a spectrum of electrons originating from the L-shell of nitrogen atoms (red curve) and a K-shell spectrum (blue curve). Inset – beam profile at plasma exit. b) dynamics of the interaction. Red curve gives the peak normalized vector potential of the laser pulse at a given position within the plasma profile (grey area). Orange histogram gives original positions of trapped and accelerated particles originating from the nitrogen L-shell, yellow histogram describes the same for K-shell electrons. c-d) longitudinal E-field of the wakefield (black curve), transverse electric field magnitude of the driver pulse (red curve) and relativistic electron density distribution at two different positions within the plasma. e) relativistic electron density distribution at the exit of the plasma.

4.3.5 Experiments with supersonic jets of argon

As previously with the subsonic jet and $f/3$ focusing, we briefly explored the features of relativistic particle beams obtained from argon gas. The *Salle Noire* laser beam with properties as described above was focused into a Gaussian plasma target with $1.6 \times 10^{20} \text{ cm}^{-3}$ peak density (assuming each molecule ionized 8 times) and $55 \mu\text{m}$ waist. This was provided by the same supersonic microjet with $P_{back} = 30 \text{ bar}$. Figure 4.28 shows the main features of an electron beam obtained with an optimally compressed driver. As seen, the beam profile exhibits divergence of $> 100 \text{ mrad}$ in both dimensions (image integrated over 100 shots). The pointing stability is again only few mrad, however, the charge stability is very poor. The total charge is estimated to be 74 fC on average, but the standard deviation exceeds

120%. The particle energies are also inferior to the similar nitrogen case and don't exceed ≈ 2.2 MeV, with a peak at 1.3 – 1.4 MeV. Such behaviour was also typical for a higher backing pressure $P_{back} = 40$ bar, peak density scaled accordingly. For $P_{back} = 10$ bar, the charge was much more stable (5.6% st. dev. for 100 ms exposures), however, the particle energies were < 500 keV only. We conclude that argon, most likely due to ionization effects on the laser pulse evolution caused by Ar^{8+} and Ar^{9+} ions, is indeed not a preferable choice for LWFA with our parameters.

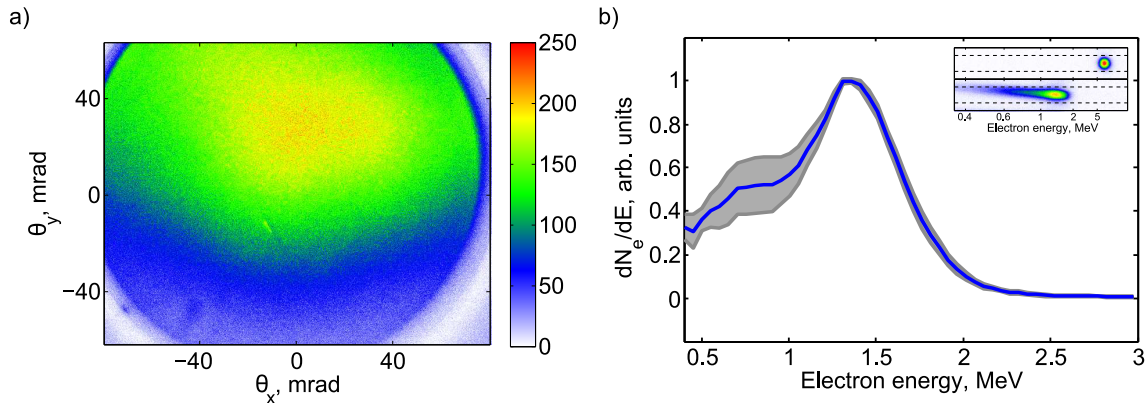


Figure 4.28 – Features of an electron beam obtained with $f/2$ focusing into supersonic microjet of argon. a) profile of a beam containing 74 fC charge (on the detector), with $> 120\%$ standard deviation fluctuations. Average divergence is > 100 mrad, pointing is stable within few mrad. b) energy spectrum (blue line) with standard deviation (grey area). Inset – raw spectral measurement data.

Conclusions

The presented experimental campaign has resulted in much more stable electron beams with significantly enhanced charge content – up to ≈ 30 pC/shot. This has been permitted by the use of tight laser focusing combined with supersonic microjet targets that optimised the driver pulse coupling into the plasma. Multiple spectral peaks have been observed with different responses to driver chirping. Those spectral peaks could be switched on or off by slight adjustments of plasma target width and peak density. PIC simulations suggest significant role of ionization-induced defocusing as well as multiple injection mechanisms occurring at different positions within the target that form the mentioned spectral peaks. The importance of fine-control over the plasma parameters in this regime is underscored.

4.4 Laser pulse duration influence study

It has been observed in several earlier cases that, due to the broad laser bandwidth combined with high plasma densities necessary for our configuration, the particle beam parameters show increased dependency on dispersion effects present in the plasma. A naturally arising question is then whether or not it is really optimal to use such short driver pulses. Perhaps several-cycle pulses, as in (Schmid et al., 2009), could still do the job despite reduced vacuum intensity at constant energy, and even provide more stability, since a lower number of laser-plasma interaction effects would come into play. The *Salle Noire* system provides an easy way to tune the transform-limited driver pulse duration while maintaining constant energy per pulse. In this section, we explore the impact of this parameter on wakefield acceleration and corresponding dispersion effects in different regimes.

4.4.1 Relativistic particles from a high-density target driven by several-cycle pulses

Experiments have been executed with 2.2 mJ kilohertz pulses, focused by an $f/2$ parabola into a mildly elliptical $2.4 \times 2.8 \mu\text{m}$ (FWHM) focal spot with slight coma aberration. The pulse duration could be varied by adjusting helium pressure in the post-hollow-core fiber chamber (see Figure 3.1), which sets the amount of broadening that a laser pulse undergoes through self-phase modulation mechanism. At each given pressure a d-scan measurement was performed to both determine the glass wedge position giving optimal compression and to characterize the resultant pulses. Figure 4.31 shows both the laser spectra for $P_{\text{HCF}} = 600, 700, 900$ and 1100 mbar (a-d), as well as corresponding pulse intensity profiles (e-h). Using these temporal profiles and the focal spot image, one may estimate peak vacuum intensities to be 1.2×10^{18} , 1.6×10^{18} , 2.1×10^{18} and 2.3×10^{18} W/cm², respectively, for the four presented cases. The laser FWHM durations are correspondingly 6.8, 6.1, 4.5 and 3.9 fs.

The gas nozzle was kept with its tip at a constant $110 \mu\text{m}$ distance away from the optical axis. This set the width for the Gaussian plasma profile experienced by the laser at $45 - 50 \mu\text{m}$ $1/e$ waist for the particular nozzle unit. For each driver pulse duration, a backing pressure scan was performed, exploring peak densities between 6.3×10^{19} cm⁻³ and 1.3×10^{20} cm⁻³. The transverse and longitudinal positions would be optimized for any configuration, and some

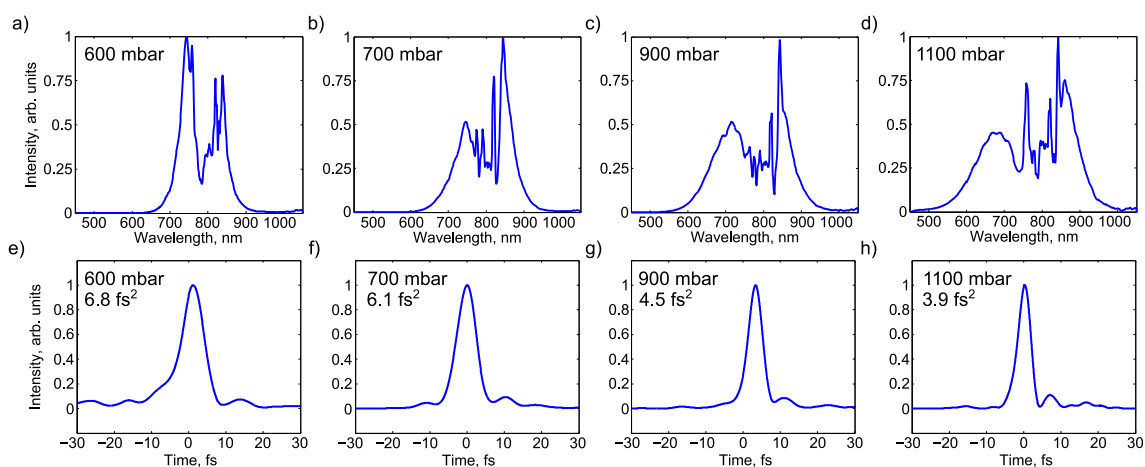


Figure 4.29 – a-d) laser spectra measured for different pressures in the hollow-core fiber. e-h) corresponding best-compression pulse intensity profiles as determined by the d-scan technique.

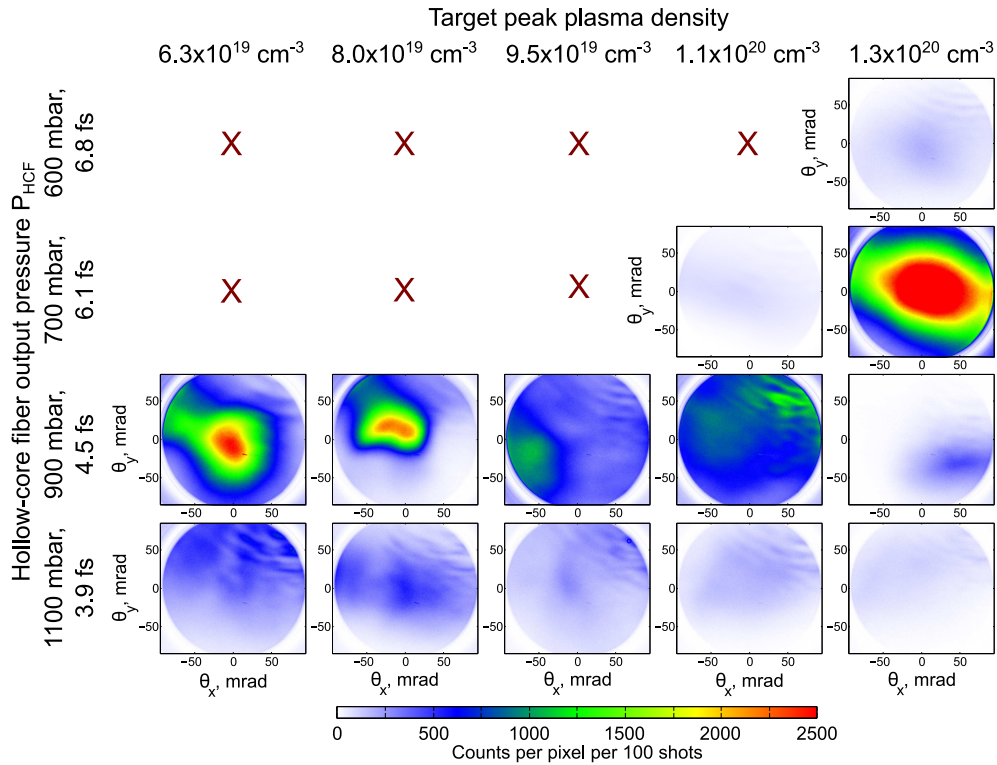


Figure 4.30 – Camera images of typical electron beams obtained for varied experimental parameters. Rows – laser pulses of different Fourier transform-limited durations used. These durations were adjusted by changing the pressure at the end of the hollow-core fiber. Columns – various peak densities, obtained by tuning the target backing pressure P_{back} . The colour scales in each image were normalized to a common peak CCD pixel count number. 'X' implies no electrons were detected at the appropriate conditions.

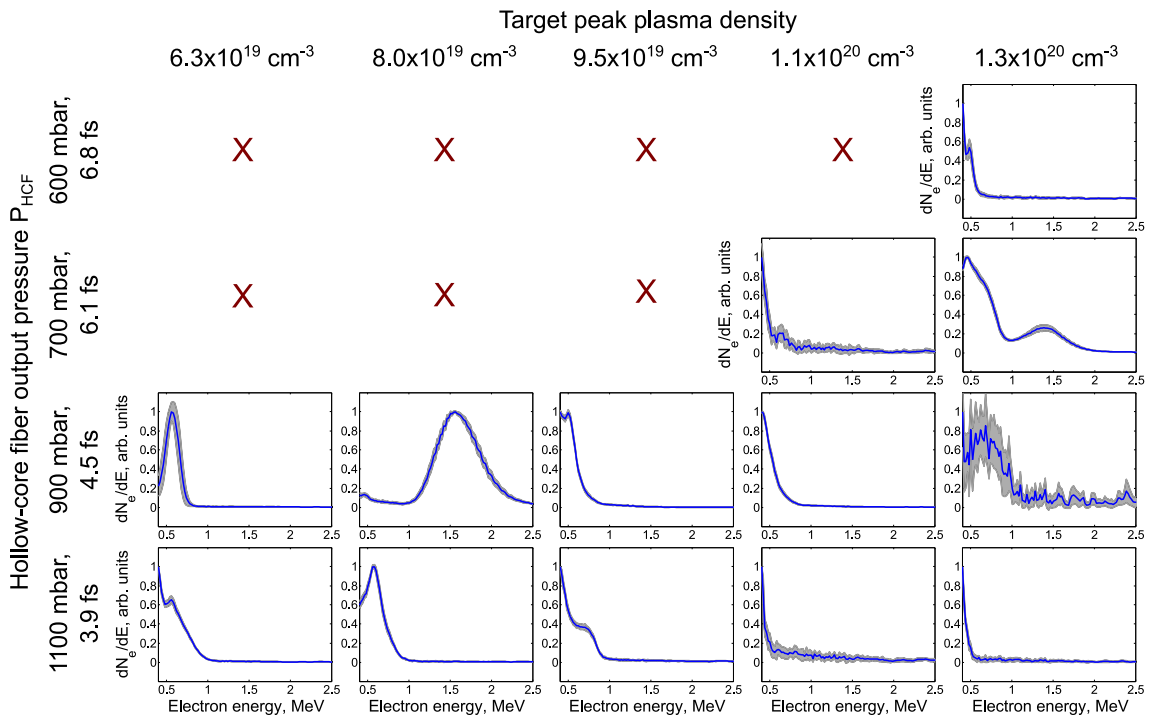


Figure 4.31 – Corresponding spectra of the electrons beams depicted in 4.30.

laser chirp introduced by moving the wedges, if needed to improve the signal. No accelerated electrons have been observed with $P_{\text{HCF}} \leq 500$ mbar, implying pulse duration $\tau_{\text{FWHM}} \geq 7.2$ fs. The beam characteristics obtained for shorter drivers are summarized in Figure 4.30 (particle spot profiles) and Figure 4.31 (particle energy spectra). The only detected electron signal for the 6.8 fs pulse was with the highest peak density, $1.3 \times 10^{20} \text{ cm}^{-3}$. However, the evaluated charge was only 16 – 48 fC/shot, and the measured energies were below 700 keV. For the 6.1 fs pulse, a similar particle beam with 12 – 42 fC/shot and sub-800 keV energies was obtained when the target peak density was set to $1.1 \times 10^{20} \text{ cm}^{-3}$. But after increasing it to $1.3 \times 10^{20} \text{ cm}^{-3}$, a ten-fold jump in electron count occurred and a relativistic energy distribution with a peak at 1.4 MeV and extending to 2 MeV emerged, as seen in the appropriate entries of Figures 4.30 and 4.31. With a positive chirp of +16 fs² added, this driver could accelerate 930 fC/shot with 7.9% standard deviation uncertainty for 100 ms integration times. The beam had turned fairly large, with an average FWHM divergence of 140×80 mrad and sub-3 mrad pointing fluctuations.

The driver duration was then reduced to 4.5 fs. In this case, electron beams were generated at all the explored peak densities, starting with $6.3 \times 10^{19} \text{ cm}^{-3}$. However, only for one target parameter value the beam was confidently relativistic. At a maximum density $8.0 \times 10^{19} \text{ cm}^{-3}$, the energy distribution exhibits a quasimonoenergetic peak at 1.6 MeV, when a +8 fs² chirp is added. The beam contains 490 fC/shot with 14.0% standard deviation at 100 ms camera exposures, it has an average FWHM divergence of 80×45 mrad and pointing fluctuations < 2.3 mrad. At all the other peak densities the particles remain weaker than 1 MeV. Finally, when 3.9 fs laser pulses are used, electron energies stay below 1 MeV for all the backing pressures, and reach barely 500 keV for peak densities exceeding 10^{20} cm^{-3} . The discrepancies from relativistic cases seen in previous campaigns could be explained by different target parameters (lower estimated peak density, narrower profile) for the particular nozzle unit used here as well as worse laser specifications (lower energy per pulse, mildly degraded focal spot).

It is worth noting that for the 6.8 fs pulse the threshold density for achieving relativistic self-focusing that can be calculated from equation 2.53 is $1.4 \times 10^{20} \text{ cm}^{-3}$, or slightly above the highest used peak density. For the 6.1 fs pulse an equivalently obtained value is $1.1 \times 10^{20} \text{ cm}^{-3}$, matching very well to the limit of where the high-charge beam occurs. Corresponding threshold densities for 4.5 fs and 3.9 fs drivers are $8.4 \times 10^{19} \text{ cm}^{-3}$ and $7.8 \times 10^{19} \text{ cm}^{-3}$ (Figure 4.32). Exact pulse shapes from the d-scan measurement have been accounted for in order to obtain correct peak powers that are then set equivalent to P_{cr} in equation 2.53. For this reason the data points do not make a completely straight line. We must also remark that the derivation of equation 2.53 in section 2.6.1 is for constant laser frequency ω_0 , an assumption becoming less and less appropriate as the transform-limited pulse duration decreases.

A last, slightly subtle remark on reading the Figure 4.30 should be added at this point. The colour scale for each individual image here has been adjusted to the same maximum value, so that the CCD count rates from every picture are comparable. However, this does not directly imply an accurate visual comparison for the beam charge. As described in section 3.3.1, the ratio of electrons incident on the scintillator to the number of emitted photons depends on the particle energy (Figure 3.9). Due to this reason the strong beam for the 6.1 fs driver appears to contain much more than twice the charge of the 4.5 fs-driven relativistic beam, as is eventually calculated once the spectra are accounted for. This is due to the former having a strong low-energy (< 1 MeV) tail, to which the detector is more sensitive. However, as many spectra are evidently continuing into the sub-400 keV region which for the used spectrometer configuration extends out of the screen, the appropriate individual factors to adjust the colour

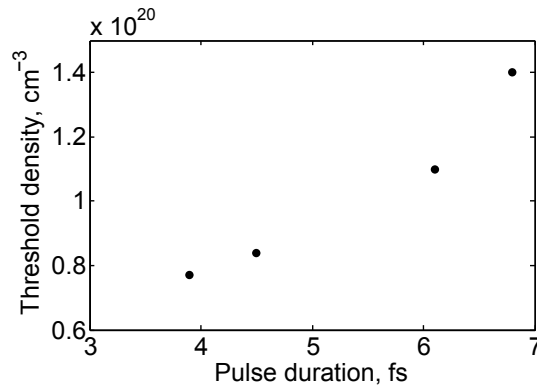


Figure 4.32 – Threshold densities for achieving the relativistic self-focusing for laser pulses of different durations. Estimation has been done using equation 2.53, and measured temporal pulse intensity profiles to correctly estimate the peak power.

scales further for charge comparison were not obtained.

In conclusion, we have found two experimental parameter combinations giving 0.5 – 1 pC/shot relativistic electron beams with only 2.2 mJ driver energy. We will explore now if they exhibit any differing behavioural traits.

4.4.2 Dispersion effects for the different regimes

In addition to the obvious differences in divergence values for the 6.1 fs and the 4.5 fs-driven relativistic beams as well as the absence of sub-1 MeV energy tail for the latter, we studied their responses to introducing chirp into the driver. Figure 4.33 shows the variations in obtained particle spectra. Evidently changing the chirp for the 6.1 fs driver (Figure 4.33a) had some influence on the < 1 MeV energy tail shape and the strength ratio between this tail and the 1.4 MeV peak. On the other hand, the position of this more energetic peak remained constant for all cases. The situation is quite different for the 4.5 fs driver (Figure 4.33b). Here the position of the relativistic peak clearly shifts from 1 MeV with slightly negative chirp of -4 fs^2 to 1.6 MeV with a positive ($+4 \text{ fs}^2$) chirp, similarly as in Figure 4.5.

This kind of behaviour is not completely unexpected from the physics point of view. A 4.5 fs has a broader bandwidth than the 6.1 fs pulse, and thus elongates quicker for a given added GDD value. Using naively the formula 2.55 one may estimate that for a positive chirp by $+12 \text{ fs}^2$ a Fourier transform-limited pulse of 4.5 fs duration elongates to 8.7 fs, or nearly double the duration and half the intensity, whereas a 6.1 fs pulse stretches only to 8.2 fs. This is not strictly valid since the Gaussian envelope approximation used to derive equation 2.55 breaks down for few-cycle pulses, but it gives a good idea on what is happening. In addition, since the 6.1 fs-driven beam is only present for much higher plasma densities, more significant influence on beam output features by self-focusing rather than by dispersion effect is expected. At these higher plasma densities it is also natural to anticipate that the signal gets optimized for fairly high second-order chirp values – from $+12$ to $+20 \text{ fs}^2$. On the contrary, the 4.5 fs-driven relativistic beam is generated at lower densities and becomes optimized closer to the best compression point.

We conclude that, for a given laser energy, higher plasma densities are required to generate relativistic electron beams for longer transform-limited pulses in order to reach comparable light intensities via self-focusing as in a short-driver case. Dispersion effects remain important, however, it becomes much more difficult to utilize them for tuning particle parameters, such

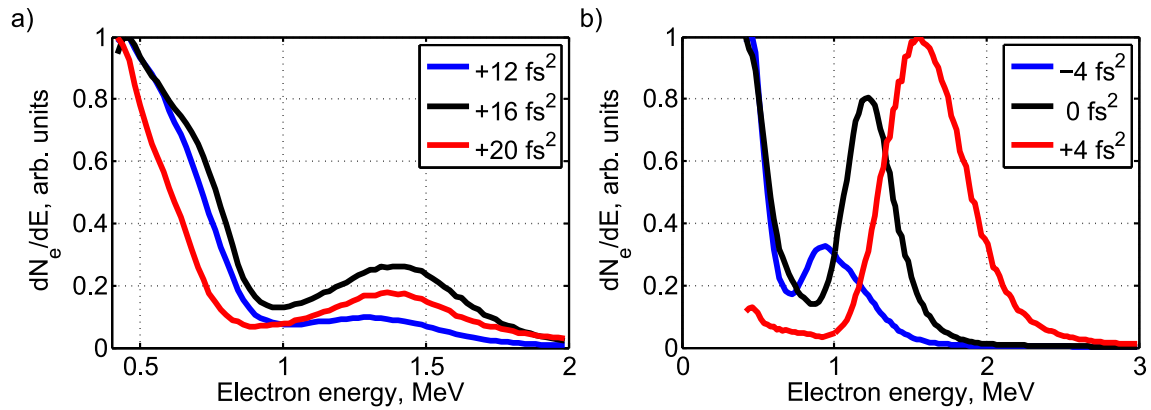


Figure 4.33 – Beam spectra dependencies on the driver pulse chirp. a) particles driven by pulses with 6.1 fs Fourier transform limit at a peak density $1.3 \times 10^{20} \text{ cm}^{-3}$. b) particles driven by pulses with 4.5 fs Fourier transform limit at a peak density $8.0 \times 10^{19} \text{ cm}^{-3}$.

as the energy. On the positive side, one could argue that this reduced chirp sensitivity makes our system more robust. In the ultrashort pulse case ($< 5 \text{ fs}$), dispersion turns dominant, so that at some point any further density increase does not bring further gain in beam energy or charge. Provided one has access to controlling the driver waveform such as chirping the pulse by glass wedges, this may allow some tunability on the output parameters. On the other hand, it brings more restrictions on the laser system. A similar approach of increasing the target density until enough self-focusing is achieved has been used by (Salehi et al., 2017), who were the first to report MeV-scale electrons with a kilohertz repetition rate mJ-scale 30 fs laser and a pulsed cryogenically cooled gas valve. Based on the scaling laws and their simulations, this experiment was not operating in the bubble, but rather in the self-modulated regime (Modena et al., 1995), leading to relatively high-divergence profiles. Our 6.1 fs relativistic case is likely to lie somewhere in the transition region between the two.

4.4.3 Strongly focused relativistic electron beam

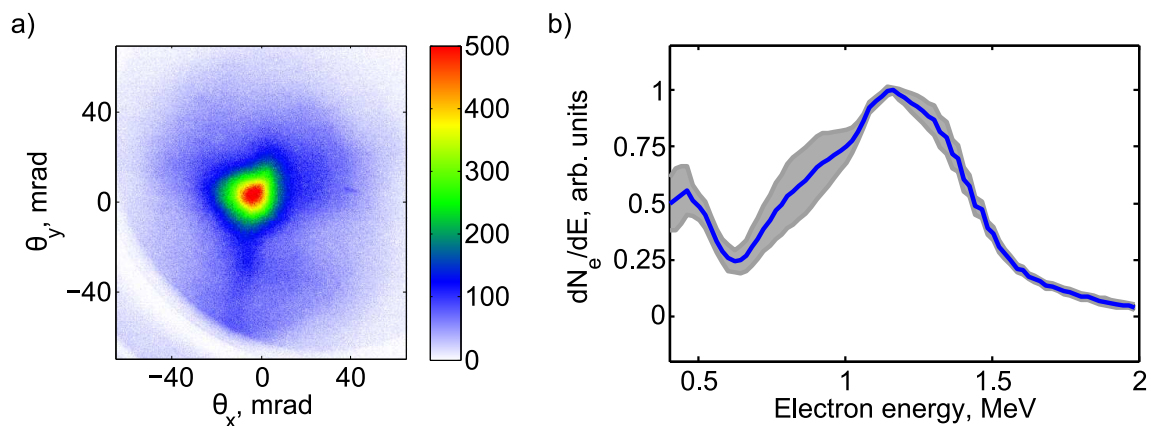


Figure 4.34 – Features of an electron beam obtained with focusing a 6.6 fs laser pulse into a supersonic gas nozzle. a) single-shot electron spot profile. A series of 40 shots had an average charge of $2.6 \pm 40\%$ pC and an average divergence of $21 \times 22 \text{ mrad}$ with $\approx 10 \text{ mrad}$ pointing deviations. b) energy spectrum (blue line) with standard deviation (grey area).

Large divergence has however not been a general output feature obtained with several-cycle low energy drivers at high density. A nearly equivalent experiment with 2.2 mJ laser pulses

was repeated on another run with $P_{\text{HCF}} = 600$ mbar. This time the estimated FWHM driver duration was slightly shorter – 6.6 fs, and the target was placed at the same earlier height so that the Gaussian plasma profile had a $1/e$ width of $45 - 50 \mu\text{m}$. A strong signal has been obtained already at a peak density $1.1 \times 10^{20} \text{ cm}^{-3}$, yielding 2.6 pC bunches with 40% standard deviation at single-shot exposures (Figure 4.34). However, now the particle beam appears relatively well focused, with an average FWHM divergence of 21×22 mrad and pointing fluctuations of ≈ 10 mrad. When integrated over 10 shots, the statistics have improved to 19.6% standard deviation in charge and 3.5 mrad in pointing, at the expense of increased average divergence of 40×34 mrad. This is still clearly superior to the earlier relativistic case for the 6.1 fs driver, even though the latter was recorded with 100 ms integration. One way to explain this is that the relativistic self-focusing is able to win the competition against dispersion in this case, elongating the accelerating and focusing wakefield channel as well as making the focusing fields within the bubble stronger. This is supported by the measured spectral distribution for this beam, which is a quasimonoenergetic peak at 1.2 MeV, followed by a weak tail below 600 keV. Increasing the peak density to $1.3 \times 10^{20} \text{ cm}^{-3}$ has led to a slight shift in energy peak to 1.4 MeV and an increase in divergence to 40×45 mrad at 10 ms exposures.

The large difference from the completely blank earlier case with a 6.8 fs pulse and $1.1 \times 10^{20} \text{ cm}^{-3}$ peak density could then be explained by being very close to the relativistic self-focusing threshold combined with plasma profile measurement uncertainties, slightly shorter driver pulse, mild difference in laser spectrum that is relatively redshifted for the experiment discussed in this section (Figure 4.35), or some other fine experimental details. More insight into this situation could perhaps be gained via numerical simulations, but they have not been performed here.

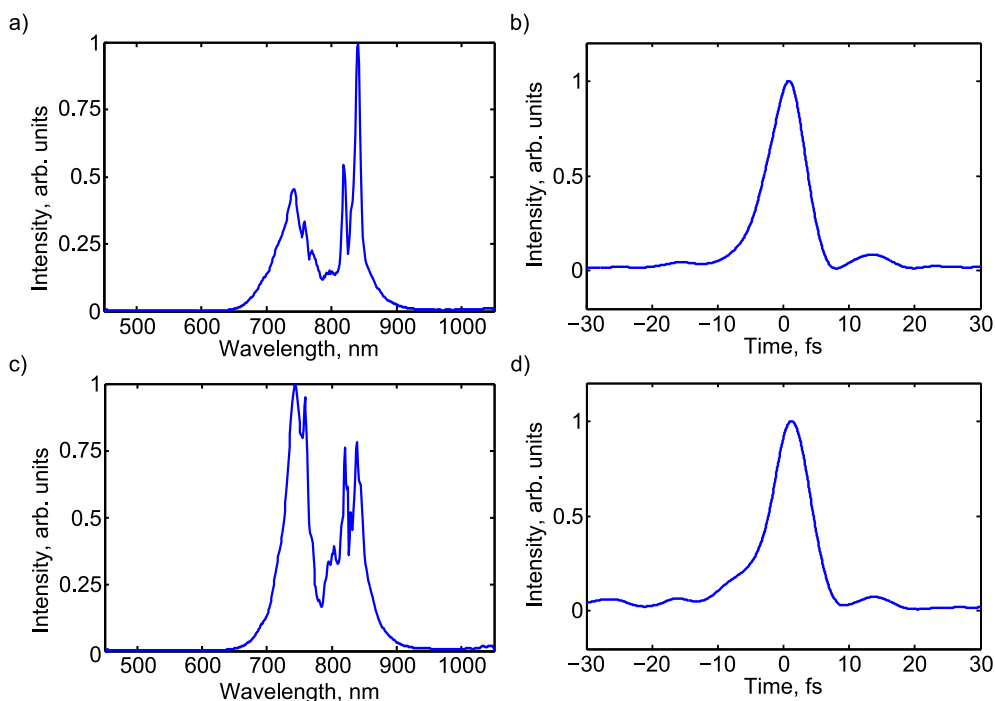


Figure 4.35 – a) and c) measured laser spectra for the case discussed in section 4.4.3 and the $P_{\text{HCF}} = 600$ mbar case presented in Figure 4.29, respectively. b) and d) reconstructed laser pulse intensity profiles for the corresponding spectra a) and c). FWHM duration for the pulse in b) is 6.6 fs, for d) it is 6.8 fs.

Conclusions

We have found another regime to obtain a relativistic electron beam without compressing the driver pulse to the shortest possible duration on our laser system. The reduced peak vacuum intensity had to be compensated via increased relativistic self-focusing at higher plasma densities. The new regime appears to be much less sensitive to dispersion effects, suggesting it might be more robust, provided the stability does not start suffering from the increasingly pronounced self-focusing phenomenon instead. These results could be useful in future design of ultrashort laser systems for wakefield acceleration applications.

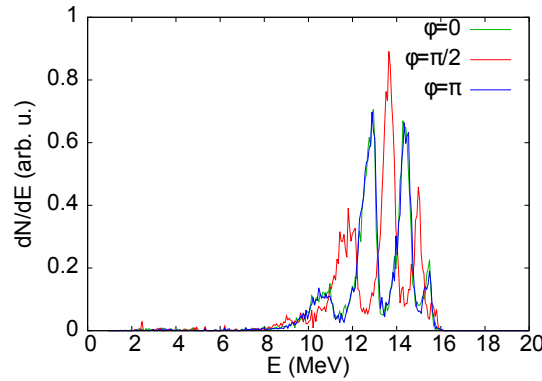


Figure 4.36 – Simulated CEP effect on an ionization-injected electron beam in (Lifschitz & Malka, 2012). Particle spectra are given for absolute CEP values of $\phi = 0$ (green), $\phi = \pi/2$ (red) and $\phi = \pi$ (blue). The energy distributions for $\phi = 0$ and $\phi = \pi$ are identical.

4.5 CEP effect measurements

When laser pulses as short as the ones in this experiment are used, not only the chirp, but also the carrier-envelope phase may be expected to have an effect on the interaction. In fact, a numerical study indeed demonstrated a significant CEP influence on the beam output properties in a case where particles are injected into the wakefield by the ionization trapping mechanism (Lifschitz & Malka, 2012). When close to the ionization threshold, a few-cycle light pulse with an absolute CEP $\phi_0 = 0$ might be causing release of electrons only around the peak of the most intense cycle. By changing the CEP to $\phi_0 = \pi/2$, one may switch to a different situation where, say, two cycles are reaching the same peak above-threshold intensity, and are ionizing additional electrons at two different positions. These two particle populations then have slightly differing initial conditions in the wakefield phase space, and thus could in principle result in two spectral peaks of the output particle beam. Additionally, varying the CEP also tunes the exact individual laser cycle maximum intensity values, therefore it may have an effect on how long the driver is able to cause this ionization trapping, implying adjustments in total accelerated charge. For example, a CALDER-CIRC simulation that we tried with parameters equivalent to the ones presented in section 4.1.3, but with the CEP changed from 0 to $\pi/2$, modified the final bunch charge by 15%. Note that the mentioned simulation also showed ionization-induced injection to be the only trapping mechanism, as is the situation discussed in (Lifschitz & Malka, 2012). We have to keep in mind, however, that the CEP keeps evolving as the pulse is propagating in the plasma. One may define the phase slippage length $L_{2\pi}$ as the propagation length over which the CEP shift equals to one full sinusoidal period of 2π :

$$L_{2\pi} = \frac{c}{v_\phi - v_g} \lambda_0 \approx \frac{n_{cr}}{n} \lambda_0, \quad (4.3)$$

where v_ϕ and v_g are the phase and group velocities of the laser pulse, respectively, and the last approximation assumes a sufficiently tenuous plasma. For our parameters, $L_{2\pi} = 8 - 20 \mu\text{m}$. CEP effects of the previously described type may be reasonably expected as long as the injection process continues only within a fraction of $L_{2\pi}$. This is indeed a strict condition, and is easier to meet at lower densities.

As presented in section 3.2.4, the *Salle Noire* laser system permits stabilization (down to 150 mrad st. dev. at best) and control of the pulse relative CEP value via f -to- $2f$ interferometer coupled to an oscillator pump diode power modulator. Note that the absolute CEP still remains unknown in all cases. We used this system feature to study possible CEP effects on the electron

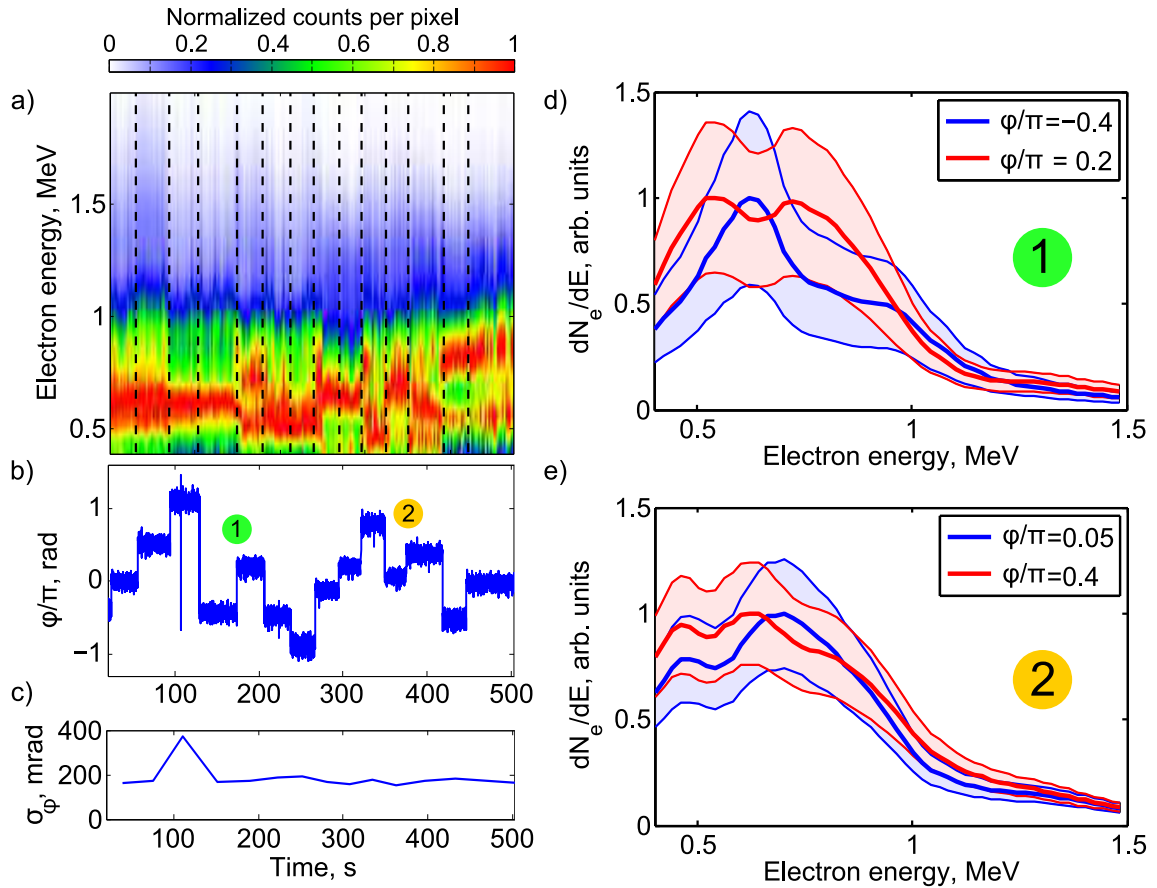


Figure 4.37 – CEP effect measurement data. a) a sequence of normalized electron spectra. The vertical dashed lines mark changes in the target relative CEP value. b) relative CEP values measured simultaneously with the electron spectra. c) RMS CEP stability between the points of switching the target CEP value. Graphs a), b) and c) share a common x-axis. d) average electron spectra comparison before (blue curve) and after (red curve) a target relative CEP jump by 0.6π , marked by '1' in graph b). Shaded areas correspond to the standard deviation of the spectral curves over all the measurements within corresponding intervals. e) similar spectra comparison before (blue curve) and after (red curve) a target relative CEP jump by $\pi/3$, marked by '2' in graph b).

beam output. Experiments have been performed with 2.4 mJ kilohertz pulses of 4 fs duration focused to a $2.4 \times 3.1 \mu\text{m}$ spot, resulting in $2.1 \times 10^{18} \text{ W/cm}^2$ peak estimated vacuum intensity. A supersonic gas nozzle was supplied with a backing pressure $P_{back} = 19$ bar, thus providing a Gaussian plasma target with $3 - 5 \times 10^{19} \text{ cm}^{-3}$ peak density and $80 - 100 \mu\text{m}$ $1/e$ waist when the tip was placed $\approx 170 \mu\text{m}$ below the optical axis. An electron beam with energies up to 1.3 – 1.5 MeV was easily obtained. We then looked at the evolution of its spectrum as the stabilized CEP was set to different target values.

Figure 4.37 presents data from one such measurement series. Graph a) gives a sequence of normalized electron beam spectra recorded at 1 s exposures for over more than 8 minutes. The dashed vertical lines mark the moments when the CEP value would be changed. We see that in several cases this is accompanied by a modification of the particle energy distribution. This is not a general rule, but it also does not need to be – if only the motivation as in the previous paragraph is considered, for example, a change in absolute CEP by π should yield the same results. On the other hand, the absence of any response can imply that the CEP effects are washed out by strong driver pulse evolution due to interaction with the high-density

plasma in the target up-ramp. Nevertheless, more concerning is the fact that one may also see some slow drifts as well as single immediate transformations of the spectrum that do not correspond to a changed CEP value. This means there are some unidentified instability sources in our system, either in the laser setup or the accelerator itself. Likely for the same reason returning to a given nominal CEP value after some time usually does not bring back the original particle energy distribution, preventing us from being able to use this feature as a fine-tuning knob of our electron beam parameters. Graphs b) and c) show the CEP values measured simultaneously during the spectral data taking and the standard deviations over the corresponding intervals. It is apparent that the stability is mostly better than 200 mrad, except one interval which exhibits a large but sudden uncontrolled spike. Figure section d) compares the average spectra with corresponding standard deviations before and after a CEP jump by 0.6π , marked by number '1' in graph b). This case somewhat resembles the situation described in (Lifschitz & Malka, 2012), since a change by close to $\pi/2$ modified the spectral distribution from a single-peaked at 600 keV to a double-peaked at 500 keV and 700 keV. In order to make stronger conclusions, however, one should study the evolution with smaller step resolution and observe the transformation dynamics, but in the presence of additional instabilities this becomes very hard. Finally, graph e) compares the average spectra before and after a CEP jump by $\pi/3$, marked in graph b) by number '2'. Here one of the present quasi-peaks shifts from 700 keV to 600 keV, while the other one remains stable at 450 keV. Once again this different behaviour suggests a high degree of nonlinearities present in this problem that are intercoupled and thus make the fine-control of such experiments really difficult to achieve.

In order to increase the relative weight of the CEP effect against other influences, we also tried looking into particle beams obtained at lower densities, which would modulate our originally near-single-cycle pulse through dispersion or self-focusing less wildly. Note that the lack of self-focusing may prevent reaching intensities required for ionization-injection, for which the CEP effect is suspected to be the most easily observable. Nevertheless, one fairly interesting set of data has been obtained and is presented in Figure 4.38. Here a pressure $P_{back} = 10$ bar of nitrogen was used, creating a Gaussian plasma profile with $1.8 \pm 0.8 \times 10^{19} \text{ cm}^{-3}$ peak density and $70 - 90 \mu\text{m}$ $1/e$ waist when the tip was placed $\approx 140 \mu\text{m}$ below the optical axis. A particle beam was obtained, and its spectra recorded while the relative CEP would be cycled three times between 0 and $\pi/2$. The CEP stability was better than 220 mrad standard deviation during any of the six intervals. Graph a) shows that now the energy distribution features are much more successfully recovered for the first 2.5 cycles, however the effect weakens towards the end, probably again due to some slow system drifts. Graph b) shows the deconvolved spectra for measurement numbers 41 – 60 ($\phi = 0$, blue curve) and 61 – 80 ($\phi = \pi/2$, red curve) as well as their uncertainties (shaded areas). Both spectra have strong energy tails, however, the blue curve also exhibits two peaks at 500 keV and 700 keV, which then disappear after the $\pi/2$ jump. It might be a sign that the driver pulse is very close to the ionization threshold and it is only reached by some laser cycles at a particular interval of absolute CEP values, but again the data is insufficient to derive any stronger conclusions on this. Nevertheless, here we have obtained the first sign that under certain conditions the CEP may in fact be used to control electron beam parameters in a reproducible manner.

We have furthermore recorded many other similar spectral sequences that show no indication of CEP sensitivity. Most of the data was however taken at higher peak densities and with a CEP standard deviation larger than 300 mrad. Day-to-day operation of the laser with this feature has turned out to be somewhat challenging. Finally, we have also looked at the electron beam profiles. CEP may be expected to have an influence on this, as well, since it might lead

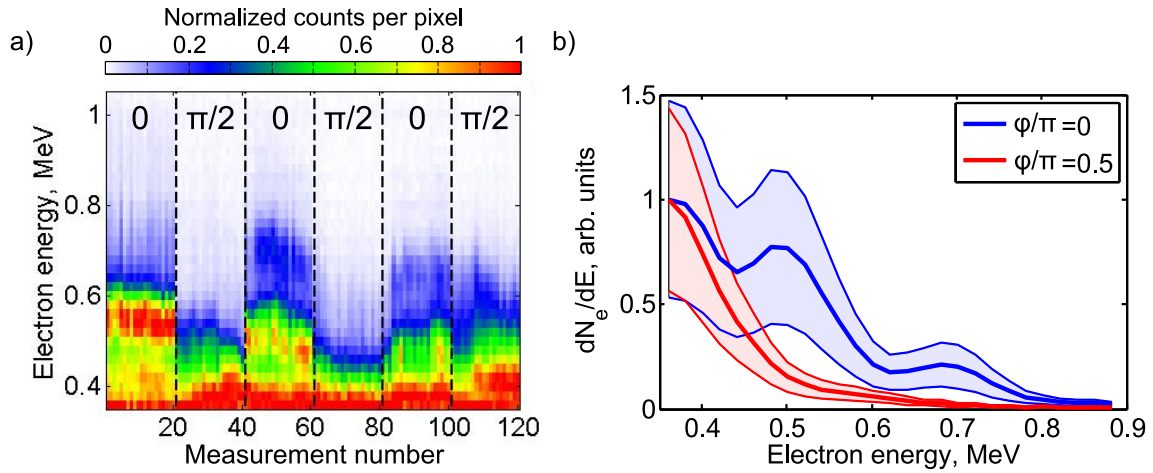


Figure 4.38 – CEP effect measurement data. a) a sequence of normalized electron spectra as the target relative CEP value was alternated between 0 and $\pi/2$. The vertical dashed lines mark those changes. The RMS CEP stability was < 220 mrad in each interval. b) average electron spectra comparison for measurements 41 – 60 (blue curve) and 61 – 80 (red curve), corresponding to a relative CEP jump by $+\pi/2$. Shaded areas indicate relevant spectral standard deviations.

to modified accelerated charge values or shape the beam differently as particles could gain variable amounts of initial momentum in the direction of laser polarization through direct interaction with the pulse. In principle, performing LWFA with CEP-stable pulses should perfectly reproduce the process at each shot and thus could lead to beams more stable in charge content, shape and pointing. However, we have not managed to get evidence for this and therefore have to conclude that other instabilities still have a much more significant effect on our accelerator.

Conclusion

To sum up, we have acquired first experimental signs of observable CEP effect for wakefield acceleration with ultrashort laser pulses. However, data also indicates this phenomenon may easily get washed out by other interaction nonlinearities and possible technical system instabilities. The significance of the CEP appears to be much less important than the other special effect in our rather exotic parameter range, i. e. dispersion. It may also not be ruled out that it has been in fact some other change in the interaction conditions induced by the CEP modulator that caused the apparent particle beam spectral shifts, and not the CEP itself. Further studies are required to answer the question whether good CEP control may become another reliable tuning knob for LWFA or help achieve superior shot-to-shot stability, and if so, in what parameter range it is worthwhile to pursue this additional complication on the laser system.

5

Discussion, future perspectives and conclusions

The results presented in this thesis explore a fairly exotic parameter range for relativistic wakefield electron acceleration. Using the scaling laws presented in (Lu et al., 2007), we successfully developed a scheme which utilizes millijoule-class near-single-cycle laser pulses to operate close to the well-known bubble regime resonance and produce high-quality particle beams in a relatively well-controlled manner. This also permitted us to be the first group in the LWFA community that could obtain electrons with energies above 1 MeV delivered continuously at a kilohertz repetition rate. As discussed earlier, it is important for a variety of reasons. It offers a more stable source both because of possibility of statistical averaging to wash out random noise, as well as in the shot-to-shot mode due to more robust laser technology. In addition, any dose-requiring applications would simply benefit from quicker dose delivery. Finally, it opens up the possibility of setting-up a feedback loop for real-time source optimization (He et al., 2015).

Indeed, in this manuscript one could see that, even though there still remain some unidentified causes of slow system drift, the hypothesis of improved stability due to high repetition rate has been verified. We have seen a significant reproducibility enhancement once the same beam would be measured over longer camera exposure times. Moreover, the shot-to-shot stability in several presented cases goes below 10%, which is a fairly impressive result bearing in mind that no highly advanced target engineering has been used (most stable beams are usually obtained in gas cells rather than gas jets (Osterhoff et al., 2008) (Hansson et al., 2014) (Vargas et al., 2014)), and experiments often operated not far from the injection threshold.

This project has successfully dealt with a problem arising from the desire to operate at a high repetition rate combined with the bubble regime scaling laws adapted to ultrashort, few-cycle laser pulses – namely the need to achieve high plasma densities at continuous flow while maintaining good quality vacuum in the regions irrelevant for acceleration. This has been achieved using specially fabricated supersonic micronozzles minimizing the gas mass flow and reducing thermal expansion effects once the fluid exits into the vacuum chamber. Furthermore, we argue pure nitrogen is a very appealing plasma source due to the fact each molecule may provide 10 plasma electrons, it is much more effectively pumped out by the

vacuum systems compared to its lighter counterparts hydrogen or helium, as well as because of the fairly unique energy gap between its L-shell and K-shell ionization levels. In addition, we have designed and tested novel "shocked" gas jets that may provide sharp gradients and extremely high plasma densities far away from the nozzle tip, suggesting possibilities for density-transition injection use and circumventing the laser-induced damage problem.

We studied the combined impact of driver focusing conditions and the plasma target gradient scale length on the electron beam generation efficiency. We concluded that detrimental ionization-related effects are necessary to account for in this experimental parameter range in order to lift-off from the wakefield injection threshold and secure the stability of the source. Fine control over the exact target density profile is desired, and it could be achieved through good accuracy in nozzle positioning with respect to the accelerator axis as well as high degree of certainty over the supplied backing pressure.

Experiments have investigated physical effects of laser-plasma interaction arising uniquely for such ultrashort drivers, namely dispersion and carrier-envelope phase. It has been found that sending positively chirped pulses into high-density plasma may precompensate the negative dispersion accumulated while propagating in the target up-ramp, and help optimize the output electron beam parameters, especially when operating close to the injection threshold. If this additional complication in physics is undesired, dispersion impact can be reduced by using few-cycle rather than single-cycle pulses. At a given laser energy, this results in lost vacuum peak intensity, which may be balanced by increased self-focusing with higher plasma densities. Note, however, that it may imply drifting away from the bubble regime conditions. CEP effects appeared to be of lesser significance, and they seem to be completely washed out by other nonlinearities for increased plasma densities. However, even if for sub-MeV electrons only, we have been the first to see their experimental evidence due to a unique parameter range used in this project.

For the intended applications in ultrafast science with superior temporal resolution, further developments are nevertheless still required. Beam stability, even though significantly improved over the course of this project, still remains an issue, as pump-probe diffraction experiments demand detecting sub-percent-level changes in Bragg peak intensities. This will be tackled by attempting different particle injection schemes and further advanced target design. An additional constraint for the discussed application is a narrow electron energy spread, where the requirement is not even expected to be met directly by the laser-plasma scheme. A magnetic beam transport line selecting a desired particle energy range, and compressing it temporally in the assigned sample plane has been designed, numerically validated, and intended to be built in the future (Faure et al., 2016). We expect this to lead to first diffraction experiments with sub-10 fs temporal resolution, or an order-of-magnitude improvement from the current best results.

Laser energy	Pulse duration	Waist at focus	Plasma density	Acceleration length	Electron energy
5 mJ	5 fs	2.5 μm	$7 \times 10^{19} \text{ cm}^{-3}$	40 μm	5 – 10 MeV
10 mJ	7 fs	3.2 μm	$4 \times 10^{19} \text{ cm}^{-3}$	90 μm	10–25 MeV
20 mJ	9 fs	4 μm	$2.5 \times 10^{19} \text{ cm}^{-3}$	170 μm	20–40 MeV

Table 5.1 – Optimum laser and plasma parameters for LWFA in the bubble regime at various laser energies, according to the model by (Lu et al., 2007). The central laser wavelength assumed to be 800 nm everywhere.

Probably the main conclusion after the entire presented sequence of experiments aiming to optimize and stabilize the resultant particle beam is after all rather simple. The collected set of data strongly suggests that our accelerator would greatly benefit from an increase in laser pulse energy. This would allow reaching necessary driver intensities with looser parabola focusing, lower degree of temporal compression, there would be less need to rely on relativistic self-focusing. It would relieve the conditions on target gradient engineering, elongate the acceleration channel increasing the bunch energy and reducing its divergence, limit the degree of laser pulse evolution inside the plasma due to dispersion and other nonlinear effects, yielding more control over the experiment and likely enhancing the shot-to-shot stability 5.1. We hope this to be the outcome of later experiments with an upgraded *Salle Noire* system, or at other kilohertz facilities, such as the ELI-ALPS site ([Budriūnas et al., 2017](#)).

Most importantly, the demonstration of relativistic electron acceleration with millijoule-class light pulses at high repetition rate opens up the way for the spread of accessible, small laboratory-scale particle beam sources. Combining state-of-the-art commercial titanium-sapphire laser technology with hollow-core fiber postcompression technique can yield reliable accelerators for a price affordable to a single well-funded university group. This would yield a major boost in crystallography, medical sciences or industrial radiography, both uncovering new secrets of physics and delivering practical applications to the society.



Additional results

In the appendices we are going to review a couple of additional peculiar observations during some of the experimental campaigns.

A.1 Plasma lensing

While running the experiments in the shocked nozzle+supersonic nozzle configuration (section 4.2.2), it has been noticed that adding a second gas jet would not only post-accelerate the electrons, but also pretty much always increase the beam divergence. On the other hand, it is commonly known that a second gas jet may also be used to focus or collimate particle bunches via laser-plasma lensing (Lehe, Thaury, Guillaume, Lifschitz, & Malka, 2014) (Thaury et al., 2014). To observe such lensing the second jet needs to be placed far enough so that a correlation between particle transverse position and propagation angle could develop. Nevertheless, no evidence of this effect has been observed during the entire longitudinal scan at $P_{back,1} = 15$ bar as described in section 4.2.2, and similarly there was no indication of lensing at $P_{back,1} = 20 - 40$ bar, which roughly imply proportionally scaled peak densities. Figure A.1a shows an electron beam obtained from a different shocked nozzle unit used alone with a nitrogen backing pressure $P_{back,1} = 10$ bar, yielding a thinner spiked profile with peak plasma density of 10^{20} cm^{-3} and $30 \mu\text{m}$ FWHM. The beam is estimated to contain between 242 and 727 fC/shot with 6.7% standard deviation for 500 ms camera exposures. The average FWHM divergence is 40 mrad in the horizontal direction and 66 mrad vertically. With the magnetic spectrometer added in the beam path, all the particles would be deviated from the screen, implying energies lying between 120 keV (aluminium stopping threshold) and 400 keV. A supersonic gas jet is then supplied with nitrogen at $P_{back,2} = 8$ bar, and its tip is brought to a point $180 \mu\text{m}$ away from the optical axis, implying a standalone Gaussian plasma profile with $\approx 2 - 3 \times 10^{19} \text{ cm}^{-3}$ peak plasma density and $150 \mu\text{m}$ FWHM. Figure A.1b shows the electron beam profile when the second nozzle was placed so that the jet symmetry axis would be a distance of $270 \mu\text{m}$ away from the shock symmetry axis. The detected charge is now estimated between 205 and 614 fC/shot with 7.2% standard deviation at 200 ms exposures. All the particles would still get completely deviated by the magnets, thus the relevant energies remain below 400 keV. Overall the beam parameters seem to reproduce well the previous case, except the average divergence is now reduced to 24 mrad horizontally and 39 mrad vertically.

The pointing stability for the two particle beams is excellent (< 1 mrad st. dev.), hence despite the lower exposure time for the second case, this measurement indicates the capability of our single-cycle pulses to drive a plasma lens in the second gas jet. However, we also conclude the current configuration to be very limited. Only slightly thicker or more dense shocked plasma profile would most likely deplete/disperse the driver pulse too much, so that it would no longer be able to create a strong enough focusing wake. In addition, only sub-400 keV electrons experienced a noticeable reduction in divergence, and reproducing the effect for relativistic beams would be more difficult. Finally, as it is known that for plasma lensing one requires to allow some free-space bunch propagation before entering the lens, our configuration becomes disadvantaged due to the tight focusing used. Laser pulses containing more energy or a double-pulse laser-plasma lens (Lehe et al., 2014) may turn out to be significantly more efficient for the purpose.

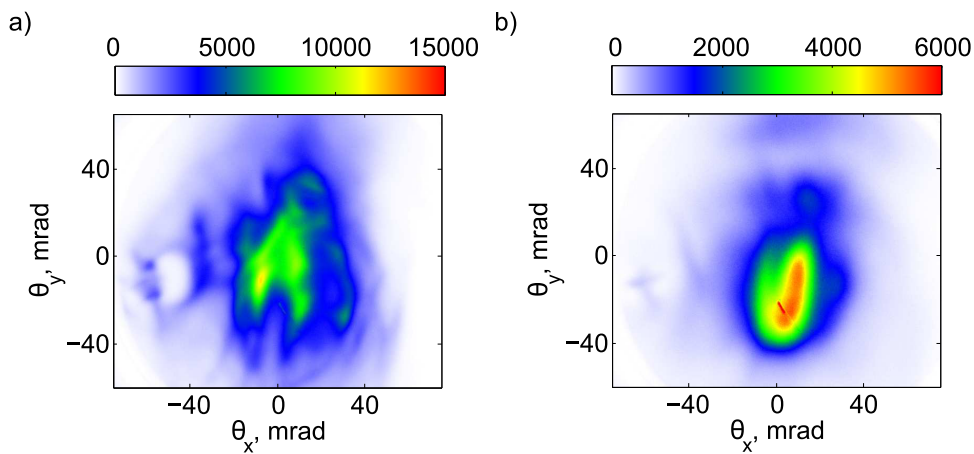


Figure A.1 – Evidence for laser-plasma lensing of sub-400 keV electron beams. a) particle spot obtained with the laser focused into the shocked nozzle spike. Detected charge is estimated between 242 and 727 fC/shot, average divergence amounts to 40×66 mrad at 500 ms image exposures. b) particle spot obtained with a second jet inserted into the beam path. Charge is estimated between 205 and 614 fC/shot, average divergence – 24×39 mrad at 200 ms exposures. Beam pointing is < 1 mrad st. dev. in both cases.

A.2 Observation of electron rings

In addition to usual relativistic particle beams distributed around the optical axis, occurrences of surrounding ring-like structures have also been reported by the community (Pollock et al., 2015). Simulations have suggested that this may happen due to a combination of several effects. Initially, beam loading by a high-charge bunch injected in the first wakefield cavity could lead to splitting of the electron sheath at its back and formation of a cylindrically symmetric "pocket" close to the edges of the second cavity. Then, as the laser pulse self-focuses forcing transition from weakly to strongly nonlinear regime, the first bubble expands, shifting the preceding defocusing region towards the space occupied by the second bunch. This defocusing may then push some of the second-bunch electrons into the "pocket", which in its own right shapes a ring of relativistic electrons.

Such ring-like structures have so far been observed only in cm-length accelerators delivering particles at a few hundred MeV. However, we have also occasionally spotted similar patterns in beam profile images obtained for our scaled-down few-MeV-class system. Figure A.3

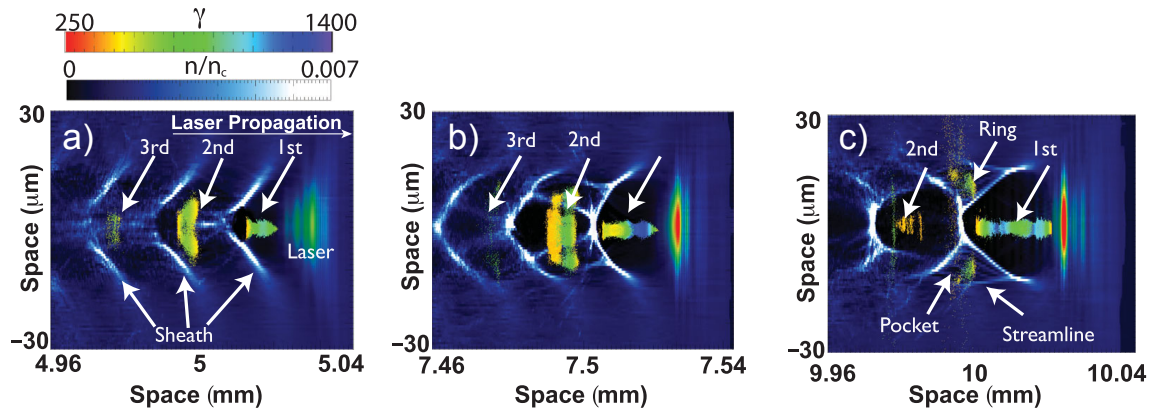


Figure A.2 – Electron density maps from a computer simulation presented in (Pollock et al., 2015), illustrating the formation of cavity "pockets", where electron rings may be shaped and accelerated. Chronological evolution from a) to c).

shows several sample pictures taken in single-shot regime where electron rings could be seen surrounding the main central spot. All of the images were taken with the driver focused in an $f/2$ configuration into a supersonic gas jet providing a Gaussian plasma profile with $1.4 \times 10^{20} \text{ cm}^{-3}$ peak density and $65 \mu\text{m}$ waist. The laser parameters were as described in section 4.3.1, and the pulse was either optimally compressed, or very close to optimal compression (chirped by -4 to $+8 \text{ fs}^2$). The rings have a typical divergence angle of $80 - 100 \text{ mrad}$. While taking a series of single-shot images, these structures would not be present each time, however, they could be seen often enough to confidently claim this feature is not completely accidental. Out of a set of 40 sequential snapshots (CCD data saving rate was around $1 - 2 \text{ Hz}$) traces of such ring-like patterns were observed $5 - 7$ times for a -4 fs^2 chirped driver, $10 - 15$ times for an optimally compressed case, $13 - 18$ times for a pulse chirped by $+4 \text{ fs}^2$, followed by $1 - 2$ occurrences for $+8 \text{ fs}^2$ driver. In most pictures only a small part of the electron circle may be seen, the rest of the beam pattern being fairly chaotic, hence the uncertainty in the given count numbers. The images presented in Figure A.3 are the ones with clearest features. It has been proposed that ring-shaped electron beams could be useful for driving positron plasma wakefield accelerators (Jain, Antonsen Jr., & Palastro, 2015).

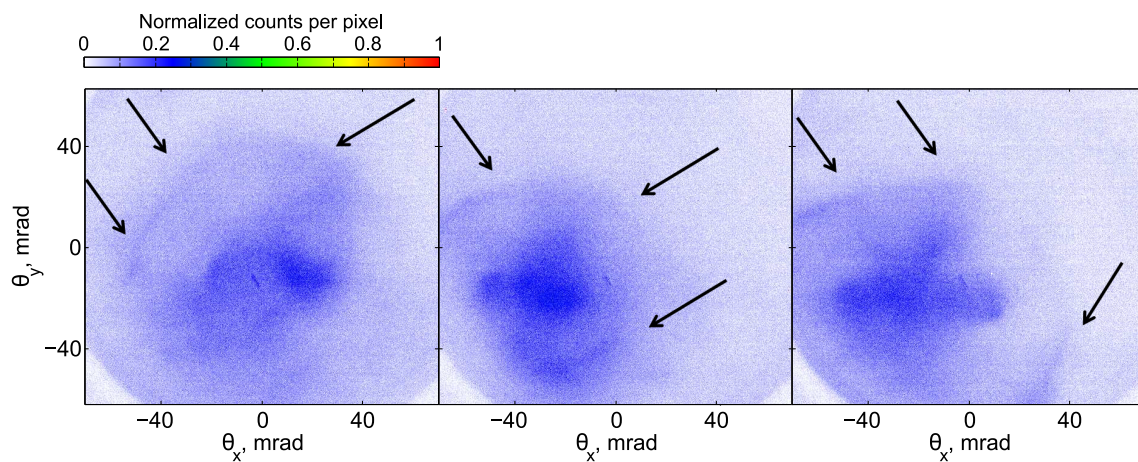


Figure A.3 – Relativistic electron beam profiles showing clearest surrounding ring-like structures (black arrows).

Bibliography

- Adli, E., Ahuja, A., Apsimon, O., Apsimon, R., Bachmann, A.-M., Barrientos, D., . . . Xia, G. (2018). Acceleration of electrons in the plasma wakefield of a proton bunch. *Nature*, *561*, 363–367. (Cited on pages 23 and 29).
- Amiranoff, F., Baton, S., Bernard, D., Cros, B., Descamps, D., Dorchie, F., . . . Najmudin, Z. (1998). Observation of laser wakefield acceleration of electrons. *Phys. Rev. Lett.* *81*, 995. (Cited on page 23).
- ATLAS Collaboration. (2012). Observation of a new particle in the search for the Standard Model Higgs boson with the ATLAS detector at the LHC. *Phys. Lett. B*, *716*, 1–29. (Cited on page 6).
- Baum, P. (2013). On the physics of ultrashort single-electron pulses for time-resolved microscopy and diffraction. *Chem. Phys.* *423*, 55–61. (Cited on page 44).
- Beaurepaire, B., Lifschitz, A., & Faure, J. (2014). Electron acceleration in sub-relativistic wakefields driven by few-cycle laser pulses. *New J. Phys.* *16*, 023023. (Cited on pages 26 and 88).
- Beaurepaire, B., Vernier, A., Bocoum, M., Böhle, F., Jullien, A., Rousseau, J.-P., . . . Faure, J. (2015). Effect of the laser wave front in a laser-plasma accelerator. *Phys. Rev. X*, *5*, 031012. (Cited on pages 66 and 76).
- Ben-Ismaïl, A., Lundh, O., Rechatin, C., Lim, J. K., Faure, J., Corde, S., & Malka, V. (2011). Compact and high-quality gamma-ray source applied to 10 μm -range resolution radiography. *Appl. Phys. Lett.* *98*, 264101. (Cited on page 45).
- Böhle, F., Kretschmar, M., Jullien, A., Kovacs, M., Miranda, M., Romero, R., . . . Nagy, T. (2014). Compression of CEP-stable multi-mJ laser pulses down to 4 fs in long hollow fibers. *Laser Phys. Lett.* *11*(9), 095401. (Cited on pages 7 and 46).
- Boot, H. A. H., & Harvie, R. B. R.-S. (1957). Charged particles in a non-uniform radio-frequency field. *Nature*, *180*(4596), 1187. (Cited on page 10).
- Bragg, W. H. (1913). The structure of some crystals as indicated by their diffraction of x-rays. *Proc. R. Soc. Lond. A*, *89*, 248–277. (Cited on page 5).
- Buck, A., Wenz, J., Xu, J., Khrennikov, K., Schmid, K., Heigoldt, M., . . . Veisz, L. (2013). Shock-front injector for high-quality laser-plasma acceleration. *Phys. Rev. Lett.* *110*, 185006. (Cited on page 26).
- Buck, A., Nicolai, M., Schmid, K., Sears, C. M. S., Savert, A., Mikhailova, J. M., . . . Veisz, L. (2011). Real-time observation of laser-driven electron acceleration. *Nat. Phys.* *7*(7), 543–548. (Cited on page 12).
- Budriūnas, R., Stanislauskas, T., Adamonis, J., Aleknavičius, A., Veitas, G., Gadonas, D., . . . Varanavičius, A. (2017). 53 W average power CEP-stabilized OPCPA system delivering 5.5 TW few cycle pulses at 1 kHz repetition rate. *Opt. Express*, *25*(5), 5797–5806. (Cited on page 105).
- Bulanov, S. V., Inovenkov, I. N., Kirsanov, V. I., Naumova, N. M., & Sakharov, A. S. (1992). Nonlinear depletion of ultrashort and relativistically strong laser pulses in an underdense plasma. *Phys. Fluids*, *4*, 1935. (Cited on page 28).
- Bulanov, S. V., Pegoraro, F., Pukhov, A. M., & Sakharov, A. S. (1997). Transverse-wake wave breaking. *Phys. Rev. Lett.* *78*(22), 4205–4208. (Cited on page 23).
- Bulanov, S., Naumova, N., Pegoraro, F., & Sakai, J. (1998). Particle injection into the wave acceleration phase due to nonlinear wake wave breaking. *Phys. Rev. E*, *58*(5), R5257–R5260. (Cited on pages 23 and 26).

- Chanteloup, J.-C. (2005). Multiple-wave lateral shearing interferometry for wave-front sensing. *Appl. Opt.* 44, 1559–1571. (Cited on page 58).
- Chen, M., Esarey, E., Geddes, C. G. R., Cormier-Michel, E., Schroeder, C. B., Bulanov, S. S., . . . Leemans, W. P. (2014). Electron injection and emittance control by transverse colliding pulses in a laser-plasma accelerator. *Phys. Rev. ST Accel. Beams*, 17, 051303. (Cited on page 27).
- Chessa, P., Wispelaere, E. D., Dorchie, F., Malka, V., Marquès, J.-R., Hamoniaux, G., . . . Amiranoff, F. (1999). Temporal and angular resolution of the ionization-induced refraction of a short laser pulse in a helium gas. *Phys. Rev. Lett.* 82(3), 552–555. (Cited on page 34).
- Cockcroft, J. D., & Walton, E. T. S. (1932). Disintegration of lithium by swift protons. *Nature*, 129(3261), 649. (Cited on page 6).
- Corde, S., Ta Phuoc, K., Lambert, G., Fitour, R., Malka, V., & Rousse, A. (2013). Femtosecond x-rays from laser-plasma accelerators. *Rev. Mod. Phys.* 85, 0034–6861. (Cited on page 13).
- Corde, S., Thaur, C., Lifschitz, A., Lambert, G., Ta Phuoc, K., Davoine, X., . . . Malka, V. (2013). Observation of longitudinal and transverse self-injections in laser-plasma accelerators. *Nat. Commun.* 4, 1501. (Cited on page 23).
- Crookes, W. (1879). On the illumination of lines of molecular pressure, and the trajectory of molecules. *Phil. Trans. R. Soc. Lond.* 170, 135–164. (Cited on page 5).
- Dawson, J. M. (1959). Nonlinear electron oscillations in a cold plasma. *Phys. Rev.* 113, 383–387. (Cited on page 13).
- Dawson, J. M. (1983). Particle simulation of plasmas. *Rev. Mod. Phys.* 55(2), 403–447. (Cited on pages 21 and 62).
- Delone, N. B., & Krainov, V. P. (1998). Tunneling and barrier-suppression ionization of atoms and ions in a laser radiation field. *Phys. Usp.* 41(5), 469–485. (Cited on pages 24 and 73).
- Doche, A., Beekman, C., Corde, S., Allen, J. M., Clarke, C. I., Frederico, J., . . . Lu, W. (2017). Acceleration of a trailing positron bunch in a plasma wakefield accelerator. *Sci. Rep.* 7, 14180. (Cited on page 23).
- Döpp, A., Hehn, L., Götzfried, J., Wenz, J., Gilljohann, M., Ding, H., . . . Karsch, S. (2018). Quick X-ray microtomography using a laser-driven betatron source. *Optica*, 5(2), 199–203. (Cited on page 45).
- Emma, P., Akre, R., Arthur, J., Bionta, R., Bostedt, C., Bozek, J., . . . Galayda, J. (2010). First lasing and operation of an ångström-wavelength free-electron laser. *Nat. Photon.* 4, 641–647. (Cited on page 6).
- Esarey, E., Hubbard, R. F., Leemans, W. P., Ting, A., & Sprangle, P. (1997). Electron injection into plasma wake fields by colliding laser pulses. *Phys. Rev. Lett.* 79, 2682. (Cited on page 24).
- Esarey, E., Sprangle, P., Krall, J., & Ting, A. (1996). Overview of plasma-based accelerator concepts. *IEEE Trans. Plasma Sci.* 24(2), 252–288. (Cited on page 28).
- Everett, M., Lal, A., Gordon, D., Clayton, C., Marsh, K., & Joshi, C. (1994). Trapped electron acceleration by a laser-driven relativistic plasma wave. *Nature*, 368, 527–529. (Cited on page 23).
- Faure, J. (2014). Plasma injection schemes for laser-plasma accelerators. In *Proceedings of the CAS-CERN accelerator school: Plasma Wake Acceleration, Geneva, Switzerland* (Pages 143–157). (Cited on page 24).
- Faure, J., Glinec, Y., Pukhov, A., Kiselev, S., Gordienko, S., Lefebvre, E., . . . Malka, V. (2004). A laser-plasma accelerator producing monoenergetic electron beams. *Nature*, 431, 541–544. (Cited on pages 6, 12 and 22).
- Faure, J., Glinec, Y., Santos, J. J., Ewald, F., Rousseau, J.-P., Kiselev, S., . . . Malka, V. (2005). Observation of laser pulse shortening in nonlinear plasma waves. *Phys. Rev. Lett.* 95, 205003. (Cited on page 35).
- Faure, J., Rechatin, C., Lundh, O., Ammoura, L., & Malka, V. (2010). Injection and acceleration of quasimonoenergetic relativistic electron beams using density gradients at the edges of a plasma channel. *Phys. Plasmas*, 17(8), -. doi:<http://dx.doi.org/10.1063/1.3469581>. (Cited on page 26)

- Faure, J., Rechatin, C., Norlin, A., Lifschitz, A., Glinec, Y., & Malka, V. (2006). Controlled injection and acceleration of electrons in plasma wakefields by colliding laser pulses. *Nature*, *444*, 737–739. (Cited on page 24).
- Faure, J., van der Geer, B., Beaurepaire, B., Gallé, G., Vernier, A., & Lifschitz, A. (2016). Concept of a laser-plasma-based electron source for sub-10-fs electron diffraction. *Phys. Rev. Accel. Beams*, *19*, 021302. (Cited on page 104).
- Fourcade Dutin, C., Dubrouil, A., Petit, S., Mével, E., Constant, E., & Descamps, D. (2010). Post-compression of high-energy femtosecond pulses using gas ionization. *Opt. Lett.* *35*(2), 253–255. (Cited on page 35).
- Fubiani, G., Esarey, E., Schroeder, C., & Leemans, W. (2004). Beatwave injection of electrons into plasma waves using two interfering laser pulses. *Phys. Rev. E*, *70*, 016402. (Cited on page 24).
- Geddes, C. G. R., Nakamura, K., Plateau, G. R., Tóth, C., Cormier-Michel, E., Esarey, E., . . . Leemans, W. P. (2008). Plasma-density-gradient injection of low absolute-momentum-spread electron bunches. *Phys. Rev. Lett.* *100*, 215004. (Cited on page 26).
- Geddes, C. G. R., Tóth, C., van Tilborg, J., Esarey, E., Schroeder, C. B., Bruhwiler, D., . . . Leemans, W. P. (2004). High quality electron beams from a laser wakefield accelerator using plasma-channel guiding. *Nature*, *431*, 538–541. (Cited on pages 6, 12 and 22).
- Gliserin, A., Walbran, M., Krausz, F., & Baum, P. (2015). Sub-phonon-period compression of electron pulses for atomic diffraction. *Nat. Commun.* *6*, 8723. (Cited on page 44).
- Goldstein, E. (1876). Vorläufige Mittheilungen über elektrische Entladungen in verdünnten Gasen. *Monatsberichte der Königlich Preussischen Akademie der Wissenschaften zu Berlin, Mai*, 279–295. (Cited on page 5).
- Gonsalves, A. J., Nakamura, K., Lin, C., Panasenkov, D., Shiraishi, S., Sokollik, T., . . . Leemans, W. P. (2011). Tunable laser plasma accelerator based on longitudinal density tailoring. *Nat. Phys.* *7*, 862–866. (Cited on page 26).
- Gorbunov, L. M., & Kirsanov, V. I. (1987). Excitation of plasma waves by an electromagnetic wave packet. *Sov. Phys. JETP*, *66*, 290–294. (Cited on page 18).
- Griffiths, D. J. (2008). *Introduction to electrodynamics* (3rd). Pearson. (Cited on page 15).
- Gschwendtner, E., Adli, E., Amorim, L., Apsimon, R., Assmann, R., Bachmann, A.-M., . . . Zhang, H. (2016). AWAKE, the advanced proton driven plasma wakefield acceleration experiment at CERN. *Nucl. Instr. Meth. Phys. Res. A*, *829*, 76–82. (Cited on page 23).
- Guillaume, E., Döpp, A., Thaur, C., Lifschitz, A., Goddet, J.-P., Tafzi, A., . . . Malka, V. (2015). Physics of fully-loaded laser-plasma accelerators. *Phys. Rev. ST Accel. Beams*, *18*, 061301. (Cited on page 29).
- Guillaume, E., Döpp, A., Thaur, C., Ta Phuoc, K., Lifschitz, A., Grittani, G., . . . Malka, V. (2015). Electron rephasing in a laser-wakefield accelerator. *Phys. Rev. Lett.* *115*, 155002. (Cited on page 29).
- Hansson, M., Senje, L., Persson, A., Lundh, O., Wahlström, C.-G., Desforges, F. G., . . . Monot, P. (2014). Enhanced stability of laser wakefield acceleration using dielectric capillary tubes. *Phys. Rev. ST Accel. Beams*, *17*, 031303. (Cited on page 103).
- He, Z.-H., Hou, B., Lebailly, V., Nees, J. A., Krushelnick, K., & Thomas, A. G. R. (2015). Coherent control of plasma dynamics. *Nat. Comm.* *6*. (Cited on pages 45 and 103).
- He, Z.-H., Hou, B., Easter, J. H., Faure, J., Krushelnick, K., Nees, J. A., & Thomas, A. G. R. (2013). High repetition-rate wakefield electron source generated by few-millijoule, 30 femtosecond laser pulses on a density downramp. *New J. Phys.* *15*, 053016. (Cited on page 76).
- He, Z.-H., Nees, J. A., Hou, B., Krushelnick, K., & Thomas, A. G. R. (2014). Ionization-induced self-compression of tightly focused femtosecond laser pulses. *Phys. Rev. Lett.* *113*, 263904. (Cited on page 35).
- He, Z.-H., Beaurepaire, B., Nees, J. A., Gallé, G., Scott, S. A., Pérez, J. R. S., . . . Faure, J. (2016). Capturing structural dynamics in crystalline silicon using chirped electrons from a laser wakefield accelerator. *Sci. Rep.* *6*, 36224. (Cited on page 36).

- Hidding, B., Karger, O., Königstein, T., Pretzler, G., Manahan, G. G., McKenna, P., . . . Daly, E. (2017). Laser-plasma-based space radiation reproduction in the laboratory. *Sci. Rep.* 7, 42354. (Cited on page 45).
- Holzwarth, R., Udem, T., Hänsch, T. W., Knight, J. C., Wadsworth, W. J., & Russell, P. S. J. (2000). Optical frequency synthesizer for precision spectroscopy. *Phys. Rev. Lett.* 85, 2264–2267. (Cited on page 51).
- Jain, N., Antonsen Jr., T. M., & Palastro, J. P. (2015). Positron acceleration by plasma wakefields driven by a hollow electron beam. *Phys. Rev. Lett.* 115, 195001. (Cited on page 109).
- Jones, D. J., Diddams, S. A., Ranka, J. K., Stentz, A., Windeler, R. S., Hall, J. L., & Cundiff, S. T. (2000). Carrier-envelope phase control of femtosecond mode-locked lasers and direct optical frequency synthesis. *Science*, 288, 635–639. (Cited on page 51).
- Kalmykov, S., Yi, S. A., Khudik, V., & Shvets, G. (2009). Electron self-injection and trapping into an evolving plasma bubble. *Phys. Rev. Lett.* 103, 135004. (Cited on page 27).
- Katsouleas, T., & Mori, W. B. (1988). Wave-breaking amplitude of relativistic oscillations in a thermal plasma. *Phys. Rev. Lett.* 61(1), 90–93. (Cited on page 23).
- Kealhofer, C., Schneider, W., Ehberger, D., Ryabov, A., Krausz, F., & Baum, P. (2016). All-optical control and metrology of electron pulses. *Science*, 352, 429–433. (Cited on pages 37 and 44).
- Kim, H. T., Pathak, V. B., Pae, K. H., Lifschitz, A., Sylla, F., Shin, J. H., . . . Nam, C. H. (2017). Stable multi-gev electron accelerator driven by waveform-controlled PW laser pulses. *Sci. Rep.* 7, 10203. (Cited on page 70).
- Kostyukov, I., Nerush, E., Pukhov, A., & Sereedov, V. (2009). Electron self-injection in multidimensional relativistic-plasma wake fields. *Phys. Rev. Lett.* 103, 175003. (Cited on page 23).
- Landgraf, B., Schnell, M., Sävert, A., Kaluza, M. C., & Spielmann, C. (2011). High resolution 3D gas-jet characterization. *Rev. Sci. Instrum.* 82, 083106. (Cited on page 57).
- Leemans, W. P., Catravas, P., Esarey, E., Geddes, C. G. R., Tóth, C., Trines, R., . . . Faure, J. (2002). Electron-yield enhancement in a laser-wakefield accelerator driven by asymmetric laser pulses. *Phys. Rev. Lett.* 89(17), 174802. (Cited on page 6).
- Leemans, W. P., Nagler, B., Gonsalves, A. J., Tóth, C., Nakamura, K., Geddes, C. G. R., . . . Hooker, S. M. (2006). GeV electron beams from a centimetre-scale accelerator. *Nat. Phys.* 2, 696–699. (Cited on pages 6 and 22).
- Lehe, R., Lifschitz, A. F., Davoine, X., Thauray, C., & Malka, V. (2013). Optical transverse injection in laser-plasma acceleration. *Phys. Rev. Lett.* 111, 085005. (Cited on page 27).
- Lehe, R., Thauray, C., Guillaume, E., Lifschitz, A., & Malka, V. (2014). Laser-plasma lens for laser-wakefield accelerators. *Phys. Rev. ST Accel. Beams*, 17, 121301. (Cited on pages 107 and 108).
- Li, F., Hua, J. F., Xu, X. L., Zhang, C. J., Yan, L. X., Du, Y. C., . . . Gu, Y. Q. (2013). Generating high-brightness electron beams via ionization injection by transverse colliding lasers in a plasma-wakefield accelerator. *Phys. Rev. Lett.* 111, 015003. (Cited on page 27).
- Lifschitz, A. F., & Malka, V. (2012). Optical phase effects in electron wakefield acceleration using few-cycle laser pulses. *New J. Phys.* 14(5), 053045. (Cited on pages 98 and 100).
- Lifschitz, A., Davoine, X., Lefebvre, E., Faure, J., Rechatin, C., & Malka, V. (2009). Particle-in-cell modelling of laser-plasma interaction using Fourier decomposition. *J. Comp. Phys.* 228, 1803–1814. (Cited on pages 21 and 63).
- Litos, M., Adli, E., An, W., Clarke, C. I., Clayton, C. E., Corde, S., . . . Yocky, G. (2014). High-efficiency acceleration of an electron beam in a plasma wakefield accelerator. *Nature*, 515, 92–95. (Cited on pages 23 and 29).
- Lu, W., Tzoufras, M., Joshi, C., Tsung, F. S., Mori, W. B., Vieira, J., . . . Silva, L. O. (2007). Generating multi-GeV electron bunches using single stage laser wakefield acceleration in a 3D nonlinear regime. *Phys. Rev. ST Accel. Beams*, 10(6), 061301. (Cited on pages 22, 28, 29, 31, 46, 103 and 104).

- Lundh, O., Lim, J., Rechatin, C., Ammoura, L., Ben-Ismaïl, A., Davoine, X., . . . Faure, J. (2011). Few femtosecond, few kiloampere electron bunch produced by a laser-plasma accelerator. *Nat. Phys.* 7, 219–222. (Cited on pages 7, 37 and 44).
- Lundh, O., Rechatin, C., Lim, J., Malka, V., & Faure, J. (2013). Experimental measurements of electron-bunch trains in a laser-plasma accelerator. *Phys. Rev. Lett.* 110, 065005. (Cited on page 29).
- Malka, V., Faure, J., Gauduel, Y. A., Lefebvre, E., Rousse, A., & Ta Phuoc, K. (2008). Principles and applications of compact laser-plasma accelerators. *Nature Physics*, 44, 447–453. (Cited on page 45).
- Malka, V., Fritzler, S., Lefebvre, E., Aléonard, M.-M., Burgy, F., Chambaret, J.-P., . . . Dangor, A. E. (2002). Electron acceleration by a wake field forced by an intense ultrashort laser pulse. *Science*, 298, 1596–1600. (Cited on page 6).
- Mangles, S. P. D., Genoud, G., Bloom, M. S., Burza, M., Najmudin, Z., Persson, A., . . . Wahlström, C.-G. (2012). Self-injection threshold in self-guided laser wakefield accelerators. *Phys. Rev. ST Accel. Beams*, 15, 011302. (Cited on page 23).
- Mangles, S. P. D., Murphy, C. D., Najmudin, Z., Thomas, A. G. R., Collier, J. L., Dangor, A. E., . . . Krushelnick, K. (2004). Monoenergetic beams of relativistic electrons from intense laser-plasma interactions. *Nature*, 431, 535–538. (Cited on pages 6, 12 and 22).
- Massimo, F., Lifschitz, A. F., Thauray, C., & Malka, V. (2017). Numerical studies of density transition injection in laser wakefield acceleration. *Plasma Phys. Control. Fusion*, 59, 085004. (Cited on page 29).
- Matlis, N. H., Reed, S., Bulanov, S. S., Chvykov, V., Kalintchenko, G., Matsuoka, T., . . . Downer, M. C. (2006). Snapshots of laser wakefields. *Nat. Phys.* 2, 749–753. (Cited on page 12).
- Maxson, J., Cesar, D., Calmasini, G., Ody, A., & Musumeci, P. (2017). Direct measurement of sub-10 fs relativistic electron beams with ultralow emittance. *Phys. Rev. Lett.* 118, 154802. (Cited on pages 37 and 45).
- McGuffey, C., Thomas, A. G. R., Schumaker, W., Matsuoka, T., Chvykov, V., Dollar, F. J., . . . Karpeev, A. V. (2010). Ionization induced trapping in a laser wakefield accelerator. *Phys. Rev. Lett.* 104, 025004. (Cited on page 25).
- McMillan, E. M. (1945). The synchrotron - a proposed high energy particle accelerator. *Phys. Rev.* 68, 143–144. (Cited on page 6).
- Meyerhofer, D. D., Knauer, J. P., McNaught, S. J., & Moore, C. I. (1996). Observation of relativistic mass shift effects during high-intensity laser-electron interactions. *J. Opt. Soc. Am. B*, 13(1), 113–117. (Cited on page 10).
- Miranda, M., Arnold, C. L., Fordell, T., Silva, F., Alonso, B., Weigand, R., . . . Crespo, H. (2012). Characterization of broadband few-cycle laser pulses with the d-scan technique. *Opt. Express*, 20(17), 18732–18743. (Cited on pages 47 and 48).
- Modena, A., Najmudin, Z., Dangor, A., Clayton, C., Marsh, K., Joshi, C., . . . Walsh, F. (1995). Electron acceleration from the breaking of electron plasma waves. *Nature*, 377, 606–608. (Cited on pages 6 and 95).
- Mollica, F. (2016). *Ultra-intense laser-plasma interaction at near-critical density for ion acceleration* (Doctoral dissertation, Université Paris-Saclay, École Polytechnique). (Cited on page 41).
- Monot, P., Auguste, T., Gibbon, P., Jakober, F., Mainfray, G., Duluieu, A., . . . Miquel, J. L. (1995). Experimental demonstration of relativistic self-channeling of a multiterawatt laser pulse in an underdense plasma. *Phys. Rev. Lett.* 74(15), 2953–2956. (Cited on page 31).
- Mora, P., & Antonsen, T. M., Jr. (1997). Kinetic modeling of intense, short laser pulses propagating in tenuous plasmas. *Phys. Plasmas*, 4(1), 217–229. (Cited on page 17).
- Musumeci, P., Moody, J. T., Soby, C. M., Gutierrez, M. S., & Westfall, M. (2010). Laser-induced melting of a single crystal gold sample by time-resolved ultrafast relativistic electron diffraction. *Appl. Phys. Lett.* 97(6), 063502. (Cited on pages 37 and 45).

- Nakajima, K., Fisher, D., Kawakubo, T., Nakanishi, H., Ogata, A., Kato, Y., . . . Tajima, T. (1995). Observation of ultrahigh gradient electron acceleration by a self-modulated intense short laser pulse. *Phys. Rev. Lett.* 74(22), 4428–4431. (Cited on page 6).
- Nisoli, M., De Silvestri, S., Svelto, O., Szipöcs, R., Ferencz, K., Spielmann, C., . . . Krausz, F. (1997). Compression of high-energy laser pulses below 5 fs. *Opt. Lett.* 22, 522–524. (Cited on page 46).
- Nuter, R., Gremillet, L., Lefebvre, E., Lévy, A., Ceccotti, T., & Martin, P. (2011). Field ionization model implemented in Particle In Cell code and applied to laser-accelerated carbon ions. *Phys. Plasmas*, 18, 033107. (Cited on page 63).
- Osterhoff, J., Popp, A., Major, Z., Marx, B., Rowlands-Rees, T. P., Fuchs, M., . . . Karsch, S. (2008). Generation of stable, low-divergence electron beams by laser-wakefield acceleration in a steady-state-flow gas cell. *Phys. Rev. Lett.* 101(8), 085002. doi:10.1103/PhysRevLett.101.085002. (Cited on page 103)
- Pak, A., Marsh, K. A., Martins, S. F., Lu, W., Mori, W. B., & Joshi, C. (2010). Injection and trapping of tunnel-ionized electrons into laser-produced wakes. *Phys. Rev. Lett.* 104, 025003. (Cited on page 25).
- Pollock, B. B., Clayton, C. E., Ralph, J. E., Albert, F., Davidson, A., Divol, L., . . . Froula, D. H. (2011). Demonstration of a narrow energy spread, ~0.5 GeV electron beam from a two-stage laser wakefield accelerator. *Phys. Rev. Lett.* 107, 045001. (Cited on page 25).
- Pollock, B. B., Tsung, F. S., Albert, F., Shaw, J. L., Clayton, C. E., Davidson, A., . . . Joshi, C. (2015). Formation of ultrarelativistic electron rings from a laser-wakefield accelerator. *Phys. Rev. Lett.* 115, 055004. (Cited on pages 108 and 109).
- Pukhov, A., & Meyer-ter-Vehn, J. (2002). Laser wake field acceleration: the highly non-linear broken-wave regime. *Appl. Phys. B*, 74, 355–361. (Cited on pages 22 and 29).
- Quesnel, B., & Mora, P. (1998). Theory and simulation of the interaction of ultra-intense laser pulses with electrons in vacuum. *Phys. Rev. E*, 58, 3719. (Cited on page 11).
- Rae, S. C. (1993). Ionization-induced defocusing of intense laser-pulses in high-pressure gases. *Opt. Comm.* 97(1), 25–28. (Cited on page 34).
- Rax, J.-M. (2005). *Physique des plasmas*. Dunod. (Cited on page 10).
- Rechatin, C., Davoine, X., Lifschitz, A., Ismail, A. B., Lim, J., Lefebvre, E., . . . Malka, V. (2009). Observation of beam loading in a laser-plasma accelerator. *Phys. Rev. Lett.* 103, 194804. (Cited on page 29).
- Röntgen, W. C. (1896). On a new kind of rays. *Nature*, 53(1369), 274–276. (Cited on page 5).
- Rouaud, M. (2013). *Probability, statistics and estimation*. Lulu Press, Inc. (Cited on page 85).
- Salehi, F., Goers, A. J., Hine, G. A., Feder, L., Kuk, D., Miao, B., . . . Milchberg, H. M. (2017). MeV electron acceleration at 1kHz with < 10mj laser pulses. *Opt. Lett.* 42(2), 215–218. (Cited on page 95).
- Schmid, K., & Veisz, L. (2012). Supersonic gas jets for laser-plasma experiments. *Rev. Sci. Instrum.* 83, 053304. (Cited on page 40).
- Schmid, K., Veisz, L., Tavella, F., Benavides, S., Tautz, R., Herrmann, D., . . . Krausz, F. (2009). Few-cycle laser-driven electron acceleration. *Phys. Rev. Lett.* 102, 124801. (Cited on page 91).
- Sciaini, G., & Miller, R. J. D. (2011). Femtosecond electron diffraction: heralding the era of atomically resolved dynamics. *Rep. Prog. Phys.* 74(9), 096101. (Cited on pages 7 and 44).
- Semushin, S., & Malka, V. (2001). High density gas jet nozzle design for laser target production. *Rev. Sci. Instrum.* 72, 2961–2965. (Cited on page 57).
- Sprangle, P., Tang, C.-H., & Esarey, E. (1987). Relativistic self-focusing of short-pulse radiation beams in plasmas. *IEEE Trans. Plasma Sci.* PS-15(2), 145–153. (Cited on page 31).
- Strickland, D., & Mourou, G. (1985). Compression of amplified chirped optical pulses. *Opt. Comm.* 56, 219–221. (Cited on page 6).
- Suk, H., Barov, N., Rosenzweig, J. B., & Esarey, E. (2001). Plasma electron trapping and acceleration in a plasma wake field using a density transition. *Phys. Rev. Lett.* 86(6), 1011–1014. (Cited on page 26).

- Tajima, T., & Dawson, J. M. (1979). Laser electron accelerator. *Phys. Rev. Lett.* 43(4), 267–270. (Cited on page 6).
- Thaury, C., Guillaume, E., Döpp, A., Lehe, R., Lifschitz, A., Ta Phuoc, K., . . . Malka, V. (2014). Demonstration of relativistic electron beam focusing by a laser-plasma lens. *Nat. Commun.* 6, 6860. (Cited on page 107).
- Thaury, C., Guillaume, E., Lifschitz, A., Ta Phuoc, K., Hansson, M., Grittani, G., . . . Malka, V. (2015). Shock assisted ionization injection in laser-plasma accelerators. *Sci. Rep.* 5, 16310. (Cited on pages 27 and 57).
- Thomson, J. J. (1901). On bodies smaller than atoms. *The popular science monthly, August*, 323–335. (Cited on page 5).
- Tonks, L., & Langmuir, I. (1929). Oscillations in ionized gases. *Phys. Rev.* 33, 195–210. (Cited on page 12).
- Tsung, F. S., Lu, W., Tzoufras, M., Mori, W. B., Joshi, C., Vieira, J. M., . . . Fonseca, R. A. (2006). Simulation of monoenergetic electron generation via laser wakefield accelerators for 5-25 TW lasers. *Phys. Plasmas*, 13, 056708. (Cited on page 22).
- Umstadter, D., Kim, J.-K., & Dodd, E. (1996). Laser injection of ultrashort electron pulses into wakefield plasma waves. *Phys. Rev. Lett.* 76, 2073. (Cited on page 24).
- Van de Graaff, R. J., Compton, K. T., & Van Atta, L. C. (1933). The electrostatic production of high voltage for nuclear investigations. *Phys. Rev.* 43(3), 149–157. (Cited on page 6).
- van Oudheusden, T., Pasmans, P. L. E. M., van der Geer, S. B., de Loos, M. J., van der Wiel, M. J., & Luiten, O. J. (2010). Compression of subrelativistic space-charge-dominated electron bunches for single-shot femtosecond electron diffraction. *Phys. Rev. Lett.* 105, 264801. (Cited on page 45).
- Vargas, M., Schumaker, W., He, Z.-H., Zhao, Z., Behm, K., Chvykov, V., . . . Thomas, A. G. R. (2014). Improvements to laser wakefield accelerated electron beam stability, divergence, and energy spread using three-dimensional printed two-stage gas cell targets. *Appl. Phys. Lett.* 104, 174103. (Cited on pages 25 and 103).
- Wan, Y., Zhang, C. J., Li, F., Wu, J. F., Hua, J. F., Pai, C.-H., . . . Mori, W. B. (2016). Colliding ionization injection in a plasma wakefield accelerator. *Plasma Phys. Control Fusion*, 58, 034015. (Cited on page 27).
- Wangler, T. P. (1998). *RF linear accelerators* (1st). Wiley-VCH. (Cited on page 36).
- Watson, J. D., & Crick, F. H. C. (1953). Molecular structure of nucleic acids: a structure for deoxyribose nucleic acid. *Nature*, 171(4356), 737–738. (Cited on page 5).
- Watts, I., Zepf, M., Clark, E. L., Tatarakis, M., Krushelnick, K., Dangor, A. E., . . . Norreys, P. A. (2002). Measurements of relativistic self-phase-modulation in plasma. *Phys. Rev. E*, 66, 036409. (Cited on page 26).
- Widerøe, R. (1928). Über ein neues Prinzip zur Herstellung hoher Spannungen. *Archiv für Elektronik und Übertragungstechnik*, 21(4), 387–406. (Cited on page 6).
- Yablonovitch, E. (1974). Self-phase modulation of light in a laser-breakdown plasma. *Phys. Rev. Lett.* 32(20), 1101–1104. (Cited on page 35).
- Zucker, R. Z., & Biblarz, O. (2002). *Fundamentals of gas dynamics* (2nd). Wiley. (Cited on pages 39, 40, 58 and 60).

Publications

- *Relativistic electron beams driven by kHz single-cycle light pulses*; D. Guénot, D. Gustas, A. Vernier, B. Beaurepaire, F. Böhle, M. Bocoum, M. Lozano, A. Jullien, R. Lopez-Martens, A. Lifschitz and J. Faure; *Nat. Photonics* **11**, 293–296 (2017).
- *High-charge relativistic electron bunches from a kHz laser-plasma accelerator*; D. Gustas, D. Guénot, A. Vernier, S. Dutt, F. Böhle, R. Lopez-Martens, A. Lifschitz and J. Faure; *Phys. Rev. Accel. Beams* **21**, 013401 (2018).
- *A review of recent progress on laser-plasma acceleration at kHz repetition rate*; J. Faure, D. Gustas, D. Guénot, A. Vernier, F. Böhle, M. Ouillé, S. Haessler, R. Lopez-Martens and A. Lifschitz; *Plasma Phys. Control. Fusion* **61**, 014012 (2019).

Relativistic electron beams driven by kHz single-cycle light pulses

D. Guénot, D. Gustas, A. Vernier, B. Beaufrepaire, F. Böhle, M. Bocoum, M. Lozano, A. Jullien, R. Lopez-Martens, A. Lifschitz and J. Faure*

Laser-plasma acceleration^{1,2} is an emerging technique for accelerating electrons to high energies over very short distances. The accelerated electron bunches have femtosecond duration^{3,4}, making them particularly relevant for applications such as ultrafast imaging⁵ or femtosecond X-ray generation^{6,7}. Current laser-plasma accelerators deliver 100 MeV (refs 8–10) to GeV (refs 11, 12) electrons using Joule-class laser systems that are relatively large in scale and have low repetition rates, with a few shots per second at best. Nevertheless, extending laser-plasma acceleration to higher repetition rates would be extremely useful for applications requiring lower electron energy. Here, we use single-cycle laser pulses to drive high-quality MeV relativistic electron beams, thereby enabling kHz operation and dramatic downsizing of the laser system. Numerical simulations indicate that the electron bunches are only ~1 fs long. We anticipate that the advent of these kHz femtosecond relativistic electron sources will pave the way to applications with wide impact, such as ultrafast electron diffraction in materials^{13,14} with an unprecedented sub-10 fs resolution¹⁵.

In a laser-plasma accelerator, a laser pulse is focused to ultrahigh intensity in an underdense plasma. The laser ponderomotive force sets up a charge separation in the plasma by displacing electrons, resulting in excitation of a large-amplitude plasma wave, also known as a wakefield. The wakefield carries enormous electric fields, in excess of 100 GV m⁻¹ (ref. 16), that are well adapted for accelerating electrons to relativistic energies over short distances, typically less than a millimetre. The accelerated electron beams have femtosecond duration and are intrinsically synchronized to the laser pulse, which could lift the temporal resolution bottleneck in various experimental situations. For example, in ultrafast electron diffraction, the temporal resolution is currently limited to more than 100 fs, but it could be improved to sub-10 fs using laser-driven electrons¹⁵. Thus, laser-plasma accelerators in the MeV range could find numerous applications with unprecedented time resolution, provided they operate reliably and at a high repetition rate. Indeed, in addition to temporal resolution, ultrafast imaging and diffraction also require statistics and a high signal-to-noise ratio^{5,14} that can only be reached with a reliable and high-repetition-rate electron source.

In this Letter, we demonstrate the reliable operation of a laser-plasma accelerator delivering 5 MeV electrons at a kHz repetition rate, with charges reaching up to 1 pC. This breakthrough was made possible by the innovative use of a multi-mJ laser system delivering near-single-cycle laser pulses of 3.4 fs duration^{17,18} (see Methods). Compared to previous kHz work^{19,20}, we obtained an increase of the electron charge and energy by two orders of magnitude. In addition, this work confirms the scalability of laser wakefield acceleration to the mJ energy level, enabling

the use of box-sized and commercial laser systems for driving laser-plasma accelerators.

It is well established that the blowout, or bubble regime, of laser-plasma acceleration^{8–10,21,22} leads to the production of high-quality relativistic electron beams with narrow energy spreads and small divergence. In this regime, the laser pulse is transversely and longitudinally resonant with the plasma wavelength λ_p ; that is, its longitudinal and transverse sizes are comparable to λ_p : $c\tau \approx w_0 \approx \lambda_p/2$, where c is the speed of light, τ is the pulse duration, and w_0 is the laser beam waist. When this condition is met at high intensity, $I \in 10^{18}–10^{19}$ W cm⁻², this results in the excitation of a very nonlinear wakefield, which takes the form of successive ion cavities surrounded by thin sheets of electrons^{22,23}. Electrons are injected in the accelerating field at the back of the ion cavity, thereby forming a bunch with femtosecond duration³. In addition, the transverse fields of the cavity are focusing, which leads to a low-divergence electron beam.

Although this regime is routinely achieved in experiments using Joule-class laser systems with 30 fs laser pulses, scaling down to the mJ level, kHz laser systems constitute a formidable challenge because of the scaling law of the bubble regime:

$$E_L \propto \tau^3 \propto \lambda_p^3$$

where E_L is the laser energy. The reduction of E_L from the scale of Joules to mJ, a factor of 1,000, must be accompanied by a reduction in both plasma wavelength and pulse duration by a factor of 10. The required pulse duration must drop from the standard ~30 fs to only ~3 fs; that is, the pulse should basically contain a single light cycle. It follows that the plasma wavelength must also be very small $\lambda_p \approx 2$ μ m, corresponding to a high electron plasma density of $n_e \approx 2.5 \times 10^{20}$ cm⁻³, which, according to scaling laws²³, leads to acceleration of electrons in the 10 MeV range. Previous attempts to accelerate electrons with high-repetition-rate mJ-class lasers^{19,20} did not reach the blowout regime because the pulse duration was too long (>20 fs). Therefore, these initial experiments produced non-relativistic 100 keV electrons beams^{19,20,24} and the bunches quickly stretched due to velocity dispersion, resulting in few-picosecond temporal resolution in time-resolved diffraction experiments^{24,25}. In recent work, relativistic energies were obtained by using very high density plasmas²⁶. However, this experiment was performed using a 10 Hz laser and resulted in rather poor beam quality. In the following, we show that operating in the resonant regime permits all these limitations to be circumvented by producing MeV high-quality electron beams at a high repetition rate.

In the present experiment, plasma waves were resonantly excited by focusing 2.1 mJ, 3.4 fs laser pulses into a continuously flowing, 100- μ m-diameter nitrogen gas jet. The vacuum laser intensity was estimated at $\sim 3 \times 10^{18}$ W cm⁻², allowing the pulse to ionize nitrogen

LETTERS

NATURE PHOTONICS DOI: 10.1038/NPHOTON.2017.46

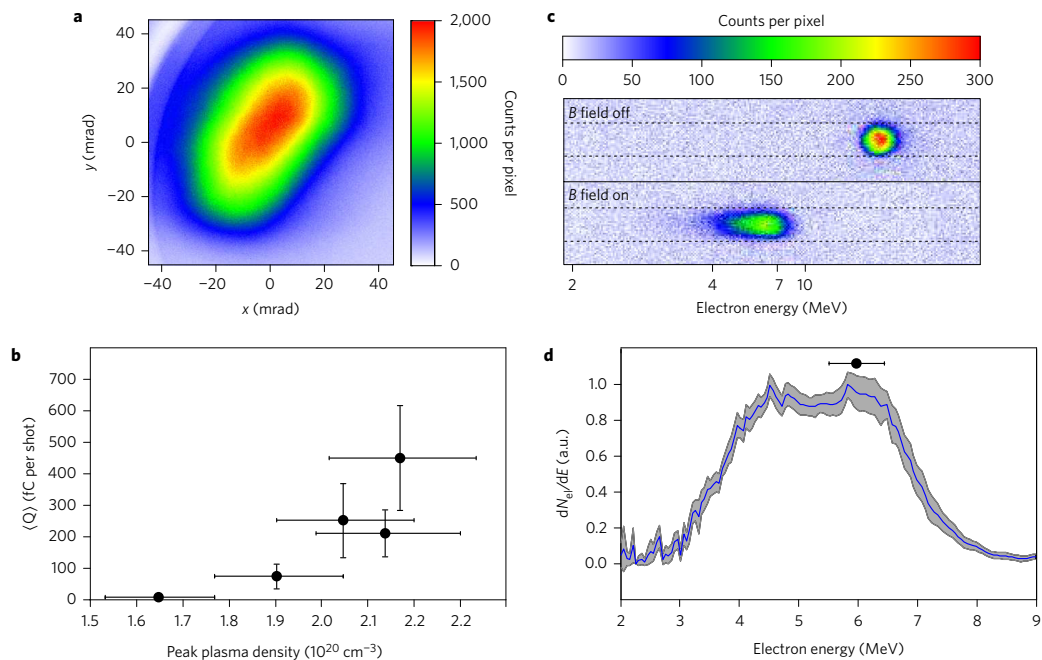


Figure 1 | Measurements of the kHz electron beam. Data shown in **a**, **c** and **d** were taken with an estimated peak electron density of $n_e = 1.8 \times 10^{20} \text{ cm}^{-3}$ ($\pm 10\%$). **a**, Typical electron beam profile obtained by integrating over 500 shots. The total beam charge is estimated to be 147 fC per shot for this particular case. **b**, Dependence of the beam charge as a function of plasma density (the density was changed by varying the height of the gas jet). Vertical error bars represent r.m.s. fluctuations, and horizontal error bars represent uncertainty over the electron density. **c**, Electron beam filtered by a $500 \mu\text{m}$ pinhole with and without magnetic field. Deviation of the electron spot by the magnetic field indicates acceleration to multi-MeV energies. **d**, Electron spectrum. The grey shaded area represents the standard deviation over 20 spectra (each spectrum was obtained by accumulating over 1,000 laser shots). The horizontal error bar represents the spectrometer resolution at ~ 6 MeV.

five times, therefore providing a background electron plasma density of $n_e \approx 1 \times 10^{20}$ to $2 \times 10^{20} \text{ cm}^{-3}$. The electron spatial and spectral distributions were measured using standard diagnostics (see Methods). Figure 1 shows the characteristics of a typical electron beam observed in our experiment. As shown in Fig. 1a, the beam has a rather small divergence of ~ 45 mrad full-width at half-maximum (FWHM). The beam pointing stability is high, with fluctuations amounting to a small fraction of the beam divergence, typically a few mrad. Figure 1b shows that the beam charge depends on the electron density, which can be increased by moving the laser closer to the nozzle. An injected beam starts to appear for $n_e > 1.5 \times 10^{20} \text{ cm}^{-3}$, but the charge increases to ~ 0.5 pC per shot when the density approaches $2 \times 10^{20} \text{ cm}^{-3}$, with the occasional observation of beams reaching 1 pC per shot. The rather large error bars in Fig. 1b show that the charge fluctuations are typically 30% root-mean square (r.m.s.), indicating that we operate close to the injection threshold, as discussed in the following.

The electron energy distribution was obtained by deflecting the electrons using an insertable pair of permanent magnets, as illustrated by the raw data presented in Fig. 1c. A typical energy distribution is shown in Fig. 1d. The electron spectrum peaks at ~ 5 MeV, with an energy spread of 3 MeV. The width of the shaded grey curve represents the r.m.s. fluctuations of the energy distribution, showing that the acceleration process is very stable.

The measured electron beams, with their small divergence and peaked energy distribution, show typical features of acceleration in nonlinear, bubble-like wakefields. However, although these results confirm the scalability of laser-plasma acceleration, the use of single-cycle laser pulses reveals new physical effects that are

usually insignificant at longer durations. For example, as the laser pulse is nearly composed of a single light cycle, the carrier envelope phase (CEP) should have an effect on injection and acceleration²⁷. In addition, such ultrashort pulses have an ultrabroad spectral bandwidth, spanning over an entire octave. Therefore, dispersion effects cannot be neglected during propagation in the plasma²⁸. From the experimental parameters, we estimate that the laser pulse accumulates a negative chirp of -11.5 fs^2 when it reaches the centre of the gas jet. At the focal plane position, that is, at $25 \mu\text{m}$ (to $50 \mu\text{m}$) before the centre of the jet, the accumulated chirp is -8.2 fs^2 (to -5.3 fs^2).

In the experiment, we attempted to compensate this plasma dispersion by adding a small positive chirp to the laser pulse. Figure 2a shows that the electron beam charge is at a maximum when a small positive chirp of $+8 \text{ fs}^2$ is added to the laser pulse. This result was reproduced on multiple experimental runs, with the optimal chirp varying between $+4 \text{ fs}^2$ and $+8 \text{ fs}^2$, depending on the exact focal plane position. These values agree quite well with our estimation of the plasma dispersion. In contrast, a negative chirp causes a decrease in the injected charge. Similarly, Fig. 2b shows that beam energy also increases when using a small positive chirp. This calls for a straightforward interpretation: a positive chirp compensates the negative plasma dispersion, allowing the laser pulse to reach higher intensities within the plasma. Consequently, the wakefield amplitude is higher, leading to higher injected charge and higher energy.

Particle-in-cell (PIC) simulations reproduced our experimental results and confirmed our interpretation. The simulations were run using the experimental parameters, and a positive chirp of $+4 \text{ fs}^2$

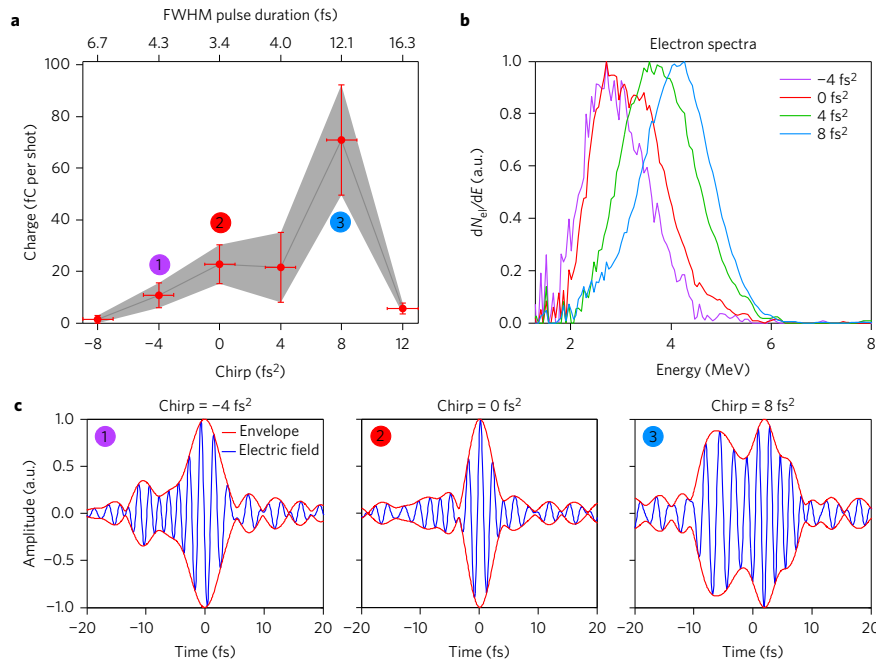


Figure 2 | Observation of dispersion effects. **a**, Evolution of accelerated charge with chirp of the pulse (in fs^2). The peak electron density is $n_e = 1.8 \times 10^{20} \text{ cm}^{-3}$ ($\pm 10\%$). Upper axis: estimated pulse FWHM duration. The grey area and vertical error bars represent r.m.s. fluctuations over 20 images (each averaged over 1 s = 1,000 shots). Horizontal error bars represent the uncertainty on the absolute value of the chirp. **b**, Normalized electron spectra for different chirp values. **c**, Laser electric field (in blue) and envelope (in red) for three different chirp values.

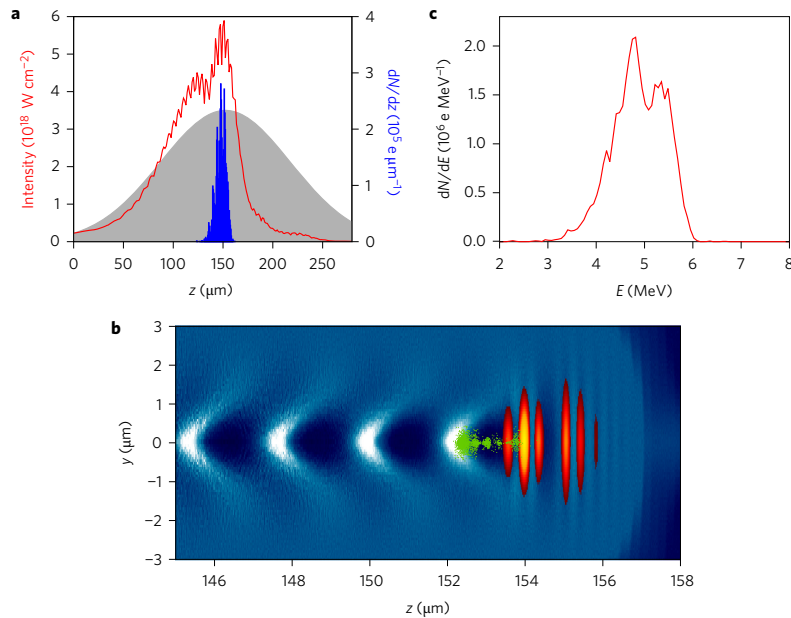


Figure 3 | Results of PIC simulations. **a**, Evolution of laser intensity (red) and injected charge (blue) during propagation in the plasma (density profile shown shaded in grey) for a pulse with a 4 fs^2 positive chirp. **b**, Snapshot of the wakefield around the middle of the gas jet. It shows the spatial distribution of electron density (in blue-white colour scale), the laser intensity (red-orange colour scale) and relativistic electrons ($E > 1.5 \text{ MeV}$) trapped in the wakefield (in green). The intensity distribution of the laser pulse shows a strong modulation as it is practically split in two. **c**, Electron energy spectrum at the accelerator exit. The simulation was run with $n_{N_2} = 1.6 \times 10^{19} \text{ cm}^{-3}$ at the centre of the gas jet, yielding an electron density of $n_e = 1.6 \times 10^{20} \text{ cm}^{-3}$ after ionization.

LETTERS

NATURE PHOTONICS DOI: 10.1038/NPHOTON.2017.46

was added to the pulse (see Methods). Figure 3a shows the evolution of the laser intensity during propagation in the plasma. The simulation shows that the initially chirped pulse compresses and self-focuses as it propagates. It reaches a high intensity of $I \approx 5.5 \times 10^{18} \text{ W cm}^{-2}$ around the middle of the plasma where the density is resonant with the laser pulse. At this point, the laser pulse is able to excite a high-amplitude wakefield. In addition, at this high intensity, N^{5+} is ionized through tunnel ionization, triggering electron injection into the wakefield^{29,30}. The blue curve in Fig. 3a shows that this ionization injection mechanism is very well localized. Local injection is an indirect but striking consequence of the large dispersion effects: the intensity stays high only over a very short distance in the plasma, that is, when the laser pulse is simultaneously short and focused. Consequently, electrons are injected in the first cavity following the laser pulse, leading to a single electron bunch with duration ~ 1 fs, as illustrated in Fig. 3b. The simulation reproduces the divergence (~ 20 mrad), charge (400 fC) and energy distribution (Fig. 3c). The simulations also confirm that negative chirps yield no accelerated electrons and that a slight positive chirp optimises the injection and acceleration process. Although simulations confirm the important role of dispersion, they also indicate that the pulse evolution is rather complex due to nonlinear effects. Dispersion, ionization and plasma wave effects all act on the laser pulse and eventually lead to a compressed and modulated laser envelope, as seen in Fig. 3b (for more details see Supplementary Fig. 3).

In addition, simulations suggest an explanation for the charge fluctuations observed in the experiment. Changing the CEP by $\pi/2$ causes the injected charge to increase by 15%, while the energy distribution is not modified (not shown). As the CEP was not stabilized in our experiment, this accounts for some of the charge fluctuations. Simulations were also run by increasing the laser intensity by 3%, resulting in a charge increase of several hundreds of fC. This indicates that the experiment operated close to the injection threshold, and that using a slightly higher laser intensity might stabilize the injection process.

This development will allow researchers to drive laser-plasma accelerators with more compact laser systems, thereby offering high-repetition-rate operation and superior reliability. These femtosecond, kHz relativistic electron beams are now available and will open unique opportunities for a wide range of experiments such as femtosecond electron diffraction, femtosecond radiolysis or X-ray generation for fast scanning of dense objects.

Methods

Methods and any associated references are available in the [online version of the paper](#).

Received 25 January 2017; accepted 6 March 2017;
published online 10 April 2017

References

- Tajima, T. & Dawson, J. M. Laser electron accelerator. *Phys. Rev. Lett.* **43**, 267–270 (1979).
- Esarey, E., Schroeder, C. B. & Leemans, W. P. Physics of laser-driven plasma-based electron accelerators. *Rev. Mod. Phys.* **81**, 1229–1285 (2009).
- Lundh, O. *et al.* Few femtosecond, few kiloampere electron bunch produced by a laser-plasma accelerator. *Nat. Phys.* **7**, 219–222 (2011).
- Buck, A. *et al.* Real-time observation of laser-driven electron acceleration. *Nat. Phys.* **7**, 543–548 (2011).
- Miller, R. J. D. Femtosecond crystallography with ultrabright electrons and X-rays: capturing chemistry in action. *Science* **343**, 1108–1116 (2014).
- Corde, S. *et al.* Femtosecond X-rays from laser-plasma accelerators. *Rev. Mod. Phys.* **85**, 0034–6861 (2013).
- Ta Phuoc, K. *et al.* All-optical Compton gamma-ray source. *Nat. Photon.* **6**, 308–311 (2012).
- Faure, J. *et al.* A laser-plasma accelerator producing monoenergetic electron beams. *Nature* **431**, 541–544 (2004).
- Geddes, C. G. R. *et al.* High-quality electron beams from a laser wakefield accelerator using plasma-channel guiding. *Nature* **431**, 538–541 (2004).
- Mangles, S. P. D. *et al.* Monoenergetic beams of relativistic electrons from intense laser-plasma interactions. *Nature* **431**, 535–538 (2004).
- Wang, X. *et al.* Quasi-monoenergetic laser-plasma acceleration of electrons to 2 GeV. *Nat. Commun.* **4**, 1988 (2013).
- Leemans, W. P. *et al.* Multi-GeV electron beams from capillary-discharge-guided subpetawatt laser pulses in the self-trapping regime. *Phys. Rev. Lett.* **113**, 245002 (2014).
- Zewail, A. H. 4D ultrafast electron diffraction, crystallography, and microscopy. *Annu. Rev. Phys. Chem.* **57**, 65–103 (2006).
- Sciaini, G. & Miller, R. J. D. Femtosecond electron diffraction: heralding the era of atomically resolved dynamics. *Rep. Prog. Phys.* **74**, 096101 (2011).
- Faure, J. *et al.* Concept of a laser-plasma-based electron source for sub-10-fs electron diffraction. *Phys. Rev. Accel. Beams* **19**, 021302 (2016).
- Malka, V. *et al.* Electron acceleration by a wake field forced by an intense ultrashort laser pulse. *Science* **298**, 1596–1600 (2002).
- Böhle, F. *et al.* Compression of CEP-stable multi-mJ laser pulses down to 4 fs in long hollow fibers. *Laser Phys. Lett.* **11**, 095401 (2014).
- Jullien, A. *et al.* Carrier-envelope-phase stable, high-contrast, double chirped-pulse-amplification laser system. *Opt. Lett.* **39**, 3774–3777 (2014).
- He, Z.-H. *et al.* High repetition-rate wakefield electron source generated by few-millijoule, 30 femtosecond laser pulses on a density downramp. *New J. Phys.* **15**, 053016 (2013).
- Beaupreire, B. *et al.* Effect of the laser wave front in a laser-plasma accelerator. *Phys. Rev. X* **5**, 031012 (2015).
- Pukhov, A. & Meyer-ter-Vehn, J. Laser wake field acceleration: the highly nonlinear broken-wave regime. *Appl. Phys. B* **74**, 355–361 (2002).
- Lu, W., Huang, C., Zhou, M., Mori, W. B. & Katsouleas, T. Nonlinear theory for relativistic plasma wakefields in the blowout regime. *Phys. Rev. Lett.* **96**, 165002 (2006).
- Lu, W. *et al.* Generating multi-GeV electron bunches using single stage laser wakefield acceleration in a 3D nonlinear regime. *Phys. Rev. ST Accel. Beams* **10**, 061301 (2007).
- He, Z.-H. *et al.* Electron diffraction using ultrafast electron bunches from a laser-wakefield accelerator at kHz repetition rate. *Appl. Phys. Lett.* **102**, 064104 (2013b).
- He, Z.-H. *et al.* Capturing structural dynamics in crystalline silicon using chirped electrons from a laser wakefield accelerator. *Sci. Rep.* **6**, 36224 (2016).
- Goers, A. J. *et al.* Multi-MeV electron acceleration by subterawatt laser pulses. *Phys. Rev. Lett.* **115**, 194802 (2015).
- Lifschitz, A. F. & Malka, V. Optical phase effects in electron wakefield acceleration using few-cycle laser pulses. *New J. Phys.* **14**, 053045 (2012).
- Beaupreire, B., Lifschitz, A. & Faure, J. Electron acceleration in sub-relativistic wakefields driven by few-cycle laser pulses. *New J. Phys.* **16**, 023023 (2014).
- McGuffey, C. *et al.* Ionization induced trapping in a laser wakefield accelerator. *Phys. Rev. Lett.* **104**, 025004 (2010).
- Pak, A. *et al.* Injection and trapping of tunnel-ionized electrons into laser-produced wakes. *Phys. Rev. Lett.* **104**, 025003 (2010).

Acknowledgements

The authors acknowledge the help of the support team at the Photo-Injector facility at Laboratoire de l'Accélérateur Linéaire for the absolute calibration of our phosphor screens. This work was funded by the European Research Council (ERC Starting Grant FEMTOELEC) under contract no. 306708. Financial support from the Région Ile-de-France (under contract SESAME-2012-ATTOLITE), the Agence Nationale pour la Recherche (under contracts ANR-11-EQPX-005-ATTOLAB and ANR-14-CE32-0011-03) and the Extreme Light Infrastructure-Hungary Non-Profit Ltd (under contract NLO3.6LOA) is gratefully acknowledged.

Author contributions

A.V., B.B., D.Gué, D.Gus and J.F. built the laser-plasma experiment. D.Gué and D.Gus performed the experiment and analysed the data. F.B., M.B., M.L., A.J. and R.L.-M. developed the near-single-cycle laser system. A.L. performed the modelling of the experiment. J.F. and D.Gué wrote the paper with inputs from all co-authors. J.F. directed the project.

Additional information

Supplementary information is available in the [online version of the paper](#). Reprints and permissions information is available online at www.nature.com/reprints. Publisher's note: Springer Nature remains neutral with regard to jurisdictional claims in published maps and institutional affiliations. Correspondence and requests for materials should be addressed to J.F.

Competing financial interests

The authors declare no competing financial interests.

Methods

Single-cycle laser pulses. The used laser system is a double chirped pulse amplification (CPA) system, delivering ~ 10 mJ in 25 fs at 800 nm wavelength with a temporal contrast better than 10^{10} . The laser pulses were spectrally broadened in a 2.5-m-long hollow core fibre filled with He gas. The pulses were post-compressed in vacuum to near-single-cycle pulses of 3.4 fs using a series of chirped mirrors. The beam was expanded in a reflective telescope to a transverse size of ~ 40 mm. The beam was then focused using an off-axis parabola with a 120 mm focal length, producing a high-quality focal spot of $3.5 \mu\text{m}$ at FWHM. The laser energy on target was typically in the range 2–2.5 mJ. The laser pulse duration was measured directly in vacuum using the D-scan technique (Sphere Ultrafast Photonics³¹): the laser pulse was frequency-doubled in a thin beta barium borate crystal and the second harmonic spectrum was measured for different insertions of two fused-silica wedges, providing a dispersion scan. An algorithm was used to reconstruct the spectral amplitude and phase of the laser pulse, providing a complete temporal characterization of the laser pulse at best compression. The laser field inferred by such a measurement is shown in Fig. 2c, in the middle panel for the unchirped case. Experimentally, the chirp was modified by changing the insertion of the two wedges in the laser beam: a positive chirp of $+4 \text{ fs}^2$ was obtained by adding $100 \mu\text{m}$ of fused silica. For the chirped pulses, the temporal envelope was estimated by taking into account the spectral phase corresponding to this additional material. We modelled the spectral phase corresponding to the propagation in the wedges using Sellmeier's equation for the refractive index of fused silica. This spectral phase was added to the measured phase of the unchirped laser field. Applying a Fourier transform, we then obtained the chirped laser field in the temporal domain, as shown in the left and right panels in Fig. 2c. Finally, to obtain realistic values of the laser intensity, we took into account the real temporal and transverse distribution of the laser intensity, giving an estimated peak intensity of $I \approx 3 \times 10^{18} \text{ W cm}^{-2}$. We also estimated that the intensity fluctuations, excluding possible fluctuations of the temporal envelope, were about 1% r.m.s.

Laser-plasma accelerator. The laser beam was focused into a continuously flowing nitrogen (N_2) gas jet. The nozzle was a simple $100\text{-}\mu\text{m}$ -diameter glass capillary, providing a sonic gas flow. We used a quadriwave lateral shearing interferometer (SID4 HR by PHASICS) to characterize the gas jet off line, before and after experiments. The measurements showed that the molecular density quickly drops above the capillary exit opening. We operated the experiment by moving the laser to as close as $80 \mu\text{m}$ above the capillary exit (approaching more closely would begin to damage the capillary). At this position, the molecular profile could be approximated by a Gaussian shape of $140 \mu\text{m}$ at the FWHM. By applying a backing pressure of 20 bar, molecular densities up to $2 \times 10^{19} \text{ cm}^{-3}$ could be obtained at the peak of the jet. The laser created the plasma by barrier-suppression ionization of the nitrogen atoms, up to N^{5+} , providing an electronic density of up to $n_e = 2 \times 10^{20} \text{ cm}^{-3}$. Experimentally, the plasma density was modified by changing the backing pressure or by changing the respective height of the laser focus and the capillary exit. The density was limited by the gas load in the vacuum chamber: for a backing pressure of

20 bar N_2 , the residual gas inside the chamber was below 10^{-2} mbar, which was acceptable for running the experiment. Higher backing pressures made our turbomolecular pump fail, causing the background pressure to increase. We therefore could not explore higher electron densities while operating at a kHz repetition rate, with a free-flowing gas jet.

For electron detection, the electron beam profile was monitored using a CsI(Tl) phosphor screen imaged onto a 14 bit charge-coupled device camera. The electron energy distribution was obtained by sending the beam through a $500 \mu\text{m}$ lead pinhole followed by a pair of circular permanent magnets, providing a magnetic field peaking at 88 mT. The phosphor screen was calibrated independently on a radiofrequency accelerator, providing picosecond electron bunches at 3 MeV. Finally, a small portion of the laser pulse was used as a probe to measure the electron density *in situ* by transverse interferometry. A schematic of the experimental set-up is presented in the Supplementary Information.

The experiment was always run at a kHz repetition rate, and all data and acquired images presented in this Letter were averaged over 200 to 1,000 shots. Statistics are usually presented by analysing fluctuations over 20 acquisitions, meaning that each data point and error bars usually involve between 4,000 and 20,000 shots.

PIC simulations. Simulations were performed using CalderCirc³², a fully electromagnetic 3D code based on cylindrical coordinates (r, z) and Fourier decomposition in the poloidal direction. Simulations were performed using a mesh with $\Delta z = 0.1 k_0^{-1}$ and $\Delta r = 0.5 k_0^{-1}$ (where $k_0 = 2\pi\lambda_0^{-1}$ is the laser wavevector and $\lambda_0 = 800 \text{ nm}$) and the two first Fourier modes. The neutral gas density profile was taken from the experimental data. The simulations started with pure neutral nitrogen, which was ionized via tunnel ionization. The number of macroparticles per cell before ionization was 500, which corresponds to $500 \times 5 = 2,500$ macro-electrons per cell in the region of full ionization of the L-shell of nitrogen. The temporal high-frequency laser field for the different values of chirp ($-4, 0, 4$ and 8 fs^2) was taken from experimental data (shown in Fig. 2c).

We explored the full range of parameters spanned by the experiment. Intensities were varied between $3 \times 10^{18} \text{ W cm}^{-2}$ and $4 \times 10^{18} \text{ W cm}^{-2}$, and N_2 densities from $1.6 \times 10^{19} \text{ cm}^{-3}$ to $2.5 \times 10^{19} \text{ cm}^{-3}$. For all cases, the only injection mechanism found was ionization injection of electrons coming from ionization of N^{5+} , yielding a peaked electron spectrum around 4–5 MeV.

Data availability. The data that support the plots within this Letter and other findings of this study are available from the corresponding author upon reasonable request.

References

- Miranda, M. *et al.* Characterization of broadband few-cycle laser pulses with the d-scan technique. *Opt. Express* **20**, 18732–18743 (2012).
- Lifschitz, A. *et al.* Particle-in-cell modelling of laser-plasma interaction using Fourier decomposition. *J. Comp. Phys.* **228**, 1803–1814 (2009).

In the format provided by the authors and unedited.

“Relativistic electron beams driven by kHz single-cycle light pulses”

¹D. Guénot, ¹D. Gustas, ¹A. Vernier, ¹B. Beaufepaire, ¹F. Böhle, ¹M. Bocoum,
¹M. Lozano, ¹A. Jullien, ¹R. Lopez-Martens, ¹A. Lifschitz and ¹J. Faure*
¹LOA, ENSTA Paristech, CNRS, Ecole Polytechnique, Université Paris-Saclay, Palaiseau, France

EXPERIMENTAL SET-UP

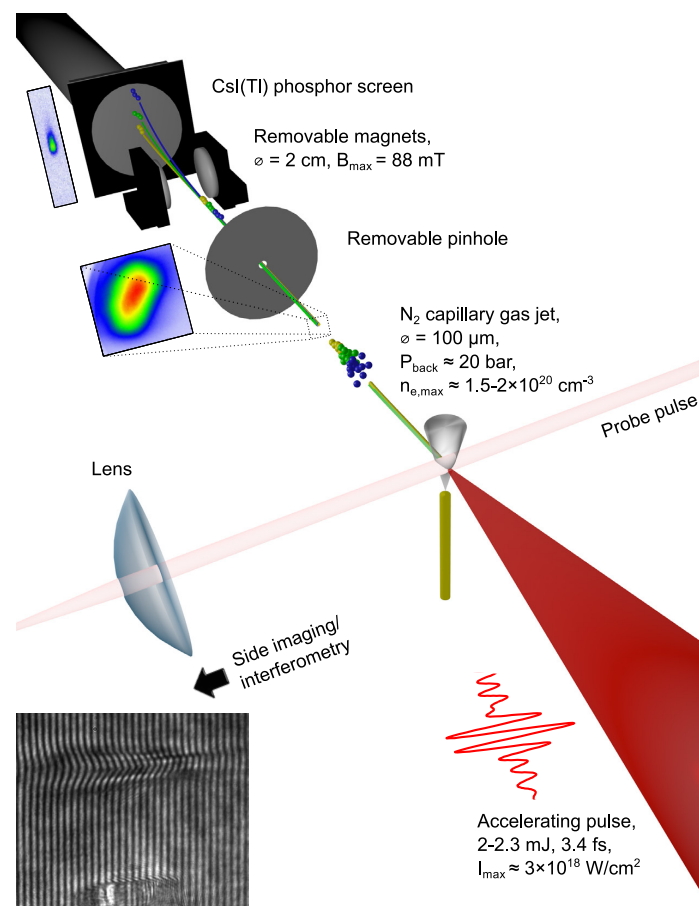


FIG. 1: **Experimental setup.** A near-single-cycle laser pulse is focused into a high density gas jet, where the electron beam is generated. A weak probe laser beam is sent perpendicularly to the main beam in order to image the plasma via shadowgraphy or interferometry. The generated electron beam is sent onto a phosphor screen imaged onto a CCD camera. A pinhole and a pair of magnets can be inserted to measure the electron spectrum.

SUPPLEMENTARY DATA ON LASER PULSE CHARACTERIZATION

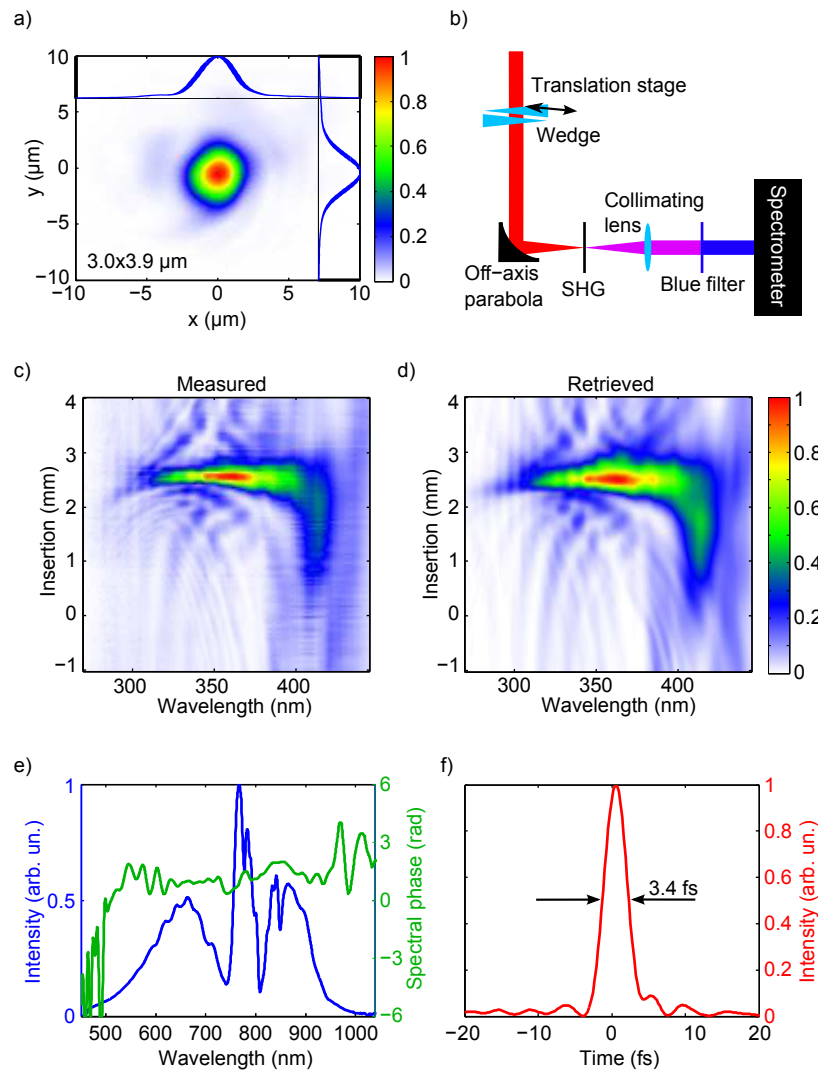


FIG. 2: Laser pulse characterization. a: Image of the laser beam at focus. b: Principle of the D-scan measurement: the laser pulse is focused onto a BBO crystal and a spectrometer records the frequency-doubled spectra versus wedge insertion. Wedge insertion can be modified using a translation stage. An algorithm retrieves the spectral amplitude and phase at best compression. c, d: Measured and retrieved scans. e: Retrieved spectral intensity and phase. f: Retrieved temporal envelope of the laser intensity.

SUPPLEMENTARY DATA ON THE LASER PULSE EVOLUTION IN THE PLASMA

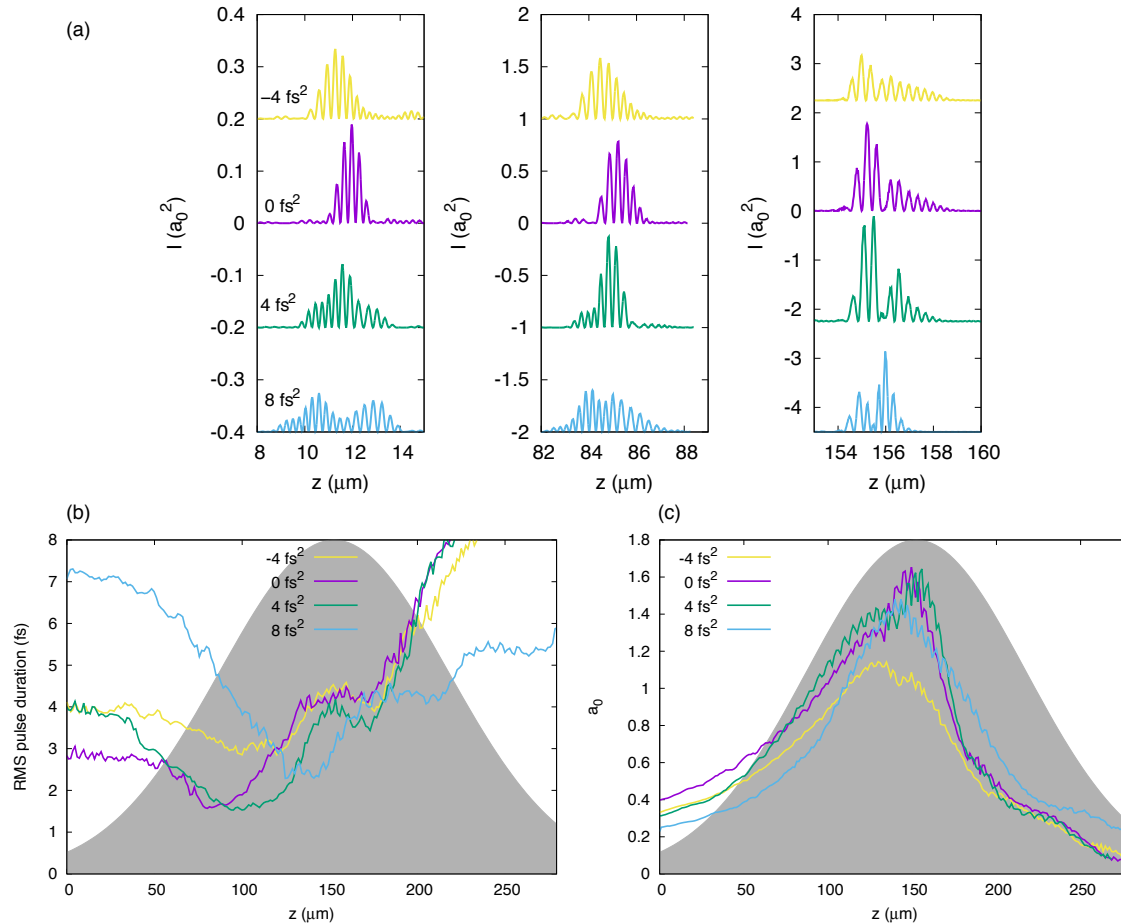


FIG. 3: **Effect of dispersion and evolution of the laser pulse.** a: Laser intensity profile at three positions inside the gas jet (10, 85 and 155 μm) for four different chirps (-4 fs^2 (yellow), 0 fs^2 (purple), 4 fs^2 (green) and 8 fs^2 (blue)). b: Evolution of the r.m.s. pulse duration in the gas jet (density profile shown in grey). c: Evolution of the normalised vector potential a_0 inside the gas jet. For these simulations, the peak electron density is $n_e = 1.6 \times 10^{20} \text{ cm}^{-3}$ and the vacuum focal plane is 125 μm , i.e. 25 μm before the center of the jet.

We investigated the effect of the chirp and the plasma dispersion using PIC simulations. The various simulations presented in Fig. 3 were performed with the same parameters, only the laser pulse initial phase varies, according to the experimental data presented in the main manuscript (Fig. 2). First, the global trend of the experiment is well reproduced: a negative chirp on the laser pulse yields no electron beam and a slight positive chirp is favorable for electron injection and acceleration. Here we attempt to explain the results by investigating the laser pulse evolution in more details.

The key point is that for injection to occur, the highest laser intensity is needed, meaning that the laser pulse needs to be simultaneously short and tightly focused. Therefore, we need to confront two scale lengths: the Rayleigh length $z_R \simeq 50 \mu\text{m}$ and the dispersion length $L_{disp} \simeq 20 \mu\text{m}$. In the linear limit, L_{disp} is the dispersion length scale in the

plasma (see ref. [28]):

$$L_{disp} \simeq 4\pi c^2 \tau_0^2 \frac{\lambda_p^2}{\lambda_0^3}, \quad (1)$$

Because the dispersion length is quite small, it is necessary to adjust carefully the chirp so that the pulse duration is shortest at focus. In particular, the negatively chirped pulse does not shorten significantly in the plasma: it mostly gets longer, see yellow curve in in Fig. 3a and b. At the focal plane $z = 125 \mu\text{m}$, the laser pulse is too long, preventing self-focusing. In consequence, the laser intensity stays low throughout propagation, yellow curve in Fig. 3c, and no electrons can be injected.

On the other hand, Fig. 3a and b clearly show that positively chirped pulses can get recompressed efficiently in the plasma. The position of the best compression can be adjusted with the chirp. Clearly, for these simulations, the best case is obtained for a chirp of 4 fs^2 for which the laser is shortest in the region $100 - 125 \mu\text{m}$, i.e. at the focal plane. This permits to obtain self-focusing and increase significantly the intensity, thereby causing electron injection via injection ionization.

In the simulation, the case of a 8 fs^2 chirp seems to be beyond the optimum: the laser pulse recompresses in the plasma but the intensity is slightly lower, resulting in less injected electrons. In the experiment, the optimum chirp is between 4 fs^2 and 8 fs^2 , depending on the exact experimental parameters: position of the gas jet, plasma density... Overall, the simulations reproduce the experimental trend very well.

In addition, although the chirp plays a very important role, simulations indicate that other effects are also at play. Ionization effects cannot be neglected, especially at the entrance of the gas jet, in the region $z < 100 \mu\text{m}$. Thus, ionization induced self-compression and defocusing is important at the beginning of the interaction where the laser intensity is considerably lower. In particular, ionization compression is responsible for the slight pulse shortening of the negatively chirped laser pulse for $z < 100 \mu\text{m}$. In the region $z > 100 \mu\text{m}$, a large amplitude plasma wave is generated and affects the laser pulse propagation. The interplay of dispersion, ionization and plasma wave effects lead to the complex evolution of the laser pulse. In particular, the pulse does not simply self-compress, as would be expected if only dispersion played a role. Indeed, the pulse eventually splits in two and appears to be modulated (see the green curve in Fig. 3a).

High-charge relativistic electron bunches from a kHz laser-plasma accelerator

D. Gustas, D. Guénot, A. Vernier, S. Dutt, F. Böhle, R. Lopez-Martens, A. Lifschitz, and J. Faure
LOA, ENSTA ParisTech, CNRS, Ecole polytechnique, Université Paris-Saclay, Palaiseau 91762, France



(Received 17 November 2017; published 29 January 2018)

We report on electron wakefield acceleration in the resonant bubble regime with few-millijoule near-single-cycle laser pulses at a kilohertz repetition rate. Using very tight focusing of the laser pulse in conjunction with microscale supersonic gas jets, we demonstrate a stable relativistic electron source with a high charge per pulse up to 24 pC/shot. The corresponding average current is 24 nA, making this kilohertz electron source useful for various applications.

DOI: 10.1103/PhysRevAccelBeams.21.013401

I. INTRODUCTION

Laser wakefield acceleration (LWFA) is an established technique for producing high-energy electrons over minuscule distances [1]. Due to its ability to generate ultrashort particle bunches [2] as well as a wide range of secondary radiation with small source sizes [3–6], the method is often considered for many applications in industry, material science, nuclear physics or medicine [7]. However, most LWFA experiments are currently performed using 100 TW class laser systems at low repetition rate (≤ 1 Hz), which limits their practical use. Increasing the repetition rate is important for a wide range of reasons: (i) it permits reaching a higher level of stability; (ii) it opens up the possibility of active feedback control and beam optimization [8]; (iii) it enables rapid averaging over many shots, thereby significantly increasing the signal-to-noise ratio of a measurement; (iv) it can boost the average current of the electron source by several orders of magnitude. Irradiation-based applications such as in medical treatment [9] or electronics hardness studies [10] would directly benefit from a high average current because the required dose could be delivered in a much shorter time. Applications relying on a pump-probe scheme, such as ultrafast electron diffraction [11,12] or pulsed radiolysis [13], would greatly benefit from the higher stability and the improved signal-to-noise ratio.

To address these points, some of the recent work has been dedicated to developing high-repetition rate laser-plasma accelerators driven by low-energy laser pulses, in the 1–10 mJ range. Initial attempts produced subrelativistic electrons with relatively low charge and relied on density

down ramp injection [14,15]. The first MeV-scale accelerator at a kHz repetition rate was obtained using ultrahigh density gas targets; it operated in the self-modulated regime, resulting in a fairly divergent beam with a Maxwellian energy distribution [16]. To improve the source performance, our group has recently adapted the well-known “bubble” regime [17] configuration for few-millijoule laser pulses by compressing them nearly to a single optical cycle, or below 4 fs. Higher quality beams were obtained, with divergences of ~ 40 mrad, stable peaked energy distribution at ~ 5 MeV and charges of hundreds of fC [18]. Simulations showed that electrons were injected via ionization [19,20] of the K-shell electrons in nitrogen, yielding ultrashort relativistic bunches generated in the first arch of the wakefield [21]. Despite kHz repetition rate, however, the electron source displayed relatively high charge fluctuations, indicating proximity to the injection threshold [22].

In the present article, we circumvent this problem by driving the accelerator at higher laser intensity. The interaction of the laser with the plasma medium is optimized by using innovative microscale supersonic gas jets providing higher density gradients and shorter plasma lengths. We demonstrate a laser-plasma accelerator running at kHz, producing few MeV electron beams with stable beam charge up to 24 pC/shot, i.e. a 2 order of magnitude improvement compared to previous results. This yields an average current of 24 nA, the largest ever measured in a laser-plasma accelerator. In Sec. II, we discuss design issues and characterization of the microscale gas jets. In Sec. III, we show the results of the experiment and discuss them in Sec. IV on the basis of particle in cell (PIC) simulations.

II. MICROSCALE SUPERSONIC JETS

The laser-plasma accelerator is operated near the bubble regime which is known to produce small divergence beams with quasimonoenergetic distributions [23–25]. This regime may be accessed once the light is focused

Published by the American Physical Society under the terms of the Creative Commons Attribution 4.0 International license. Further distribution of this work must maintain attribution to the author(s) and the published article's title, journal citation, and DOI.

to relativistic intensities $\approx 10^{18} - 10^{19}$ W/cm², and the resonance condition is satisfied [26]: $c\tau \approx w_0 \approx \lambda_p/2$, where c is the speed of light, τ is the FWHM pulse duration, w_0 is the laser beam waist, and λ_p is the target plasma wavelength. For a few mJ laser systems, these conditions can be fulfilled provided that the laser pulse is extremely short, typically < 4 fs, and is focused tightly, $w_0 \approx 2-3$ μm in a high density plasma of $n_e \approx 1-2 \times 10^{20}$ cm⁻³ for a 800 nm laser wavelength. At this high density, the dephasing length and the pump depletion length are very short [26], of order ≈ 20 μm , which calls for the use of very thin gas targets. In addition, while laser pulses with octave-spanning spectrum are used, strong dispersion effects similarly limit the high-intensity interaction to no more than a few tens of microns [18,27]. Finally, the most important issue originates from laser beam propagation: for a waist of $w_0 = 2$ μm , the Rayleigh length is estimated to be $z_R = 16$ μm . Therefore, sharp density gradients are crucial for optimizing the coupling of the laser pulses into the jet and avoiding ionization-induced defocusing [28]. This effect is particularly detrimental when using high-Z gases, as in our experiment. Figure 1(a) illustrates beam propagation in the case where the density gradient is longer than the Rayleigh length. In this arrangement, ionization-induced defocusing prevents the laser from reaching intensities required to drive a large amplitude wakefield. In the contrary case of Fig. 1(b), the density gradient is short enough to allow the laser beam to self-focus in the jet, resulting in the excitation of a strong wakefield. These considerations clearly indicate that gas nozzles providing jets of ≈ 100 μm with sharp density gradients are ideal.

There are also more practical considerations that need to be considered for nozzle design. First, the tip of the nozzle cannot be brought closer than 100 μm to the laser focus without getting damaged by the laser itself. Second, the nozzle needs to provide high density in a continuous gas

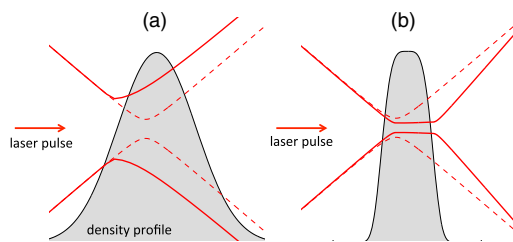


FIG. 1. Schematic of beam propagation issues in microscale jets. The dashed line represents the vacuum laser beam whereas the full line shows the beam size considering plasma effects. (a) The density gradients are large compared to z_R preventing the laser beam from reaching high intensity in the jet. (b) With sharper density gradients, coupling into the jet is optimized and the laser beam can reach higher intensities through self-focusing.

flow in order to enable operation at high repetition rates. This is considerably challenging for the vacuum pumping system as it needs to keep the background pressure in the chamber below 10^{-2} mbar. Consequently, the nozzle should be designed in order to minimize the mass flow while maximizing the density at heights above 100 μm . This calls for microscale supersonic nozzles that are able to provide high densities well above the tip opening.

In Fig. 2, we compare a 100 μm -diameter nozzle, providing a subsonic flow to a supersonic conical De Laval nozzle with a 40 μm throat [29], specially manufactured for this experiment by microspark erosion. The N_2 gas jets are characterized with a quadriwave lateral shearing interferometer (SID4 HR by PHASICS). The density maps are obtained via Abel inversion of the measured phase maps. The backing pressure ($P = 12$ bar for the subsonic nozzle and $P = 60$ bar for the supersonic nozzle) is chosen such that the background pressure in the vacuum chamber is similar in both cases, enabling a direct comparison of the density profiles. Clearly, the supersonic jet provides higher density above 100 μm , while preserving a thinner length and sharper gradients compared to the

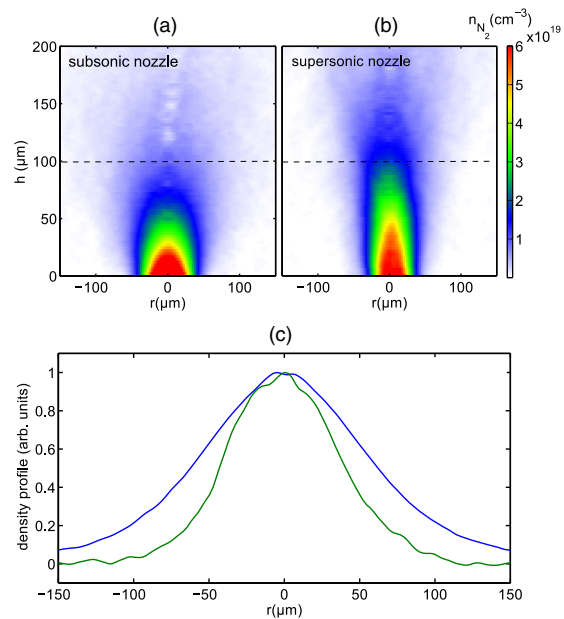


FIG. 2. Molecular density map $n_{N_2}(r, h)$ (a) for the subsonic nozzle with backing pressure $P = 12$ bar and (b) for the supersonic nozzle, with backing pressure $P = 60$ bar. Both cases lead to similar background pressure in the vacuum chamber but the peak density at $h = 100$ μm is $n_{N_2} = 1.8 \times 10^{19}$ cm⁻³ for the supersonic jet and $n_{N_2} = 8 \times 10^{18}$ cm⁻³ for the subsonic nozzle. (c) Normalized density profiles obtained at height $h = 100$ μm [dashed line in (a) and (b)]. The $1/e$ width is 51 μm (80 μm) for the supersonic (subsonic) nozzle.

subsonic nozzles. The supersonic jets fulfill the stringent experimental requirements of a high-repetition rate laser-plasma accelerator.

III. EXPERIMENTAL RESULTS

The experiment at LOA was performed using the Salle Noire laser system delivering 3.9 fs pulses (≈ 1.5 optical cycle at $\lambda_0 \approx 800$ nm) at 1 kHz with 2.5 mJ of energy on target [30]. A pair of motorized fused-silica wedges could be adjusted in the beam path to introduce some predominantly second-order chirp. An $f/2$ parabola was utilized to focus the light into a near-Gaussian spot with dimensions $2.9 \times 2.5 \mu\text{m}$ (FWHM), implying an approximate Rayleigh range of 20–25 μm and a maximum vacuum intensity $I_{\text{vac}} \approx 5 \times 10^{18}$ W/cm², estimated using the real focal spot image. An electron detection setup, independently calibrated at a linear accelerator facility and consisting of a CsI(Tl) phosphor screen, imaging lenses and a CCD camera, was used to measure the charge and visualize the electron spot. A pinhole and a pair of circular permanent magnets could be inserted into the beam path to measure particle spectra. Compared to our previous experiments [18], we now operate well above the injection threshold by focusing the laser tighter and thus increasing the peak intensity by a factor of 2. While this leads to a shorter Rayleigh length, we used the supersonic nozzles with sharp gradients in order to optimize coupling of the laser pulse into the gas jet. Nitrogen gas was used because each nitrogen molecule releases ten electrons assuming immediate ionization of nitrogen to N^{5+} . Therefore, the required high electron density can be achieved while keeping the background pressure in the vacuum chamber at a reasonable level. It also gives the opportunity of ionization injection from K-shell electrons. The density profile experienced by the driver pulse depends on the backing pressure and the nozzle orifice distance to the optical axis [Figs. 2(a) and 2(b)], which can be adjusted mechanically. The plasma profile can be well approximated by a Gaussian function characterized by its peak density and its $1/e$ width, see Fig. 2(c).

Experiments with the subsonic jet yielded no relativistic electrons. As discussed earlier (see Fig. 1), this was likely due to ionization-induced beam propagation issues. Using the supersonic jet, such detrimental effects were clearly suppressed as a multi-pC electron beam could be obtained easily.

We found the electron beam energy distribution to be very sensitive to the density profile. Figure 4 shows the electron beam spectra obtained in three different cases corresponding to various densities and jet profiles. In case 1, a relativistic beam with a charge of 2.5 pC/shot was obtained by focusing the laser into the rising edge of a Gaussian plasma profile with peak electron density 1.45×10^{20} cm⁻³ and $1/e$ width of 65 μm (Fig. 4, case 1).

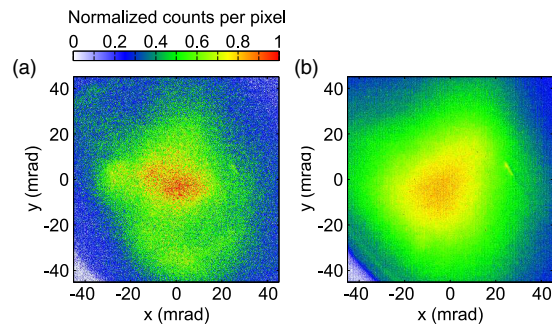


FIG. 3. Electron beam profiles corresponding to case 1. (a) Single-shot image. Divergence— 44×57 mrad FWHM (b) 40-shot average, 74×75 mrad FWHM. Estimated charge—2.5 pC/shot ($\pm 14\%$ st. dev.).

The measured spectral distribution was nearly a plateau extending from 1.5 to 5 MeV [Fig. 4(b), solid line]. In this regime, we observed that the electron beam parameters could be varied by chirping the driver pulse. For example, introducing a slight negative chirp roughly preserved the total charge but produced a narrower energy spread, leaving only a peak at ≈ 3.5 MeV [-4 fs², Fig. 4(b), dashed line].

In case 2, a higher peak density (1.7×10^{20} cm⁻³) and thinner profile ($1/e$ width of 55 μm) was obtained by moving the nozzle closer to the optical axis. We observed an increase in charge by almost a whole order of magnitude to ≈ 24 pC, accompanied by the appearance of a very strong peak at around 1 MeV, while the previous high-energy spectral feature at 3–4 MeV was preserved [Fig. 4(a), line 2]. Small chirp variations did not introduce any obvious trends, suggesting the entire injection process was well above the threshold. This data shows that sharper gradients and higher densities are beneficial for optimizing the beam charge. Finally, in case 3, the density was similar as above (1.6×10^{20} cm⁻³), but the $1/e$ width was made larger than in case 2 (70 μm). A roughly twofold decrease in charge was recorded, together with the disappearance of the high energy feature and a lengthening of the low-energy tail [Fig. 4(a), line 3, and Fig. 4(d)].

This data demonstrates large sensitivity not only to the peak plasma density, but also to the profile width. Hence, both these parameters should be considered as potential tuning knobs for the system, and precise control over them is desired. With supersonic jets, the accelerator now operates in a stable mode: the energy distribution is rather steady [see the grey lines in Figs. 4(b)–4(d) indicating the standard deviation of the distribution] and the shot-to-shot charge rms fluctuations are in the 15% range. Typical electron beam profiles are shown in Fig. 3: sub-60 mrad FWHM divergence is obtained. The comparison between single shot images and averaged images indicate that the

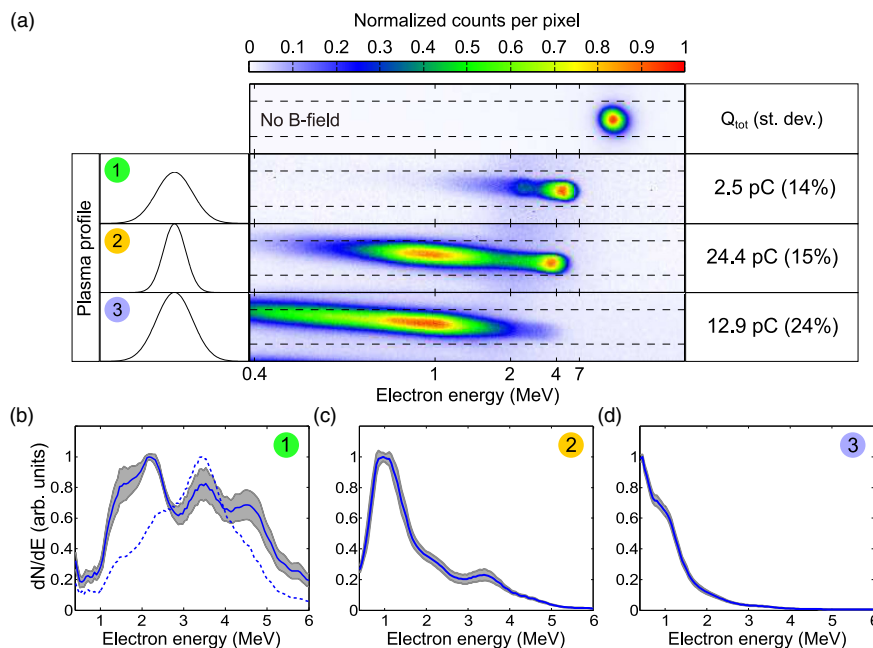


FIG. 4. Electron spectra and measured average charges for three different target density profiles from the supersonic jet. (a) Raw data and average charge values. Top row—electron beam spatially filtered by a pinhole but not deviated by magnets. Case 1—spectrum obtained with peak electron density $1.45 \times 10^{20} \text{ cm}^{-3}$ and $1/e$ width of $65 \mu\text{m}$. Case 2 corresponds to the case with $1.7 \times 10^{20} \text{ cm}^{-3}$ peak and $55 \mu\text{m}$ width, case 3—with $1.6 \times 10^{20} \text{ cm}^{-3}$ peak and $70 \mu\text{m}$ width. (b) Solid line—deconvolved spectrum 1 with standard deviation (grey area). Dashed line—deconvolved spectrum when the driver pulse was negatively chirped by -4 fs^2 (raw data not given). (c) and (d) Deconvolved spectra 2 and 3 with corresponding standard deviations.

beam pointing fluctuations are only a fraction of the beam divergence.

IV. PIC SIMULATIONS AND DISCUSSION

To get an insight into what types of injection mechanisms might be taking part in the process, we performed particle-in-cell (PIC) simulations using CALDER-CIRC [31], a fully electromagnetic 3D code based on cylindrical coordinates (r, z) and Fourier decomposition in the poloidal direction. The simulations were performed using a mesh with $\Delta z = 0.1k_0^{-1}$ and $\Delta r = 0.5k_0^{-1}$ (where k_0 is the laser wave vector), and the first five Fourier modes. We started with pure neutral nitrogen, which then experienced tunnel ionization, as described in [32]. The neutral N gas density profile was a Gaussian with a peak value of $1/5 \times 1.7 \times 10^{20} \text{ cm}^{-3}$ and a $1/e$ width of $55 \mu\text{m}$, corresponding to the experimental case 2. The number of macroparticles per cell before ionization was set to 500, which corresponds to $500 \times 5 = 2500$ macroelectrons per cell in the region of full ionization of the L-shell of nitrogen. The temporal high-frequency laser field, its peak normalized amplitude ($a_0 = 1.44$) and the beam focal spot size ($2.7 \mu\text{m}$ FWHM) were also matched to experimental inputs.

PIC simulations suggest that ionization injection is responsible for the trapping of electrons in the wakefield. This can be seen in Fig. 5(c), showing the histogram describing particle injection loci as well as evolution of the peak laser amplitude. The laser pulse self-focuses up to a maximum amplitude of $a_0 = 1.8$ around $10 \mu\text{m}$ before the middle of the gas jet. It becomes intense enough to trigger ionization injection of electrons from the K-shell of nitrogen. A snapshot of the electron density spatial distribution at the end of the first injection is shown in Fig. 5(a). As can be seen, these inner electrons (represented by yellow dots) are injected in the first wakefield period, making up a total charge of $\approx 5 \text{ pC}$ and extending over a $\approx 2 \mu\text{m}$ distance. Right before the center of the gas jet ($z = 150 \mu\text{m}$), the laser intensity drops, stopping this first injection event.

The rapid evolution of the laser pulse then results in a second injection process. As described in [27], the laser pulse undergoes a strong redshift, causing its envelope to slip backwards because of the slower group velocity at red wavelengths. This results in a slow-down of the wakefield [see Fig. 5(b)] and triggers the second injection event. Indeed, the slower phase velocity of the wakefield enables efficient trapping of electrons even if the laser amplitude is significantly decreased [27]. The injection mechanism still

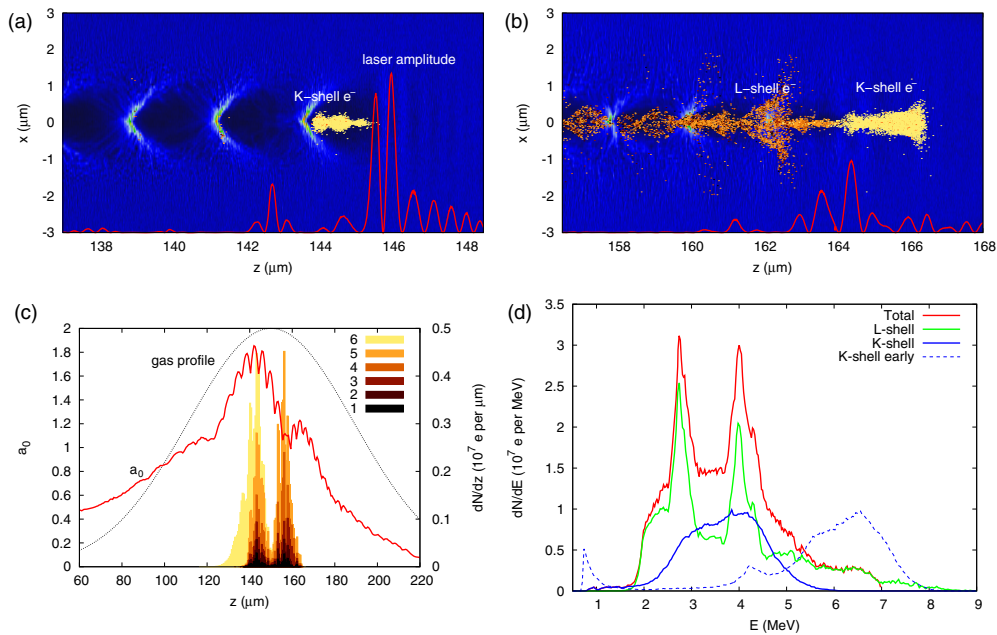


FIG. 5. Results of 3D PIC simulations. (a) and (b) Electron density spatial distribution at two time steps. Trapped electrons are represented by dots. The red curve shows the laser E-field amplitude on the optical axis. (c) Red curve—evolution of the laser normalized amplitude. Histogram—particle trapping locations, decomposed into separate groups based on nitrogen ionization levels from which they originate. For example, electrons marked by “1” originate from ionization of N^0 , electrons “6” stem from ionization of N^{5+} , etc. (d) Final electron spectra of K-shell electrons (“6”), L-shell electrons (“1”–“5”) and a sum of both. An early spectrum of K-shell electrons when the laser is around the middle of the gas jet is shown by the dashed line.

relies on ionization even though the laser intensity is now too low to ionize K-shell electrons. We observe that the electrons originating from the $2p$ subshell are more often trapped than the ones coming from the $2s$ subshell [see Fig. 5(c)], confirming the role of ionization in this injection process. Contrary to the first injection event, a significant fraction of the electrons is trapped in the second bucket of the wakefield. The trapped charge due to this second injection event is close to the first one (≈ 5 pC).

The final spectrum, shown in Fig. 5(d), extends from 2 to 8 MeV, and possesses two peaks of roughly equal strength at 2.8 and at 4 MeV. The total accelerated charge is 10 pC. Except the similar amplitudes of the two peaks, the simulation reproduces experimental results fairly closely. If only the electrons originating from the K-shell are considered, a broad peak between 2 and 5 MeV is obtained, similar to the dashed curve spectrum in Fig. 4(b). We note that at the center of the gas jet, these electrons are faster, between 5 and 8 MeV [dashed curve in Fig. 5(d)]. They are soon dephased because of the backward slip of the bubble and therefore start losing energy. The peaks at 2.8 and 4 MeV correspond to L-shell particles injected into the second and first buckets respectively. The peak appears because of the rotation of the bunches in phase space (z, p_z) beyond the dephasing length.

The rms duration of the entire electron bunch is 10 fs, whereas its rms divergence is 90 mrad.

The PIC simulation results suggest that two injection events occur in the experiment. At first, K-shell electrons are ionization injected into the first bucket. Then, after massive self-focusing and reshaping of the driver pulse, the wakefield is slowed down, aiding the second injection process that results in the filling of several buckets. In the experimental case 1 (as labeled in Fig. 4), where the peak density is lower, this second injection might be mitigated, yielding lower charge, but higher energy and likely shorter electron bunches. At increased density, as in case 2, self-focusing is more pronounced, triggering the second injection event, which leads to significantly higher charge but lower energy electrons because of dephasing in the slower wakefield. If an overly wide N_2 gas jet is used, the K-shell electron peak might be lost, as in case 3, most probably due to stronger ionization-induced defocusing. We therefore suggest that precise control over the target profile might be a way to tune not only the injected charge or resultant spectrum, but also the number of buckets that are filled with accelerated electrons. To be fully validated, this hypothesis would still need to be tested experimentally through bunch length measurements [2,21].

V. CONCLUSION

In summary, we produced a kilohertz relativistic electron wakefield accelerator with high bunch charge, high average current and with significantly enhanced stability. We have shown how its properties can be manipulated through small target width adjustments. The recorded broadband 24 pC source could be used to generate bright x rays for radiography [33] or to provide a laboratory-scale electronics damage testing environment for space industry, as the flux and spectrum are similar to those in Van Allen radiation belts [10]. In addition, these particle bunches could be of large interest for sub-10 fs jitter-free ultrafast electron diffraction experiments [11,12]. Previous work showed that with such large charge, the electron beam can be filtered spectrally and spatially to yield a sufficiently narrow energy spread and small emittance source for time-resolved matter studies [34]. In conclusion, we believe the presented experiment plays an important role in the quest for providing stable, controllable and accessible particle sources to a wider user community.

ACKNOWLEDGMENTS

This work was funded by the European Research Council (ERC Starting Grant No. FEMTOELEC) under Contract No. 306708. Financial support from the Région Île-de-France (under Contract No. SESAME-2012-ATTOLITE), the Agence Nationale pour la Recherche (under Contracts No. ANR-11-EQPX-005-ATTOLAB and No. ANR-14-CE32-0011-03) and the Extreme Light Infrastructure-Hungary Non-Profit Ltd (under Contract No. NLO3.6LOA) is gratefully acknowledged.

-
- [1] E. Esarey, C. B. Schroeder, and W. P. Leemans, Physics of laser-driven plasma-based electron accelerators, *Rev. Mod. Phys.* **81**, 1229 (2009).
 - [2] O. Lundh, J. Lim, C. Rechatin, L. Ammoua, A. Ben-Ismaïl, X. Davoine, G. Gallot, J.-P. Goddet, E. Lefebvre, V. Malka, and J. Faure, Few femtosecond, few kiloampere electron bunch produced by a laser-plasma accelerator, *Nat. Phys.* **7**, 219 (2011).
 - [3] A. Rousse, K. Ta Phuoc, R. Shah, A. Pukhov, E. Lefebvre, V. Malka, S. Kiselev, F. Burgy, J.-P. Rousseau, D. Umstadter, and D. Hulin, Production of a keV X-Ray Beam from Synchrotron Radiation in Relativistic Laser-Plasma Interaction, *Phys. Rev. Lett.* **93**, 135005 (2004).
 - [4] S. Kneip *et al.*, Bright spatially coherent synchrotron X-rays from a table-top source, *Nat. Phys.* **6**, 980 (2010).
 - [5] M. Fuchs, R. Weingartner, A. Popp, Z. Major, S. Becker, J. Osterhoff, I. Cortrie, B. Zeitler, R. Hörlein, G. D. Tsakiris, U. Schramm, T. P. Rowlands-Rees, S. M. Hooker, D. Habs, F. Krausz, S. Karsch, and F. Grüner, Laser-driven soft-X-ray undulator source, *Nat. Phys.* **5**, 826 (2009).
 - [6] K. Ta Phuoc, S. Corde, C. Thauray, V. Malka, A. Tafzi, J.-P. Goddet, R. C. Shah, S. Sebban, and A. Rousse, All-optical Compton gamma-ray source, *Nat. Photonics* **6**, 308 (2012).
 - [7] F. Albert and A. G. R. Thomas, Applications of laser wakefield accelerator-based light sources, *Plasma Phys. Controlled Fusion* **58**, 103001 (2016).
 - [8] Z. H. He, B. Hou, V. Lebailly, J. A. Nees, K. Krushelnick, and A. G. R. Thomas, Coherent control of plasma dynamics, *Nat. Commun.* **6**, 7156 (2015).
 - [9] V. Malka, J. Faure, Y. A. Gauduel, E. Lefebvre, A. Rousse, and K. Ta Phuoc, Principles and applications of compact laser-plasma accelerators, *Nat. Phys.* **4**, 447 (2008).
 - [10] B. Hidding, O. Karger, T. Königstein, G. Pretzler, G. G. Manahan, P. McKenna, R. Gray, R. Wilson, S. M. Wiggins, G. H. Welsh, A. Beaton, P. Delinikolas, D. A. Jaroszynski, J. B. Rosenzweig, A. Karmakar, V. Ferlet-Cavrois, A. Costantino, M. Muschitiello, and E. Daly, Laser-plasma-based Space Radiation Reproduction in the Laboratory, *Sci. Rep.* **7**, 42354 (2017).
 - [11] G. Sciaïni and R. J. D. Miller, Femtosecond electron diffraction: heralding the era of atomically resolved dynamics, *Rep. Prog. Phys.* **74**, 096101 (2011).
 - [12] Z.-H. He, B. Beaurepaire, J. A. Nees, G. Gallé, S. A. Scott, J. R. S. Pérez, M. G. Lagally, K. Krushelnick, A. G. R. Thomas, and J. Faure, Capturing structural dynamics in crystalline silicon using chirped electrons from a laser wakefield accelerator, *Sci. Rep.* **6**, 36224 (2016).
 - [13] Y. Muroya, M. Lin, Z. Han, Y. Kumagai, A. Sakumi, T. Ueda, and Y. Katsumura, Ultra-fast pulse radiolysis: A review of the recent system progress and its application to study on initial yields and solvation processes of solvated electrons in various kinds of alcohols, *Radiat. Phys. Chem.* **77**, 1176 (2008).
 - [14] Z.-H. He, B. Hou, J. H. Easter, J. Faure, K. Krushelnick, J. A. Nees, and A. G. R. Thomas, High repetition-rate wakefield electron source generated by few-millijoule, 30 fs laser pulses on a density downramp, *New J. Phys.* **15**, 053016 (2013).
 - [15] B. Beaurepaire, A. Vernier, M. Bocoum, F. Böhle, A. Jullien, J.-P. Rousseau, T. Lefrou, D. Douillet, G. Iaquaniello, R. Lopez-Martens, A. Lifschitz, and J. Faure, Effect of the Laser Wave Front in a Laser-Plasma Accelerator, *Phys. Rev. X* **5**, 031012 (2015).
 - [16] F. Salehi, A. J. Goers, G. A. Hine, L. Feder, D. Kuk, B. Miao, D. Woodbury, K. Y. Kim, and H. M. Milchberg, MeV electron acceleration at 1 kHz with < 10 mJ laser pulses, *Opt. Lett.* **42**, 215 (2017).
 - [17] A. Pukhov and J. Meyer-ter-Vehn, Laser wake field acceleration: the highly non-linear broken-wave regime, *Appl. Phys. B* **74**, 355 (2002).
 - [18] D. Guénot, D. Gustas, A. Vernier, B. Beaurepaire, F. Böhle, M. Bocoum, M. Lozano, A. Jullien, R. Lopez-Martens, A. Lifschitz, and J. Faure, Relativistic electron beams driven by kHz single-cycle light pulses, *Nat. Photonics* **11**, 293 (2017).
 - [19] A. Pak, K. A. Marsh, S. F. Martins, W. Lu, W. B. Mori, and C. Joshi, Injection and Trapping of Tunnel-Ionized Electrons into Laser-Produced Wakes, *Phys. Rev. Lett.* **104**, 025003 (2010).

- [20] C. McGuffey, A. G. R. Thomas, W. Schumaker, T. Matsuoka, V. Chvykov, F. J. Dollar, G. Kalintchenko, V. Yanovsky, A. Maksimchuk, K. Krushelnick, V. Y. Bychenkov, I. V. Glazyrin, and A. V. Karpeev, Ionization Induced Trapping in a Laser Wakefield Accelerator, *Phys. Rev. Lett.* **104**, 025004 (2010).
- [21] O. Lundh, C. Rechatin, J. Lim, V. Malka, and J. Faure, Experimental Measurements of Electron-Bunch Trains in a Laser-Plasma Accelerator, *Phys. Rev. Lett.* **110**, 065005 (2013).
- [22] S. P. D. Mangles, G. Genoud, M. S. Bloom, M. Burza, Z. Najmudin, A. Persson, K. Svensson, A. G. R. Thomas, and C.-G. Wahlström, Self-injection threshold in self-guided laser wakefield accelerators, *Phys. Rev. ST Accel. Beams* **15**, 011302 (2012).
- [23] S. P. D. Mangles, C. D. Murphy, Z. Najmudin, A. G. R. Thomas, J. L. Collier, A. E. Dangor, E. J. Divall, P. S. Foster, J. G. Gallacher, C. J. Hooker, D. A. Jaroszynski, A. J. Langley, W. B. Mori, P. A. Norreys, F. S. Tsung, B. R. Walton, and K. Krushelnick, Monoenergetic beams of relativistic electrons from intense laser-plasma interactions, *Nature (London)* **431**, 535 (2004).
- [24] C. G. R. Geddes, C. Tóth, J. van Tilborg, E. Esarey, C. B. Schroeder, D. Bruhwiler, C. Nieter, J. Cary, and W. P. Leemans, High-quality electron beams from a laser wakefield accelerator using plasma-channel guiding, *Nature (London)* **431**, 538 (2004).
- [25] J. Faure, Y. Glinec, A. Pukhov, S. Kiselev, S. Gordienko, E. Lefebvre, J.-P. Rousseau, F. Burgy, and V. Malka, A laser-plasma accelerator producing monoenergetic electron beams, *Nature (London)* **431**, 541 (2004).
- [26] W. Lu, M. Tzoufras, C. Joshi, F. S. Tsung, W. B. Mori, J. Vieira, R. A. Fonseca, and L. O. Silva, Generating multi-GeV electron bunches using single stage laser wakefield acceleration in a 3D nonlinear regime, *Phys. Rev. ST Accel. Beams* **10**, 061301 (2007).
- [27] B. Beaulieu, A. Lifschitz, and J. Faure, Electron acceleration in sub-relativistic wakefields driven by few-cycle laser pulses, *New J. Phys.* **16**, 023023 (2014).
- [28] S. C. Rae, Ionization-induced defocusing of intense laser pulses in high-pressure gases, *Opt. Commun.* **97**, 25 (1993).
- [29] K. Schmid and L. Veisz, Supersonic gas jets for laser-plasma experiments, *Rev. Sci. Instrum.* **83**, 053304 (2012).
- [30] F. Böhle, M. Kretschmar, A. Jullien, M. Kovacs, M. Miranda, R. Romero, H. Crespo, U. Morgner, P. Simon, R. Lopez-Martens, and T. Nagy, Compression of CEP-stable multi-mJ laser pulses down to 4 fs in long hollow fibers, *Laser Phys. Lett.* **11**, 095401 (2014).
- [31] A. Lifschitz, X. Davoine, E. Lefebvre, J. Faure, C. Rechatin, and V. Malka, Particle-in-Cell modelling of laser-plasma interaction using Fourier decomposition, *J. Comput. Phys.* **228**, 1803 (2009).
- [32] R. Nuter, L. Gremillet, E. Lefebvre, A. Lévy, T. Ceccotti, and P. Martin, Field ionization model implemented in Particle In Cell code and applied to laser-accelerated carbon ions, *Phys. Plasmas* **18**, 033107 (2011).
- [33] Y. Glinec, J. Faure, L. L. Dain, S. Darbon, T. Hosokai, J. J. Santos, E. Lefebvre, J. P. Rousseau, F. Burgy, B. Mercier, and V. Malka, High-Resolution γ -Ray Radiography Produced by a Laser-Plasma Driven Electron Source, *Phys. Rev. Lett.* **94**, 025003 (2005).
- [34] J. Faure, B. van der Geer, B. Beaulieu, G. Gallé, A. Vernier, and A. Lifschitz, Concept of a laser-plasma-based electron source for sub-10-fs electron diffraction, *Phys. Rev. Accel. Beams* **19**, 021302 (2016).

A review of recent progress on laser-plasma acceleration at kHz repetition rate

J Faure , D Gustas, D Guénot, A Vernier, F Böhle, M Ouillé , S Haessler, R Lopez-Martens and A Lifschitz

LOA, ENSTA ParisTech, CNRS, Ecole polytechnique, Palaiseau, France

E-mail: jerome.faure@ensta.fr

Received 10 July 2018, revised 5 September 2018

Accepted for publication 11 September 2018

Published 13 November 2018



CrossMark

Abstract

We report on recent progress on laser-plasma acceleration using a low energy and high-repetition rate laser system. Using only few millijoule laser energy, in conjunction with extremely short pulses composed of a single optical cycle, we demonstrate that the laser-plasma accelerator (LPA) can be operated close to the resonant blowout regime. This results in the production of high charge electron beams (>10 pC) with peaked energy distributions in the few MeV range and relatively narrow divergence angles. We highlight the importance of the plasma density profile and gas jet design for the performance of the LPA. In this extreme regime of relativistic laser-plasma interaction with near-single-cycle laser pulses, we find that the effect of group velocity dispersion and carrier envelope phase can no longer be neglected. These advances bring LPAs closer to real scientific applications in ultrafast probing.

Keywords: laser-plasma accelerator, relativistic laser-plasma interaction, single-cycle laser pulse, high-repetition rate plasma accelerator

(Some figures may appear in colour only in the online journal)

1. Introduction

Electron accelerators play a major role in material science: electron microscopes and synchrotron light sources are currently the most advanced tools for studying condensed matter at the atomic level. In an electron microscope, sub-300 keV particles are used to image crystal lattices with Angström resolution, either in real space or in reciprocal space via diffraction. In synchrotrons, x-rays with energies ranging from 10 eV to 10 keV are used for a variety of spectroscopies, such as photoemission, diffraction and absorption, and provide a wealth of valuable information on the electronic and lattice structure of matter. These techniques provide static information and allow scientists to study materials in their ground state. The past two decades have been witnessing tremendous progress in the study of ultrafast structural dynamics based on the development of pump-probe experiments [1, 2]. The fundamental motivation is to bring matter in out-of-equilibrium conditions and to explore the relaxation pathways that the system follows. Further goals could be to create new exotic excited states and to use light to control phenomena such as magnetism [3] or super-conductivity [4]. Here again,

the most powerful tools are accelerator based: ultrafast electron microscopes [5], pulsed electron guns [6, 7] for ultrafast electron diffraction (UED), or x-ray free electron lasers [8]. These sources have been used successfully to unravel ultrafast dynamics in a large variety of materials [1, 2, 6]. It is important to note that most of these accelerators operate at high repetition rate, typically more than 1 kHz. In addition, although electron bunches shorter than 20 fs can now be produced [9], reaching temporal resolution below 100 fs remains a challenge due to time jitter between the radio-frequency (RF) field and the laser. This time jitter is inherent to RF accelerator technology and no technique can completely suppress it so far.

In this context, laser-plasma accelerators (LPAs) might be of interest when very short time resolutions (sub-100 fs or even sub-10 fs) are desirable. Laser-plasma acceleration [10, 11] is an emerging technique for accelerating electrons to high energies over very short distances. The accelerated electron bunches may have femtosecond duration [12, 13], and are in principle perfectly synchronized with the laser pulses, making them particularly relevant for applications such as ultrafast imaging [1] or femtosecond x-ray generation

[14, 15]. However, most LPAs currently rely on 100 TW class or even PW laser systems at low repetition rate (≤ 1 Hz), which limits their practical use. Increasing the repetition rate to the kHz range is important for a wide range of reasons. First, at kHz repetition rate, lasers reach a thermal steady state and are more stable, which should translate into a higher level of stability for the electron beam. Second, it opens up the possibility of active feedback control and beam optimization [16]; third, it enables rapid averaging over many shots, thereby significantly increasing the signal-to-noise ratio of a measurement. Finally, it can boost the average current of the electron source by several orders of magnitude. With current laser technology, increasing the repetition rate implies smaller laser systems at the sub-10 TW level, but also lower energy electron beams. However, the 5–10 MeV range is well-suited for applications such as UED or pulsed radiolysis [17], that would greatly benefit from the higher stability and the improved signal-to-noise ratio.

Recently, there have been attempts to use kiloHertz lasers with energies in the 10 mJ range for laser-plasma acceleration experiments. Initial experiments produced sub-relativistic electrons with relatively low charge and relied on density down ramp injection [18, 19]. The measured electron beams exhibited enhanced stability and a proof-of-principle UED experiment was carried out [20, 21], demonstrating the potential of LPAs for probing ultrafast dynamics in materials. In [22], relativistic electron beams at kHz repetition rate were obtained using ultra-high density gas targets. This experiment operated in the self-modulated regime, resulting in a fairly divergent beam with a maxwellian energy distribution. Finally, kHz electron sources based on laser-plasma interaction with solid targets [23, 24] or liquid targets [25] have also been demonstrated. Even though relativistic electrons were obtained, the very large divergence of the electron beam currently makes these sources unsuitable for the above mentioned applications. Indeed, transporting and focusing electron beams with large divergence angles and energy spreads is nearly impossible unless a large amount of charge is thrown away, resulting in a very low electron flux.

In this article, we review our recent achievements in the field of high-repetition rate LPA. Our approach was to find a regime in which electron beams have superior beam quality and multi-MeV energies. It is well established that the blowout, or bubble regime of laser-plasma acceleration [26–30] leads to the production of high-quality relativistic electron beams with a narrow energy spread and small divergence. In this regime, the laser pulse is transversely and longitudinally resonant with the plasma wavelength λ_p , i.e. its longitudinal and transverse sizes are comparable to λ_p : $c\tau \approx w_0 \approx \lambda_p/2$, where c is the speed of light, τ the pulse duration, and w_0 the laser beam waist. In order to reach the resonance condition with few-mJ laser kHz systems, we demonstrate that it is necessary to use near-single-cycle laser pulses with sub-4 fs durations. The paper is organized as follows: section 2 discusses scaling laws and experimental design issues, section 3 displays the main results on electron beam production while section 4 focuses on the specificities of relativistic laser-plasma interaction using near-single-cycle laser pulses.

2. Specificity of laser-plasma acceleration at kHz repetition rate

2.1. Scaling laws

Scaling laws for LPAs have been available for more than a decade. Although there are several ways to design and operate an LPA, the blowout (or bubble) regime is favorable for obtaining high gradient acceleration, high quality electron beams with low divergence and narrow energy spread, provided that injection is controlled. Therefore, here, we rely on the scaling laws developed by Lu in [31] for reaching the blowout regime and generating strongly nonlinear plasma wakefields.

In this regime, the laser pulse drives a nonlinear wake which has the shape of a near-spherical cavity of radius R . Evidently, the laser can drive the wakefield most efficiently in the resonant regime, which requires its transverse (waist w_0) and longitudinal (pulse length $c\tau$) dimensions to be close to R . The first condition focuses on transverse resonance: the laser pulse should be transversely matched to the plasma wavelength, i.e. the transverse ponderomotive force exerted on electrons is balanced by the transverse restoring force of the ion cavity:

$$k_p w_0 = k_p R = 2\sqrt{a_0}, \quad (1)$$

where $w_0 \simeq R$ and a_0 is the normalized vector potential. In addition, the interaction between the laser pulse and the plasma wave creates etching of the front of the pulse via energy depletion and red shifting of the laser light [32–34]. This pulse erosion occurs at velocity v_{etch} and causes the pulse to be fully etched after a distance $L_{\text{etch}} = \omega_0^2 / \omega_p^2 c\tau$. By etching the pulse front, this erosion also causes an effective decrease of the pulse group velocity, therefore impacting the wakefield phase velocity $v_\phi = v_g - v_{\text{etch}}$, where v_g is the laser linear group velocity. Consequently, electron acceleration is limited by dephasing with respect to the accelerating structure (i.e. the wakefield). The dephasing length reads:

$$L_{\text{deph}} = \frac{c}{c - v_\phi} R = \frac{2}{3} \frac{\omega_0^2}{\omega_p^2} R.$$

We then assume that wakefield excitation and electron acceleration are optimal when all the etching occurs during the dephasing length and equating $L_{\text{etch}} = L_{\text{deph}}$ leads to the second condition on the pulse duration:

$$c\tau = \frac{2R}{3} \simeq \frac{2w_0}{3}. \quad (2)$$

When both transverse and longitudinal boundary conditions are met, the wakefield maximum amplitude is $E_z = E_0 \sqrt{a_0}$, where $E_0 = m_e c \omega_p / e$ is the cold wavebreaking field. The maximum electron energy gain is then:

$$\frac{\Delta E}{m_e c^2} = \frac{2}{3} \frac{\omega_0^2}{\omega_p^2} a_0. \quad (3)$$

Finally, we conclude with considerations on laser propagation. Propagation is crucial as many experiments have shown that the onset of self-focusing is in general correlated with

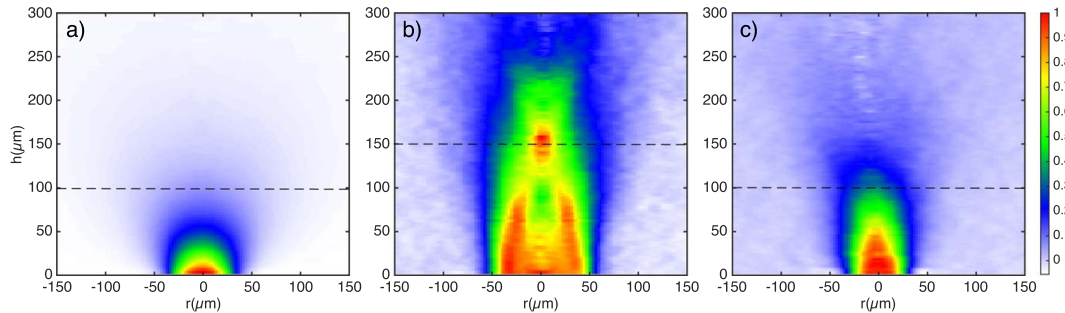


Figure 1. Nitrogen molecular density map $n_{N_2}(r, h)$ (a) for the subsonic nozzle, (b) for the shock jet case and (c) for the supersonic nozzle. The density is normalized to allow for a direct comparison of the jet distribution.

Table 1. Scaling laws for laser-plasma accelerators in the blowout regime, assuming a $\lambda_0 = 0.8 \mu\text{m}$ laser wavelength. Different laser peak powers are considered, from multi-Joule, PetaWatt laser systems to millijoule, TeraWatt system.

Laser class	a_0 (a_{0c})	E_L	τ (fs)	w_0	z_R	n_e (cm^{-3})	L_{deph}	ΔE
0.5 PW	4.8 (4.8)	30 J	60 fs	26 μm	2.6 mm	$6.6 \times 10^{17} \text{cm}^{-3}$	4.5 cm	4.2 GeV
30 TW	3.5 (3.3)	1 J	25 fs	10 μm	0.4 mm	$4.2 \times 10^{18} \text{cm}^{-3}$	2.8 mm	500 MeV
1 TW	2 (1.8)	3 mJ	5 fs	2.1 μm	18 μm	10^{20}cm^{-3}	25 μm	10 MeV

strong injection of electrons, regardless of the injection mechanism. Therefore, for scaling and design reasons, we assume that parameters should be chosen so that the self-focusing threshold is reached. The usual threshold for relativistic self-focusing requires the laser peak power to satisfy $P/P_c > 1$, where P_c is the power for relativistic self-focusing [35, 36]. However, this relation does not hold in the blowout regime because the wakefield has a predominant effect on propagation. In [31], Lu uses heuristic arguments to define a new threshold $a_0 > a_{0c} \simeq (n_e/n_c)^{1/5}$. This is the third condition that we will use for our scaling considerations.

In practice, for designing a LPA in the blowout regime, we start with a given laser energy E_L and wavelength λ_0 . We fix the value of a_0 , which *in fine* will have to satisfy $a_0 > a_{0c}$. Knowing the value of a_0 and using equation (2), we obtain a value for the pulse duration and the pulse waist. With equation (1), it is then possible to find the optimum plasma wavelength, i.e. the optimum electron density for the plasma. Table 1 shows typical design parameters for LPA, using Joule-class to millijoule-class laser systems. These scalings are confirmed by a large body of experiments, giving 100s MeV beams with 30 TW class lasers [28–30] and GeV beams with PW lasers [37, 38].

The scaling at low energy is of particular interest to our work. Indeed, it shows that mJ lasers are sufficient to reach the blowout regime provided that extremely short laser pulses (here 5 fs) are used. Indeed, lasers in this energy range are available at kHz repetition rate and reaching few cycle pulse duration can be achieved through post-compression techniques [39]. The electron energy, in the 10 MeV range, is relevant for some of the applications that were mentioned earlier, provided that the duration of the electron bunch is on the order of a few femtoseconds.

2.2. Experimental considerations

In addition to the few-cycle pulse duration, the previous scalings show that resorting to mJ and high-repetition-rate systems lead to a number of new challenges. First, all distances are shrunk to the micrometer scale (versus the more accessible millimeter scale for the 30 TW case): the dephasing length and the Rayleigh length are both only 10–20 μm calling for extremely thin gas targets. The most important issue originates from laser beam propagation: with a Rayleigh length of $z_R < 20 \mu\text{m}$, diffraction through the gas jet is a critical effect. Therefore, density gradients should be on the order of z_R , or even smaller, for optimizing the coupling of the laser pulses into the jet and avoiding ionization-induced defocusing [40]. Second, the nozzle needs to provide a high electron density in excess of $n_e = 10^{20} \text{cm}^{-3}$ in order to reach the resonant regime. Such density should be reached at least 100 μm above the jet opening so that the laser does not damage the gas nozzle. Finally, the gas jet should provide a continuous gas flow in order to enable operation at high repetition rates. This is a considerable challenge for the vacuum pumping system as it needs to keep the background pressure in the chamber below 10^{-2} mbar. All these considerations put stringent constraints on the gas nozzle design. An optimized nozzle should typically minimize the mass flow while maximizing the density well above its opening.

We have designed, characterized and implemented three different gas nozzles, resulting in significant differences in the accelerated electron beams. In figure 1, we compare a 100 μm diameter cylindrical subsonic flow nozzle to a ‘shocked’ jet, implying a supersonic De Laval nozzle with a slight wall bending close to the exit to create an oblique shock, and finally a simple supersonic conical De Laval nozzle with a

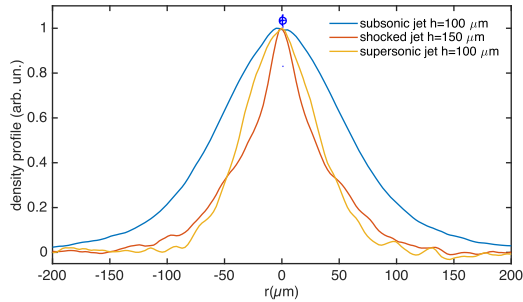


Figure 2. Normalized density profiles obtained at various heights (see dashed line in figures 1(a)–(c)). The blue cross at $r = 0$ represents the error bar for these measurements. The backing pressure was $P = 45$ bars, giving the following peak molecular density $n_{N_2} = 3 \times 10^{19} \text{ cm}^{-3}$ for the subsonic nozzle, $n_{N_2} = 2.3 \times 10^{19} \text{ cm}^{-3}$ shocked nozzle and $n_{N_2} = 2.3 \times 10^{19} \text{ cm}^{-3}$ for the supersonic jet. (c) The FWHM width is $125 \mu\text{m}$, $50 \mu\text{m}$ and $70 \mu\text{m}$ respectively.

$40 \mu\text{m}$ throat [41]. The nozzles were specially manufactured by micro spark erosion which is necessary for reaching sub- $100 \mu\text{m}$ dimensions. The gas jets were characterized with a quadriwave lateral shearing interferometer (SID4 HR by PHASICS) and the density maps are obtained via Abel inversion of the measured phase maps.

Line-outs of the density profiles are shown in figure 2. The subsonic jet provides a gaussian-like density profile with the largest width of $125 \mu\text{m}$ full width half maximum (FWHM) and smooth density gradients. Note that the density falls down very rapidly with the height because of the subsonic nature of the flow. In the shocked jet, the shock lines converge to produce a density peak located at $h = 150 \mu\text{m}$. The density peak is quite sharp, with a FWHM of $50 \mu\text{m}$, but it is preceded by a longer pedestal. Finally, the supersonic jets also provides a thin jet plume of $70 \mu\text{m}$ with rather sharp gradients. Both the shocked and the supersonic nozzles permit to obtain high densities above $100 \mu\text{m}$ while minimizing the mass flow and the load on the pumping system by a rough factor of 4, compared to the cylindrical nozzle. Finally, in all experiments described in this paper, nitrogen gas was used because each nitrogen molecule releases 10 electrons assuming immediate ionization of nitrogen to N^{3+} . Therefore, the required high electron density can be achieved while keeping the background pressure in the vacuum chamber at a reasonable level.

2.3. Experimental set-up

The experimental set-up is represented in figure 3. The experiments at LOA were performed using the Salle Noire laser system delivering down to 3.5 fs pulses (< 1.5 optical cycle at $\lambda_0 \approx 800 \text{ nm}$) at 1 kHz with $2\text{--}3 \text{ mJ}$ of energy on target [39]. Several focusing parabolas were tested, with f -number of $f/2$ and $f/3$, leading to near-Gaussian focal spots with dimensions ranging from 2.5 to $3.5 \mu\text{m}$ (FWHM), implying an approximate

Rayleigh range of $20\text{--}50 \mu\text{m}$ depending on the focusing conditions. Therefore, the maximum vacuum intensity was in the range $I_{\text{vac}} \approx 3\text{--}6 \times 10^{18} \text{ W cm}^{-2}$, estimated using the real focal spot image. An electron detection setup, independently calibrated at a linear accelerator facility and consisting of a CsI (TI) phosphor screen, imaging lenses and a CCD camera, was used to measure the charge and visualize the electron spot. A pinhole and a pair of cylindrical permanent magnets could be inserted into the beam path to measure electron spectra.

3. Results on electron source generation at kHz repetition rate

All electron beam and spectrum images presented in this article were obtained by exposing the CCD camera during 1 ms to 1 s , corresponding to accumulation over $1\text{--}1000$ shots, depending on experimental conditions. Statistics were typically obtained by acquiring a sequence of $10\text{--}20$ images, from which the average value and standard deviations can be extracted. We always present typical results, rather than best results, in order to give a faithful account of the reality of the experiment.

3.1. Relativistic electron beams from subsonic gas jets

In the first experiments, we started by using the cylindrical nozzles, providing a wider gas jet [42]. The $f/3$ focusing parabola provided a slightly smoother focusing and the Rayleigh length was estimated to be $\approx 50 \mu\text{m}$. With a pulse duration of 3.4 fs and a density of $n_e \approx 1.2 \times 10^{20} \text{ cm}^{-3}$, $c\tau \approx \lambda_p/3$, i.e. we operated close to the resonant condition. Typical results on the electron beam are shown in figure 4.

As seen in the inset of figure 4, the beam has a rather small divergence of $\sim 35 \text{ mrad}$ FWHM. The beam pointing stability is high, with fluctuations amounting to a small fraction of the beam divergence, typically a few mrad. The electron energy is peaked at 6 MeV and extends to about 9 MeV . Note that the gray shaded area around the electron spectrum represents the standard deviation of the electron distribution, showing that the acceleration mechanism is robust. Concerning the charge, we found a strong dependence on the electron density, which can be increased by sending the laser closer to the nozzle or by increasing the backing pressure. While an injected beam starts to appear for $n_e > 1 \times 10^{20} \text{ cm}^{-3}$, the charge goes up to 500 fC /shot when the density approaches $2 \times 10^{20} \text{ cm}^{-3}$. Obtaining higher charges was challenging because it required bringing the gas jet closer to the laser, resulting in target damage, or increasing the backing pressure resulting in a failure of the turbomolecular pumps.

The measured electrons beams, with their relatively small divergence and peaked energy distribution, show typical features of acceleration in nonlinear, bubble-like wakefields. We used PIC simulations to investigate the electron trapping and acceleration mechanisms. Simulations were performed using CalderCirc [43], a fully electromagnetic 3D code based on cylindrical coordinates (r, z) and Fourier decomposition in

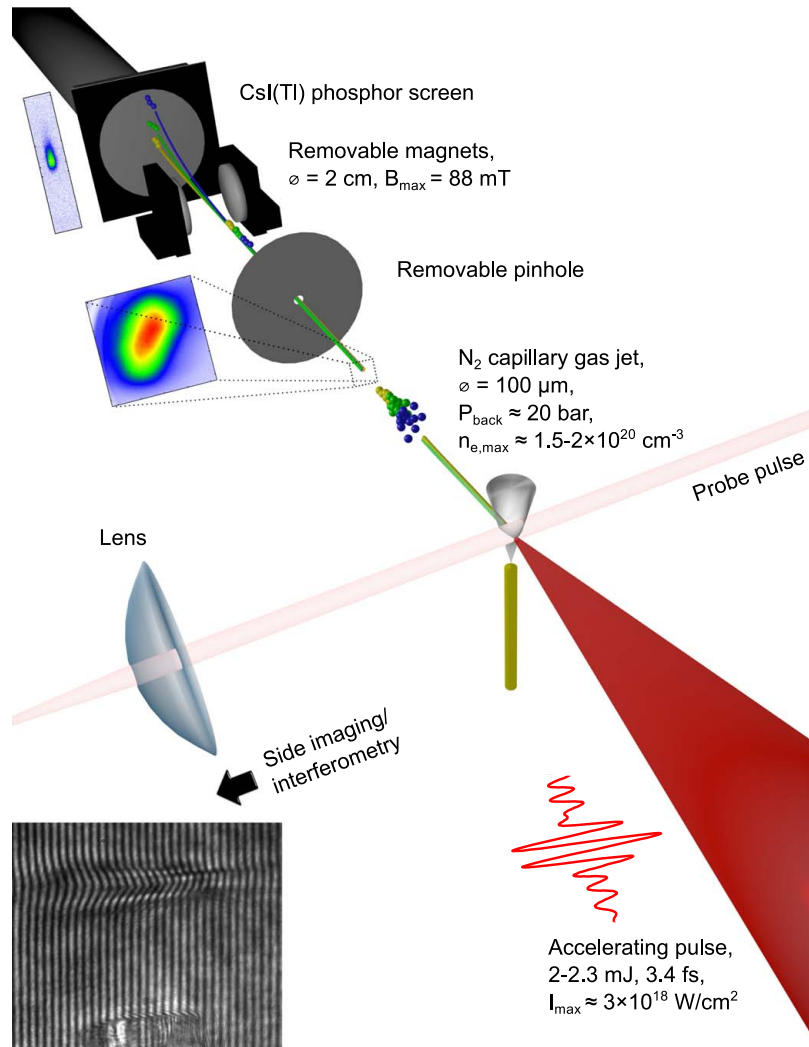


Figure 3. Schematic of the experimental set-up. From [42] Guénot *et al*, 2017 *Nat. Photonics* **11**, 293.

the poloidal direction. All simulations presented in this work were performed using a mesh with $\Delta z = 0.1 k_0^{-1}$ and $\Delta r = 0.5 k_0^{-1}$ (where $k_0 = (2\pi\lambda_0)^{-1}$ is the laser wave vector and $\lambda_0 = 800$ nm), and the two first Fourier modes (simulations with up to 5 modes essentially converge to the same results, see [44]). The simulation box is large enough ($32 \lambda_0$) compared to the radius of the laser, so that there are no issues at the boundary. The neutral gas density profile was taken from the experimental data. The simulations start with pure neutral nitrogen, which is ionized via tunnel ionization, as described in [45]. The number of macro-particles per cell before ionization is 500, which corresponds to $500 \times 5 = 2500$ macro-electrons per cell in the region of full ionization of the L-shell of nitrogen. Finally we found that in order to

reproduce the experimental results, it was necessary to use the exact experimental density profile of figure 2(a) as well as the actual experimental laser spectrum and spectral phase. Indeed, using a simple gaussian laser pulse centered at 800 nm resulted in a significant overestimation of the injected charge. The simulation was run with a vacuum laser amplitude at focus of $a_{0,vac} = 1.17$, corresponding to $I = 3 \times 10^{18} \text{ W cm}^{-2}$ and a nitrogen atomic density of $n_{N_2} = 3.2 \times 10^{19} \text{ cm}^{-3}$, corresponding to $n_e = 1.6 \times 10^{20} \text{ cm}^{-3}$ after ionization of the L-shell.

Figure 5(a) shows quantitative agreement between experiments and simulations: a 5 MeV beam is obtained with ~ 20 mrad divergence and 400 fC charge. The computed transverse normalized emittance is $\epsilon_n = 0.3 \times 0.7 \text{ mm.mrad}$. The only significant difference is visible on the beam

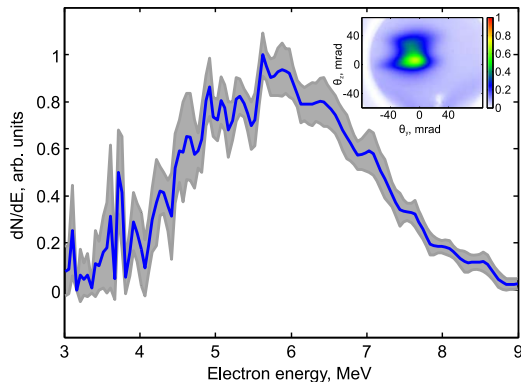


Figure 4. Multi-MeV electron beam obtained using the cylindrical nozzle providing a subsonic flow: electron energy distribution and transverse distribution (inset). Data were taken by accumulating over 1000 shots. The blue curve represents the average normalized spectrum, while the gray area represents $2\sigma_{rms}$. The estimated electron density was $n_e \approx 1.2 \times 10^{20} \text{ cm}^{-3}$, the estimated laser peak intensity $\sim 2.5 \times 10^{18} \text{ W cm}^{-2}$ for an energy of 2.1 mJ, a pulse duration of 3.4 fs. The electron beam has a charge of 120 fC/shot, 35 mrad divergence at FWHM.

transverse distribution which is elongated along the laser polarization direction in the simulation. This might be due to the fact that the electron distribution is computed at the exit of the gas jet while it is measured 20 cm downstream in the experiment. Space charge forces could further increase the beam divergence and erase the initial beam asymmetry. In figure 5(b) shows the evolution of the laser amplitude and injected electrons during propagation. Clearly the laser undergoes self-focusing as it reaches $a_0 = 1.5 > a_{0,vac}$, around the middle of the plasma where the density is resonant with the laser pulse. At this point, the laser pulse is able to excite a high-amplitude wakefield, see figure 5(c). In addition, at this high intensity, N^{5+} is ionized through tunnel ionization, triggering electron injection into the wakefield [46, 47]. The simulation confirms that injected electrons all originate from ionization of the L-shell of nitrogen. The yellow bars in figure 5(b) also show that this ionization injection mechanism is very well localized, eventually leading to a rather peaked electron distribution. Local injection is an indirect but striking consequence of the violent nonlinear pulse evolution: the intensity stays high only over a very short distance in the plasma, i.e. when the laser pulse is simultaneously short and focused. Consequently, electrons are injected in the first cavity following the laser pulse, leading to a single electron bunch with duration ~ 1 fs, as illustrated in figure 5(d).

3.2. Results with shocked jets

While acceleration in subsonic jets was successful, obtaining reproducible accelerator performance on a day-to-day basis remained a challenging task as we operated rather close to the injection threshold. The wide density profile obtained in subsonic flows is not optimal for coupling the laser beam into

the plasma: it is likely that there is a competition between ionization induced refraction and self-focusing at the entrance of the plasma. When self-focusing is not strong enough, the intensity required for ionization injection might not be reached and the electron beam is not generated. In order to circumvent this problem, we performed experiments with the shocked gas jets with the idea that very sharp gradients might help coupling into the gas jets.

Typical results are presented in figure 6 which shows that this regime is not very favorable: the divergence is large, >100 mrad and the energy distribution does not reach beyond 1 MeV. Obtaining the electron beam was however much easier and could be done routinely. In particular, all technical problems related to pumping the high gas load were solved since similar electron densities could be reached while minimizing the gas mass flow compared to the previous case. Because the performance of the LPA was not satisfactory in this regime, we did not investigate the physics in details through simulations. A possible scenario is that electrons are injected in the density downramp as in [18, 48, 49] at the exit of the gas jet. Since there is no plasma medium after the downramp, the acceleration could remain limited and explain the low energy gain.

3.3. High charge electron beams from supersonic jets

In principle, supersonic jets provide an optimal coupling between the laser and the plasma because they have sharp gradients. In comparison to the previous case of the shocked jet, the plasma is longer so that self-focusing and electron acceleration should be able to occur. In this series of experiments, we used a tighter focusing geometry with the $f/2$ off-axis parabola in order to operate well above threshold [44]. The laser pulse was focused down to $\approx 2.5 \mu\text{m}$, providing intensities of $5\text{--}6 \times 10^{18} \text{ W cm}^{-2}$, implying that the threshold for tunnel ionization of N^{5+} ions could be reached even in the absence of self-focusing.

Typical results are presented in figure 7. We observed electron beams with a double peaked energy distribution in the few MeV range and with a divergence of 42×77 mrad were observed. The striking feature is the increase of the beam charge by two orders of magnitude up to 19 pC/shot, confirming that the accelerator operated well-above threshold. This regime could be reproduced for weeks at a time and similar electron beams could be obtained routinely. This obviously is an important step toward the realization of an electron source suitable for application experiments.

In order to understand the injection mechanism and the dramatic increase in the electron charge, we performed PIC simulations with the numerical parameters presented above. The density profile was taken from the experimental data, assuming a nitrogen density of $n_N = 1/5 \times 1.7 \times 10^{20} \text{ cm}^{-3}$ at the center of the jet. The laser spectrum and spectral phase was again taken from experimental results and $a_{0,vac} = 1.44$. Simulation results are shown in figure 8 and confirm the general trend of experiments: a 10 pC beam is obtained with energy in the MeV range and a double peak in the energy distribution, see figure 8(a). The angular distribution is

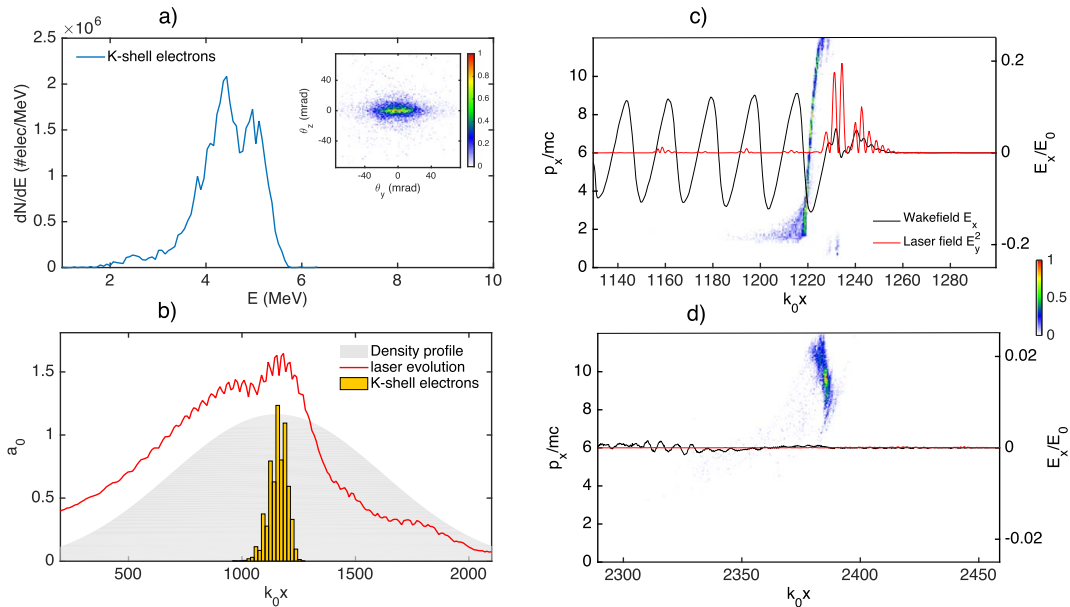


Figure 5. PIC simulations of electron acceleration in a subsonic gas flow. (a) Electron energy distribution and transverse distribution (inset). (b) Gray: gas jet profile; red curve: evolution of the laser amplitude a_0 along propagation. The yellow bars show the initial location of injected electrons. Analysis indicates that they all originate from ionization of N^{5+} ions. (c) and (d) represent electrons with energies larger than 1 MeV in the longitudinal phase space (x , p_x). The red curves represent the on-axis laser intensity $|E_y|^2$ and the black curve represents the on-axis longitudinal wakefield E_x/E_0 . (c) Shows the phase space just after injection has occurred, whereas (d) shows it at the exit of the plasma.

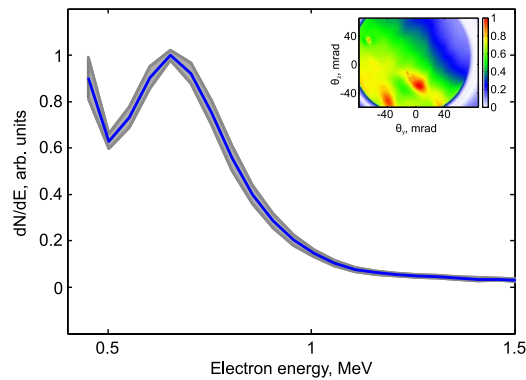


Figure 6. Typical electron beam obtained using the shocked nozzle: electron energy distribution and transverse distribution (inset). Data were taken by accumulating over 100 shots. The estimated electron density was $n_e \approx 1.2 \times 10^{20} \text{ cm}^{-3}$, the estimated laser peak intensity $\sim 3.5 \times 10^{18} \text{ W cm}^{-2}$ for an energy of 2.5 mJ, a pulse duration of 3.8 fs. The electron beam has a 600 fC/shot charge, >100 mrad divergence at FWHM.

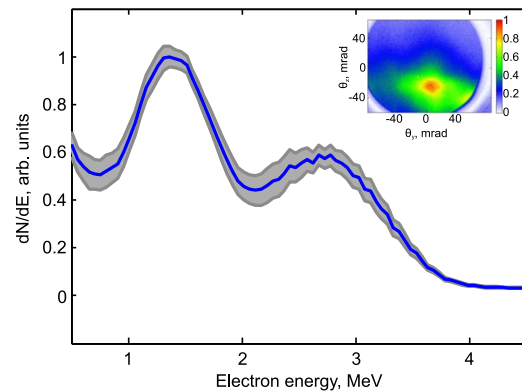


Figure 7. Typical electron beam obtained using the supersonic nozzle: electron energy distribution and transverse distribution (inset). Data were taken using single shot images. The estimated electron density was $n_e \approx 1.2 \times 10^{20} \text{ cm}^{-3}$, the estimated laser peak intensity $\sim 5.5 \times 10^{18} \text{ W cm}^{-2}$ for an energy of 2.6 mJ, a pulse duration of 3.8 fs. The electron beam has a 19 pC/shot charge, 42×77 mrad divergence at FWHM.

considerably narrower than in the experiment, indicating that space charge forces were likely to have an even larger effects on these high charge beams. In the simulation, the computed transverse normalized emittance is $\varepsilon_n = 0.9$ mm mrad. Detailed

analysis of the simulations indicate that two injection processes occur. The first one is identical to what has been discussed above: the laser pulse self-focuses to high intensities, $a_0 = 1.8$ which triggers massive ionization injection of K-shell electrons,

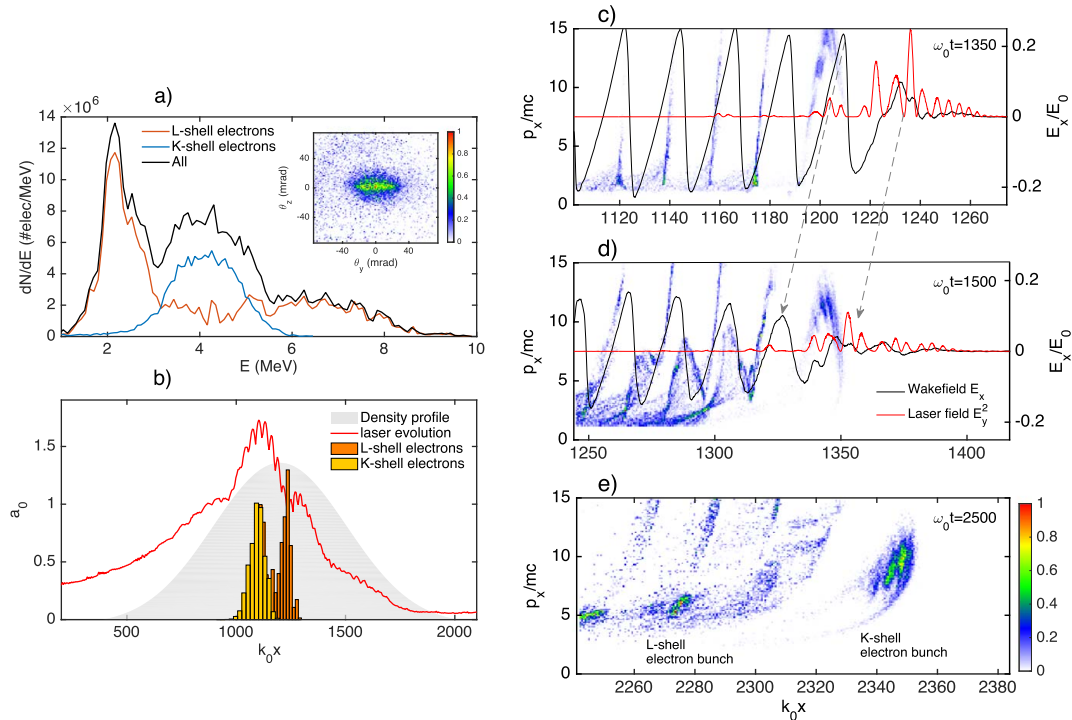


Figure 8. PIC simulations of electron acceleration in a supersonic gas flow. (a) Electron energy distribution and transverse distribution (inset). (b) Gray: gas jet profile; red curve: evolution of the laser amplitude a_0 along propagation. The yellow bars show injected electrons from the K-shell, and the orange bars from L-shell. (c), (d) and (e) show the electron distribution in phase space (x , p_x) at key moments: (c) after ionization injection, (d) after second injection, (e) at the exit of the plasma.

Table 2. Main parameters of the electron beam for the various experimental cases. σ_Q represents the rms fluctuations of the beam charge.

Case	Shots/image	Q /shot	σ_Q	Divergence	Point. stab.	E_{peak}
$f/3$, subsonic	1000	0.12 pC	17.4%	35 mrad	<0.7 mrad	5.6 MeV
$f/3$, shocked	100	0.62 pC	13.3%	>100 mrad	<1.5 mrad	0.7 MeV
$f/2$, supersonic	1	19 pC	14%	72×77 mrad	<4 mrad	2.7 (1.2) MeV

see yellow bars in figure 8(b). Ionization injection accounts for about a third of the charge (up to 3 pC) and produces a well-defined energy peak at 4 MeV. As the intensity decreases, a second injection mechanism occurs, injecting large amounts of L-shell electrons. A phase space representation, figures 8(c)–(e), shows that ionization injection produces trapped electrons in the first bucket while the second injection mechanism fills up several successive plasma buckets with about 7 pC, resulting in a longer electron bunch.

The second injection process is caused by the rapid nonlinear evolution of the laser pulse as it starts to be severely pump depleted. The mechanism was described in details in [50]: the laser pulse undergoes a strong red shift, visible in figures 8(c) and (d), causing its envelope to slip backwards because of the slower group velocity at red wavelengths. This results in a slow-down of the wakefield, see the gray arrows in

figures 8(c) and (d), and triggers the second injection event. Indeed, the slower phase velocity of the wakefield enables efficient trapping of electrons even if the laser amplitude is significantly decreased [50].

3.4. Comparison of different results

In table 2, we summarize the various parameters of the electron beams obtained with the different jets. The supersonic jet allowed us to produce high charge beams at relativistic energy with the highest level of reliability in terms of day-to-day operation. The shot-to-shot charge fluctuations are at the 10% rms level which is better than the other experimental cases where images were obtained by averaging over 100 or even 1000 shots. We still need to demonstrate that the accumulation of 1000 shots in this regime can bring down the

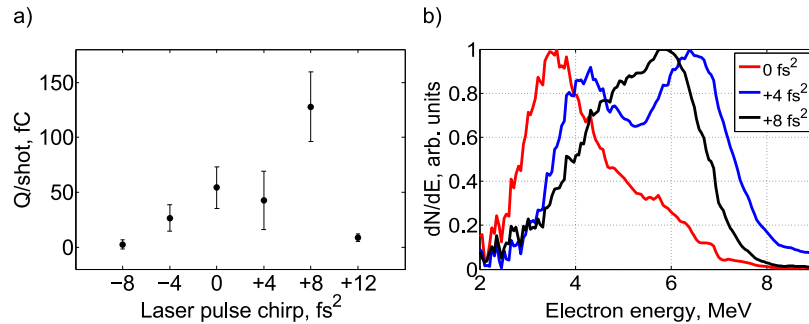


Figure 9. (a) Accelerated charge as a function of chirp introduced in the laser beam path. $+(-)4 \text{ fs}^2$ corresponds to an insertion (removal) of $100 \mu\text{m}$ of fused silica. (b) Corresponding electron spectra. This data were taken using a subsonic gas jet.

charge fluctuations to the percent level, which is needed for most applications. It should be noted that this level of fluctuations does not seem to come from the laser system: assuming that the pulse duration does not vary, recorded data of the focal spot indicates that the intensity varies by less than 1% rms, i.e. one order of magnitude better than the electron beam charge fluctuations.

In general, the large body of experimental data that we have accumulated allows us to conclude that the performance of the LPA in this regime is extremely sensitive to the gas jet density profile and backing pressure. Quite dramatic changes of the electron spectra were observed by translating the gas jet by $5 \mu\text{m}$ steps only, confirming that the physics is extremely sensitive to the details of the density distribution and that all phenomena occur at the micrometer scale. This calls for improved control of the density profile through advanced nozzle design.

Finally, we also note that in current experiments, the generation of the electron beam relies heavily on nonlinear pulse evolution, either via self-focusing for ionization injection or via pump depletion and red shifting for the second injection mechanism. This tends to amplify the role of fluctuations and it seems highly desirable to be able to operate in a regime where such nonlinear effects could be avoided. Density downramp injection might improve the current situation. In particular, tailoring the density profile with a sharp density downramp followed by a plateau could further stabilize the injection [51]. While this has been done previously using a blade inserted in the gas flow for producing a shock, the challenge will be to adapt this technique to sub- $100 \mu\text{m}$ nozzles.

4. Laser-plasma interaction in the few-cycle regime

The interaction between few/single-cycle laser pulse and a dense plasma at relativistic intensity is quite exotic and has not been studied previously, except for some cases in lower density plasmas [52]. Here we focus on these specificities and unveil new physical effects.

4.1. Group velocity dispersion effects

The near-single-cycle laser pulses used in the experiment have an ultra-broad spectral bandwidth, spanning over an entire octave, starting at 500 nm and reaching $1 \mu\text{m}$ wavelengths [39]. Therefore, the negative dispersion introduced by the plasma cannot be neglected during propagation [50]. In the linear limit, the pulse duration in the plasma evolves as $\tau(z) = \tau_0 \sqrt{1 + z^2/L_{\text{disp}}^2}$, where τ_0 is the rms Fourier transform limited duration and L_{disp} is the dispersion length scale in the plasma [50]:

$$L_{\text{disp}} \simeq 4\pi c^2 \tau_0^2 \frac{\lambda_p^2}{\lambda_0^3}, \quad (4)$$

For our parameters, the plasma introduces an accumulated chirp of -11.5 fs^2 in the center of the gas jet which corresponds to $L_{\text{disp}} \simeq 20 \mu\text{m}$ at the peak density. At the focal plane position, i.e. $25 \mu\text{m}$ (to $50 \mu\text{m}$) before the center of the jet, the accumulated chirp is -8.2 fs^2 (to -5.3 fs^2). This indicates that the negative dispersion of the plasma causes rapid stretching of the single-cycle laser pulse. Therefore, in experiments, we compensate plasma dispersion by adding a small positive chirp to the laser pulse. In practice, this is done by translating a pair of motorized fused-silica wedges to introduce some predominantly second-order chirp. Figure 9(a) shows that the electron beam charge is maximum when a small positive chirp of $+8 \text{ fs}^2$ is added to the laser pulse. This result was reproduced on multiple experimental runs, with the optimal chirp varying between $+4 \text{ fs}^2$ and $+8 \text{ fs}^2$, depending on the exact focal plane position. On the contrary, a negative chirp causes a decrease of the injected charge. Similarly, figure 9(b) shows that beam energy also increases when using a small positive chirp. This calls for a straightforward interpretation: a positive chirp compensates the negative plasma dispersion, allowing the laser pulse to reach higher intensities within the plasma. Consequently, the wakefield amplitude is higher, leading to higher injected charge and higher energy. PIC simulations however indicate that the pulse evolution is strongly nonlinear, as seen above and that simple arguments based on linear dispersion and propagation do not account for all the complexity of the physics. PIC simulations provide a

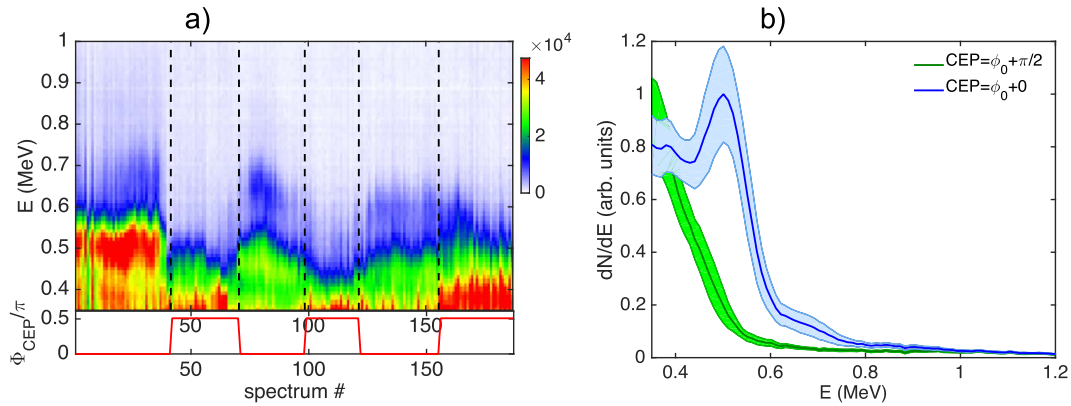


Figure 10. (a) Bottom: CEP switching between 0 and $\pi/2$, top: cascade plot of electron spectra (each spectrum was averaged over 500 shots). (b) Average spectra from the beginning of the scan shown in (a), up to spectrum #70. The blue curve corresponds to a CEP of ϕ_0 and the green one to a CEP of $\phi_0 + \pi/2$. The average is performed over 40 spectra (corresponding to a total of 20 000 shots). The shaded area represents the $2\sigma_{\text{rms}}$ taking into account fluctuations of the charge and the energy distribution. The data were taken using a supersonic jet and the laser intensity was $3 \times 10^{18} \text{ W cm}^{-2}$.

qualitative interpretation in this respect as the injected charge is indeed higher for small positive chirps [42].

4.2. Carrier envelope phase (CEP) effects

As the laser pulse is nearly composed of a single light cycle, the CEP is expected to have an effect on injection and acceleration. In [53], the effect of the CEP in an LPA was studied. It was shown that the CEP can have an observable effect on the electron energy distribution when ionization injection occurs. Indeed, changing the CEP in near-single-cycle pulses changes both the amplitude and the phase of the most intense laser cycle. Therefore, if one considers that most of the trapped electrons have been ionized by the most intense cycle, the CEP will typically control the exact initial conditions of the trapped electron through the phase, and also the number of injected electrons through the amplitude of the most intense cycle [53]. It is important to note that the absolute CEP is no longer conserved as the laser pulse propagates in the plasma because the group velocity v_g is different from the phase velocity v_ϕ . We define the phase slippage length as the propagation length needed to dephase the CEP by 2π . The phase slippage length reads:

$$L_{2\pi} = \frac{c}{v_\phi - v_g} \lambda_0 \simeq \frac{n_c}{n_e} \lambda_0, \quad (5)$$

where the right-hand side was obtained assuming that $n_e/n_c \ll 1$. In our case, this typically gives $L_{2\pi} = 8 \mu\text{m}$. Therefore, CEP effects on the electron beam can be reasonably expected, provided that the injection process happens in a fraction of $L_{2\pi}$, which is a very restrictive condition.

Our laser system is currently able to produce CEP controlled laser pulses, with a typical phase stability of 150 mrad rms (including an average over 30 shots for each CEP measurement). We have performed numerous CEP scans where no detectable effect could be observed, probably because CEP effects are easily washed out when injection occurs on

extended distances, as in figure 8. However, we have obtained clear evidence of CEP effect in some scans. Figure 10(a) shows a cascade plot of electron spectra obtained while the CEP is cycled from 0 to $\pi/2$. Note that the absolute CEP ϕ_0 is not known, we only record relative changes. In figure 10(a) the high energy part of the spectrum at 500 keV clearly disappears when using a $\pi/2$ CEP, especially at the beginning of the scan. This effect repeats itself over a couple of CEP cycles and then tends to disappear toward the end of the scan, indicating its extreme sensitivity to all experimental parameters and variations. Averaging the electron spectra involved in the first CEP cycle (from spectrum 1 to spectrum 70), as shown in figure 10(b) clearly shows the change in electron spectrum, well above the rms error bars.

These preliminary results suggest that the CEP can play a significant role in the electron beam production. These effects need to be further studied and confirmed because in these initial experiments, the accelerator produced rather low energy beam $< 1 \text{ MeV}$. This was probably due to an imperfect focal spot resulting in a lower laser intensity ($3 \times 10^{18} \text{ W cm}^{-2}$ instead of $6 \times 10^{18} \text{ W cm}^{-2}$ as in the previous supersonic jet experiments). It would be highly desirable to accelerate electrons in the multi MeV range and restrict electron injection to ionization triggered injection.

5. Conclusion

Our results firmly establish the scalability of LPAs to the low laser energy range, enabling the use of smaller and higher repetition rate lasers. We demonstrated routine operation of a kHz laser plasma accelerator in the multi-MeV range, with highly stable electron energy distribution. By increasing the repetition rate by several orders of magnitude compared to the state-of-the-art, applications such as the ultrafast probing of materials are now within reach. At the moment, the limiting

factor for such applications is the charge fluctuations, amounting to about 10% rms. Understanding the origins of these remaining fluctuations will be necessary for providing a competitive source that could truly be of interest to users. This might imply setting up more controlled injection schemes, such as density transition injection in a specially tailored shocked gas nozzle [41]. There is still a lot of room for optimization of the beam quality but it is unlikely that the energy spread reaches the percent level, as required for ultrafast diffraction for example. Therefore, beam transport and filtering will also be crucial to move from the proof of concept to usable electron sources [54].

Acknowledgments

This work was funded by the European Research Council (ERC Starting Grant FEMTOELEC) under Contract No. 306708. Financial support from the Région Île-de-France (under contract SESAME-2012-ATTOLITE), the Agence Nationale pour la Recherche (under contracts ANR-11-EQPX-005-ATTOLAB and ANR-14-CE32-0011-03) and the Extreme Light Infrastructure-Hungary Non-Profit Ltd (under contract NLO3.6LOA) is gratefully acknowledged.

ORCID iDs

J Faure  <https://orcid.org/0000-0003-0538-5774>
M Ouillé  <https://orcid.org/0000-0002-1295-6419>

References

- [1] Miller R J D 2014 *Science* **343** 1108–16
- [2] Bostedt C, Boutet S, Fritz D M, Huang Z, Lee H J, Lemke H T, Robert A, Schlotter W F, Turner J J and Williams G J 2016 *Rev. Mod. Phys.* **88** 015007
- [3] Bigot J Y, Vomir M and Beaurepaire E 2009 *Nat. Phys.* **5** 515
- [4] Fausti D, Tobey R I, Dean N, Kaiser S, Dienst A, Hoffmann M C, Pyon S, Takayama T, Takagi H and Cavalleri A 2011 *Science* **331** 189–91
- [5] Zewail A H and Thomas J M 2009 *4D Electron Microscopy* (London: Imperial College Press)
- [6] Sciaini G and Miller R J D 2011 *Rep. Prog. Phys.* **74** 096101
- [7] Weathersby S P et al 2015 *Rev. Sci. Instrum.* **86** 073702
- [8] Emma P et al 2010 *Nat. Photon.* **4** 641
- [9] Maxson J, Cesar D, Calmasini G, Ody A, Musumeci P and Alesini D 2017 *Phys. Rev. Lett.* **118** 154802
- [10] Tajima T and Dawson J M 1979 *Phys. Rev. Lett.* **43** 267–70
- [11] Esarey E, Schroeder C B and Leemans W P 2009 *Rev. Mod. Phys.* **81** 1229–85
- [12] Lundh O, Lim J, Rechatin C, Ammoura L, Ben-Ismaïl A, Davoine X, Gallot G, Goddet J P, Lefebvre E, Malka V and Faure J 2011 *Nat. Phys.* **7** 219–22
- [13] Buck A, Nicolai M, Schmid K, Sears C M S, Savert A, Mikhailova J M, Krausz F, Kaluza M C and Weisz L 2011 *Nat. Phys.* **7** 543–8
- [14] Corde S, Ta Phuoc K, Lambert G, Fitour R, Malka V and Rousse A 2013 *Rev. Mod. Phys.* **85** 0034–6861
- [15] Ta Phuoc K, Corde S, Thauray C, Malka V, Tafzi A, Goddet J P, CShah R, Sebban S and Rousse A 2012 *Nat. Photon.* **6** 308–11
- [16] He Z H, Hou B, Lebailly V, Nees J A, Krushelnick K and Thomas A G R 2015 *Nat. Commun.* **6** 7156
- [17] Muroya Y, Lin M, Han Z, Kumagai Y, Sakumi A, Ueda T and Katsumura Y 2008 *Radiat. Phys. Chem.* **77** 1176–82
- [18] He Z H, Hou B, Easter J H, Faure J, Krushelnick K, Nees J A and Thomas A G R 2013 *New J. Phys.* **15** 053016
- [19] Beaurepaire B et al 2015 *Phys. Rev. X* **5** 031012
- [20] He Z H, Thomas A G R, Beaurepaire B, Nees J A, Hou B, Malka V, Krushelnick K and Faure J 2013 *Appl. Phys. Lett.* **102** 064104
- [21] He Z H, Beaurepaire B, Nees J A, Gallé G, Scott S A, Pérez J R S, Lagally M G, Krushelnick K, Thomas A G R and Faure J 2016 *Sci. Rep.* **6** 36224
- [22] Salehi F, Goers A J, Hine G A, Feder L, Kuk D, Miao B, Woodbury D, Kim K Y and Milchberg H M 2017 *Opt. Lett.* **42** 215–8
- [23] Mordovanakis A G et al 2009 *Phys. Rev. Lett.* **103** 235001
- [24] Bocoum M, Thévenet M, Böhle F, Beaurepaire B, Vernier A, Jullien A, Faure J and Lopez-Martens R 2016 *Phys. Rev. Lett.* **116** 185001
- [25] Feister S et al 2017 *Opt. Express* **25** 18736–50
- [26] Pukhov A and Meyer-ter-Vehn J 2002 *Appl. Phys. B* **74** 355–61
- [27] Lu W, Huang C, Zhou M, Mori W B and Katsouleas T 2006 *Phys. Rev. Lett.* **96** 165002
- [28] Faure J, Glinec Y, Pukhov A, Kiselev S, Gordienko S, Lefebvre E, Rousseau J P, Burgu F and Malka V 2004 *Nature* **431** 541–4
- [29] Geddes C G R, Tóth C, van Tilborg J, Esarey E, Schroeder C B, Bruhwiler D, Nietzer C, Cary J and Leemans W P 2004 *Nature* **431** 538–41
- [30] Mangles S P D et al 2004 *Nature* **431** 535–8
- [31] Lu W, Tzoufras M, Joshi C, Tsung F S, Mori W B, Vieira J, Fonseca R A and Silva L O 2007 *Phys. Rev. ST Accel. Beams* **10** 061301
- [32] Mori W B 1997 *IEEE J. Quantum Electron.* **33** 1942–53
- [33] Ren C, Duda B J, Hemker R G, Mori W B, Katsouleas T, Antonsen T M Jr and Mora P 2001 *Phys. Rev. E* **63** 26411
- [34] Faure J, Glinec Y, Santos J J, Ewald F, Rousseau J P, Kiselev S, Pukhov A, Hosokai T and Malka V 2005 *Phys. Rev. Lett.* **95** 205003
- [35] Sun G, Ott E, Lee Y C and Guzdar P 1987 *Phys. Fluids* **30** 526–32
- [36] Borisov A B, Borovskiy A V, Shiryayev O B, Korobkin V V, Prokhorov A M, Solem J C, Luk T S, Boyer K and Rhodes C K 1992 *Phys. Rev. A* **45** 5830
- [37] Leemans W P, Nagler B, Gonsalves A J, Tóth C, Nakamura K, Geddes C G R, Esarey E, Schroeder C B and Hooker S M 2006 *Nat. Phys.* **2** 696–9
- [38] Leemans W P et al 2014 *Phys. Rev. Lett.* **113** 245002
- [39] Böhle F et al 2014 *Laser Phys. Lett.* **11** 095401
- [40] Rae S C 1993 *Opt. Commun.* **97** 25
- [41] Schmid K and Weisz L 2012 *Rev. Sci. Instrum.* **84** 053304
- [42] Guénot D et al 2017 *Nat. Photon.* **11** 293–6
- [43] Lifschitz A, Davoine X, Lefebvre E, Faure J, Rechatin C and Malka V 2009 *J. Comput. Phys.* **228** 1803–14
- [44] Gustas D, Guénot D, Vernier A, Dutt S, Böhle F, Lopez-Martens R, Lifschitz A and Faure J 2018 *Phys. Rev. Accel. Beams* **21** 013401
- [45] Nuter R, Gremillet L, Lefebvre E, Lévy A, Ceccotti T and Martin P 2011 *Phys. Plasmas* **18** 033107
- [46] McGuffey C et al 2010 *Phys. Rev. Lett.* **104** 025004
- [47] Pak A, Marsh K A, Martins S F, Lu W, Mori W B and Joshi C 2010 *Phys. Rev. Lett.* **104** 025003

- [48] Geddes C G R, Nakamura K, Plateau G R, Tóth C, Cormier-Michel E, Esarey E, Schroeder C B, Cary J R and Leemans W P 2008 *Phys. Rev. Lett.* **100** 215004
- [49] Faure J, Rechatin C, Lundh O, Ammoura L and Malka V 2010 *Phys. Plasmas* **17** 083107
- [50] Beaulieu B, Lifschitz A and Faure J 2014 *New J. Phys.* **16** 023023
- [51] Schmid K, Buck A, Sears C M S, Mikhailova J M, Tautz R, Herrmann D, Geissler M, Krausz F and Veisz L 2010 *Phys. Rev. ST Accel. Beams* **13** 091301
- [52] Schmid K *et al* 2009 *Phys. Rev. Lett.* **102** 124801
- [53] Lifschitz A F and Malka V 2012 *New J. Phys.* **14** 053045
- [54] Faure J, van der Geer B, Beaulieu B, Gallé G, Vernier A and Lifschitz A 2016 *Phys. Rev. Accel. Beams* **19** 021302

Titre : L'accélération des électrons relativistes à haute cadence dans les sillages plasma générés par des impulsions laser de quelques cycles optiques

Mots clés : accélération des particules, laser, plasma, sillage

Résumé : Le progrès continu de la technologie laser a récemment permis l'avancement spectaculaire d'accélérateurs de particules par onde de sillage. Cette technique permet la génération de champs électriques très forts, pouvant dépasser de trois ordres de grandeurs ceux présents dans les accélérateurs conventionnels. Les paquets de particules ainsi générés peuvent atteindre des durées de l'ordre de la femtoseconde, qui en fait un outil prometteur pour la réalisation d'expériences de diffraction ultra-rapide avec une résolution inégalée. Le taux de répétition est important pour une bonne statistique de mesure. Notre groupe a utilisé un laser de pointe développé au laboratoire par le groupe PCO générant des impulsions de quelques millijoules, d'une durée

de 3.4 fs - à peine 1.3 cycle optique - à une cadence de 1 kHz, pour accélérer des électrons par onde de sillage. Ce travail de thèse présente d'une part la première démonstration d'un accélérateur des particules relativistes opéré dans le régime de la bulle à haute cadence. L'utilisation de buses microscopiques a permis l'obtention de charges de dizaines de pC par tir. De plus, cette thèse vise à l'élargissement de notre compréhension des lois d'échelle d'accélération laser-plasma. Nous espérons que notre travail visant à la fiabilisation et l'optimisation de cette source permettra à terme de proposer un instrument accessible et fiable à la communauté scientifique, que ce soit pour la diffraction d'électrons, l'irradiation ultra-brève d'échantillons ou la génération de rayons X.

Title : High-repetition-rate relativistic electron acceleration in plasma wakefields driven by few-cycle laser pulses.

Keywords : particle acceleration, laser, plasma, wakefield

Abstract : Continuing progress in laser technology has enabled dramatic advances in laser wakefield acceleration (LWFA), a technique that permits driving particles by electric fields three orders of magnitude higher than in conventional radio-frequency accelerators. Electron bunches achieved this way may reach durations of the order of a femtosecond, making them a candidate tool for ultrafast diffraction experiments with unprecedented temporal resolution. High repetition rate is desirable to improve data collection statistics and thus wash out shot-to-shot fluctuations inherent to plasma accelerators. Our group utilized a cutting edge laser system producing few-mJ pulses

compressed nearly to a single optical cycle (3.4 fs) to demonstrate for the first time an MeV-grade particle accelerator with properties characteristic to the well-known bubble regime operating at 1 kHz repetition rate. We further investigate the plasma density profile and exact laser pulse waveform effects on the source output, and show that using special gas microjets a charge of tens of pC/shot can be achieved. We expect this technique to lead to a generation of highly accessible and robust instruments for the scientific community to conduct UED experiments or to be used for other applications. This work also serves to expand our knowledge on the scalability of laser-plasma accelerators.

